Development of a low-cost multi-parameter probe for marine and continental waters

Raul Sanchez Olvera

RÉPUBLIQUE FRANÇAISE
Liberté Égalité Fraternité

Université de Toulouse

Doctorat de l'Université de Toulouse

préparé à l'Université Toulouse III - Paul Sabatier

Développement d'une sonde multiparamètres à bas coût pour les eaux marines et continentales

---

Thèse présentée et soutenue, le 11 juin 2024 par

Raul SANCHEZ OLVERA

École doctorale
GEETS - Génie Electrique Electronique,Télécommunications et Santé : du système au nanosystème

Spécialité
MicroNano Systèmes

Unité de recherche
LAAS - Laboratoire d'Analyse et d'Architecture des Systèmes

Thèse dirigée par
Vincent RAIMBAULT et Mireille PUJO-PAY

Composition du jury
M. Philippe MENINI, Président, Université Toulouse III - Paul Sabatier
Mme Florence RAZAN, Rapporteure, Université de Rennes
M. Serge BERNARD, Rapporteur, CNRS Occitanie Est
M. Jonathan FLYE-SAINTE-MARIE, Examinateur, Université de Bretagne Occidentale
M. Vincent RAIMBAULT, Directeur de thèse, CNRS Occitanie Ouest
Mme Mireille PUJO-PAY, Co-directrice de thèse, CNRS Occitanie Est

To my dear Family

Acknowledges

This thesis work was achieved thanks to the support of various people whom I would like to gratefully acknowledge.

First of all, I would like to thank my supervisor Vincent RAIMBAULT for giving me this great opportunity to do my PhD at the renowned laboratory LAAS CNRS, I thank my supervisor for having guided me in this stage of my life, as well as having taught me to understand the physical phenomena used in this project in a more analytical and experimental way, to never give up and always go ahead no matter how difficult the project was, I thank him for all the patience he had with me and for all the teaching I received. I would like to emphasize that it was a great pleasure to have done my work with him because I always felt supported in good and bad times.

I thank my co-supervisor Mireille PUJO-PAY for giving me the opportunity to do this project, for guiding me to understand more applied topics to oceanography, of which I had a very basic knowledge, for giving me the necessary material to perform the necessary tests, for his kindness and availability.

I thank the MICA team for having received me and being present at all the meetings, for giving me feedback on my project and brainstorming ideas which helped me to find solutions to problems encountered during the internship.

It is important to thank all the support I received from the I2C team, especially Marie-Charline Blatche and Sandrine Assie-Souleille for all the necessary training I received for the correct use of the equipment found in the C211, and for being always available for any doubt or problem I had. I would also like to thank Vincent Brossa for having supported me in doing all the assembly work between components and PCBs, for his kindness and availability to do this work, without his knowledge and help this project would have been very difficult to achieve in this short period of time.

I would like to thank my family, who, although they were not with me, I always had their unconditional support at all times. I thank them for being there, every weekend to listen to my experiences lived and learned in this chapter of my life, I thank my dad, my mom and my brother for coming on this important day of my professional life.

I thank all the people I had the opportunity to meet in this project, especially all the people with whom I created a great friendship, because thanks to them I was never alone in this project, especially Refik Baris Yimaz, that although it seems that we have different personalities, was a person who supported me and gave me that boost that sometimes I needed to achieve what I had in mind, also to the members of the ELIAS, MEMS, ZARA team for having adopted me in their social circle, especially Ophelie Thomas-Chemin, Victor-Fourni, Elise Ponthier, Leonardo Cancellara, Damien Ourmet, Mohamed Ali, Benajmin Paret, Tao Wu, Vidushi Singh, Isabel Mendoza, Luis Abraham Lozano, Alejandro Hernandez Wences, Ernestro Garcia Ciganda, Nahuel Soparano Loto, Cecilia Daniela Páez, Camila Varela with whom I spent very pleasant moments inside and outside the laboratory.

Abstract

Observing the ocean is crucial for enhancing our comprehension of the impact climate change has on its metabolism, carbon uptake, primary production, and many other parameters directly linked to human society and all forms of life. While remote sensing delivers extremely valuable data, in-situ sensors are still essential for understanding the complex physical and biogeochemical processes. Various sensors are available on the market that can perform the required measurements, such as Argo floats: these floats are capable of making vertical profiles in the water column while measuring Conductivity, Temperature, and Depth. Biogeochemical-Argo (BGC) floats have recently added parameters such as oxygen, nitrate, chlorophyll, and pH to the list of variables acquired by standard Argo floats. Despite the success of this international program, one of the most limiting factors of these floats is directly related to their cost, which is between 10,000 and 15,000 euros per unit in the case of Argo, and around 100,000 euros for a BGC Argo. With about 40% of the world's population living within 100 km of the coast, reinforcing our ability to collect data in these key areas is particularly important for improving spatial and temporal measurements. Coastal areas cannot be accurately measured by remote sensing, and are currently not yet routinely covered by the Argo program; this is achieved by various programs and observatories (like COAST-HF).

For all these use-cases, oceanographers express the need to have access to affordable, compact, low-power, robust sensors with the ability to operate in-situ in remote locations without human intervention for long periods of time. The OpenProbe project aims to provide a low-cost device to complement these existing in-situ observation systems by developing a low-cost multi-parametric probe that can be integrated into all types of marine vectors (drones, profilers, buoys...). The parameters measured include conductivity, temperature, depth (CTD), dissolved oxygen, chlorophyll a, turbidity, and photosynthetically active radiation. The main objective is to deliver relevant accuracy, resolution, and dynamic range for each parameter to generate useful data, at a fraction of the cost of current solutions like multiparameter sondes. To do so, our approach builds upon the use of Commercial Off-The-Shelf (COTS) components which are repurposed from their primary use and turned into environmental sensors. Integration and marinization are achieved using rapid prototyping techniques like stereolithography, xurography, or overmolding. A modular, open-source/open-hardware strategy ensures that the system can be easily replicated or modified by potential users for specific use-cases, and paves the way towards citizen science projects to increase spatial and temporal coverage of coastal areas.

Ultimately, this work demonstrates the capability of building a functional multiparameter probe capable of measuring seven parameters for a manufacturing cost of less than 300€ with adequate performance to generate scientifically meaningful data. This data could, in the near future, contribute to the monitoring of coastal areas, understanding ocean circulation, climate processes, and phenomena related to climate change.

Resumé

L'observation de l'océan est essentielle pour mieux comprendre l'impact du changement climatique sur son métabolisme, l'absorption du carbone, la production primaire et de nombreux autres paramètres directement liés à la société humaine et à toutes les formes de vie. Si la télédétection fournit des données extrêmement précieuses, les capteurs in situ restent essentiels pour comprendre les processus physiques et biogéochimiques complexes. Il existe sur le marché différents capteurs capables d'effectuer les mesures requises, tels que les flotteurs Argo : ces flotteurs sont capables d'établir des profils verticaux dans la colonne d'eau tout en mesurant la conductivité, la température et la profondeur. Les flotteurs biogéochimiques-Argo (BGC) ont récemment ajouté des paramètres tels que l'oxygène, les nitrates, la chlorophylle et le pH à la liste des variables acquises par les flotteurs Argo standard. Malgré le succès de ce programme international, l'un des facteurs les plus limitants de ces flotteurs est directement lié à leur coût, qui se situe entre 10 000 et 15 000 euros par unité dans le cas d'Argo, et autour de 100 000 euros pour un BGC Argo. Étant donné qu'environ 40 % de la population mondiale vit à moins de 100 km des côtes, il est particulièrement important de renforcer notre capacité à collecter des données dans ces zones clés afin d'améliorer les mesures spatiales et temporelles. Les zones côtières ne peuvent pas être mesurées avec précision par télédétection et ne sont pas encore couvertes de manière routinière par le programme Argo ; ceci est réalisé par divers programmes et observatoires (comme COAST-HF).

Pour tous ces cas d'utilisation, les océanographes expriment le besoin d'avoir accès à des capteurs abordables, compacts, de faible puissance, robustes et capables de fonctionner in situ dans des endroits éloignés sans intervention humaine pendant de longues périodes. Le projet OpenProbe vise à fournir un dispositif à bas coût pour compléter ces systèmes d'observation in-situ existants en développant une sonde multi-paramétrique à bas coût qui peut être intégrée dans tous les types de vecteurs marins (drones, profileurs, bouées...). Les paramètres mesurés sont la conductivité, la température, la profondeur (CTD), l'oxygène dissous, la chlorophylle a, la turbidité et le rayonnement photosynthétiquement actif. L'objectif principal est de fournir une précision, une résolution et une gamme dynamique appropriées pour chaque paramètre afin de générer des données utiles, à une fraction du coût des solutions actuelles telles que les sondes multiparamètres. Pour ce faire, notre approche repose sur l'utilisation de composants commerciaux disponibles sur étagère (COTS) qui sont réaffectés de leur utilisation principale et transformés en capteurs environnementaux.

L'intégration et la marinisation sont réalisées à l'aide de techniques de prototypage rapide telles que la stéréolithographie, la xurographie ou le surmoulage. Une stratégie modulaire, open-source/open-hardware garantit que le système peut être facilement reproduit ou modifié par des utilisateurs potentiels pour des cas d'utilisation spécifiques, et ouvre la voie à des projets de science citoyenne visant à accroître la couverture spatiale et temporelle des zones côtières.

En fin de compte, ce travail démontre la capacité de construire une sonde multiparamétrique fonctionnelle capable de mesurer sept paramètres pour un coût de fabrication inférieur à 300 € avec des performances adéquates pour générer des données scientifiquement significatives. Ces données pourraient, dans un avenir proche, contribuer à la surveillance des zones côtières, à la compréhension de la circulation océanique, des processus climatiques et des phénomènes liés au changement climatique.

Table of Contents

Table of Figures

Chapter 1 General introduction

Observing the ocean is crucial to enhance our comprehension of the profound impact climate change has on society and all terrestrial life. The gathered information proves invaluable to policymakers and nations, offering guidance for transformative actions on a global, regional, and local scale. The importance of oceans is underlined by the Ocean Decade launched in January 2021 by the United Nations, where developing ocean observation tools and methods is one of the 10 identified challenges.

Beyond climate-related insights, ocean observing is indispensable for accurate weather forecasting. Timely information aids in issuing early warnings for hazards such as tsunamis, storm surges, and extreme waves, contributing to life-saving efforts and maintaining the efficiency of marine operations. In contemplating the future, fostering a sustainable ocean economy (blue economy) emerges as a promising avenue. This approach holds the potential to become a significant source of food, employment, and energy, laying the groundwork for long-term ecological and economic viability. The knowledge of the ocean changes can help us to understand the climate change, the forecast, and the ocean health:

- Climate: Each year, approximately a quarter of anthropogenic carbon dioxide (CO_2) emissions is absorbed by the ocean. Oceans play a role in absorbing 93% of excess heat. The exponential growth of the human population and the rise in atmospheric CO_2 concentration have precipitated significant shifts in climate patterns and extremes. The ocean, acting as a sink for these anthropogenic CO_2 emissions, undergoes a warming process, accompanied by increased acidity, with very tangible effects like coral bleaching. This rise in ocean temperatures contributes to a reduction in the solubility of oxygen, a vital element for the majority of marine life. Projections indicate an expansion of areas with compromised water quality due to decreased oxygen levels, referred to as Oxygen Minimum Zones (OMZ) or dead zones. The recent surge in ocean heat correlates with a steady increase in global sea levels. Melting ice in land-locked regions like Antarctica and Greenland contributes to additional water to ocean basins, raising sea levels but modifying the salinity levels. Simultaneously, the water expands due to elevated levels of greenhouse gases trapping heat in the atmosphere.

- Forecasts and warnings: With 40% of the world's population living within 100km of the coast, forecasting aids these communities, societies, and participants in the blue economy in safeguarding against challenges such as high waves, storm surges, tsunamis, or environmental disasters like oil or chemical spills. The information supplied by the GOOS (Global Ocean Observing System) is instrumental for organizations in the blue economy, furnishing them with crucial real-time and historical data encompassing the physical and ecosystem aspects of the ocean. This data enables them to strategically plan and execute their business processes.

- Ocean health: The well-being of the ocean yields human benefits encompassing food provision, carbon storage, tourism, recreation, and the sustenance of coastal livelihoods and economies. However, these aspects face threats, notably ocean acidification resulting from excessive human carbon dioxide (CO_2) emissions, which disrupts the entire marine food chain. Intensifying fishing practices pose a danger to predator fish populations like tuna or swordfish, crucial for maintaining the balance of prey fish such as herring. A decline in predator fish prompts fishermen to target lower trophic levels,

causing shifts in ocean ecosystems. Additionally, coastal areas contend with stressors like storm damage, flooding, and the erosion of natural buffers. Safeguarding against these challenges not only ensures the safety of people but also holds the potential to mitigate the loss of personal and economic properties, cultural landmarks, and natural resources.

The Global Climate Observing System (GCOS) is co-sponsored by the World Meteorological Organization (WMO), and is in charge in observing all types of variables related to global climate; these variables presented Figure 1.1 are called Essential Climate Variables (ECVs). The GOOS is related to the GCOS through its climate module, and its role extends to the constant observation of the ocean through so-called Essential Ocean Variables (EOVs). These variables play a vital role in connections between the ocean, one main component of the hydrosphere and the other Earth Systems[1]: the atmosphere, biosphere, cryosphere, and anthroposphere.

Key EOVs of significance encompass those associated with ocean circulation, as well as the distribution and transport of heat, salt, and other water properties. EOVs, being enduring in nature, allow the observing system to adapt and progress alongside technological advancements and enhanced capabilities. By prioritizing EOVs, ocean observations can seamlessly traverse diverse observing platforms, presenting an efficient and cost-effective strategy to attain an optimal global perspective for each identified EOV[1], [2].

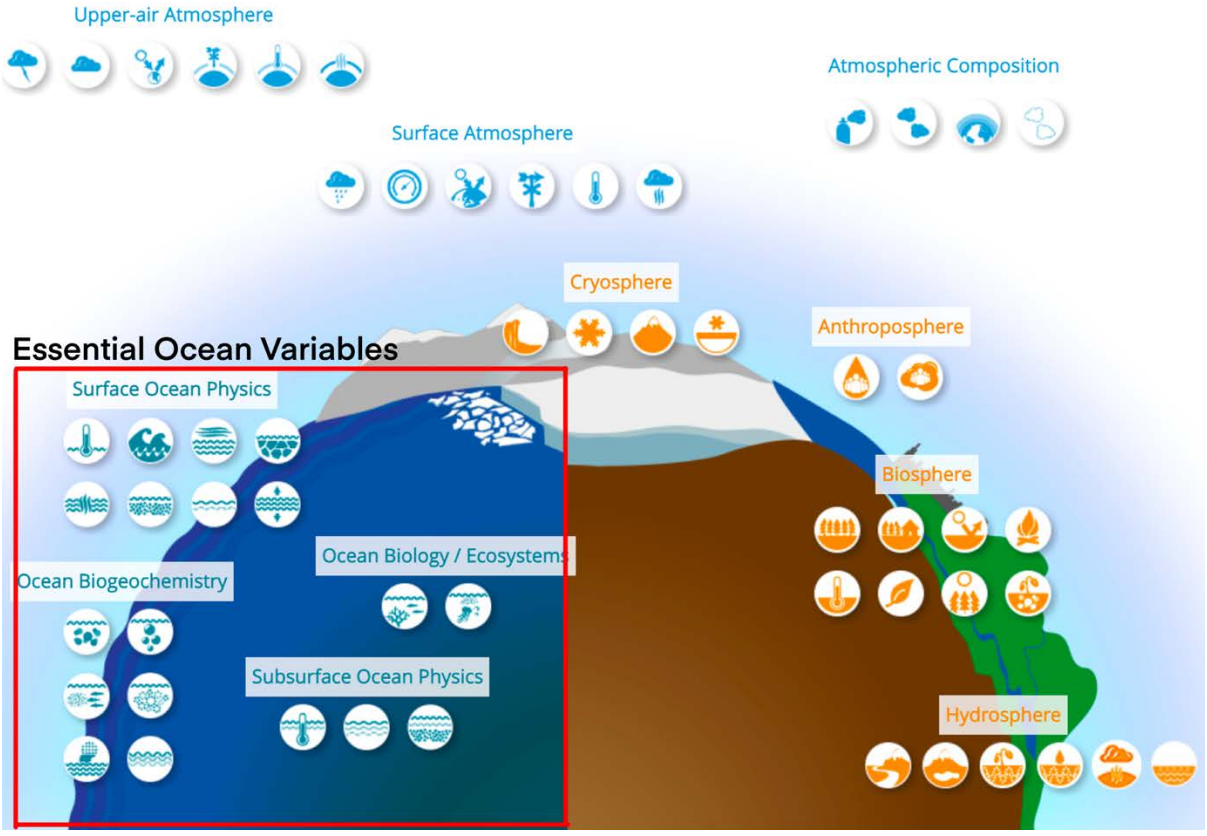

Figure 1.1 Essential Climate Variables[3]

In the ocean there are different layers, the sea surface and subsurface, each with distinct characteristics and features:

[1] https://mynasadata.larc.nasa.gov/basic-page/about-earth-system-background-information

- Temperature and Sunlight:
  - Sea Surface: Experiences direct exposure to sunlight and atmospheric influences, leading to higher temperatures compared to deeper layers. In this layer is where most of the ocean heat is exchanged with the atmosphere.
  - Subsurface: Temperature decreases with depth, and sunlight radiation is rapidly attenuated. Deeper layers may have more stable and lower temperatures.
- Biological Activity:
  - Sea Surface: Supports a significant amount of biological activity, as sunlight penetrates this layer, facilitating photosynthesis. It is home to phytoplankton, fish, and various marine organisms.
  - Subsurface: In this region the biological activity exists, however is generally lower compared to the sea surface. Deep-sea ecosystems are characterized by unique and adapted life forms.
- Oceanographic Observations:
  - Sea Surface: Easily accessible for direct observations, satellite monitoring, and other remote sensing techniques. Sea surface temperature, currents, and chlorophyll concentrations are often measured from this layer.
  - Subsurface: Requires more specialized equipment such as oceanographic instruments, profiling floats, and remotely operated systems for direct observations and measurements at different depths.
- Physical Characteristics:
  - Sea Surface: Exhibits dynamic features such as waves, wind-driven currents, and surface temperatures that are responsive to atmospheric conditions.
  - Subsurface: Features include ocean currents, thermoclines (temperature gradients), and salinity gradients, which may vary with different depths.

Understanding the differences between the sea surface and subsurface layers is essential for studying oceanography, marine biology, and climate change, as these layers play distinct roles in the functioning of the marine environment[4].

In the context of oceanographic observations in open ocean, and more especially in coastal areas where more than 40% of the population worldwide lives, there is a strong necessity to improve the spatial and temporal resolution of physical and bio-geochemical measurements. In the market there are numerous probes which can generate extremely accurate and valuable data, but these probes are expensive (from a few k€ to tens of k€ typ.), requires dedicated trained users, and sometimes cannot operate autonomously in-situ. This severely hinders the number of units that can be deployed, which leads to the situation where oceans are generally considered as undersampled, as highlighted more than 20 years ago by Walter Munk[5]. Oceanographers are advocating for alternative sensors and protocols to complement the actual observation systems, through the development of low-power, multiparameter probes capable of operating in situ autonomously for long periods of time, and deployable by non-specialists. This was notably underlined by the OpenMODs[2] project supported by the Partnership for Observation of the Global Ocean.

The most renown initiative for ocean observation that relies on in-situ autonomous sensors is Argo, an international program started in 1999 that measures water properties across the oceans using a fleet of automated instruments that drift with the ocean currents and move

[2] https://pogo-ocean.org/innovation-in-ocean-observing/activities/openmods-open-access-marine-observation-devices/

up and down between the surface and a mid-water level. The data that Argo collects describes the temperature and salinity of the water and some of the floats measure other properties that describe the biology/chemistry of the ocean. The Argo program is now collecting approximately 12,000 data profiles each month (400 a day). This greatly exceeds the amount of data that can be collected below the ocean surface by any other method.

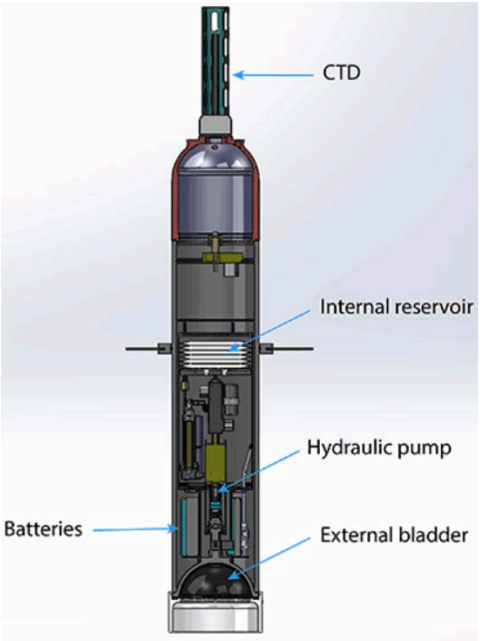

Figure 1.2 Schematic of Argo SOLO-II float. Each float moves vertically by inflating or deflating an external bladder to change its buoyancy, drifts freely with the currents, and measures a profile of temperature and salinity from a depth of 2000 meters to the surface every 10 days

Each Argo float cost $20,000 for regular Argo which has the CTD variables measurements, and around $150,000 for Biogeochemical-Argo which adds biogeochemical variables such as oxygen, nitrate, pH, chlorophyll *a*, suspended particles, and downwelling irradiance to the CTD. Due to their size (height up to 1.75 m), deploying the floats is mostly performed by oceanographic ships; operational costs, that includes deploying the float, handling data and managing the project is considered to double the aforementioned cost. The float's buoyancy is automatically adjusted so that, as it sinks, it eventually stabilizes at a pre-set level, usually 1000m, where it drifts during ten days. It then descends to a so-called profiling depth, between 2000 to 6000 m depth and finally return to the surface while measuring the variables listed above. The buoyancy adjustment is achieved thanks to an internal battery-driven pump that transfers oil between a reservoir inside the float and an external bladder. This makes the float first descend to the programmed diving depth and then return to the surface measuring ocean properties as it rises. The data and the float position are transmitted to receiving stations on shore through Iridium satellite communication. The float then sinks again to repeat the 10-day cycle until its batteries are exhausted. A typical Argo float will work for about 4 years, performing approximately 150 profiles during his lifetime which is limited by the battery life, hence the power consumption of the bladder, the sensors, and the data transmission combined.

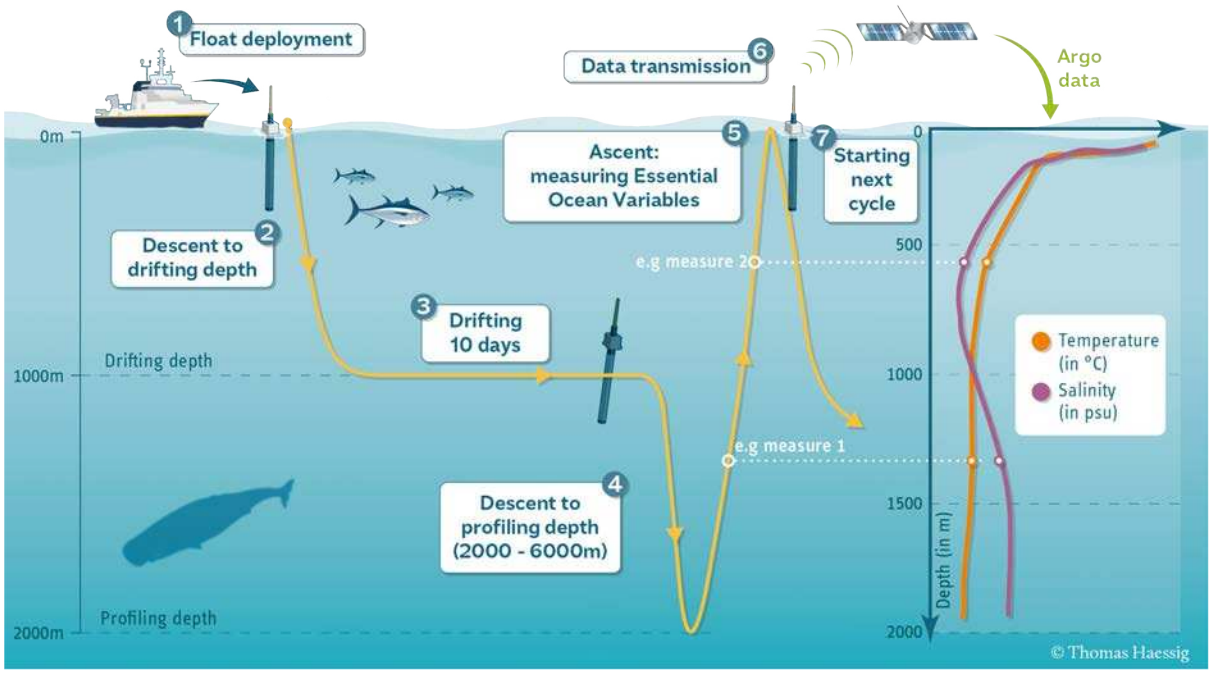

Figure 1.3 Typical cycle of an Argo float profiler.

The Argo float measurements are sent to regional data centers where they are given rigorous quality checks and then passed to two global data centers from where they can be accessed by anyone wishing to use them. Argo data are stored in data files that first must be decoded before being readable. To address this difficulty for non-experts, several websites and web applications have been developed to showcase and interact with Argo data and metadata without having to understand how to decode it. The Argo Program is managed by international teams of scientists and data experts who ensure that the program is run as efficiently and effectively as possible and that standards are maintained at the highest possible level. Argo is part of the GCOS and the GOOS. The total annual cost of the Argo program is estimated at $40million per year.[6]

The necessity of having low-cost alternatives is increasing and is of great importance for oceanographic research, especially in coastal areas which are currently not covered by the Argo program, and where remote sensing techniques suffers from severe limitations. As the commercial market for these sensors is small, only specialized SMEs are commercializing such products. Combined to the difficulties of developing efficient sensors able to work in challenging environments like seawater, and the long research and development time required, the cost of multiparameter probes spans from 3000 $ to more than 80000 $ depending on the parameters addressed, and more than 100000 $ with remote data transmission.

With this context, the main objective of this thesis project is to develop a viable alternative to commercial multiparameter probes. In this work, the development of a low-cost open-source multiparameter probe is presented. This multiparameter probe, dubbed OpenProbe, has to measure different parameters which are all parts of the EOVs we decided to measure the following parameters: temperature, pressure, conductivity, chlorophyll-a, dissolved oxygen, turbidity, and photosynthetically active radiation, on the other hand, even though it is important to measure Ph in seawater for several reasons such as marine life health, ecosystem balance, carbon cycle monitoring, human impact and environment monitoring [7], [8], and there are several know methods to measure it, as Glass Electrode pH, Ion-Sensitive Field Effect Transistor (ISFET) Sensors, Spectrophotometric Methods, pH Indicator Papers

and Strips, Automated pH Sensors on Buoys and Floats of which the most used for measurements in seawater is the Ion-Sensitive Field Effect Transistor sensors, because these sensors are favored for their durability and suitability for continuous monitoring, making them ideal for both handheld devices and larger sensors deployed on ships and buoys [7], [9]. We decided not to include the Ph sensor in this project due to its high production cost which would considerably increase the final price of our sensor, in addition to the difficulty and technology necessary to develop it [10], [11]. The complete OpenProbe system includes electronics, optics, programming, data acquisition, signal processing, and marinization using 3D printing, with a total cost of about 350 € in raw materials.

Developing a significantly more affordable multiparameter probe, while maintaining a sufficiently high level of performance to offer scientifically meaningful data is pivotal in the development of in-situ observation systems in marine environments, and one of the possible approaches to improve the spatial and temporal resolution of the measurements. Our challenge is to realize this probe using commercially available electronic components for easy replication, and target coastal areas within 20 km from the shore (typical communication distance achievable with LoRa protocol) and at a depth of 100 m, with low-power consumption and a compact size to facilitate its deployment using vessels of opportunity[12].

The manuscript structure reflects the specificity of the OpenProbe project, during which a complete system including seven sensors was developed. Instead of separating the whole manuscript in state of the art, design, fabrication and characterization chapters, it was preferred to describe each sensor (or group of sensors) in its own chapter, and conclude with a final integration chapter. This structure should improve readability of the manuscript, as some readers will probably be interested by individual sensors and not necessarily the complete multiparameter probe. It is also more appropriate for the state of the art, as there is currently only a handful articles or thesis on complete multiparameter probes, most of the published works addressing only one or a couple of sensors. A short description of each chapter is given below.

Chapter 2 focuses on Conductivity, Temperature and Depth (pressure) also known as CTD. It explains what conductivity in water is, as well as the existing methods to measure conductivity in-situ, using contact or non-contact methods. Each of the described sensors has a higher efficiency in different conductivity ranges. It also explains the problems that can occur when using these sensors over a long period of time due to the biofouling or polarization effect. In this project it was decided to use the two-electrode method due to its simplicity and its compatibility with our low-cost, low-power objectives. While this method is usually favored for low conductivity levels due to polarization effects, the latter can be mitigated by using a high frequency excitation source and a larger cell constant. The device is described, specifying the electronic components, as well as the electrodes that were used, the microcontroller, and the communication between the sensor and the computer, along with the experiments that were carried out in laboratory conditions from real seawater samples, in comparison with existing commercial sensors. Furthermore, it is explained why it is important to collect data on temperature and depth, as well as the strong relationship between these two parameters. For temperature and depth, low-cost commercial sensors were used with minor modifications to make them usable underwater using rapid-prototyping techniques.

Chapter 3 presents the development of a turbidimeter, to quantify turbidity, which can be defined as water clarity and is obtained by measuring the number of particles in the

sample. The reference methods are presented and described; in this project it was decided to use the optical method, which can be based either on attenuation or scattering of the light due to the particles in the sample. This method basically consists of LEDs as the excitation source and photodetectors for the detection of the attenuated or scattered light. As in the previous chapter, the device is also described, specifying the electronic components such as the LEDs, the photodetectors and the electronics necessary for data acquisition. In this case, designs were made on standard and flexible Printed Circuit Boards (PCB), that were integrated into 3D printed enclosures with silicone overmolding to make them water resistant and create the optical ports. Tests were carried out under laboratory conditions using the Formazin 4000 standard to measure different turbidity values. Intercomparison with a calibrated, commercial handheld sensor was conducted to demonstrate the capabilities of the OpenProbe turbidity sensor.

Chapter 4 describes the development of a dissolved oxygen sensor. Conventional methods are presented and discussed against the OpenProbe objectives of a low-cost, in-situ sensor. To measure this parameter, we chose to build an oxygen optode, using commercially available sensor spots (containing the luminophore), and developing a custom opto-electronic devices to perform phase-shift measurements and quantify the fluorescence decay time which is related to the dissolved oxygen concentration. The chapter explains in detail how this measurement technique operates, and the different prototypes that were conceived, built and evaluated in a laboratory environment. The developed oxygen optode is finally intercompared with a commercial oxygen meter, the PreSens Fibox 4.

Chapter 5 touches on the Photosynthetically Active Radiation (PAR) measurement, which is a useful indicator to estimate the quantity of light which is available for photosynthesis. This parameter is particularly interesting when used in conjunction with other parameters related to primary producers, like chlorophyll a, dissolved oxygen or temperature. In this chapter we describe how PAR is typically measured, and present relevant academic works which are mostly related to land plants. We then report on our approach to develop such a sensor, which is based on a commercially available, multi-spectral optical sensor that is slightly modified by the adjunction of a diffuser, and programmed to obtain good quality PAR data. The multi-spectral features of this sensor are also exploited to quantify the diffuse attenuation coefficient K_d, a parameter which is of high interest for remote sensing applications, and we present how it can be used for Ocean Color determination, K_d and ocean color both being EOV products.

Chapter 6 tackles the measurement of chlorophyll a, which is a photopigment that is present in all species capable of photosynthesis, and is one of the most widely used proxy to estimate primary production in the oceans. The reference methods currently in use, as well as the state of the art on chlorophyll a sensors is presented, followed by the description of two prototypes of chlorophyll a fluorometers that were developed in this work. Emphasis is put on the difficulty to achieve the required sensitivity to quantify in-situ, in-vivo chl. a, especially in daylight conditions, due to the nature of this measurement. A synchronous detection circuit is developed and characterize against Fluorescein, a molecule which is often used as a calibration standard for chl. a fluorometer. Encouraging results are obtained, and a few improvements are proposed to further refine the already satisfying chl. a fluorometer, especially for low-primary productivity areas.

Chapter 7 concludes this manuscript by discussing the integration of all the sensors developed through chapters 2 to 6. While were not able to test this complete prototype due to a lack of time, we managed to design and build a full multiparameter probe as a proof of concept. The bill of materials (BOM) is presented and estimated at around 350 € for a single unit, which is on the same order of magnitude that the targeted cost at the beginning of the OpenProbe project. Several ways of reducing this BOM cost are suggested. This chapter ends with a final conclusion and the perspectives offered by the OpenProbe multiparameter probe.

Chapter 2 CTD: Conductivity, Temperature, and Pressure

2.1 Introduction

The conductivity, temperature, and depth (CTD) is an ubiquitous instrument to measure the physical characteristics through the water column. While providing essential contextual data for other parameters such as dissolved oxygen, fluorescence, pH, optical backscattering (turbidity) and many other bio-geochemical variables, oceanographers generally still call it CTD multiparameter probes that measures additional parameters. The water column extends from the ocean surface to the seafloor; it is essential for ocean observers to study the physical and chemical properties through the water column in order to identify how water circulates around the ocean. The primary function of the CTD is to detect how the conductivity and temperature of the water column changes at different depth. Salinity, which exhibit a robust correlation with conductivity, and temperature are the two main properties used to identify water masses and are probably the most common measurements made in the ocean with the first instruments introduced int the late 1960's. When combined with temperature, pressure, and salinity measurements can be used to determine seawater density, which allows to define water masses and then predict their movements [13]. For water samples collection, a rosette is commonly used in combination with a CTD, in order to grab samples at specific depths using Niskin bottles. Figure 2.1.

When the CTD is used for a long-term data acquisition in seawater, like it is the case for Argo floats with deployment times of several years, it is subject to biofouling. The biofouling is the growth of marine organisms on and inside the sensors, a phenomenon which is more common in productive areas, like warm surface waters[14]. In such use-cases, anti-foulant devices are required to keep the sensors clean and maintain their accuracy.

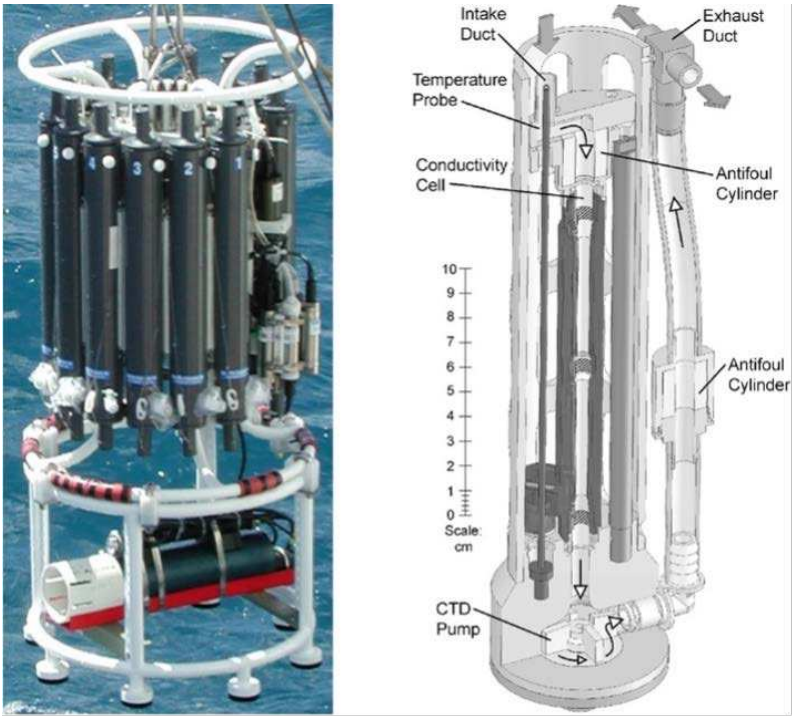

Figure 2.1 Left: CTD rosette runs profiles of the water column and along the way, collects discrete water samples in different bottles. Right: Schematic cross-section view of the Seabird SBE41 commonly used on Argo floats[15].

Several CTD sensors are currently used in the Argo program. Due to the nature of this program, very high accuracies and stabilities are required, with target values set at ± 0.005 °C for temperature, ± 0.01 PSS-78 for salinity and ± 5 dbar for pressure, and these criteria must be maintained globally, both spatially and temporally [16]. Sea-Bird company produced more than 10000 CTD sensors (SBE41) for Argo floats over the years, maintaining the high quality to meet the Argo criteria. Initially, when the Argo program started in 1999, this CTD had problems with accuracy and long-term stability, but these problems have greatly improved due to upgrades[17]. The SBE41 uses a thermistor and piezoelectric sensors for temperature and pressure measurements, respectively. For conductivity, from which salinity is calculated, electrodes are used inside a glass tube. The SBE41 CTD has special features that make it stable over the long term, mainly it is calibrated with proven long-term stability, it has an antifouling protection system to minimize biological growth on the sensors, and most importantly, it has a pumping system that directs the water flow over the temperature sensor and then over the conductivity sensor. A cross-section view of this CTD is shown Figure 2.1. This design helps to minimize salinity peaks, and the conduit and pump precisely coordinate the responses of the temperature and conductivity sensors, which allows for more stable and accurate salinity measurements. On the other hand, one of the disadvantages of depending on the pump is that if there is a failure in the pump it will affect the quality of the data taken, has a high energy consumption, which reduces the operating time for long-term data collection, as well as requiring additional maintenance for correct pump operation[16]. Another CTD used in the Argo program is the RBR*argo³*, which offers an alternative for CTD measurements without the need for a pump, in the 2000s the RBR introduced inductive conductivity cell technology method, which will be detailed in the methods section. Compared to the Seabird SBE41, the absence of a pump makes the RBR a lower power consumption alternative, which is crucial to the next generation of ocean gliders and Argo floats that are expected to sample for longer periods and carry more sensors. The power consumption is 90 percent lower than a common pumped CTD, while maintaining similar accuracy[18], [19], [20].

2.1.1 Conductivity

Conductivity is a measure of the ability of how well water conducts an electrical current, this property is directly affected by the presence of inorganic dissolved solids such as chloride, nitrate, sulfate, and phosphate anions (ions that carry a negative charge) or sodium, magnesium, calcium, iron, and aluminum cations (ions that carry a positive charge). The more ions that are present, the higher conductivity of water. For example, a 10% acid solution is a very good conductor because it contains many ions that transport the charge. In contrast to this, pure and ultra-pure water are bad conductors because they contain only few ions.

Conductivity has a temperature dependence, that is commonly expressed as a “relative change per degree Celsius”. This dependance is caused by the modification of the ion’s mobility, hence in most cases conductivity increase with temperature, with a typical coefficient of 2 % per Celsius degree [13][21].

The conductivity unit is defined as the reciprocal of the resistivity normalized to a cm^{-1} cube of a liquid at a specified temperature, by common use, the reciprocal of an ohm is called “mho”. Thus, units of conductivity in natural waters can be expressed in micromhos cm^{-1} (μmhos cm^{-1}), however the μSiemen/cm (μS/cm)[22]. Due to the temperature dependance of conductivity, the standardized method of reporting it is at 25° C[23].

Conductivity and salinity exhibit a robust correlation. To obtain the values for ocean salinity, it is necessary to know the temperature, pressure and conductivity. As the conductivity is not only dependent on the salinity of the seawater, is also a function of temperature and pressure, the impact of temperature and pressure on the measured conductivity must first be removed. This is achieved using a non-linear equation that is considered the international standard for computing salinity from conductivity. This is referred to as the Practical Salinity Scale 1978[24], or more commonly known as PSS-78 and it is also expressed in practical salinity units (PSU). Salinity is pivotal in oceanography. For example, changes in salinity caused by the climate change can harm the coral reefs[25]. The ocean's salinity profile reveals the changes in the seawater cycle. Measuring the seawater salinity over a long period in a specific sea area can benefit the marine observation, development and security[26], [27]. Given the simplicity of measuring conductivity, it became the go-to parameter to measure for estimating salinity and Total Dissolved Solids (TDS), both of which impact water quality and aquatic life. Salinity holds particular significance as it influences the solubility of dissolved oxygen. Higher salinity levels correspond to lower concentrations of dissolved oxygen. Specifically, oxygen is approximately 20% less soluble in seawater than in freshwater at the same temperature. This implies that, on average, seawater has a lower concentration of dissolved oxygen compared to freshwater sources. The impact of salinity on the solubility of dissolved gases is governed by Henry's Law, with the constant used undergoing changes based on salt ion concentrations[22], [28].

Conductivity is also routinely used as a water quality standard that measures how much salt is in the water. It ranges from 0 to 50,000 µS/cm. Sea water usually has a high conductivity of around 50,000 µS/cm, while freshwater has a low conductivity of 0 to 1,500 µS/cm. Salts are essential for the growth of plants and animals in waterways, but too much ions in freshwater can harm aquatic life [29]. For drinkable water, the World Health Organization (WHO) recommends that conductivity should not exceed 400µS/cm/.

2.1.2 Temperature and Depth

Considering temperature is crucial in water bodies observation, as it is influences most of the processes and bio-geo-chemical parameters. Several ambient conditions can influence water temperature. These factors encompass sunlight or solar radiation, heat transfer from the atmosphere, stream confluence, and turbidity. Shallow and surface waters tend to be more susceptible to the impact of these elements compared to deeper water. Beyond its direct effects, temperature plays a role in influencing various other parameters, potentially modifying both the physical and chemical properties of water. Therefore, it is essential to take into account water temperature when making determinations related to water quality[30].

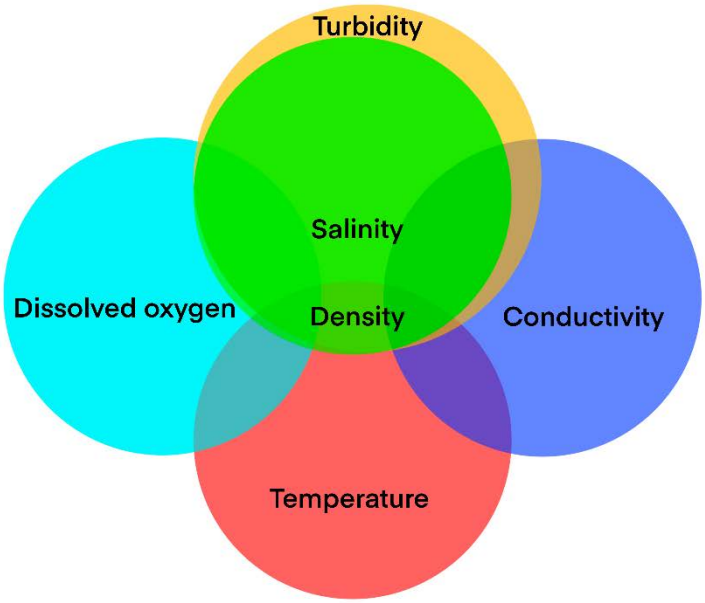

Figure 2.2 Water temperature affects other water quality parameter.

Besides, in aquatic life the water temperature has the capacity to impact the metabolic rates and biological activity of aquatic organisms, at the exception of few and big ones, because their internal body temperature is dependent on the environmental temperature. Consequently, it plays a role in determining the preferred habitats of various aquatic life forms. Certain organisms, especially aquatic plants, tend to thrive in warmer temperatures[30]. Additionally, temperature can impede plant respiration and photosynthesis. Algal photosynthesis, in general, tends to increase with rising temperatures, although different species may have distinct peak temperatures for optimal photosynthetic activity. Both above and below these optimal temperatures, photosynthesis tends to be diminished[31]. For most fishes, a 10°C rise in water temperature is associated with approximately doubling the rate of physiological functions. Temperature fluctuations can influence the behavioral choices of aquatic organisms, such as the inclination to move towards warmer or cooler waters after feeding, predator-prey responses, and decisions related to resting or migration routines[32]. Temperature affects the density of water, the solubility of constituents (such as oxygen in water)[23]. Besides, elevated water temperatures can enhance the solubility and, consequently, the toxicity of specific compounds[33]. Among these are heavy metals like cadmium, zinc, and lead, along with compounds such as ammonia. Not only does water temperature raise the solubility of toxic compounds, but it also affects an organism's tolerance limit. Mortality rates for zinc, for instance, are notably higher at temperatures exceeding 25°C compared to temperatures below 20°C[34], [35].

As previously mentioned, studying the ocean implies to localize each measurement in the water column, hence measuring depth with good precision is crucial. It is a fundamental aspect that oceanographers use to understand various processes and characteristics of the ocean. With an average depth of 3,700 meters, experts have divided the oceans into various layers according to their depths:

- Epipelagic Zone (0-200 meters): Also known as the sunlight zone, this is the topmost layer where sunlight penetrates, supporting photosynthesis and most marine life.
- Mesopelagic Zone (200-1000 meters): Often referred to as the twilight zone, sunlight is limited, and organisms here are adapted to low light conditions.

- Bathypelagic Zone (1000-4000 meters): No sunlight reaches this zone, and organisms have unique adaptations to survive in the dark.
- Abyssopelagic Zone (4000-6000 meters): The abyssal zone is characterized by extreme pressure, low temperatures, and diverse, specialized life forms.
- Hadalpelagic Zone (6000 meters to ocean floor): The hadal zone includes the ocean trenches, the deepest parts of the ocean, with unique geological and biological features[36]

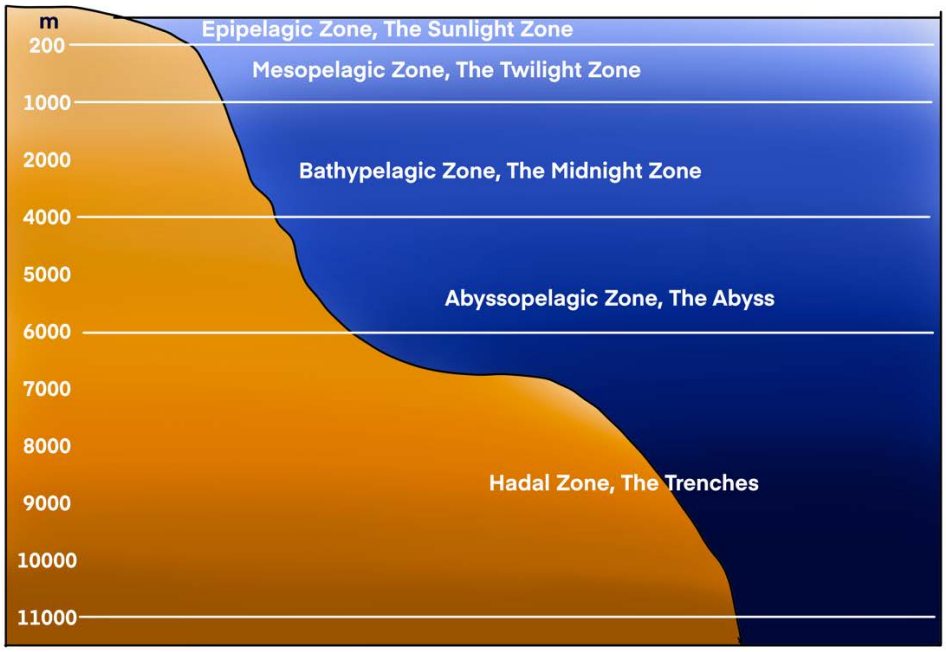

Figure 2.3 Ocean depth, different zones based on depth.

Understanding depth in oceanography is essential for comprehending the complex interactions within the marine environment. It provides insights into ocean circulation, marine life distribution, and the physical properties of the ocean at different layers.

Finally, it should be noted that there is a relationship between temperature and depth; the water gets colder with depth because cold, salty ocean water sinks to the bottom of the ocean basins below the less dense, warmer water near the surface. The sinking and transport of cold, salty water at depth, combined with the wind-driven flow of warm water at the surface, creates a complex pattern of ocean circulation called the global conveyor belt through a phenomenon called thermohaline circulation, which is illustrated Figure 2.4. Complex deep ocean currents driven by density variations in temperature and salinity are constantly replacing the bottom layer of ocean water with cooler water[37].

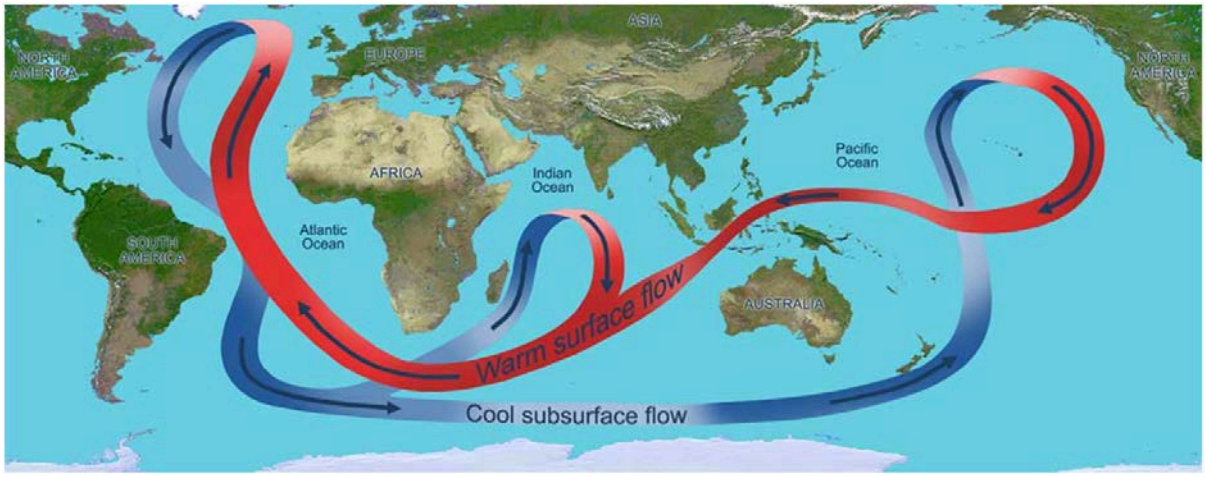

Figure 2.4 The global conveyor belt. Cold, salty water is dense and sinks to the bottom of the ocean, while warm water is less dense and remains on the surface.

Figure 2.5 shows a typical temperature profile for open water at different depths. In general, the surface water is the warmest water, because it is warmed by the sun's rays, which can only penetrate to depths of no more than 1000m in perfect conditions, but are in most cases limited to the first 200m of the water column. As warm water is less dense than cold water, it stays at the surface where it can be warmed even more. The temperature at these depths, between 100-200m is basically constant, and this layer is called the mixed layer. Below the mixed layer is the thermocline, where a rapid decrease in temperature occurs, which decreases with depth, finally below the thermocline the temperature of the ocean is already quite constant around 2 °C with a slight decrease with depth. These depths are considered as some most thermally stable regions of the Earth.

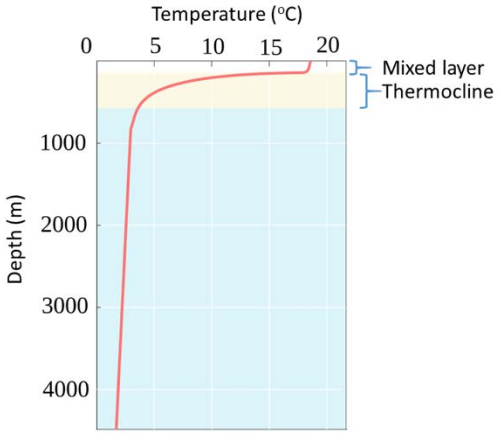

Figure 2.5 Typical open ocean temperature profile for a mid-latitude region, showing the mixed layer, thermocline, and relatively stable temperature at depth[38].

Temperature profiles will vary according to latitude, with the warmest temperature at the equator and the coldest at the poles. Temperature profiles can be divided into different latitude regions: low-latitude or tropical waters, mid-latitude waters, and high-latitude or polar waters as illustrated Figure 2.6. For water in tropical regions where the surface water is warmer, there is a drastic temperature drop in the thermocline zone, but water temperature in the mixed layer stays rather constant with seasonal changes. In comparison, temperature drop in the thermocline zone is less pronounced for mid-latitude waters, but the drop is more affected by seasonal changes, as these regions have the highest seasonal fluctuations in surface temperature, with a difference of 8 to 15 °C from summer to winter as shown Figure 2.6.

Finally, temperature drop in the thermocline zone is almost null, in the high latitude or polar regions, since both the surface and deep temperature are similar; with almost, and as in the low-latitude regions, there are no seasonal temperature changes in this region, no seasonal temperature changes [38]

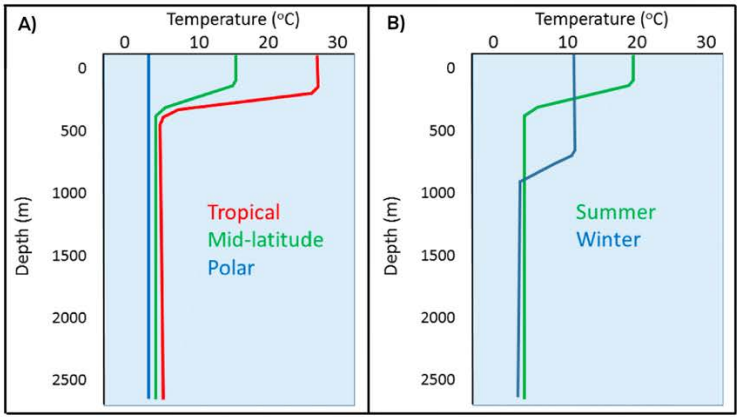

Figure 2.6 Temperature and depth profile. A) Profiles for low-latitude or tropical water, mid-latitude water, and high-latitude or polar water. B) Mid-latitude water at different season temperature, on summer and winter[38].

2.2 Measurement methods and state of the art

This section focusses on the most common methods to measure conductivity, temperature and depth (CTD). While the section will detail each of these parameters separately, it should be noted that several developments of complete low-cost CTDs can be found in the literature. Compared to our target objective of a complete multiparameter probe at around 100 €, which should be easy to replicate, the potential problems with the CTDs encountered in the literature are their manufacturing process, as they require microfabrication techniques which require the use of special equipment that is not easily accessible for replication [39], [40], [41], or their cost which ranges from $370 to more than $800 [42], [40], [43]. While most commercial CTDs are one order of magnitude more expensive, a commercial Decagon CTD (now sold as the Meter Hydros 21), the cheapest CTD on the market to our knowledge, is sold around $500.

The challenge in developing a low-cost CTD focuses more on the conductivity sensor, as solutions almost off-the-shelf are now available for temperature and pressure. The literature shows that most low-cost CTDs use the conductivity sensor provided by Atlas Scientific, which is based around a classic two-electrode setup (graphite electrodes) which costs approximately $165 in its cheapest version. While the performance of this sensor seems to satisfy some authors, some articles clearly highlight the large error compared to commercial CTDs, especially in the field intercomparison done by Méndez-Barrosso et al.[44]. As this Atlas Scientific conductivity sensor is widely used, we choose to evaluate it against another solution developed within this project, that does not require the use of special microfabrication equipment or the use of a clean room. For the conductivity, temperature and pressure sensors, we used readily available commercial sensors, which were adapted to be deployed underwater.

Conductivity sensors for water measurements can be classified in two categories, contact and non-contact sensors. For the contact sensors there are two and four-electrodes options, and for non-contact sensor there are inductive and optical option. Each of these options are briefly described in the next paragraphs.

2.2.1 Contact-based conductivity sensors

Two-electrodes

In this type of sensors, two-electrodes are immersed in the sample at a fixed distance. An AC voltage is applied to the electrodes to avoid the hydrolysis, because DC provides a constant electrical field that causes ions in the solution to move towards the electrodes. When these ions reach the electrodes, reactions can occur. For example, in solution with water, at the cathode, water can be reduced to form hydrogen gas and hydroxide ions, while at the anode, water can be oxidized to form oxygen gas and hydrogen ions. These reactions change the composition of the solution, which can affect the conductivity measurement. This is why AC excitation is often used instead, as it prevents the build-up of ions at the electrodes that leads to hydrolysis[45]. The AC voltage generates a current in the medium, with the cations moving to the negatively charged electrode, while the anions move to the positively charged electrode.

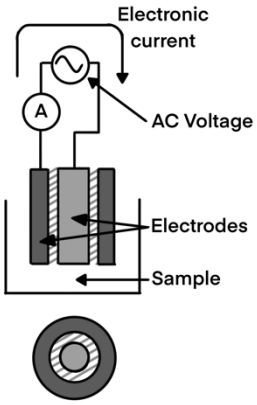

Figure 2.7. Two-electrodes sensor configuration

Conductivity is directly correlated with ion concentrations. However, when ion concentrations reach high levels, the Coulombic force increases. This electrostatic force induces mutual repulsion among ions, consequently diminishing the current. This phenomenon, known as polarization, manifests particularly in highly concentrated media, as shown Figure 2.8 [46], [47]. The two-electrode method is hence typically recommended for measuring low conductivity values.

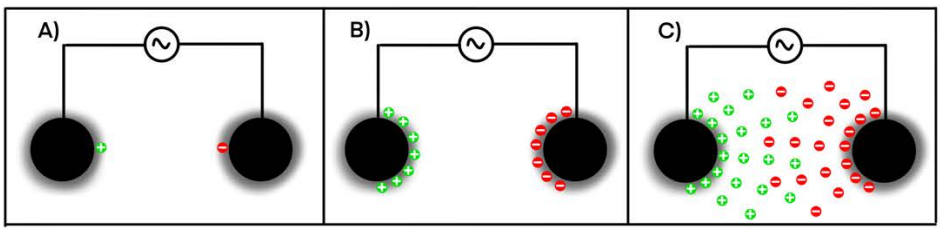

Figure 2.8. Two-electrodes method. A) Low ions concertation. B) High ions concentrations. C) Polarization effect

Figure 2.9 shows a typical electrical equivalent model of a two-electrode conductivity sensor[48], that consist in a solution capacitance C_S, a polarization capacitance C_P and a restistance $R_{measured}$.

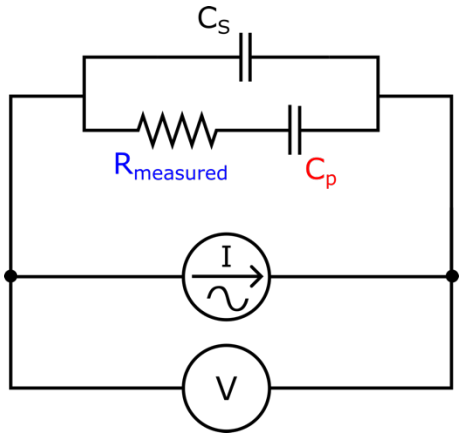

Figure 2.9. Typical electrical equivalent model of a two-electrode configuration, consisting of a solution capacitance C_s in parallel with a polarization capacitance C_p and a resistance $R_{measured}$. An AC current source is used as the excitation, and the resultant voltage is measured.

Ohm's law enables the calculation of electric resistance or its reciprocal, the conductance, based on the measured voltage at a known excitation current. To determine specific conductivity from conductance, the cell constant must be established [49]. In its simplest form, the cell constant (noted K, expressed in cm-1) is defined by the distance between each electrode divided by the cross-sectional area of the electrodes, according to the following equation:

$$K = {}^{d}/_{A} \tag{1}$$

Where d [cm] is the distance between electrodes and A [cm^2] is the cross-sectional area of the electrodes. To cover different conductivity ranges, the cell constant can be adapted: even though the two-electrode method is recommended for low conductivity values, increasing its cell constant allows to measure high conductivities as well.

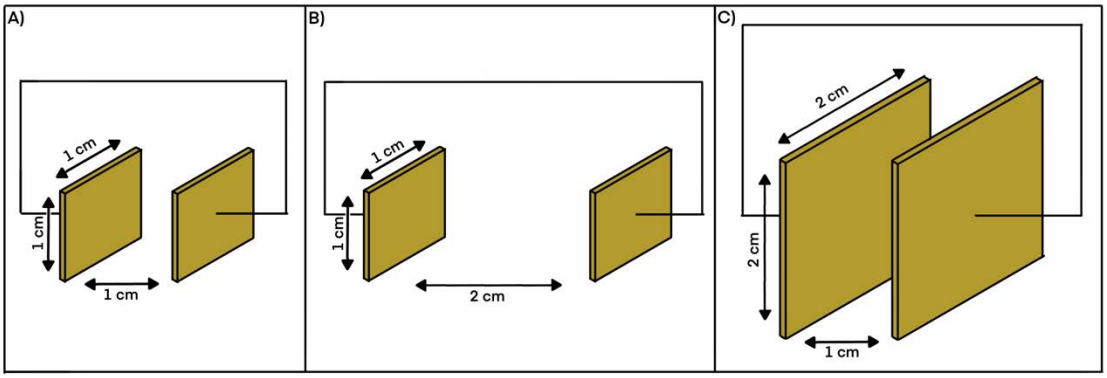

Figure 2.10. Different cell constant. A) Cross-sectional Area 1 cm^2, distance 1 cm, cell constant of 1 per centimeter. B) Cross-sectional Area 1 cm^2, distance 2 cm, cell constant of 2 per centimeter. C) Cross-sectional Area 4 cm^2, distance 1 cm, cell constant of 0.25 per centimeter.

The mathematical relationship between conductivity, conductance and cell constant is showed in the following equation.

$$\sigma[S/m] = S \times K \tag{2}$$

Where σ is the conductivity, S the conductance and K the cell constant.

While cell constant determination is straightforward to calculate for parallel plate configuration, planar electrode configurations make this calculation more complex. In the case of planar interdigitated electrodes for example, an expression for the cell constant considering the number of electrode fingers, their width, and the space between adjacent fingers can be derived[50], however most of the time the cell constant is derived experimentally, by measuring the sensor output in calibration solution of known conductivities. Two-electrode conductivity sensors are commonly criticized for their sensitivity to polarization effects in high conductivity waters like seawater, but this influence can be drastically limited by using a sufficiently large cell constant, and increasing the excitation signal frequency, typically in the tens of kHz range.

Four-electrodes

The principle of the four-electrode method for measuring conductivity consists of two current electrodes and two potential electrodes; an alternating current is applied through the two outer electrodes which gives a traceable current value, while the inner pair of electrodes measures the voltage. These electrodes carry negligible current, so they don't contribute to the voltage measurement. This method has a fouling compensation because the fouling affects only the current source, however, this doesn't impact the voltage detected by the inner electrodes as the current passes through the liquid, since the voltmeter measures only the voltage drop across the liquid solution, the readings are not influenced by the resistive effects of electrode fouling.[51], [52], [53]. Figure 2.11 show the four-electrode configuration.

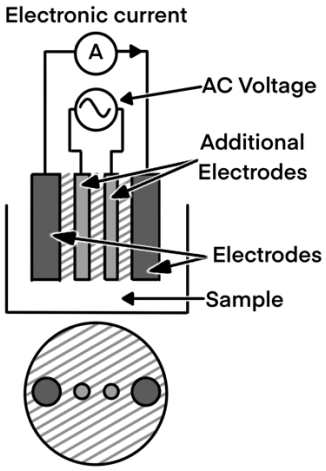

Figure 2.11. Four-electrodes sensor configuration

Moreover, the four-electrode method minimizes the polarization effect by employing a configuration where current is applied through two outer electrodes, while potential is measured across two inner electrodes. This spatial segregation of current and voltage electrodes contributes to the mitigation of polarization effects. Theoretically, the four-electrode method has the potential to entirely eliminate the influence of polarization, rendering it a dependable technique for measuring electrolytic conductivity, even in solutions characterized by high conductivity levels.[54].

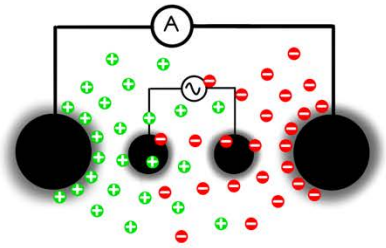

Figure 2.12. Four-electrodes high ions concentration, no polarization effect

Figure 2.13 shows a simple electrical model of a four-electrode conductivity sensor. The object's conductance, denoted by G_s, is what the sensor measures. The components R_1 to R_4 and C_1 to C_4 are the model of the electrical behavior of the electrode surface or cell constant. The contact potentials, noted E_1 to E_4, depends mostly on the electrode material. The components G_{s1} and G_{s2} are the conductance paths between the current and potential electrodes of the sensor through the object. To get an accurate measurement of G_s, these parasitics should be minimized or removed.

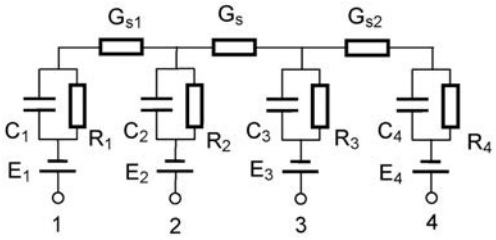

Figure 2.13. Four-electrode electrical model [52]

Using an ac excitation signal for the sensor can get rid of the contact potentials effect on the G_s measurement. A four-wire measurement can get rid of the effect of the impedances R_1 to R_4, G_{s1} and G_{s2}, and the lead-wire resistance. Figure 2.14 shows a simplified diagram of the four-wire measurement method. In this method, a constant ac current source I_{ex} excites the four-electrode sensor. An electronic circuit with high input-impedance measures the voltage across the sensor conductance. When G_s is low, this method can produce a very high voltage across G_s because of the constant-current excitation signal. This can lead to a measurement that is not linear. Also, the voltage between electrodes 2 and 3 can go beyond the free corroding potential[52].

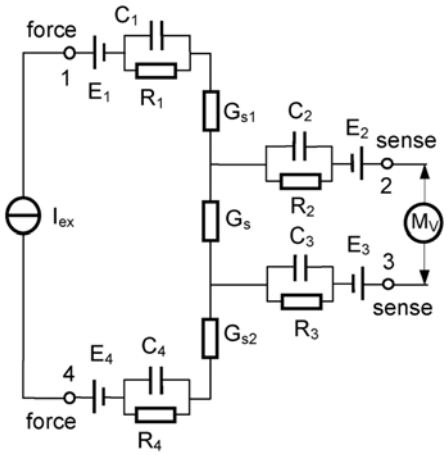

Figure 2.14. Four-electrode conductivity sensor with a constant current excitation [52]

Four-electrodes sensor is perfectly suited for wide measuring ranges. How the distance between the electrodes can affect the results of conductivity, for applications in extreme temperature fluctuations is important to select materials with almost identical expansion coefficient for the body and electrodes, so in that way gaps will not occur. A ceramic body and platinum electrodes are ideal materials for extreme temperature variations, and also guarantees maximum cleanability [49].

2.2.2 Non-contact conductivity sensors

Optical method

The optical method typically involves the use of sensors that detect changes in the refractive index of seawater, which is actually a function of the wavelength of the light, as well as the salinity, temperature, and pressure of the water. Simple handheld devices called salinity refractometer uses this principle to measure salinity, and are commonly used by salt workers. Another method is based on total internal reflection (TIR), where a sensor detects changes in the angle of reflection inside a medium with varying salinity, the refractive index measurements provide advantages such as non-contact measurements and real-time data, on the other hand has a complex system setup, require a careful calibration and maintenance, it can be affected by ambient light, turbidity and other environmental factors.[55], [56], [57]. The NKE company recently brought to the market the NOSS sensor, which is an in-situ refractometer capable of measuring absolute salinity. To our knowledge, this is the only in-situ sensor using this transducing principle.

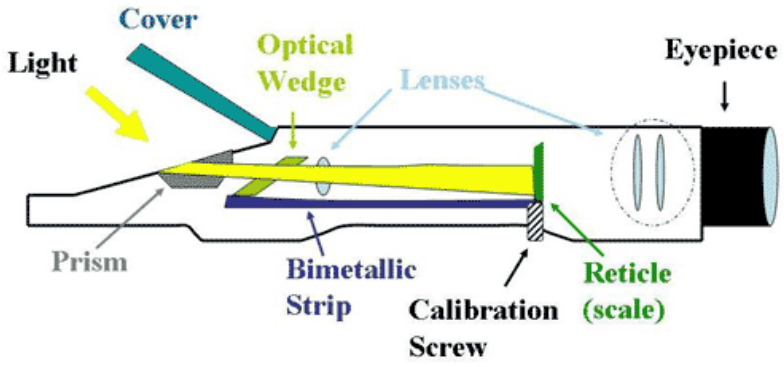

Figure 2.15 - A handheld refractometer, which is commonly used by salt workers to measure the absolute salinity of a water sample.

Inductive conductivity sensors

Inductive measuring principle is based on Faraday's law of induction. Two toroidal coils are immersed in the water: a transmission coil is excited by an AC signal to generate a magnetic flux and a resultant electric field that induces a current in the water sample. This current passes through the center of the reception coil and induces a secondary current which is influenced by the water conductivity [58]. The intensity of the current depends on the number of free ions in the medium. The advantage of inductive conductivity measurement is the galvanic isolation from the medium. Polarization effects cannot occur, and the measuring principle is less sensitive to biofouling compared to contact-based sensors.

Otherwise this method is not suitable for low conductivity measurements (less than 15µS/cm), generally is more expensive than contact methods, has a complex design, requires regular calibration and high power consumption, can be sensitive to temperature changes, and has to be far away from the other electronic components to avoid Electromagnetic interferences (EMI). The inductive conductivity measurement is suited for media with a high conductivity such as brine, acids, bases and seawater [49], [59].

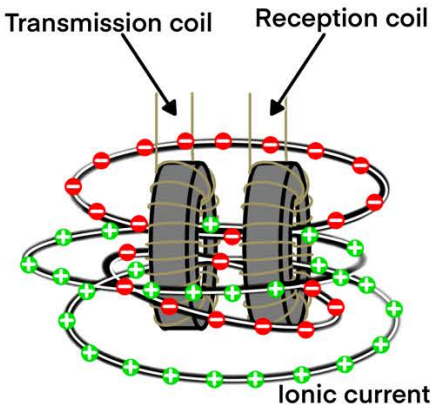

Figure 2.16. Inductive Sensor, transmission toroid coil to apply Voltage, reception toroid coil to measure the current

2.2.3 Temperature sensing sensors

Temperature is probably one of the most widely measured physical parameters, as such many different types of temperature sensors have been developed through the years. The role of the temperature sensor in the multiparameter probe is particularly important, as the temperature measurement is required by several other sensors for compensation, especially the oxygen optode. The most common technologies are thermistors, thermocouples and RTDs (Resistance Temperature Devices) [60].

The thermistors are temperature sensitive resistors that change their resistance value with changes in temperature. NTC (negative temperature coefficient) thermistors decrease their resistance with increasing temperature, while PTC (positive temperature coefficient) thermistors increase their resistance. Their advantages are high sensitivity, compact size, and low cost, the disadvantages are limited temperature range, and especially non-linearity which sometimes requires additional circuitry for linearization.

The thermocouples work according to the Seebeck effect, which occurs when two dissimilar metals meet at a point and are subjected to a temperature difference. This generates an electrical voltage that is proportional to the temperature difference between the hot junction and the cold junction. Their advantages are that they are able to measure a wide range of temperatures, are quite fast (depending on the size and thermal inertia of the junction), low-cost and easy to install, while their disadvantages are lower accuracy compared to other sensors, susceptible to errors due to electromagnetic radiation and may require periodic calibration [61].

The RTDs are based on the fact that the electrical resistance of certain metals changes predictably with temperature, the resistance increases with increasing temperature, the RTDs use this change in resistance to measure temperature, their advantages are that they provide very accurate and stable measurements, and have good linearity, and their disadvantages are that they are generally more expensive sensors than thermistors and thermocouples [62].

2.2.4 Depth sensors

Pressure sensors work by converting the physical pressure they detect into an electrical signal. The central component of a pressure sensor is the sensing element, which is typically a diaphragm that deforms when pressure is applied. This deformation is measured by strain gauges arranged in a Wheatstone bridge configuration, which changes its electrical resistance. The change in resistance causes a change in the output voltage of the sensor[63]. There are several types of pressure sensors, each suitable for different applications and operating principles, some of the types of sensors used to measure deep-sea are shown below:

Piezoresistive strain gauge

Its principle of operation is based on the piezoresistive effect, which refers to the change in electrical resistance of a material when subjected to mechanical stress or strain. A piezoresistive pressure sensor consists of a diaphragm, which is a thin, flexible membrane that deflects under the influence of an applied pressure, on the surface of the diaphragm, piezoresistive elements (also known as strain gauges) are arranged in a specific pattern, often in the form of a Wheatstone bridge circuit, when pressure is applied to the diaphragm, it deforms, causing the strain gauges to experience mechanical stress, this stress leads to a change in the electrical resistance of the strain gauges, which is proportional to the applied pressure, the change in resistance can be measured and converted into an electrical signal that corresponds to the pressure being sensed. Piezoresistive sensors are considered to be the best choice for water depth measurement because of their key advantages, its exhibit high sensitivity, allowing them to detect even the slightest pressure change, has a wide measurement range from very low to very high, has a fast response time which allows a pressure change detection per minute which is crucial in deep-sea environment, furthermore has a good long-term stability and is harsh environment resistance, these sensors can operate effectively in extreme temperatures [64].

Piezoelectric pressure sensor

This sensor consists of the piezoelectric effect, piezoelectric pressure sensors consist of a piezoelectric material (usually a crystal or ceramic) sandwiched between two electrodes, when pressure is applied to the sensor, the piezoelectric material deforms, causing a voltage difference across the electrodes, this voltage can be measured and correlated to the applied pressure. Piezoelectric sensors can come in very small sizes, making them a good choice for space-constrained applications [65].

Capacitive pressure sensor

A capacitive pressure sensor operates based on the principle that the capacitance between two parallel plates is inversely proportional to their separation distance. A capacitor consists of two parallel conducting plates separated by a small gap, when pressure is applied to a flexible diaphragm, one of the plates causes the diaphragm to deflect, altering the distance between the two plates, this change in capacitance can be measured and calibrated to represent the pressure exerted on the sensor [66].

2.3 Development of a low-cost CTD sensor

2.3.1 Conductivity

In a low-cost CTD, conductivity is the trickiest parameter to measure, especially for marine application where salinity is an important parameter, for which the required precision can be very high. This is the case for monitoring small salinity variations related to the climate change, which cause an amplification in evaporation in some areas, and of precipitations in some others, both impacting salinity in opposite ways. Based on the cost and power consumption constraints of our project, we choose to select a contact-based method for our conductivity sensor. While it is feasible to build conductivity electrodes in a frugal way, by using pencil graphite rods and epoxy glue, as notably demonstrated by Camilo Rada [67], this fabrication involves delicate manual operations, which will inevitably lead to relatively large discrepancies in the performance of the electrodes, and will require individual calibration. While this can be an option for decreasing the overall cost of the probe, we decided to use the commercially available LF1K0 electrodes which are manufactured by the IST company. These electrodes are realized by common cleanroom manufacturing techniques: platinum electrodes are deposited on a ceramic substrate and structured by photolithography. Four electrodes are available, but the sensor can also be used in a two-electrode configuration. Depending on the target conductivity range, i.e. freshwater or seawater, the two inner-electrodes or the two outer-electrodes can be used, to get a smaller or a larger cell constant respectively. On the center of the sensor is a Pt1000 sensor which can be used for precise temperature compensation of the conductivity measurement. A screen printed-glass passivation covers the PT1000 as well as the electrical access to the electrodes, visible in dark gray on Figure 2.17.

Figure 2.17 – Left: Photo of the IST LFS1K0 conductivity sensor. Dimensions of the ceramic substrate are 12.9x5.5m. Courtesy of IST company. Right: photo of the sensor after marinization for laboratory testing. The Pt-Ni wires are soldered to a Molex Picoblade connector and inserted into a 5mL plastic syringe with its plunger removed. Hot-glue and heatshrink tube is added at the tip of the syringe to make the sensor waterproof.

For our measurement, the LFS1K0 is simply inserted in a plastic syringe with its plunger removed, and potted with hot-glue to isolate the Pt-Ni wires, as show Figure 2.17. The marinized electrodes are connected to a circuit which is derived from the Circuit Note CN0349 from Analog Devices, presented in a simplified version Figure 2.18. The AD5934 is an impedance-to-digital converter; its output feeds U2A which is configured as a follower, and bias the signal to half the power-supply, while U2B is configured as a current to voltage converter. U1 is an analog switch that routes the excitation sine signal to either a calibration resistor network (R_{cal}), a temperature sensor (the Pt1000 of the LF1K0 electrodes in our case) or the conductivity electrodes (Y_{cell}).

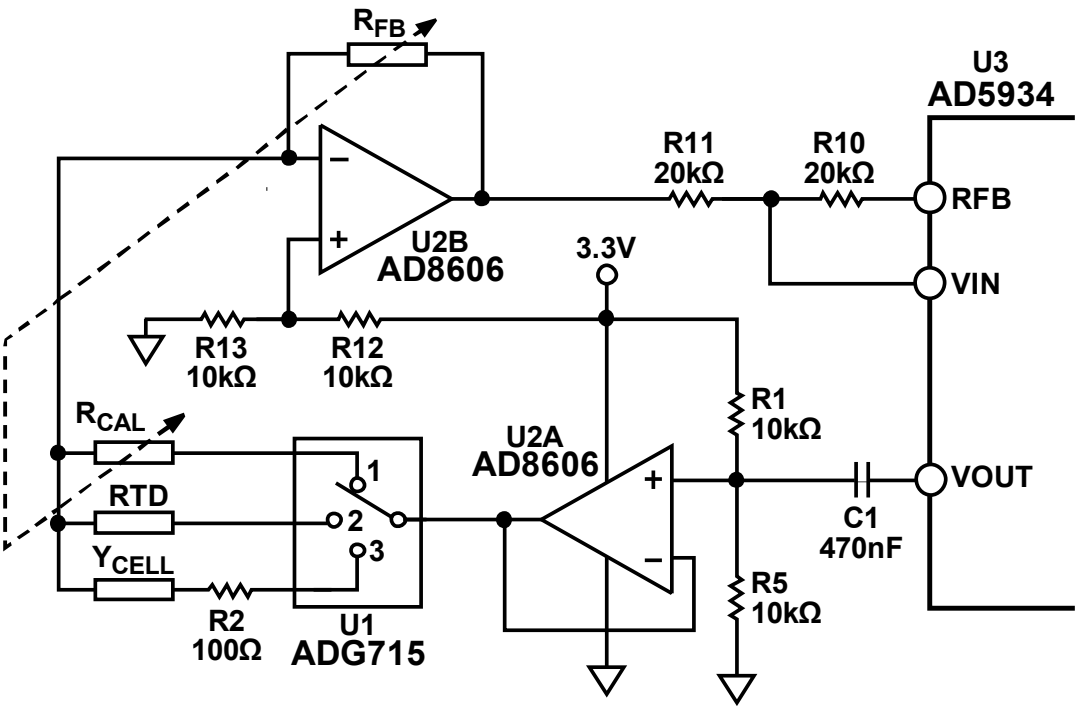

Figure 2.18 - Simplified schematic showing the operating principle of the CN0349 conductivity measurement system. The AD5934 is an impedance converter, that can generate sine signals at a programmed frequency, and analyze complex impedances. Adapted from Analog Devices Circuit Note CN-0349.

As mentioned in the previous section, most of the published academic work on low-cost CTDs are using a conductivity sensor commercialized by Atlas Scientific. This sensor is based on a classic 2-electrode graphite configuration, with a main polycarbonate and nylon body, that connects to a specific conductivity circuit. While the graphite electrodes are a common sight in electrochemistry, with similar electrodes sold by many manufacturers, the Atlas Scientific EZO-EC circuit is a bit of a black-box, with almost no technical details given. It is known that it generates a square wave current at varying frequencies to cover a wide range of conductivities (from 20 Hz to 40 kHz approximately), but the measurement technique is not described in the datasheet. We purchased the Atlas Scientific Mini Conductivity Probe with a cell constant K =1.0 as well as an EZO-EC circuit in order to compare it to our developed sensor. A Decagon CTD-10 was obtained from the Oceanographic Observatory of Banyuls sur Mer in order to have a reference sensor.

The developed conductivity sensor was tested against the Atlas Scientific Mini Conductivity Probe and the Decagon CTD-10 in laboratory conditions with the following protocol: the three sensors were immersed in a 600mL beaker filled with seawater (collected from the Port du Plomb, Lauzières, France). The conductivity of seawater was then diminished with sequential addition of 10mL of tap water (x11), and increased with sequential addition of a high salinity solution (10g per 50mL of tap water) with a first addition of 5mL (x1), and following additions were 2mL (x11). Homogeneity of the solution was guaranteed by constant stirring using a magnetic stirrer. The temperature remained constant during the whole experiment at 21°C.

Both the Atlas Scientific EZO EC board and our conductivity sensor were connected to an Adafruit Feather M0 microcontroller and interfaced using an I2C bus. The Feather M0 was connected to a laptop and data was acquired through a serial port connection and saved locally

as a .CSV file. The Decagon CTD-10 was connected to an Arduino Uno through an SDI-12 communication, and data was acquired similarly to the other sensors using another serial port.

The Decagon CTD-10 was factory calibrated and was used without modifications, while the Atlas Scientific sensor was calibrated based on the manufacturer recommendations with their calibration solutions. The AD5934 impedance-to-digital converter of our sensor was set with a 7 kHz excitation frequency, an excitation voltage of 200mV and a feedback resistor of 100 Ω. The cell constant was set at K = 4.16 based on the two-electrode parallel-plate equation previously described.

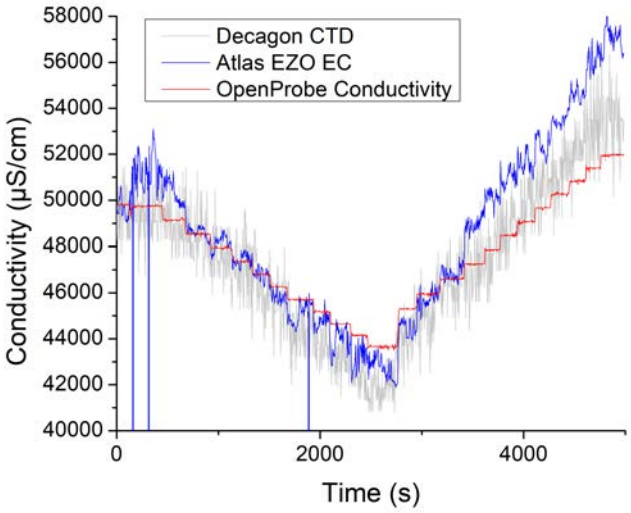

Figure 2.19 - Intercomparison of the Decagon CTD-10, the Atlas Scientific Mini Probe Conductivity sensor, and our conductivity sensor in seawater. Conductivity is decreased in steps using tap water, and then increased with high salinity solution.

The results are presented Figure 2.19. It can be observed that the three sensors are following the overall variation of conductivity. The Atlas Scientific and our sensor were offset corrected to fit initial readings of the Decagon CTD-10 at time=0s, as the Decagon was used as the reference sensor. The response of the Decagon shows a relatively high noise level, with up to +/- 2000µS.cm^{-1} noise around the average value. The Atlas Scientific sensor noise level is lower than the Decagon, but the readings are less stable over time, with apparent drift in some cases; this drift was also observed by some colleagues from IUEM in Brest, France who conducted extensive testing of these sensors in laboratory and field conditions. Comparatively, our sensor is the only one where the sequential addition of tap water or high concentration salinity solution are clearly visible. It should be noted that no averaging was performed on any of the sensors and that the data presented is the raw data (with only offset correction for the Atlas Scientific and our sensor).

While further testing is required to ensure long-term stability, from our experiments the combination of the CN0349-based circuit and the LFS1K0 appears very promising compared to the Atlas Scientific: the resolution proved to be better, the overall size of the sensor is smaller, and the purchase cost is lower. Marinization can be done with moderate efforts, and it offers integrated temperature measurement with the Pt1000 sensor for precise temperature compensation (data not shown here as temperature was constant in laboratory conditions). Additional benefit of our sensor is that the response time is shorter, with a sampling rate that can be set at 10 Hz or more, while the Atlas Scientific is limited to 1Hz maximum: while it's

not necessary in stationary deployments, having a high sampling rate is particularly beneficial for profiling applications as it allows for faster diving speed of the sensors.

Atop of these promising results, it should be added that improvements are still possible: the AD5934 was set at a frequency of 7 kHz, as the quartz crystal associated with it was a 1MHz version, but this frequency could be increased in the tens of kHz range with a higher quartz crystal frequency. This increase in frequency can be beneficial for high conductivity range as it limits the polarization effect in two-electrode configurations.

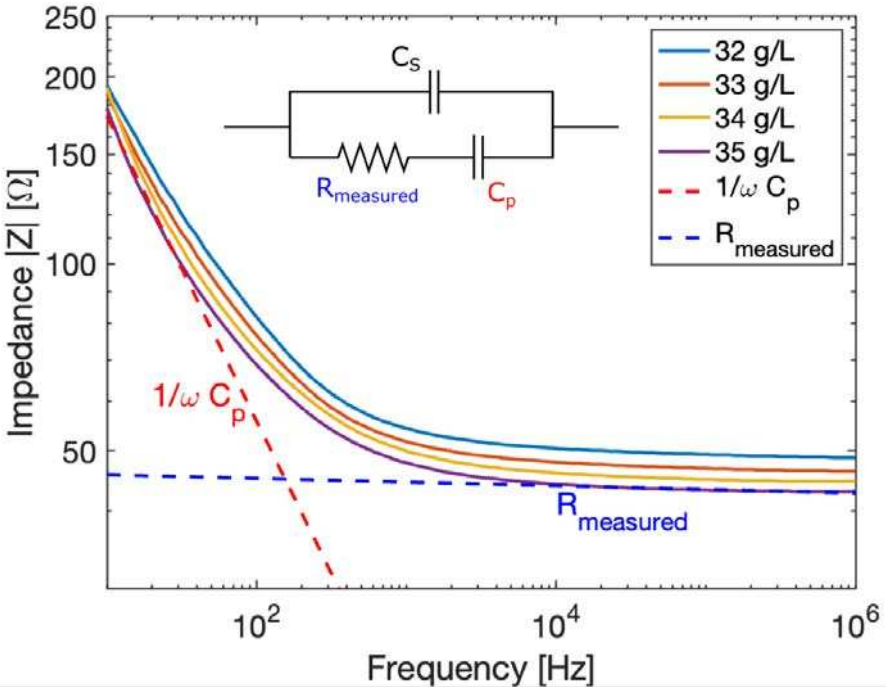

Figure 2.20 - Frequency characterization of the LF1K0 conductivity electrodes with a Hyoki IM3570 impedance analyzer in artificial seawater (from 32 to 35g/L), corresponding to typical seawater salt concentrations. The inset is the typical electrical equivalent model of the two-electrode system. Dotted lines represent the contribution of the polarization capacitance which is dominant at low frequencies, and the measured resistance which is dominant at high frequencies.

As the IST LFS1K0 electrodes are supposed to be limited to a frequency range of 100Hz to 10kHz according to the manufacturer, we conducted an experimental frequency analysis of our marinized electrodes using a Hyoki IM3570 impedance analyzer, with the electrodes immersed in artificial seawater obtained by dissolving coarse Guérande salt in tap water at various concentrations, from 32 to 35g/L (typical salt concentration of seawater). The results are shown Figure 2.20, and are typical of the behavior of a two-electrode system [48]. Using the simple electrical equivalent model presented Figure 2.9, the contribution of the polarization capacitance is materialized as the red dotted line, highlighting the fact that this polarization capacitance dominates the measured impedance at low frequencies, but rapidly diminish with at higher frequencies, where the solution resistance starts to prevail. At the 7 kHz frequency used in our experiment, the solution resistance is the major contribution, but there is still residual effect from the polarization capacitance, hence further increasing the frequency could potentially improve the measurement accuracy.

2.3.2 Temperature and pressure

For temperature, although the IST LFS1K0 contains a temperature sensor itself, it was decided to use the TSYS01 sensor from TE Connectivity, since this sensor is commonly used in oceanography applications and for pressure it was decided to use the MS5837 sensor from TE Connectivity. These components are used in Blue Robotics commercial sensors, that has developed waterproof enclosures to make them usable underwater, and have been used extensively in open-source CTD projects [43], [68], [69], demonstrating suitable performance for oceanography [60].

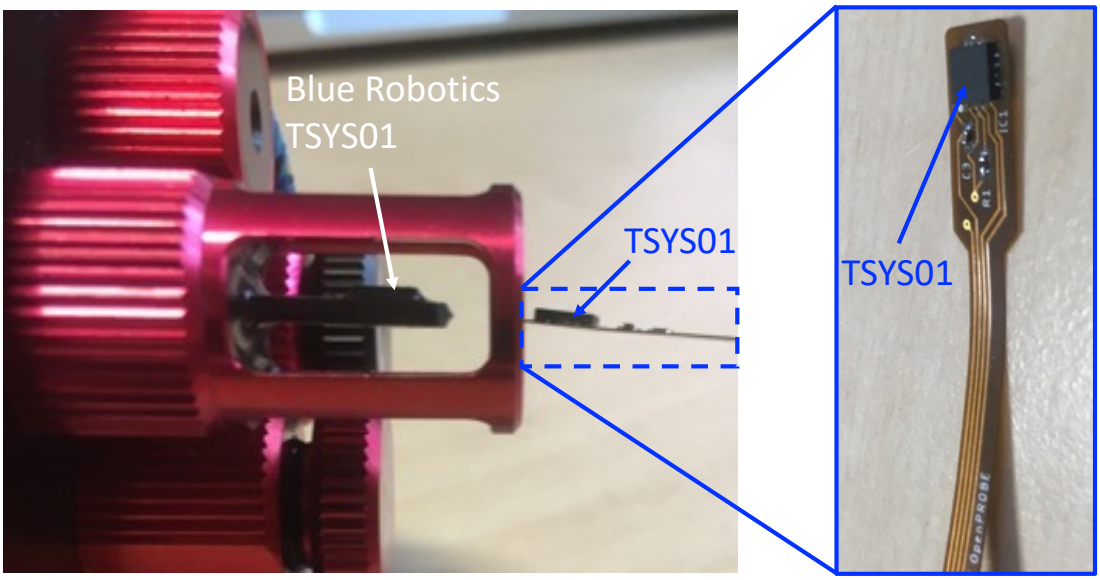

Figure 2.21. Picture of the commercially available Blue Robotics temperature sensor, which is a TSYS01 IC mounted on a FR4 PCB and marinized by an epoxy coating. The sensor is protected by an anodized aluminum cage. The commercial Blue Robotics pressure sensor is visible just above the temperature sensor. A TSYS01 mounted on a polyimide substrate is pictured next to it, visible on the right of the picture, highlighting the thickness difference compared to a FR4 PCB. Inset shows a top view of the TSYS01 assembled on this flexible polyimide substrate, prior to epoxy coating.

The TSYS01 is a high accuracy digital temperature sensor [59], based on a RTD which is factory calibrated and combined with a ΔΣ 24 bits ADC. It is available in several versions; the model we're using has an accuracy of ±0.1°C from -5°C to 50°C, and a resolution of 0.01°C, which makes it particularly interesting in our case to obtain precise temperature measurements for compensation of the other sensors, especially the conductivity sensor and the dissolved oxygen optode, as both these parameters are heavily influenced by temperature. This temperature sensor can be directly interfaced with the I2C protocol, and has a low power consumption (12.5µA in normal operation, and less than 0.14 µA in standby mode). Its time constant is directly related to the thermal inertia of its PCB and its packaging. In the Blue Robotics version, shown Figure 2.22, the response time is typically 2 seconds in still water, and 1 second at a 0.5m/s flow. The Blue Robotics version is made with a standard FR4 PCB which is 1.57mm thick, and coated with a thermally conductive epoxy (MG Chemicals 832TC): this response time can be improved by using a thinner PCB to decrease the overall thermal inertia, something we investigated by mounting the TSYS01 on a flexible polyimide substrate (approx. 0.11 mm thick, manufactured by OSH PARK company, USA) as shown in Figure 2.21 as a proof of concept, however this option was not retained due to the lack of manufacturers able to provide affordable flexible substrates.

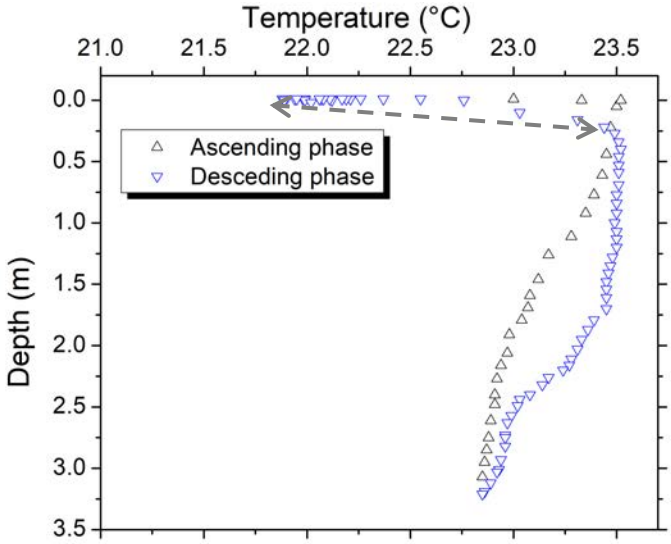

Figure 2.22. Temperature profile versus depth captured by the TSYS01 and the MS5837 sensors in the port of Villefranche sur Mer on the 6th of October 2021 at 8H40 AM. Both descending and ascending phase are shown/ The hysteresis highlighted by the gray arrow is due to the air to water transition when the probe is initially immersed into the water. It shows that the temperature equilibration is achieved in less than 2 seconds.

The MS5837 is a high-resolution pressure sensor designed by TE Connectivity, and based around a piezo-resistive pressure cell which deforms when pressure is applied, modifying the resistance of the strain gauges in the cell. It contains an amplifier and an integrated 24-bit ΔΣ ADC which processes the signal from the pressure cell. It also incorporates a temperature sensor, however it has limited accuracy, hence it cannot replace the TSYS01. This pressure sensor is available in different pressure ranges. We're using the 30-bar version, which can cover depths from 0 to 300 meters, with a theoretical resolution of 0.2mbar which corresponds to a water depth variation of 2mm. Similarly to the TSYS01, it is easily interfaced with an I2C bus [70].

While these both these sensors have been validated in several references mentioned earlier, we conducted a quick experiment to ensure that they were providing appropriate performance. Figure 2.22 presents the results obtained while doing a temperature profile in the port of Villefranche sur Mer on the 6th of October 2021 at 8H40 AM (simultaneously with the PAR experiment that will be presented in Chapter 5). Even with a limited depth of 2.80 meters, the temperature variation is precisely captured by the TSYS01. Both the descending and ascending phase are shown: it can be observed that when the sensor transitions from air to water, it quickly attains the water temperature in less than 2 seconds as expected.

Chapter 3 Turbidity

3.1 Introduction

Turbidity, a fundamental physical characteristic of fluids, serves as a metric for the degree of cloudiness within water bodies, indicating the presence of suspended and dissolved particles that impede or scatter light, thus altering water transparency[71]. This property plays a pivotal role in environmental assessments and public health considerations, offering insights into water quality into various aquatic environments including rivers, lakes, seas, and watersheds[72]. The composition of particles influencing turbidity can originate from both organic or inorganic sources. Organic particles, such as microorganisms or algae, can contribute significantly to elevated turbidity levels, hinting at potential biological contamination, but in the case of having a lot of phytoplankton turbidity levels will increase, and the water is no necessary contaminated. Conversely, inorganic particulates like clay or silt, can indicate heightened turbidity resulting from natural erosion or human activities[73], [74].

Turbidity also correlates with climatic and surface water conditions, with fluctuations indicative of environmental alterations[75]. Beyond serving as a measure of water clarity, turbidity measurements serve as a valuable proxy for potential pollution, as particles may harbor other contaminants like metals or bacteria. Notably, the straightforward measurement of turbidity presents an advantage over more intricate biochemical analyses, being directly quantifiable.

The prevailing approach to turbidity assessment involves offline systems requiring skilled operators to collect samples and perform analyses either on-site (portable systems) or in laboratories (benchtop systems). Although offering high accuracy, this method suffers from limitations in spatial and temporal resolution, and fails to capture sudden events. Moreover, it incurs additional operational expenses, encompassing human resources, travel and, sample storage alongside equipment cost. Consequently, in certain scenarios, the utilization of in-situ turbidity sensors is preferred. However, their widespread adoption is hindered by substantial costs, typically several thousands of US dollars, thereby constraining spatial and temporal coverage.

While the necessity for low-cost, in-situ turbidity sensors has been recognized in existing literature, our objective is to support these efforts with a sensor that can be applied in low turbidity areas such as the French coastal area of the Mediterranean Sea, as well as in more turbid freshwater systems.

3.2 Measurement methods and state of the art

While complementary methods like acoustic[76] or time resolved [77] are preferred for specific scenarios, optical transduction is the most commonly used principle for measuring turbidity. Optical methods utilize the interaction between light and the suspended particles: using a light source and a photodetector, attenuation and/or scattering caused by particles in the water sample is/are measured and analyzed.

Scattering is the physical process in which the light deviates from its straight trajectory to one or more directions due to the presence of particles in the sample, while absorption, also referred as attenuation, is mostly related to the uptake of photons by the matter in the sample.

The scattering pattern and is direcly affected by the particles properties, such as color and size, and by the light source parameters such as its wavelength and intensity [71]. Figure 3.1 illustrates the influence of particle size on the scattered light.

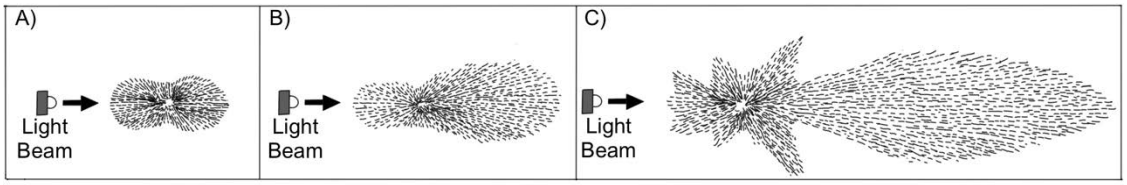

Figure 3.1. Angular patterns of scattered light of three different particles sizes. A) Small particles: smaller than 1/10 the wavelength of light, symmetric scattering, B) Medium particles: approximately ¼ the wavelength of light, scattering concentrated in forward direction, C) Large particles: Larger than the wavelength of light, extreme scattering in forward direction.

Both scattering and absorption of light can provide information about turbidity, but turbidimeters do not necessarily uses the two. Sensing methods are classified according to the angle of the photodetector relative to the light source. Scattering-based sensors can be qualified as backscattering (0°-90°), 90° scattering (90°) - also referred as nephelometric -, forward scattering (90°-180°) or attenuation/absorption (180°), as summarized Figure 3.2. The two common units for measuring optical nephelometric turbidity are Nephelometric Turbidity Units (NTU) and the equivalent Formazin Nephelometric Units (FNU), while the unit for measuring attenuation is Formazin Attenuation Unit (FAU)[73]. As these units are not part of the International System of Units, there is some debate about the adoption of new methods for reporting turbidity data[78] however these considerations are out of the scope of this work.

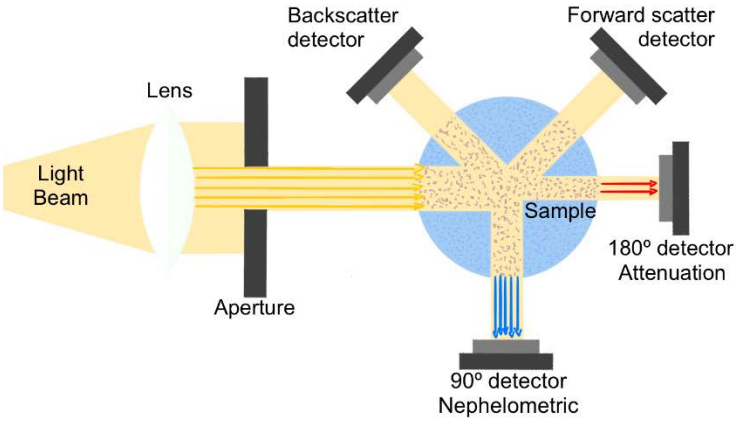

Figure 3.2. Incident light beam and position of photodetectors related to the light source for scattered and attenuation light. The 90° angle configuration (blue arrows) corresponds to nephelometric method, while the 180° placed (red arrows) is referred as the attenuation method.

The World Health Organization (WHO) recommends that drinking water should not exceed 5 NTU, and ideally be smaller than 1 NTU. While it is typically mentioned that turbidity is visible to the naked eye from 4 NTU, in our experience it is hard to observe below 10 NTU. The reader can find a visual illustration of samples of various turbidities Figure 3.4.

Nephelometric configuration (90° detection angle), is considered to be the most appropriate angle to light scattering regardless of particle size[79] and is generally applied to lower turbidity levels with good accuracy from 0 to 40 NTU, where light scattering and turbidity have a linear dependency[76]. The higher the intensity of the scattered light, the higher the turbidity[77].

Turbidity

Attenuation, or forward scattering method, is influenced by both light scattering and absorption and is favored for high turbidity values (above 40 NTU [80], [81]) as it offers a larger linearity range than nephelometry. In that case, the lower the intensity of the transmitted light, the higher the turbidity values [68], [69]. This angle is more sensitive to absorbance and water color, but these effects can be limited by the use of an infrared incident light source, as most of the compounds in water absorb mostly in the UV-VIS range.

As an essential water quality parameter and a widely used indicator in environmental water analysis, turbidity measurement is standardized by internationally recognized certification bodies, with ISO 7027-1 and US-EPA Method 180.1 being the most prominent. Other methods such as Standard Methods 2130B and Great Lakes Instrument Method 2 (GLI Method 2) are also approved by the United States Environmental Protection Agency[80], [82], [83], [84]. A brief overview of three of these methods is provided in this work to justify our design choices.

3.2.1 US EPA 180.1

This method is based on a nephelometric measurement, with an angle between the light beam and the detector between 90° +/-30° [82]. The light source is a tungsten lamp with a color temperature between 2000K and 3000K, a polychromatic output and a spectral peak response between 400-600 nm. In this wavelength range, some color interferences can occur due to the medium and organic particles, which can result in absorption, reducing the accuracy of the turbidimeter. The large variation in wavelengths, detection angles and the absence of specifications regarding the excitation light beam profile[85] leads to considerable variations between instruments, with intercomparison describing up to five-fold differences in recorded values[86]

Compared to a monochromatic light source, the use of a tungsten lamp with polychromatic light is more sensitive for samples with very fine particles, and EPA Method 180.1 is appropriate for measuring turbidity levels between 0-40 NTU and should have a resolution of 0.02 NTU. However, this method will not be accurate at levels above 40 NTU, as the relationship between light scattering and turbidity becomes non-linear [80], [82]. Compared to benchtop turbidimeter, in-situ instruments imply additional constraints in terms of portability, power consumption and stability; therefore, a LED source is generally favored over a tungsten light source. Another constraint for in-situ measurements is the need to eliminate ambient light effects, hence infared light sources are generally preferred.

3.2.2 ISO 7027

This method employs both light scattering and light attenuation. The main distinction from EPA Method 180.1 is the use of a near infrared monochromatic light source with a wavelength of 860 nm +/-30 nm. The infrared light is less affected by the medium color and less absorbed by particles and molecules, which reduces most color interferences, and makes this method applicable for low to high turbidity values. For low turbidity values, the instrument should use the nephelometric technique expressed in Formazin Nephelometric Units (FNU) for the range from 0 to 40 FNU.

In this case, the photodetector must be placed at +/- 2.5° from 90° relative to the light beam. For high turbidity values (> 40 FNU), the instrument should use light attenuation, with the photodetector placed at 180° relative to the light beam [87]. Turbidity in this case is

expressed in Formazin Attenuation Units (FAU) for the range from 40-4000 FAU. Due to stricter specifications (wavelength, bandwidth, detection angles), instruments complying with the ISO 7027 have slightly better comparability, but large discrepancies between instruments are still an issue[86] The use of a LED source is also preferable for portable, field deployable systems.

3.2.3 GLI 2

Great Lakes Instruments Method 2 (GLI-2), also known as a modulated four-beam turbidimeter, uses two light sources and two photodetectors to combine nephelometric (refereed to active signal) and attenuation (referred to reference signal) readings. The operating principle is summarized Figure 3.3. It is based on infrared light at 860 nm as ISO 7027. This method enhances instrument stability by eliminating errors due to the degradation of the light source, water color effects, or biofouling on the sensor optics [85] [81].

GLI-2 is a ratio technique that relies on an algorithm to calculate the turbidity value from the four readings. However, the algorithm is not explicitly described in the method, which creates some uncertainties when comparing two commercial instruments, especially if the manufacturer does not disclose the ratio calculation details. Instrument range is typically 0-100 NTU, but it loses some accuracy at levels above 40 NTU due to the increased light intensity (more intensity = more scattered light). GLI-2 is known to be very accurate for lower turbidity ranges, especially within the 0-1 NTU range[83].

The ability to reduce the influence of light source drift and biofouling is also an advantage when considering in-situ deployment. However, the design layout makes this method more difficult to integrate into a field deployable instrument, compared to a conventional nephelometric or backscattering configuration where both the light source and the photodetector can be shielded by a flat optical surface.

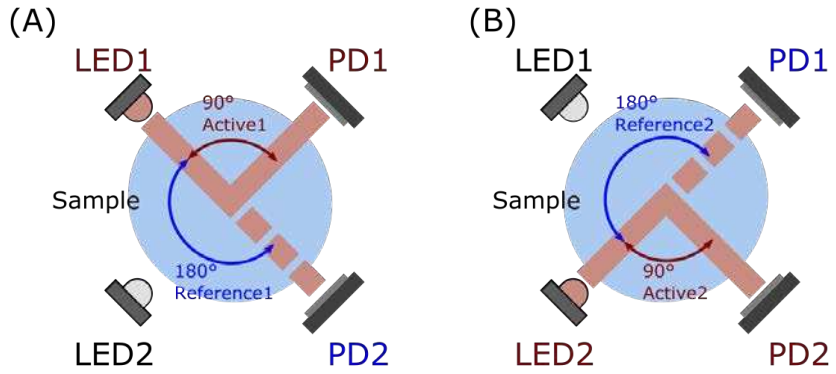

Figure 3.3. Illustration of the GLI-2 method, a ratiometric method based on a modulated 4-beam design. (A) Phase one, light source LED1 is on, photodetector PD1 measures the Active1 signal (90° nephelometric) and photodetector PD2 the Reference1 signal (180° attenuation). (B) Phase two, light source LED2 is on, photodetector PD1 is the Reference2 signal (180° attenuation) and photodetector PD2 is the Active2 signal (90° nephelometric).

3.2.4 Commercial turbidimeters

Most of the commercial turbidimeters are based on optical measurement in the infrared using side-scattering, back-scattering, attenuation or a combination of these to comply with the officially endorsed methods described earlier. The instruments can be categorized into four types: (i) benchtop instruments, which offer the best accuracy, (ii) hand-held portable devices,

which are the cheapest options, (iii) inline sensors, which are designed for analysis in water pipes and (iv) in-situ sensors, which can be either "self-contained" or available as an add-on for multiparameter sondes. Both (i) and (ii) require sampling the water bodies for further analysis, and thus are not suitable for real-time monitoring, remote monitoring, or high spatial-temporal resolution measurements, as it would imply an impractical amount of work for sampling, storage and analysis.

In terms of price, a commercial turbidimeter costs between 600 to more than 5000 €, with portable hand-held devices being the most affordable option, and high-precision benchtop instruments being the most expensive. In-situ sensors, which are the focus of this work, are usually in the middle of the range, but need additional equipment such as a logger or a display, which makes a complete setup costing several hundreds of euros.

Due to the constraints of in-situ measurements of water bodies, which include instrument damages due to natural phenomena, theft, degradation by humans or wildlife, and the need in some cases to collect data at a better spatial-temporal resolution, the relatively high cost of commercial instruments has motivated a lot of research on alternative, low-cost turbidity sensors, that while compromising on measurement quality, can provide valuable data at a fraction of the cost. Table 1 shows recent achievements reported in the literature. A comprehensive list of commercially available turbidimeters can be found in the Aquaref report [88] as well as in the inter-comparison study of Rymszewicz et al. [86] that concentrates on in-situ instruments.

Table 1 - Recent achievements in the literature on turbidimeter developments.

Sensor	Price	Range	Resolution	In-situ	Method	Reference
Fay et al.		0-100 NTU 0-1000 NTU		No	ISO 7027	[89]
Kitchener et al.		N.A.		No	TARDIIS	[90]
Gillett et al.		0-100 NTU	1 NTU	No (continuous)	Nephelometry	[91]
Trevathan et al.		100-400 NTU		Yes	Attenuation	[92]
Zang et al.		40-300 NTU	3 NTU	No	Nephelometry and attenuation	[93]
Matos et al.		0-4000 NTU	N.A.	Yes	IR backscatter, nephelometry and attenuation	[94]
Metzger et al.		0.1-1000 NTU	0.04 to 3 NTU	No	ISO 7027	[95]
Parra et al.		0-200 NTU	N.A.	No	Attenuation	[96]
Kelley et al.		0-1000 NTU	0.02 NTU	No	Nephelometry	[97]

3.3 Formazin calibration

The calibration of turbidimeters using a natural sediment source is challenging in most cases, due to the diversity of turbidity sources, and it hampers the intercomparison between different instruments[86]. To achieve a more standardized, repeatable calibration method a polymer called Formazin has been adopted by most of the industry manufacturers. It is produced by mixing solutions of hydrazine sulfate and hexamethylenetetramine in water[98] to obtain different chain lengths in random configurations, spanning a range of particle shapes and sizes from less than 0.1 to over 10 microns, making it a relatively simple light-scattering calibration standard. One of its main advantages is that it can be repeatedly and reproducibly prepared from raw materials into a calibrated stock solution that is diluted to obtain virtually any concentration. Formazin standards are stable over a year under proper storage conditions, except for very low concentrations (< 2 NTU) where long-term stability is compromised. Figure 3.4 shows Formazin samples from 0 to 40 NTU.

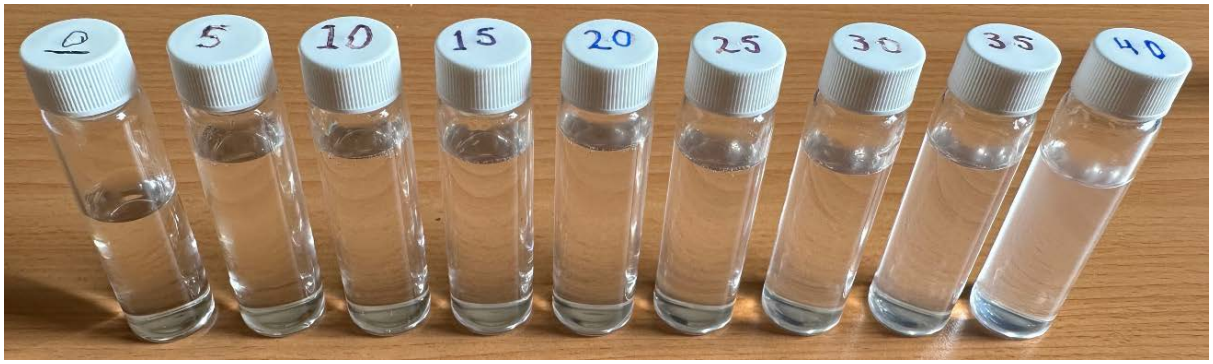

Figure 3.4. Different Formazin values samples, from 0 to 40 NTU. It is difficult for human eyesight to detect values below 10 NTU.

Despite being the calibration standard for most methods, Formazin also has some inherent drawbacks that have been summarized in Kitchener et al. work [85]. Specifically, the shape of Formazin particles is not standardized, although particle shapes can have a strong impact on side-scattering. It should also be noted that uncertainties arise due to the high dilution ratios typically required at low turbidity, exacerbated by the lack of stability of these highly diluted solutions. It is often observed that commercial turbidimeters that meet the requirements of the same official standard (EPA/ISO) can yield different turbidity values when used with the same Formazin calibration solution. This has been reported on laboratory benchtop instruments, as well as on in-situ instruments[86], [99].

Research on improved calibration methods of existing turbidimeters, as well as design of new instruments that overcome the lack of comparability between current instruments[100] are beyond the scope of this present work, but some design recommendations have been integrated in our sensor as suggested by other authors.

3.4 Development and testing of different types of turbidity sensors

Depending on the objectives in terms of sensitivity, range, and operating conditions, different measurement techniques can be considered. As our objective is to deploy the sensor in the coastal areas of the Mediterranean Sea, where the turbidity level is low (0 to 10 NTU range), it would be ideal to start with the GLI-2 method, but at the beginning of the project we were in the pandemic era of COVID and most of the identified components were not available,

with for some references up to 24 months of delivery time announced. As several articles in the literature reported on the use of off-the-shelf washing-machine sensors to measure turbidity by the attenuation method, we decided to evaluate one [74], [101]. A second prototype was developed around an optical sensor, initially made for optical heart rate measurement in fitness watches, that integrates an infrared light source and several photodetectors on the same plane which makes it suitable to implement the backscattering method. Finally, a third prototype based on the GLI-2 method is presented.

3.4.1 Off-the-shelf washing-machine, attenuation-based sensors

The TS-300B sensor was one of the available references; it is advertised to cover a range of 0 to 1000 NTU with a precision of +/- 30 NTU, and uses an infrared emitting diode at 910 nm and a phototransistor with an 880 nm peak sensitivity. In order to get the data from the phototransistor, an additional resistor R_1 is added to convert the photocurrent to a voltage which is sampled by a Texas Instrument ADS1115 16-bit Analog To Digital Converter (ADC). An Arduino UNO is connected to the ADC with an I2C bus, and the data is collected through a serial port between the Arduino and a computer as shown in Figure 3.5

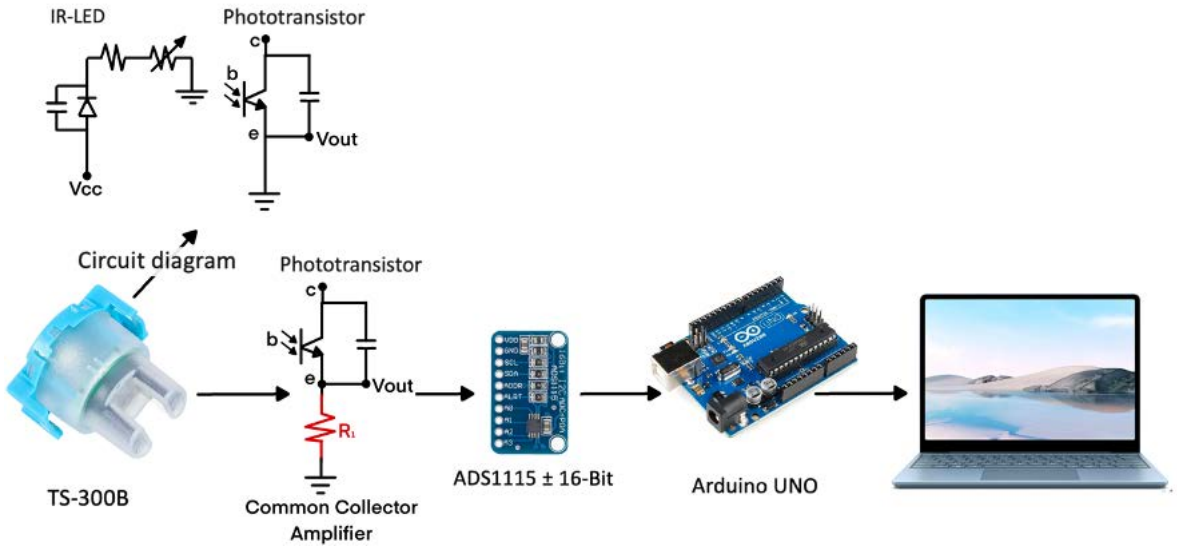

Figure 3.5. Implementation of the TS_300B sensor as an attenuation method turbidity sensor.

Formazin 4000 was used to obtain samples of increasing turbidity. Fresh samples were prepared prior to the analysis to avoid stability issues, and obtained by appropriate dilution in deionized water. Each sample was shaken thoroughly prior to measurements to avoid suspension to settle out. Once we had the control over the samples, we proceeded with the experiment by measuring 11 different concentrations from 0 to 1000 NTU with increments of 100 NTU each using the Arduino program available in GitLab, in which the data output from the ADS1115 ADC can be configured with different gains.

Turbidity

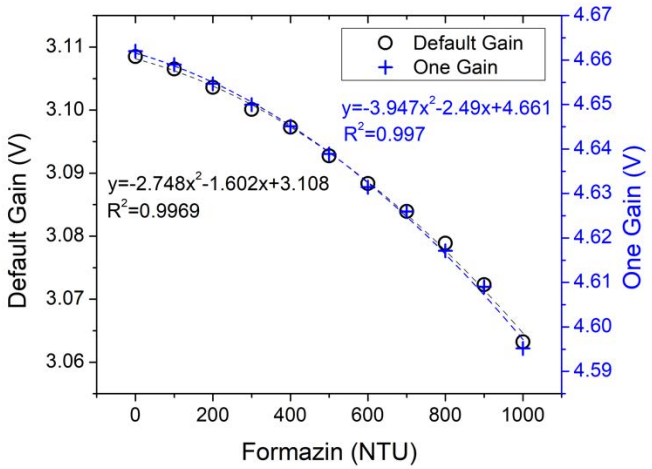

Figure 3.6.Plot of Voltage versus Formazin samples of increasing turbidities using attenuation method with the TS-300B sensor, measured with a 2/3X gain (1 bit=0.1875mV) or a 1X gain (1 bit = 0.125mV).

Figure 3.6 shows the measured voltage versus turbidity with two different ADC gains. As the sensor uses the attenuation technique the voltage value is higher at lower NTU values, because the higher the NTU the less light reaches the photodetector. It can be observed that the dependency of voltage to turbidity is not linear, and the total voltage drop is very small even from 0 to 1000 NTU, with 45 mV for gain 2/3X and 67mV at gain 1X. This implies that a variation of 1 NTU would correspond to a voltage variation of 67µV at 1X gain, and would be highly challenging to measure, confirming that this type of washing machine sensors is not suitable for low turbidity range [102]. It was decided to continue with the next method.

3.4.2 Heart monitor optical sensor as a backscattering turbidity sensor

Backscattering IR method is particularly useful for higher turbidity levels where the suspended particles cause sufficient light to be scattered. As we were still in the pandemic and we had an Analog Devices ADPD144RI heart monitor optical sensor available in the laboratory, we decided to evaluate it as a low-cost turbidity sensor in a backscattering configuration. The ADPD144RI is a fully integrated photometric Front End optimized for heart rate monitoring by photoplethysmography (PPG) detection of blood oxygenation (SpO2). It contains four photodiodes with a transimpedance amplifier, an Analog Front-End, a 14-bit ADC, two LED drivers and two LED sources (one at 660 nm and one at 880). This component implements synchronous detection which helps removing the ambient light contribution and improves signal to noise ratio. As photodiodes and LED sources are in the same plane, it can be used as a backscatter sensor. Furthermore, the ADPD144RI IR light source is compatible with ISO 7027 which specifies a non-visible wavelength at 860 nm +/-30 nm, as infrared light is not influenced by the medium color and is rarely absorbed by particles and molecules.

Turbidity

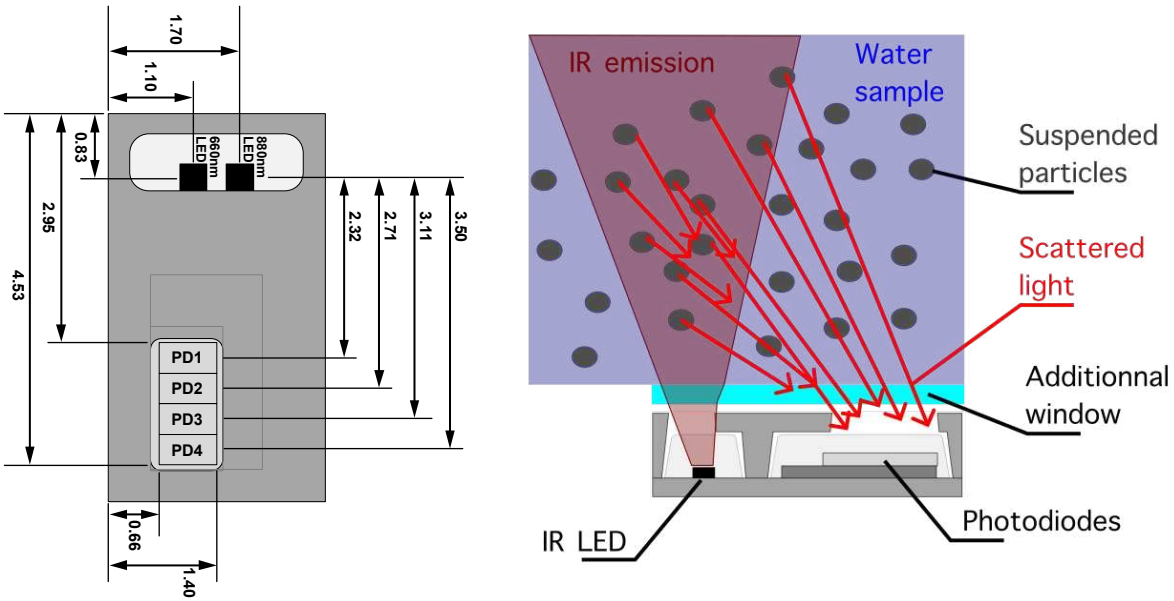

Figure 3.7 - Left: schematic top view of the ADPD144RI showing the physical dimensions of this optical sensor and the position of the photodetectors (PD1 to PD4) as well as the two light sources. Adapted from Analog Devices ADPD144RI datasheet. Right: cut-off side view of the ADPD144RI with an additional window showing its implementation as a turbidity sensor in a backscattering configuration.

In order to evaluate the ADPD144RI as a turbidity sensor, it was necessary to develop a custom PCB, a waterproof housing and an Arduino library to interface the optical sensor with an Adafruit Feather M0 microcontroller.

This optical sensor is highly integrated and only requires a few external passive components, mainly decoupling caps and a large external capacitor for the LED driver. As a low-power component, it uses a 1.8V power supply and 1.8V logic level, so a Texas Instruments PCA9306 level shifter was added to adapt to the Adafruit Feather M0 3.3V logic levels for the I2C communication bus, while a AP73134 low dropout regulator converts the 3.3V power supply to 1.8V. The integrated LEDs anodes must be connected to a power source through the V_{LED} pin. To enhance the LEDs' pulse current in pulse mode, an external capacitor C_{VLED} must be positioned near the V_{LED} pin. The C_{VLED} capacitor provides a local, low impedance current source that reduces the dynamic requirements on the V_{LED} supply. A properly sized C_{VLED}typically has a sufficient storage capacity to prevent the forward voltage on the LED from dropping less than the minimum voltage required for the maximum pulse current. C_{VLED} is dimensioned using the following equation:

$$C_{VLED} = \frac{t_{LED\_PULSE} * I_{F\_PEAK}}{V_{LED\_MIN} - (V_{F\_PEAK} + 0.2)} \quad (3)$$

Where $C_{VLED}$is the minimum size of capacitor in Farads, t_{LED_PULSE} is the LED pulse width, I_{F_PEAK} is the maximum forward-bias current on the LED used in operating the device, V_{LED_MIN} is the voltage from the V_{LED} supply under I_{F_PEAK}, $V_{F_PEAK}$is the maximum forward-bias voltage required on the LED to achieve I_{F_PEAK}. The absence of this capacitor could negatively impact the LEDs' pulsed output due to the increased impedance from the LED power supply.

A custom PCB was designed using Autodesk Eagle CAD software, and manufactured by OSH PARK. Assembly of the components was made in-house at the LAAS electronic

facility with a reflow oven. Additionally, a waterproof case was designed with Autodesk Fusion 360 software, and manufactured with a desktop Formlabs Form 3 stereolithography (SLA) 3D printer [95] using Grey Pro resin. SLA was favored over FDM (Fuse Deposition Modelling), as it can produce waterproof parts without specific treatments [103]. The 3D housing incorporates an optical port in front of the ADPD144RI LEDs and photodiodes which is covered by a polydimethylsiloxane (PDMS) 1mm thick window, made with Sylgard 184 PDMS with a ratio of 1:10, and glued with epoxy resin. PDMS was used because is a polymer which is commonly use in microfluidics notably due to its optical transparency. Figure 3.8 shows the assembled PCB and its integration in the 3D printed housing with the PDMS window.

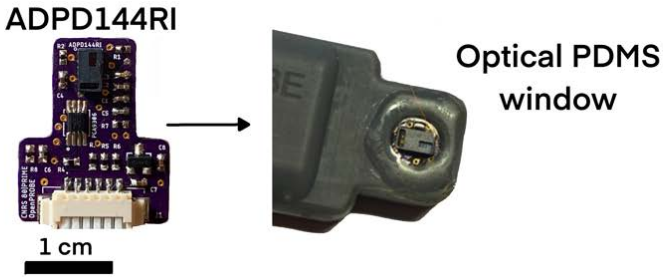

Figure 3.8. Left: ADPD144RI custom PCB, with the sensor visible on the upper part of the circuit. The two rectange openings corresponds to the LED light sources and the photodiodes. A Molex Picoblade connector, visible at the bottom of the PCB, is used to connect the circuit to the Adafruit Feather M0 microcontroller. Right: detailled view of the 3D printed waterproof housing and the PDMS window developed for the ADPD144RI PCB.

The sensor works by synchronously measuring the light which is reflected by a surface or backscattered by particles from series of excitation pulses. It allows to adjust the number of pulses and LED current, enabling the designer to optimize the trade-off between sampling frequency, detection sensitivity, and energy efficiency for their specific application needs. All these settings can be modified by programming the internal registers through the I2C protocol. We developed an Arduino library to program and use the sensor, which is given in GitLab. Two time slots, SLOTA and SLOTB, are available in this component, and allows for individual settings in terms of pulse number, pulse period, pulse width, pulse delay, LED current, TIA gain and LED source (660nm or 880nm). For our tests we used only SLOTA configured with the 880nm IR LED and experimented with the numerous settings to optimize the ADPD144RI for backscattering measurement of turbidity. This optical sensor incorporates a burst accumulator that sums all the pulse energy minus the ambient light contribution into a 20-bit value. The number of pulses can be adjusted from 1 to 255 pulses.

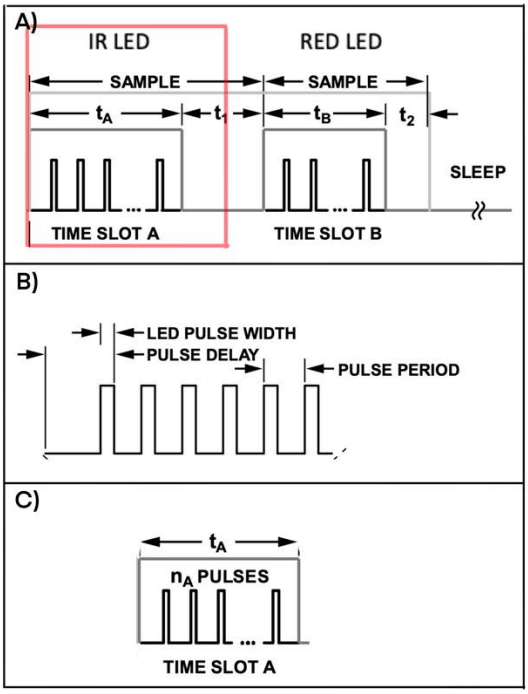

Figure 3.9. ADPD144RI configuration. A) Time Slot A for IR LED, and Time Slot B for RED LED. In our case only Time Slot A is used. B) Pulse period of 19 µs, pulse width from 3 to 16 µs, and pulse delay of 25 µs. C) Number of pulses from 0 to 255.

The sensor possesses a state machine with three modes of operation: STANDBY, PROGRAM, and SAMPLE, which are activated as required by the Arduino code. The next step is to test our sensor, using turbidity samples which were prepared with the same protocol as in the previous section from dilution of Formazin 4000 in deionized water according to the following equation:

$$C_2 = \frac{C_1 * V_1}{V_2} \tag{4}$$

Where C1 is the initial concentration, V1 is the initial volume, C2 is the final concentration and V2 is the final volume. In order to check that our samples have the desired NTU value we used a commercial Thermo Scientific Aquafast AQ3010 Turbidity Meter, a handheld device that uses 90° nephelometric method and outputs turbidity in NTU units. Figure 3.10 show the data obtained with this instrument of all our samples from 0 to 50 NTU.

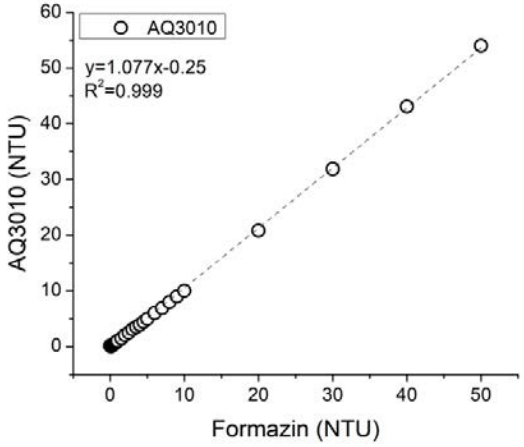

Figure 3.10. Graph of AQ3010 Turbidity meter to Formazin 4000 Standard.

Turbidity

The next step is to select the parameters for the best performance of the ADPD144RI, to do that achieving the best signal-to-noise ratio (SNR). In the ADPD144RI the SNR improves as a square root of the number of pulses averaged together, whereas LED power consumed is directly proportional to the number of LED pulses. For every doubling of the LED pulse count, there is a doubling of the LED power consumed and a 3 dB SNR improvement. There is a setting that maintains the same SNR while minimising total system power. To optimise the maximum SNR, we must find the right TIA gain and LED intensity level where the number of LED pulses remains constant. A TIA gain of 50,000 is recommended for maximum SNR, assuming no saturation of the photodiode and provided that the lowest LED current setting (8 mA) does not saturate the photodiode. In cases where this condition is not fulfilled, a TIA gain of 25,000 is considered as a starting point. Sometimes the tuning system may impose an upper limit on the gain to avoid clipping of ambient signals. Finally, increasing the number of pulses achieves the desired SNR of the system. First experiment was conducted by placing the packaged sensor inside a container with the Formazin sample.

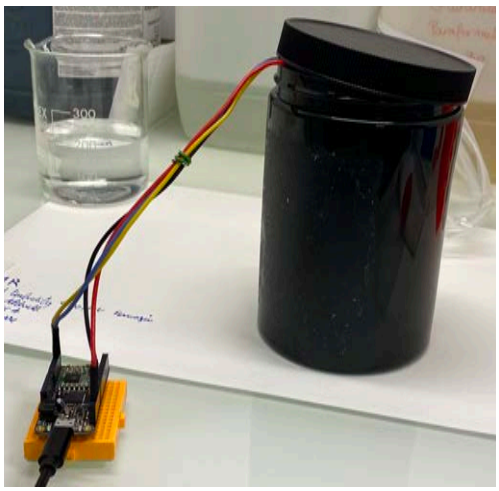

Figure 3.11 – Testing set-up for the ADPD144RI, the sensor is immersed in the turbidity sample inside the black container.

Several tests were done to see how modifying the pulse width, number of pulses within the Time Slot, and current affects the data acquisition. Backscattering is a method that is regarded as not very sensitive at low turbidities, as such it is necessary to have a high LED intensity, so a large value of 235mA was selected for the first experiment where the pulse width was modified while keeping the other parameters constant.

Turbidity

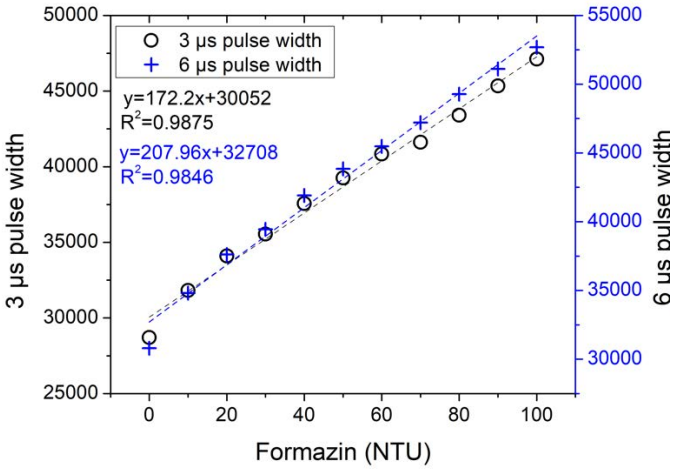

Figure 3.12. Plot of counts versus NTU for varying the pulse width, black line for 3µs pulse width and blue line for 6µs pulse width, both with 80 number of pulses, 235mA and 50,000 TIA.

In the Figure 3.12 we can see as expected that higher turbidity causes higher backscattering which is visble by the increasing counts. It is also observed that there is not much sensitivity difference between using 3 or 6 µs as pulse width with similar slopes. It was decided to keep a pulse width of 3 µs, as it offers similar sensivity while consuming half the power. In this configuration, the sensor was near the saturation at 100 NTU (which is attained at 65536 counts), but the starting point at 0 NTU can be set with an offset, thus enlarging the dynamic range covered. A second test was conducted to observe the influence of the IR LED excitation current, with the results visible Figure 3.13.

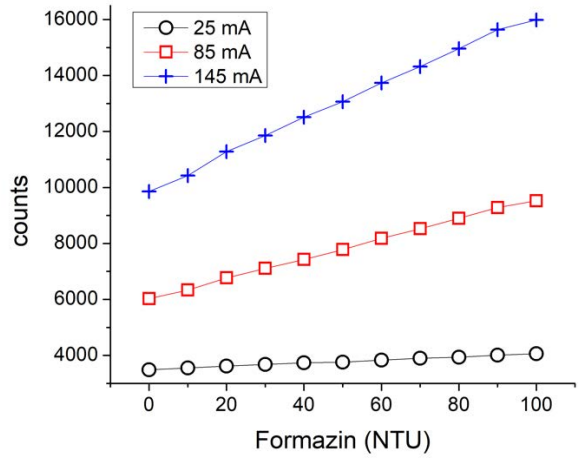

Figure 3.13. Plot of counts versus NTU for varying current, black line for 25 mA, red line for 85 mA and blue line for 145 mA, all of them with 80 number of pulses, 3µs pulse width and 50,000 TIA.

Increasing the excitation current increases the scattered light that is collected by the photodiodes, which increases the number of counts, hence the sensitivity. As expected, a higher current maximizes the counts. Finally, we investigate the influence of the number of pulses with a 205mA excitation current (Figure 3.14).

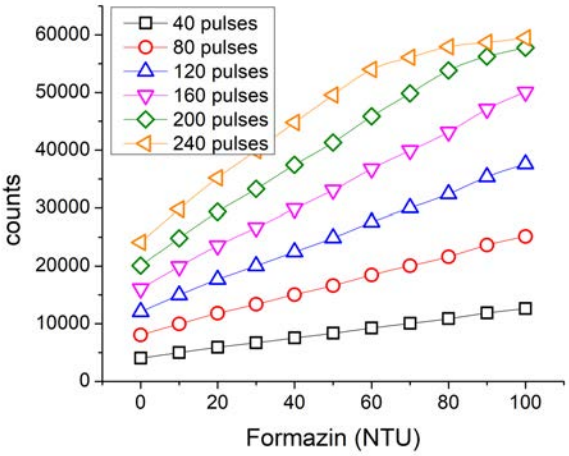

Figure 3.14. Plot of counts versus NTU for varying number of pulses, black line for 40 pulses, red line for 80 pulses, blue line for 120 pulses, pink for 160 pulses, green for 200 pulses, and orange line for 240 pulses, all of them with 205 mA, 3µs pulse width and 50,000 TIA.

As it can be seen in Figure 3.14, varying the number of pulses has the same behavior as varying the current, as the sensitivity increases linearly with the number of pulses, going from 85 counts per NTU with 40 pulses to 495 counts per NTU with 240 pulses (roughly a 6X increase). It is important to say that the limit of our sensor is based on the number of counts, as we use a 16-bit ADC the highest number of counts possible is 65535, after this number of counts our sensor is saturated. Taking into account this limitation, the choice of current and number of pulses will depend on the range of NTU values we want to measure, i.e. if we use a current of 205 mA and 240 number of pulses, our sensor will only be able to measure between 0 and 60 NTU with a sensitivity of 495 counts per NTU, whereas if we use a current of 205 mA and 120 number of pulses, our sensor will only be able to measure between 0 and 180 NTU values with a sensitivity of 255 counts per NTU.

Based on these results, we selected settings that would allow a sensitivity of about 100 counts per NTU, so it was decided to use 80 pulses and a current of 205 mA, and established a 3-point calibration using 0, 20, and 100 NTU samples. Using the following equation, we can obtain the relationship between counts and NTU values:

$$NTU = \frac{counts - 9744.85}{166.40} \tag{5}$$

Once having our calibration equation, we tested the sensor for different turbidity values samples from 0 to 100 NTU in 10 NTU steps, and from 0 to 10 NTU with 0.5 NTU steps.

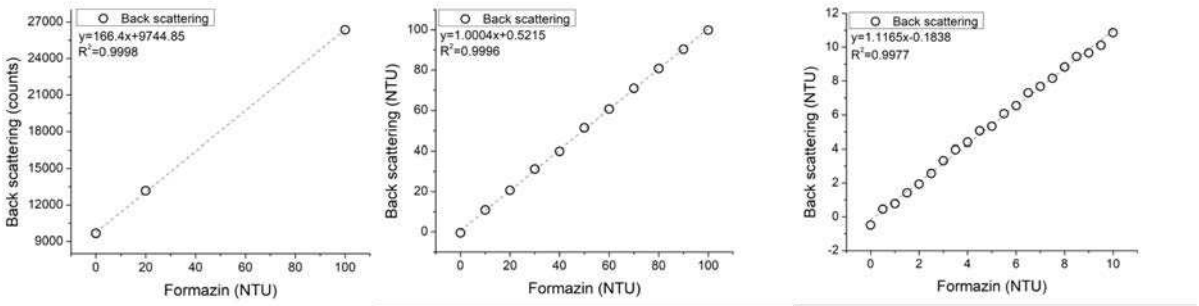

Figure 3.15 - Data obtained with the optimized settings of 205mA IR LED current, 80 number of pulses, 3 µs pulse width, and 50,000 TIA gain. Left: three-point calibration curve with 0, 20 and 100 NTU samples. Center: Calibrated sensor response from 0 to 100 NTU in 10 NTU steps. Right: Sensor response from 0 to 10 NTU in 0.5 NTU steps.

The results obtained with these optimized settings are presented Figure 3.15. We observed the increasing linear trend line on the 0 to 100 NTU range as expected, however we were surprised to observe that a high accuracy was achieved for low NTU values in the 0 to 10 NTU range as well.

This result was not expected, as backscattering is supposed to be inappropriate for low turbidity values as almost no particles are present. The experiment was repeated several times in the same conditions, with similar results. After further investigation, we discovered that contrary to our initial belief, the measurement was not only caused by backscattering, but was a combination of two mechanisms: backscattering by particles (which should be very small for low turbidities), but also absorption, as the IR LED excitation light was reflected on the edge of the container showed Figure 3.11, and was hitting back the photodetector. Due to the fact that the IR light was not visible by the naked eye, this artefact was only identified toward the end of the experiments. As the sensor was always positioned in the same place during each experiment, the absorption path (twice the distance between the sensor and the edge of the container) was kept constant, hence the results were apparently plausible.

So, while not a backscattering sensor as expected, the ADPD144RI proved to be an interesting sensor, however for in-situ field deployment it would require a reflective surface in front to reproduce the results we obtained in this section. The distance of the reflector would actually condition the sensitivity of the sensor at low turbidities, as according to the Beer-Lambert law the absorption contribution is linearly dependent on the optical path length, which in our case is defined as twice the distance between the sensor and the reflector.

For the next step, and as mentioned at the beginning of this section, we should have started with the GLI-2 method, but had to postpone this development due to the unavailability of key components caused by the COVID pandemic. The main component we had to wait for was the ADPD1080: it is from the same family as the ADPD144RI, so the same Arduino code can be used as they share the same memory registers. The main difference is that the ADPD1080 uses external LEDs and external photodetectors, which was required to implement the geometric configuration of the GLI-2 method.

3.4.3 GLI-2 Method

The multiparameter probe developed in this project is conceived to operate in coastal waters near the Oceanological Observatory of Banyuls sur Mer (OOB), France. In this area of the Gulf of Lion in the Mediterranean Sea, turbidity levels are considered quite low with average values ranging from 0 to 10 NTU typically during the year, which implies that the sensor must offer sufficient resolution (i.e. 0.5 NTU or better). Biofouling is also a common occurrence during long-term deployment of optical sensors in this area, as observed at the OOB as a part of the French Coastal Monitoring Network SOMLIT. Based on these constraints, we choose to design a sensor implementing the GLI-2 Method as it offers good sensing performance at low turbidities, and its ratiometric-based method can cancel out measurement errors due to biofilm formation on the optics as seen in the introduction of this chapter.

Another advantage of the GLI-2 design is the ability to get information on both side-scattered light (nephelometric) and attenuation (transmission); the latter being recommended to be included in new turbidity instrumentation by Kitchener et al. [104], as it allows for the use of SI based units for calibration. Compared to conventional nephelometric instruments which are calibrated with Formazin, this allows better intercomparison to other turbidimeters,

a characteristic that is currently lacking from commercial systems as highlighted by Rymszewicz et al. [105]. To our knowledge, our sensor is the first academic work on a GLI-2 based design that can operate continuously in-situ.

Absorption underwater is stronger for longer wavelengths, so the use of IR photodiodes limits the influence of daylight during in-situ measurements. However, due to the relatively small variations caused by turbidity, an ambient light rejection strategy is still required, and is taken care of by synchronous detection. While each of these functions can be achieved by discrete components, we choose to design our system around the ADPD1080 from Analog Devices, a highly integrated photometric front-end initially designed for photoplethysmography (PPG) in wearables or smartwatches, as it includes all the required features in a single low-power Integrated Circuit (IC), which is highly beneficial in terms of cost, miniaturization, and power consumption. It is similar to the ADPD144RI tested in the previous section, but uses external LEDs and photodiodes. It shares the same internal functions with minor differences: it possesses three LEDs drivers with up to 370mA current capability, the possibility to connect up to 8 photodetectors to its transimpedance amplifier (TIA) with digitally adjustable gains, and has an Analog Front End (AFE) which is in charge of the rejection of signal offset and corruption due to the interference caused by ambient light, and has a 14-Bit ADC. Our turbidity sensor has two external infrared LEDs and two external infrared photodiodes to implement the GLI-2 method. For the infrared LEDs we use OSRAM SFH 4718A that has its peak wavelength at 860 nm, a Full Width at Half Maximum (FWHM) of 34 nm, and supports up to 1000 mA of forward current. For the photodetectors we use Vishay VEMD5160X01 silicon photodiodes with a daylight blocking filter that translate to a relative spectral sensitivity from 700 to 1070 nm. These optoelectronics components are connected to the photometric ADPD1080.

The block diagram on Figure 3.16 describes the overall architecture of the turbidimeter. An Adafruit Feather M0 microcontroller is used to control the different components, as it is a popular open-hardware configuration for environmental sensor projects [106], [107]. The microcontroller controls the ADPD1080 photometric front end through an I2C interface, in order to adjust the various settings for LED drivers, TIA gain and various timings.

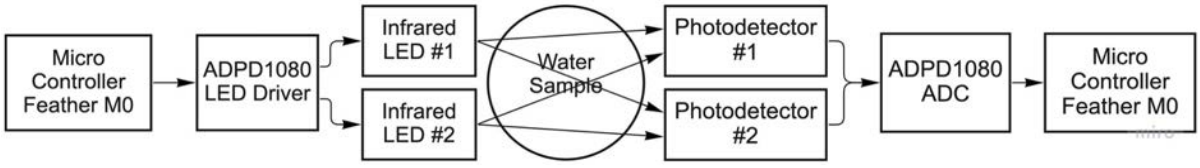

Figure 3.16. Functional block diagram of the GLI-2 sensor developed around the ADPD1080.

A custom PCB was developed for the ADPD1080, once again using Autodesk Eagle CAD software. The PCB was manufactured by OSH PARK, and components were assembled in-house with a reflow oven. The same external components used for the ADPD144RI PCB are used to interface the 3.3V Adafruit Feather M0 to the 1.8V ADPD1080: an AP7313 low dropout voltage regulator is used to supply a clean 1.8V and a PCA9306 I2C bus voltage-level translator is used for the SDA and SCL lines, with 2.2 kΩ pull-up resistors. An additional component, the ADG3304 bidirectional logic level translator is used for the GPIO0 and GPIO1 pins which are used for generating hardware interrupts on the microcontroller when data is available.

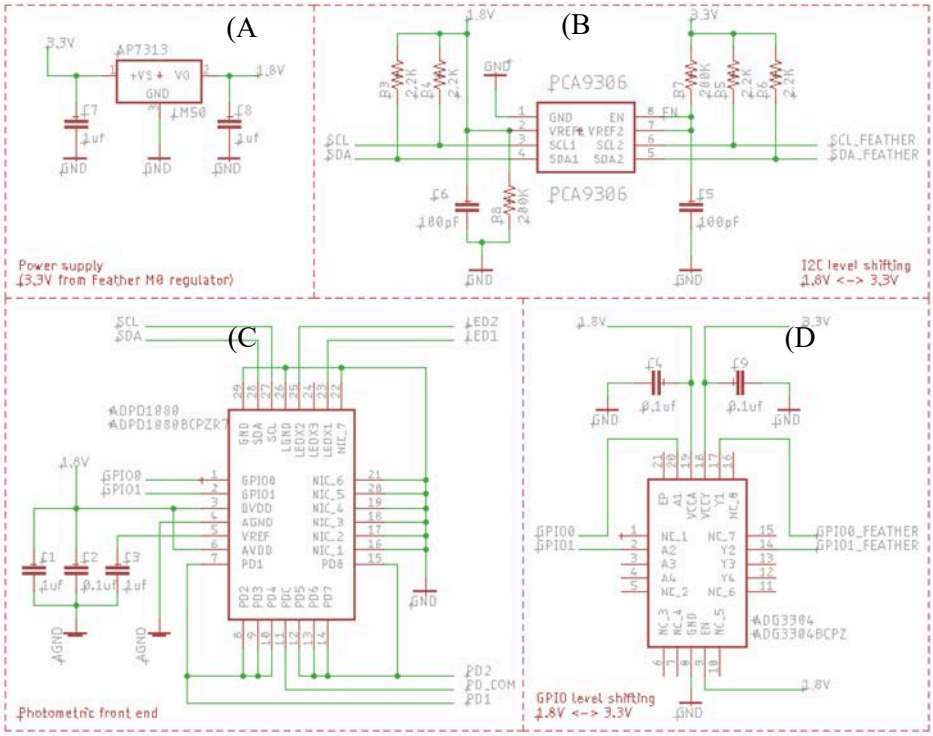

Figure 3.17. Circuit schematic of the main functions. (A) Low voltage dropout power 1.8V supply. (B) PCA9306 I2C bus voltage translator, to interface between the 3.3V logic of the microcontroller and the 1.8V logic of the photometric front end. (C) Photometric Front End ADPD1080, with photodiodes PD1 and PD2 connected to PD1-PD4 and PD5-PD8 respectively, to improve dynamic range. (D) ADG3304 bidirectional logic level translator for GPIO0 and GPIO1 pins which can be used to generate hardware interrupts when data is available.

Optoelectronics components, i.e. LEDs and photodiodes, are integrated on a separate PCB in order to implement the GLI-2 method. Due to the use of SMD components, the spatial distribution required, and the need of integration in a waterproof enclosure for in-situ measurements, we chose to design a custom polyimide flexible PCB (also obtained from OSH PARK) that is bent in a circular shape to obtain proper positioning of the optical elements This configuration is shown Figure 3.18. Both PCBs are connected through Molex Picoblade 6 pins cable and connectors.

The waterproof enclosure is 3D printed by stereolithography (SLA) with a desktop Formlabs Form 3 and Black V4 Resin, a methacrylate-based material. The flexible PCB with its mounted LEDs and photodiodes is bent to be inserted within the enclosure, with mechanical features that guides the LEDs and photodiodes to ensure proper alignment. We then used overmolding with polydimethylsiloxane (PDMS, Sylgard 184 – Dow Corning) to ensure waterproofness and optical transparency for the optical elements. This also ensures that air is not trapped into the housing, which is a key factor to obtain a sensor that can be used at depth in the water column. A 1:10 ratio PDMS mixture is used to cover the 3D printed enclosure and the flexible PCB, with the help of an extra 3D printed piece we insert the sensor housing in it, with a Kapton film in the center covering the optical windows to create a smooth PDMS windows. The whole assembly is polymerized at 65°C overnight, and then the insert with the Kapton film is removed, leaving optically clear and smooth windows in front of each optical elements, as visible in Figure 3.18 closeup views. In order to facilitate sensor testing, we designed and printed a M10 penetrator adapter to make our turbidity sensor compatible with the Blue Robotics waterproof enclosures that are regularly used in environmental sensor development [108].

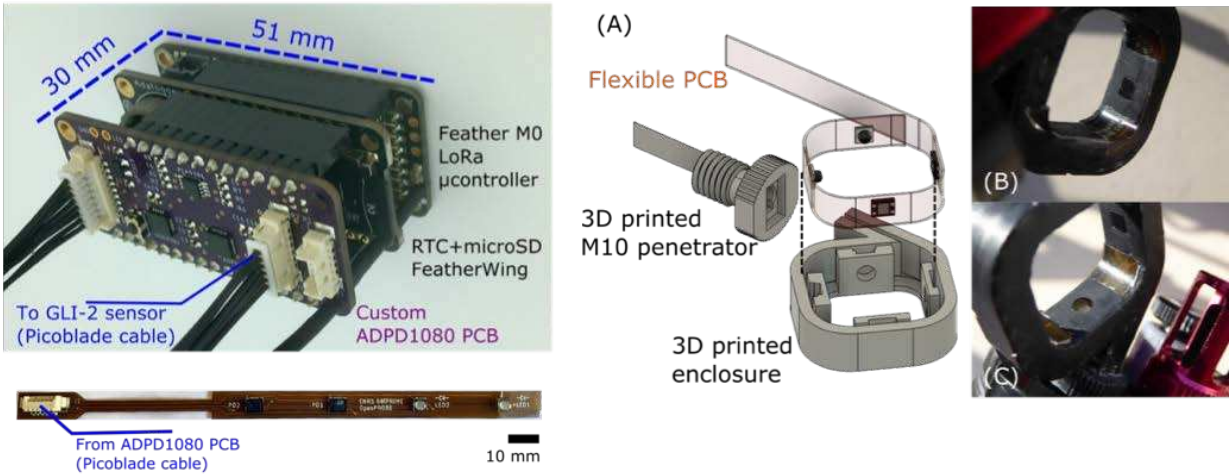

Figure 3.18. Upper left: picture showing the custom ADPD1080 PCB, stacked upon an Adafruit Adalogger Featherwing that hosts a Real Time Clock, CR1220 battery and microSD card, and the Adafruit Feather M0. Lower left: Flexible PCB with LED1, LED2, PD1 and PD2 as well as a Molex Picoblade 6 pin. Right: (A) CAD illustration of the GLI-2 sensor, with the flexible PCB, the 3D printed enclosure and a 3D printed M10 penetrator. (B) and (C) Close-up pictures of a photodiode and a LED optical port respectively, after the PMDS overmolding step.

The Adafruit Feather M0 is programmed through the Arduino IDE environment, with a custom library derived from the ADPD144RI code to handle the specific functionalities of the ADPD1080. The operation principle of the photometric front end is similar to the ADPD144RI, but this time we used both SLOTA for IR LEDA and SLOTB for IR LEDB to implement the GLI-2 method. Additionally, the ADC output is read by the microcontroller either through the use of hardware interrupts (using GPIO0 and GPIO1 pins of the ADPD1080), which are generated each time new data is available in the ADC output register, or by data polling at regular interval. While data polling is easier to implement, the use of hardware interrupt is more robust and allows for better efficiency of the code, especially if one consider optimizing the battery life of the system.

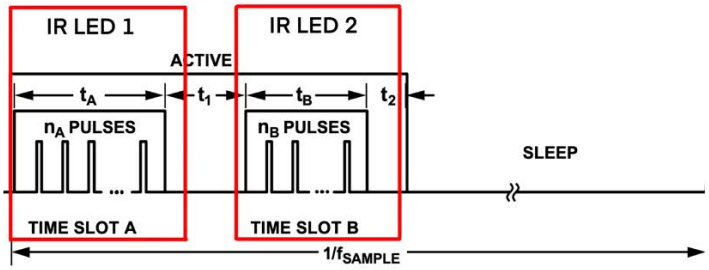

Figure 3.19. ADPD1080 configuration. Time Slot A for IR LED1, and Time Slot B for IR LED2, the pulse period, pulse width, pulse dalay, number of pulses, and current in each slot can be configured. Adapted from Analog Devices ADPD1080-ADPD1081 datasheet.

As the ADPD144RI, the ADPD1080 photometric front end is a complex component with many different settings that can influence drastically its performance. Prior to its use, we choose to validate the behavior of our optoelectronic component's selection. How we used external optical components, the Analog Front End (AFE) integration offset needs to be adjusted for rejection of signal offset and corruption due to modulated interference commonly caused by ambient light. The timing within each pulse is important for optimizing the operation of the ADPD1080, the AFE integration width must be equal or larger than the LED width. As AFE width increases, the output noise increases and the ability to suppress high frequency content from the environment decreases. It is therefore desirable to keep the AFE integration

width small. However, if the AFE width is too small, the LED signal is attenuated. The AFE width produces the optimal SNR at 1 µs more than the LED width. After setting LED width, LED offset, and AFE width, the ADC offset can then be optimized. If the AFE window is not correctly sized or located, all receive signal is not properly reported and system performance is not optimal; therefore, it is important to verify proper AFE position for every new hardware design or pulse LED width. Figure 3.20 shows the timing waveforms for a single time slot as an LED pulse response propagates through the analog block of the AFE.

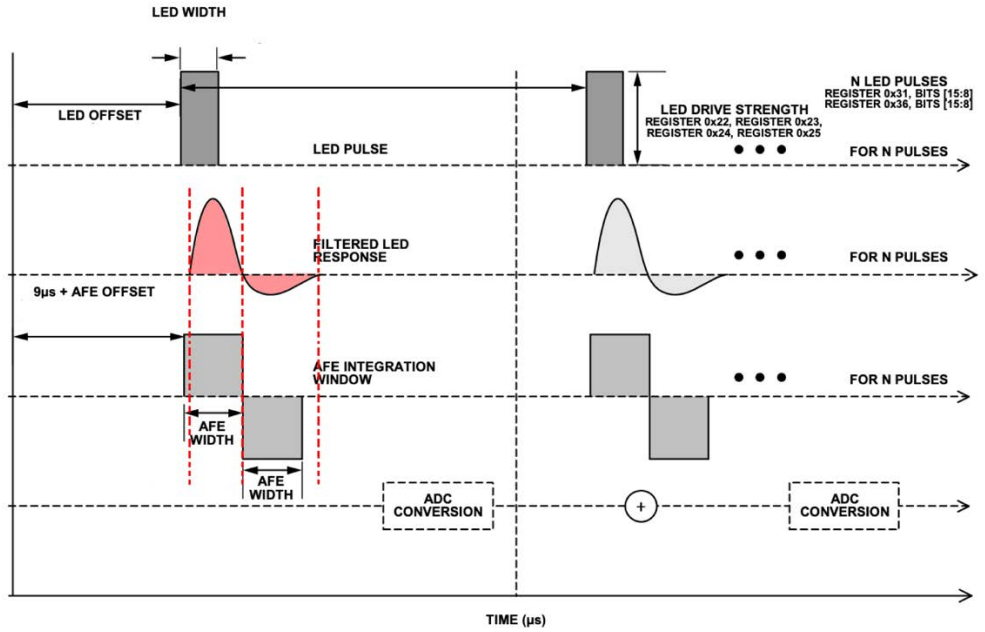

Figure 3.20. AFE Operation Diagram. Adapted from Analog Devices ADPD1080-ADPD1081 datasheet.

The starting point of the AFE integration offset, expressed in microseconds, is set such that the falling edge of the integration window aligns with the falling edge of the LED, then it is incremented step by step to find the best AFE integration or local maximum. AFE offsets for Time Slot A and Time Slot B are controlled by bits, each LSB representing one cycle of the 32 MHz clock, i.e. 31.25 ns. Optimization is illustrated in Figure 3.21.

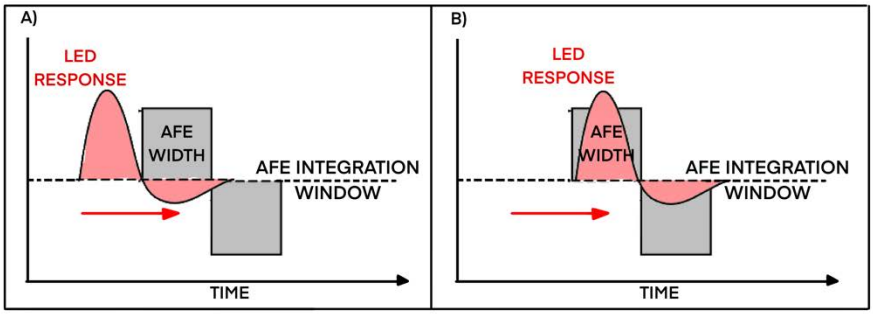

Figure 3.21. AFE offset integration. A) Starting AFE offset point (unaligned). B) Local maximum of the AFE offset (Aligned).

Sweeping the AFE position from the starting point is the recommended way to optimize the AFE offset and to find the local maximum. The setup for this test is to allow the LED light to fall on the photodiode in a static way. This test is typically done with a reflecting surface at a fixed distance. The AFE position can then be swept to look for changes in the output level. When adjusting the AFE position, it is important to sweep the position using the 31.25 ns steps. Typically, a local maximum is found within 2 µs of the starting point for most systems. As we

used two LEDs and two photodetectors, the AFE offset integration was performed for each LED and photodetector.

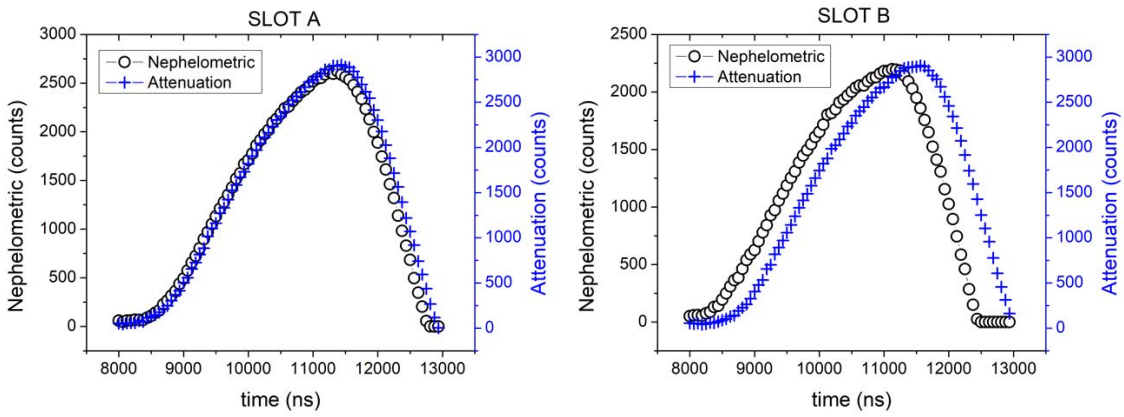

Figure 3.22. AFE offset interaction for both Slots, and both method to each one, the nephelometric and attenuation.

The Figure 3.22 shows the result of the AFE offset sweep for each Slot, (LED1 SlotA, LED2 SlotB) the configuration used for this test was 1 pulse per Slot with a current of 50 mA. The X axis indicates the number of steps or µs that the offset has to be configured to find the local maximum. The results are very similar since the same LEDs and photodetectors references were used for both Slots. It is observed that an offset of approximately 85 steps has to be configured, which is equivalent to an AFE offset of 2.65 µs, which is in accordance with the description in the ADPD1080 datasheet where it is specified that for most of the configurations the AFE is around 2 µs.

Due to the complexity of the ADPD1080 chip and the GLI-2 method, we first conducted an experiment using only the sensor head (flexible PCB with optoelectronics components) connected to benchtop instruments to stimulate LEDs and measure photodiodes currents when exposed to a range of turbidity calibration solutions of Formazin in controlled laboratory conditions (i.e. no variations in ambient light).

Briefly, a Keithley 2400 Source Meter was used to stimulate the LEDs with a constant current of 80 mA, while the photocurrent issued from the photodiodes was measured using a Keithley 2100 Multimeter setup as an Ampere meter. The LEDs excitation current is only briefly maintained during the measurement to avoid detrimental heating effects. The two optical configurations required by the GLI-2 method, i.e. 90° nephelometric (referred also as Active) and 180° attenuation (referred also as Reference) are measured with this setup, and showed Figure 3.23 for turbidity solutions varying from 0 to 40 NTU. It can be noted that the photocurrents behavior was as expected: in 90° nephelometric configuration, an increase in turbidity results in an increase of light diffraction and consequently to an increase of the collected light by the active photodetector. In the attenuation configuration, an increase of turbidity leads to an increase of light scattering and absorption, which turns into a decrease of the collected light by the 180° photodiode. A linear relationship between photocurrent and turbidity is observed in all configurations.

For both Active and Reference optical configuration, slight discrepancies can be observed, which could be attributed to individual optoelectronic components differences or optical effects due to misalignment or differences in the PDMS transparency. It should be emphasized that the photocurrent variations are rather small, and correspond to approximately 0.01 µA per NTU in 90° nephelometric configuration, and 0.04 µA per NTU in 180°

attenuation configuration. Thus, the corresponding photocurrent variation to a 0.1 NTU turbidity variation shall be in the range of a nA. Nonetheless, these tests confirmed that our sensor design worked as expected in the 0 to 40 NTU range.

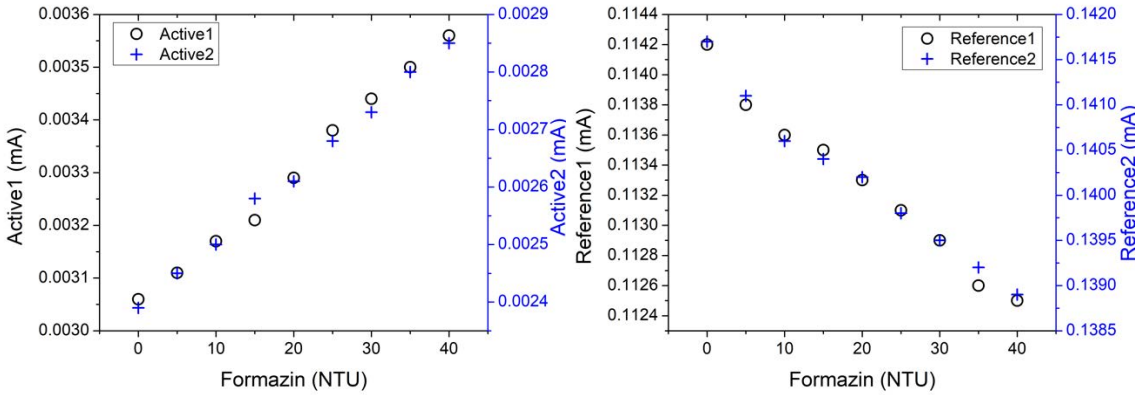

Figure 3.23. Photodetector current characterization obtained with benchtop instruments with Formazin solutions ranging from 0 to 40 NTU. Left: 90° nephelometric configuration current for Active1 and Active2 signals. Right: 180° attenuation configuration current for Reference1 and Reference2 signals.

After this sensor design validation using benchtop instruments, we then replaced the benchtop Source Meter and the Ampere Meter by our custom PCB hosting the ADPD1080 photometric front end and its additional components. In order to implement ambient light rejection, the excitation light is now modulated and consists in trains of short 3 µs pulses, while scattered/and or absorbed resultant signal is synchronously sampled. Photocurrents generated by the photodiodes are internally amplified by the TIA and conditioned, prior to being converted by the 14-bit ADC, giving an output in counts.

Similarly to the ADPD144RI, the ADPD1080 also has the possibility to configure several parameters, such as the pulse width, the number of pulses in each SLOT, the current and the internal gain, this configuration will depend on the method to be used. As mentioned above, for the GLI-2 Method it is necessary to use the Nephelometric and Attenuation Method. To operate the GLI 2 method, four steps are required, Table 2 describes the configuration used for each method. We used 50 pulse numbers for both methods. We varied the current and gain, as mentioned before, for Nephelometric method it is necessary to have a higher intensity of the LED, for this reason we used a current of 290 mA and a TIA gain of 200k. On the other hand, for Attenuation method it is necessary to have a lower intensity of the LED, as the photodiode directly faces the LED, for this reason we used a current of 90 mA and a TIA gain of 25k.

Table 2 - Main settings of the ADPD1080 for the four steps required to implement the GLI 2 method.

Description	Step#	LED#	Time SLOT#	PD#	Pulse count	TIA gain	Current
Nephelometric 90°, Active 1	1	1	A	1	50	200k	290mA
Attenuation 180°, Reference 1	2	1	A	2	50	25k	90mA
Nephelometric 90°, Active 2	3	2	B	2	50	200k	290mA
Attenuation 180°, Reference 2	4	2	B	1	50	25k	90mA

The Figure 3.24 shows how the acquisition of each signal is achieved with the 4 steps described in Table 2, to obtain both active and reference signals, along with acquisition time of each signal. Total acquisition time for a complete GLI-2 reading sequence is 96 ms, which is a much shorter time compared to commercial turbidity sensors. As a comparison, the AQ3010 reference sensor that we used for solution calibrations takes about 30 seconds to perform a single measurement. When LED1 is ON, PD2 takes the active signal and PD1 takes the reference signal, while when LED2 is ON, PD2 takes the reference signal and PD1 takes the active signal. It is important to note that all the data obtained is in counts, hence the sensor must be calibrated to obtain values in NTU. Different Formazin samples were prepared, covering a range from 0 to 10 with 0.5 NTU increments and from 0 to 40 NTU with 5 NTU increments.

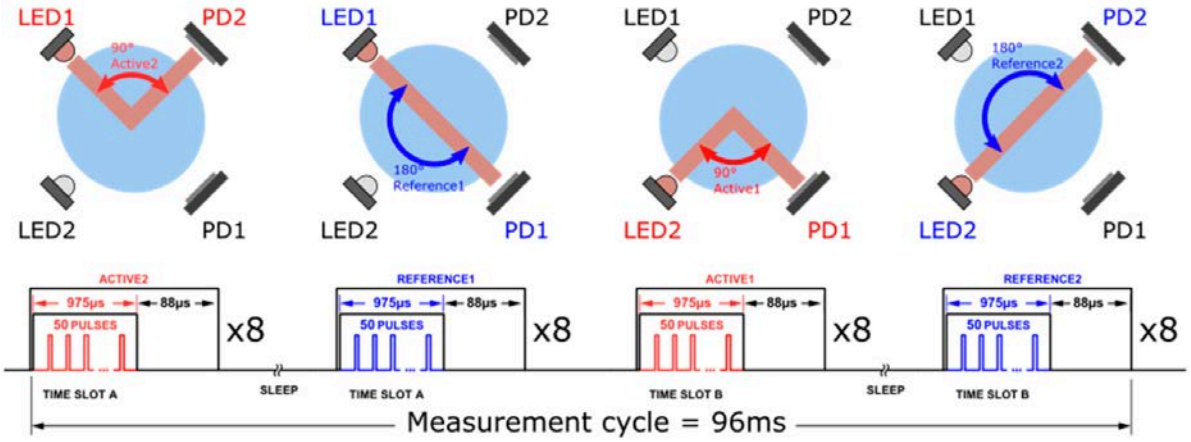

Figure 3.24. Measurement sequence to measure Active1, Active2, Reference1, and Reference2 signals. Each step was taken 8 times to perform internal averaging, which allows to improve signal-to-noise ratio. Total measurement time in this configuration is 96 ms.

Turbidity

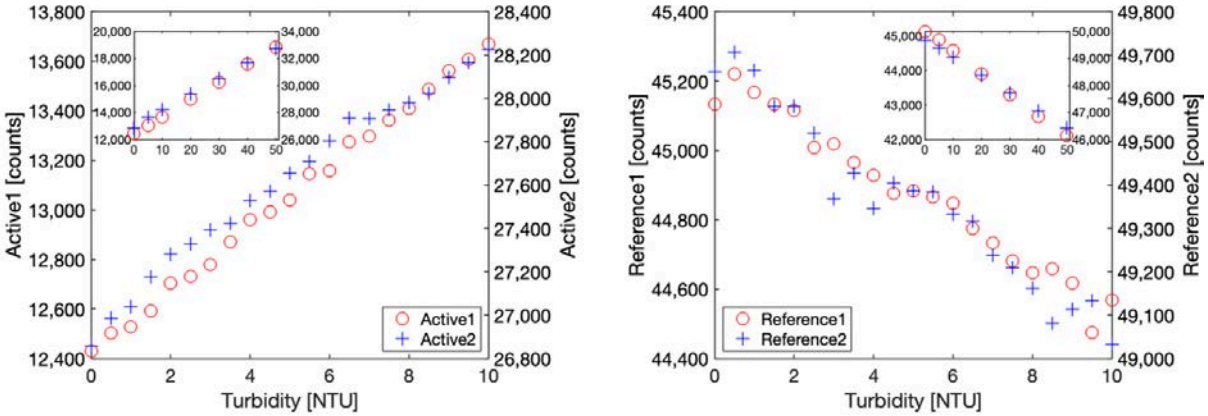

Figure 3.25. Calibration experiment with Formazin solutions ranging from 0 to 10 with 0.5 NTU increments and from 0 to 40 NTU with 5 NTU increments, with raw ADC output expressed in counts. A) Nephelometric method for time SLOTA and time SLOTB. B) Attenuation method for time SLOTA and time SLOTB.

Figure 3.25 shows the obtained results in both configurations for the two time slots, which corresponds to Active1, Reference1 and Active2, Reference2 respectively. It can be observed that each channel has different characteristics in terms of offset and sensitivity but exhibits similar tendencies. However, these differences are not considered as a major issue as they are cancelled out thanks to the ratiometric nature of the GLI-2 method. In the nephelometric configuration (Active1 and Active2), sensitivity varies from 200 to 400 counts per NTU approximately, while in the attenuation configuration (Reference 1 and Reference 2) sensitivity varies from 20 to 35 counts per NTU approximately.

A three-point calibration was performed, as recommended by the U.S geological Survey for submersible turbidity sensors [87]. The sensor is immersed in three Formazin calibration solutions of 0, 10 and 40 NTU, while the ADC counts for Active1, Reference1, Active2 and Reference2 signals are recorded. The raw GLI-2 output is calculated according to equation (6), and plotted in Figure 3.26.

$$GLI2_{raw} = \sqrt{\frac{Active1 * Active2}{Reference1 * Reference2}} \tag{6}$$

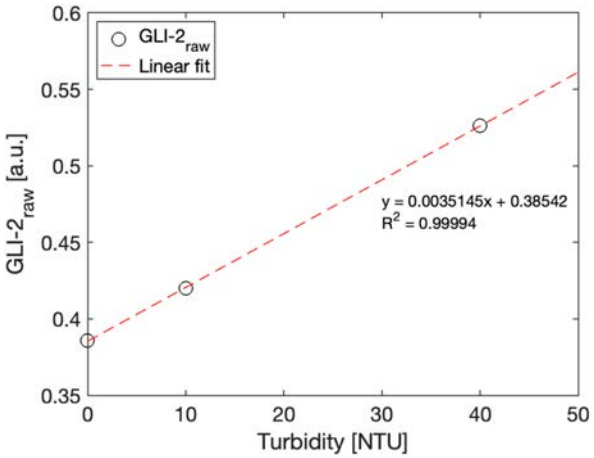

Figure 3.26. Three-point calibration of the sensor. GLI2raw values are calculated from the Active1, Active2, Reference1 and Reference2 signals against three Formazin calibration solutions of 0, 10 and 40 NTU.

Turbidity

From this calibration curve, the calibration coefficients Cal_{slope} and Cal_0 were calculated from the linear regression fit on the three-point calibration curve shown in Figure 3.26 to according to the following equation:

$$NTU = Cal_{slope} \sqrt{\frac{Active1 * Active2}{Reference1 * Reference2}} - Cal_0 \quad (7)$$

With the optimized settings from Table 2, the final calibration equation corresponds to the values below:

$$NTU = 285.714 \sqrt{\frac{Active1 * Active2}{Reference1 * Reference2}} - 110.257. \quad (8)$$

These calibration coefficients were then used to update corresponding variables in the microcontroller code, so the sensor is able to directly output turbidity values in NTU units. Figure 3.27 shows the results obtained in a range from 0 to 10 with 0.5 NTU increments and from 0 to 50 NTU with 5 NTU increments. The calibrated GLI-2 sensor data was plotted together with a confidence interval of +/- 0.4 NTU around the ideal value, showing good fidelity of the sensor even low turbidity values.

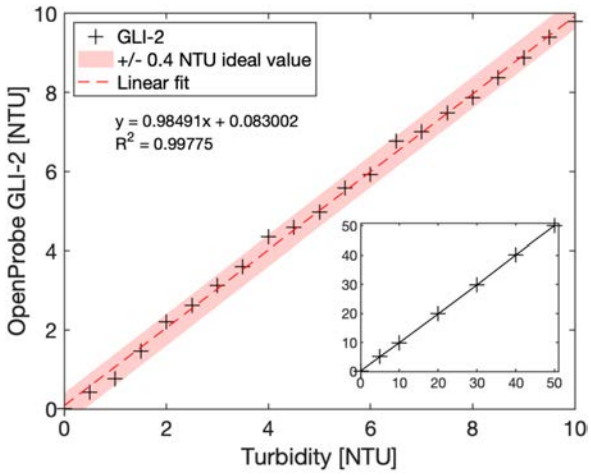

Figure 3.27. Calibrated OpenProbe GLi-2 sensor exposed to Formazin calibration solutions from 0 to 40 NTU.

While we focused on the 0 to 50 NTU range, good linearity has been observed up to 100 NTU. While we did not perform any testing above 100 NTU, the sensor could probably work at higher turbidity values, to the extent that the photometric front-end settings and the calibration curve are optimized for this range. We finally took the opportunity to compare our sensor implementing the GLI-2 method to the commercial Thermo Fisher AQ3010 instrument, a portable handheld device that costs approximately 1000 $ USD. The intercomparison plot is given in Figure 3.28.

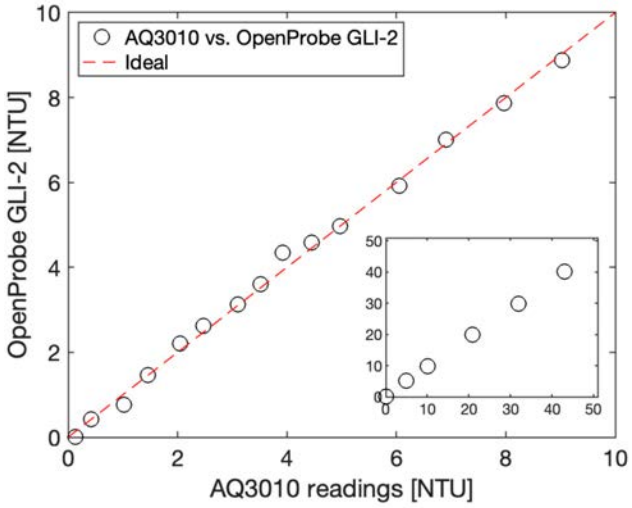

Figure 3.28. Intercomparison of our turbidity sensor, OpenProbe GLI-2, versus a portable handheld Thermo Fisher AQ3010.

The data shows that our sensor compares nicely, despite an overall BoM (Bill of Materials) cost of approximately 50 $ USD for a single prototype. Our calibrated sensor shows an average percentage error of +/- 5% or better, while the AQ3010 shows a percentage error of 3.6% in the same conditions. However, the commercial system is not capable of in-situ measurement, as it requires manual water sampling, followed by pipetting of the sample into a clean vial, and as a response time of 30 seconds, compared to the 96 ms response time of our sensor. To our knowledge, the Hydrolab 4-beam turbidity sensor is the only commercial sensor capable of implementing the GLI-2 method in-situ, and costs several thousands of dollars.

3.5 Conclusion

Three sensors implementing various turbidity measurement methods were developed in this chapter: attenuation, backscattering and GLI-2. Low-cost attenuation-based turbidity sensors found in washing-machines proved to be unsuitable for quality measurements due to their lack of sensitivity and their non-linearity, despite being used in many scientific articles.

Unexpected results were obtained with the backscattering sensor prototype based on the ADPD144RI, as it was giving good performance in low turbidities (0 to 10 NTU), while this sensing scheme is supposed to be inappropriate in such cases; upon further investigation, we discovered that our results were influenced by unwanted effects of our testing setup, and that the measurements were actually a combination of backscattering and absorption, explaining the good sensitivity observed. This sensor could have a good potential for laboratory measurements, as with a precisely positioned reflector placed in front, it offers very good precision at a very low cost (about 20 € in total). However, the necessity to add a reflector makes it less suited for in-situ deployment as the reflecting surface would be prone to biofouling, and would make its integration challenging.

Finally, the GLI-2 sensor based on the ADPD1080 and external LEDs and photodiodes allowed us to obtain good results in the 0 to 10 NTU range, with a confidence interval of +/- 0.4 NTU using the following settings: 50 pulses, TIA of 200K and 290 mA for Nephelometric configuration and 50 pulses, TIA of 25K and 90 mA for Attenuation configuration. While the optimal objective would have been to reach +/- 0.1 NTU, this result is nonetheless satisfying

and is an improvement compared to the state of the art of low-cost turbidity sensors. It should be noted that the performance could probably be improved by using a rigid PCB and a different layout: due to the absence of ground planes on the flexible PCB, and its small thickness, isolation between the high pulsed current LED excitation tracks (> 200mA) and the small photocurrent photodiode tracks (< 0.04 µA) is far from ideal in terms of noise. We can however safely assume that this architecture is valid and can be used as a low turbidity sensor, and that with minor refinements it could achieve +/- 0.01 NTU precision.

Chapter 4 Dissolved Oxygen

4.1 Introduction

Oxygen is the most abundant element on Earth and obviously a vital parameter for all the ecosystems. The presence of oxygen on Earth, and as such habitability for humans on the planet, is a result of photosynthesis by so called primary produces through one of the most successful biological processes of the Evolution, which is photosynthesis. It is estimated that phytoplankton currently produces at least half of the oxygen on Earth, i.e. as much as if not more than all the land plants. The oxygen cycle relies on constant exchanges between the hydrosphere and the atmosphere through both physic-chemical and biological mechanisms [109]. The hydrosphere both produces and consumes oxygen; the ocean surface layer can gain oxygen from the atmosphere by the pressure, and from phytoplankton as a result of photosynthesis, and it can consume oxygen by the aquatic organisms, decomposition, and various chemical reactions [110]. Oxygen in water is measured as Dissolved Oxygen (DO). Measuring this parameter is critical to understand the marine ecosystem as it is essential to the metabolism of all aerobic aquatic organisms. It is identified as a biogeochemistry Essential Ocean Variable by the GOOS, and is closely associated to the understanding of anthropogenic climate change, as current observations tend to indicated that it is causing a decrease of dissolved oxygen in the oceans. In particular, the extension of Oxygen Minimum Zones (OMZ), also referred as Dead Zones, is observed with great attention by the scientific community [109].

When more oxygen is consumed than produced, low levels of DO tend to increase marine life mortality. DO knowledge is basic to the understanding of the distribution, behavior, and growth of aquatic organisms [111]. The highest DO concentration is found on the surface layer of the sea, with contribution from the atmosphere and from the euphotic zone where light can be received easily, and the process of photosynthesis from phytoplankton, algae, seaweed and other aquatic plants occurred. All marine photosynthetic organisms use sunlight to synthesize nutrients, involving photo-pigments as chlorophyll resulting in oxygen production[112], [113]. Below 200 meters depth, where the sunlight is less received, the oxygen concertation is lower, as illustrated Figure 4.1. There are some modeling studies of DO focus specially on the global ocean [114] and few studies focus on Mediterranean Sea[115].

4.1.1 Dissolved Oxygen Saturation and Temperature dependency

Water bodies contains dissolved gasses that are very important to living organisms, particularly oxygen and carbon dioxide. All these gasses are found in the atmosphere, and are soluble in water, however the amount of each gas in the air is different from the amount in the water samples. Water bodies can be saturated in oxygen, meaning that water holds as many dissolved gas molecules as it can in equilibrium with the atmosphere gasses. The water slowly absorbs the gasses molecules from the atmosphere until it reaches equilibrium at complete saturation. We can know if the water is in air saturation with the formation of bubbles [116]. Typically, on the surface layer of the sea is where oxygen dissolves into the water from the atmosphere. As depth increase, DO decrease, reaching a minimum between a few hundred to 1000 meters depth typically, in the aptly-named oxygen minimum layer [117]. Oxygen solubility is affected nonlinearly by the temperature change and has a seasonal and daily cycle. Colder waters can hold more DO while warmer waters can hold less DO. As such in winter

and spring, the DO tends to be higher and in summer and fall the DO tends to be lower [118], both behaviors are showed in the Figure 4.1.

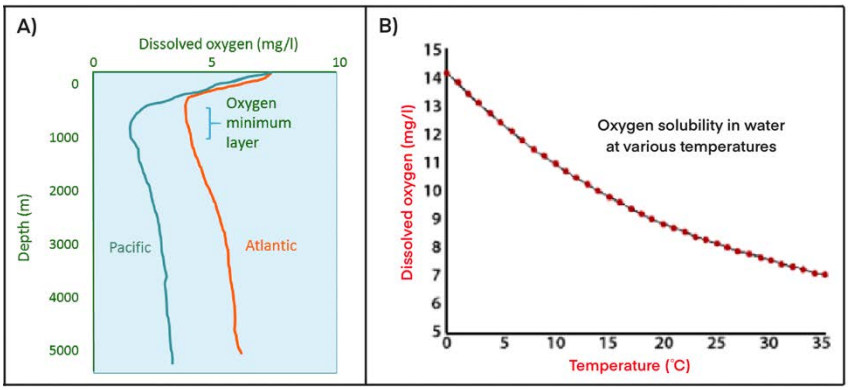

Figure 4.1. A) Typical DO profiles in the Pacific and the Atlantic Ocean. B) Temperature influence on the oxygen solubility in water.[118]

Dissolved oxygen is among the three most-often measured parameter in oceanography, after temperature and salinity. Several methods have been developed through the years, but we'll see that it was only recently that a satisfying in-situ method was developed. The Winkler Method, the electrochemical sensor, and oxygen optode are detailed in the next sections.

4.2 Measurement methods and state of the art

4.2.1 Winkler method

The Winkler method is considered as the reference method for dissolved oxygen measurement. It is a highly accurate titration-based method, and involves a series of reagents that form an acid compound in a bottle containing the water sample, as summarized Figure 4.2. During the test, an excessive amount of manganese (II) salt, iodide (I^-), and hydroxide (OH^-) ions are introduced in the water sample, leading to the formation of a white precipitate of Mn(OH)2. This precipitate undergoes oxidation from the oxygen present in the water, resulting in the formation of a brown precipitate containing manganese in a more oxidized state (either Mn(III) or Mn(IV)). In the subsequent step, a strong acid (either hydrochloric acid or sulfuric acid) is added to the solution to acidify it. This acidic environment causes the brown precipitate to convert iodide ions (I^-) into iodine. The quantity of dissolved oxygen is directly correlated with the titration of iodine using a thiosulfate solution. This method is extremely accurate, and is routinely used to calibrate the other sensors, but so far no in-situ equipment is capable of implementing it, hence it requires to sample water first and perform laboratory analysis [119].

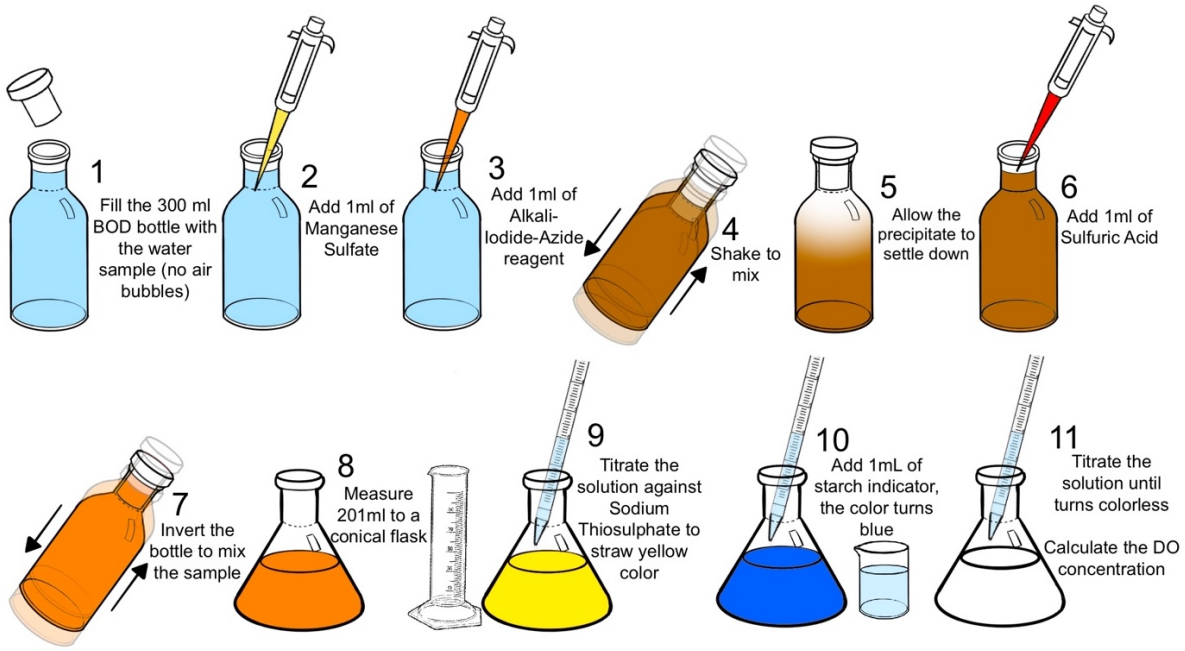

Figure 4.2. The Winkler method

4.2.2 Electrochemical method

Electrochemical sensors are widely used for measuring dissolved oxygen. They are referred to as Clark-type sensors, measure DO concentration in water based on electrical current. There are two types of electrochemical DO sensor: galvanic and polarographic. Both consists in an anode and a cathode electrode of different metals, surrounded by an electrolytic solution. The cathode electrode is covered with an oxygen-permeable membrane, often made from an organic fluoropolymer [120]. This membrane is permeable to oxygen and allows O_2 to diffuse through at a rate proportional to the partial pressure of the gas in the sample. It uses the oxidation and reduction at the electrodes, when there is a difference of partial pressure between the inner and the outer part of the membrane, the oxygen that enters from the cathode is reduce to OH^-; then the anode is oxidated, accepting the OH^- results in a current flow proportional to the amount of transformed oxygen [121]. The polarographic sensor can require between 5 to 60 minutes to polarize the electrodes prior calibrating or measuring, while the galvanic sensor can skip this step [120]several drawbacks like instability of readings, uniform signal drift, changes in sensor response time or formation of gas bubbles in electrolyte [122] and have been slowly replaced by oxygen optodes since their advent.

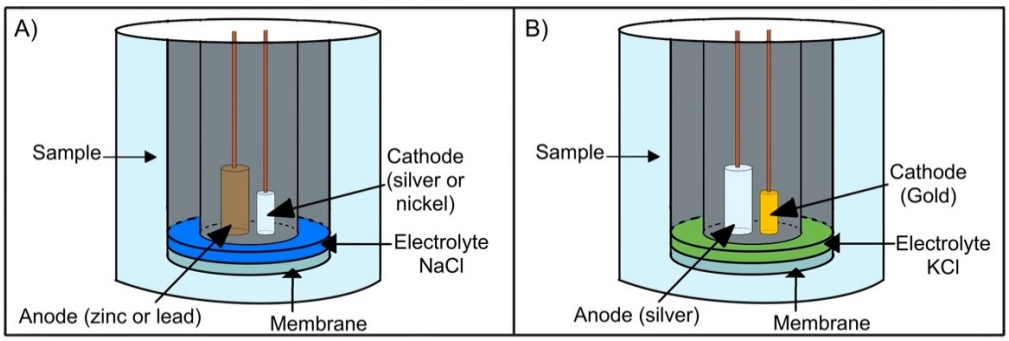

Figure 4.3. Electrochemical sensors. A) Galvanic sensor. B) Polarographic sensor

4.2.3 Optode method

Oxygen optode technology originates from Kautsky in 1939, and is actually older than Clark electrodes published by Kanwisher in 1959, however it was only very recently introduced to aquatic research, around 2005 [123]. Due to its performance, it rapidly replaced Clark electrodes for in-situ measurements. In its modern form, this type of sensor uses the dynamic luminescence quenching method, where a luminescent dye incorporated in a sensing foil is excited with light-emitting diode (LED) and photodetector collects the fluorescence signal, as shown Figure 4.4. The sensing foil is excited by the LED and responds with a longer wavelength, usually a dark red fluorescence light, which is detected by the PD. When the excitation occurs over the sensing foil, the oxygen molecules are attached to the marker molecules in the sensing foil and attenuate the fluorescence light, this is known as quenching, the light is detected by the photodetector and the decreasing light intensity reflects the partial oxygen in the medium. A very large diversity of luminescent dyes has been developed through the years. Wang and Wolfbeis did a remarkable review of several hundred of indicators in their 2014 review [110], illustrating the important of this topic in many research areas, including medicine, biology, geosciences and of course oceanography.

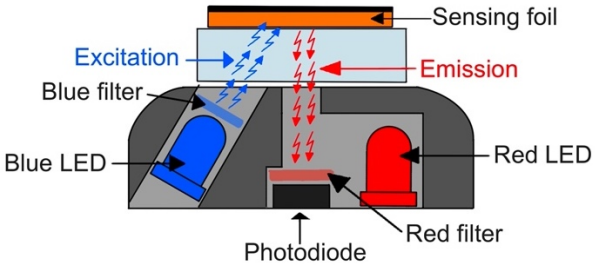

Figure 4.4. Optical Sensor, Optode configuration.

4.3 Development of a low-cost oxygen sensor based on Optode

In this project we choose to develop a low-cost oxygen optode, as it is currently the go-to method for in-situ measurements, which exploits the dynamic luminescence quenching by oxygen. Quenching is defined as the process that leads to a reduction of the luminescence intensity of any luminophore/dye, the luminophore being a molecule or group of molecules that emits light when it is illuminated. The luminophore absorbs light at one wavelength and emits light in another wavelength, generally at a longer wavelength corresponding to a lower energy level [124]. Different commercial oxygen optode sensors are available, with prices ranging from 1.5 k€ (like the PME Minidot) to more than 5 k€ (like the Aanderaa found on BGC Argo floats), but most of the time they rely on the same sensor spots, which is considered as a consumable in such sensors. We choose to use commercially available PreSens Sensor Spots SP-PSt3, as these have been thoroughly studied and validated for long-term operation through the Biogeochemical Argo float program as reported by Bittig et al. [123]. As these spots can be purchased individually at around 30 € per unit in 5mm diameter (price being directly related to the spot diameter), we decided to work on a low-cost optoelectronic readout device to interface them. Pst3 spots are excited at 505nm, and fluoresces at 633 nm, with a measurement range of 0 - 100 % oxygen in liquids and in gas phase and is routinely used for dissolved oxygen measurements [125].

Fluorescence signal intensity is affected by the O_2 molecules attached on the marker molecules of the sensing material, but it is adversely affected by other parameters like ambient

light. The fluorescence signal is also characterized by its lifetime decay, which is related with the amount of O_2 molecules in the medium, and is a more common way to measure dissolved oxygen levels as it is less affected by ambient light levels.

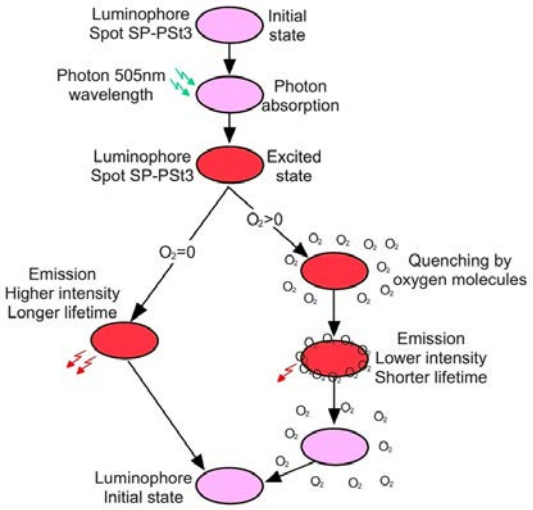

Figure 4.5. Dynamic luminescence quenching by oxygen molecules.

In order to measure this lifetime decay, the dye is excited by a sine wave modulated excitation light, and measures the emitted fluorescence signal which is phase shifted in relation with the fluorescence lifetime decay. In the presence of O_2 molecules the lifetime decay is lower, corresponding to a lower phase shift. The relationship between the lifetime and the phase shift for a single exponential decay is:

$$\tau = \frac{\tan\theta}{2\pi f} \tag{9}$$

Where τ is the fluorescence lifetime, θ is the phase shift between excitation and fluorescence (emission) signal and f is the frequency. An optimal frequency must be selected depending on the lifetime of the luminophore/dye. As mentioned previously, both the emission intensity and lifetime are reduced in the presence of oxygen [126], as shown Figure 4.6.

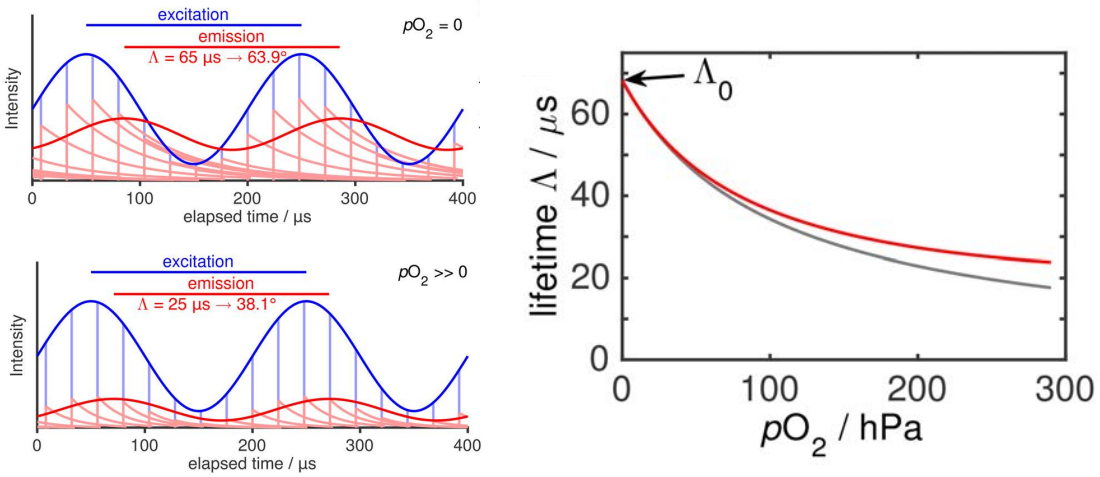

Figure 4.6. Left: excitation (blue) and emission (red) signals from an oxygen optode with sine wave excitation in absence (upper left) and presence (lower left) of oxygen. It can be seen that both intensity and fluorescence lifetime/phase shift are affected. Right: relation between lifetime (or phase shift) and oxygen concentration (expressed here in partial pressure) is always non-linear. Adapted from [123].

While PSt3 sensor spots are advertised as durable for about 12 months, deployments of several years have been successful through the BGC Argo float program. It should be emphasized that the durability of the spot is notably affected by the excitation light, hence it is preferable to limit the excitation light intensity and the cumulated excitation duration to enhance the longevity of the spot. In applications where access to the sensor is easy, replacing the spot is an easy task as they are sold as little stickers.

4.3.1 Optode Sensor design

In order to start designing our optode readout device, and since the Spot PSt3 is going to be used as a sensing foil, it is necessary to confirm at which wavelength it must be excited, because each sensing foil or luminophore is excited at a different wavelength. While a few references mention a 505nm wavelength, the manufacturer does not communicate on this information. Thanks to the Oceanographic Observatory of Banyuls sur Mer, we had the opportunity to use a PreSens Fibox 4 as the reference system, which is a device that measures the concentration of oxygen using Spot PSt3 as a sensing foil. We used a spectrometer in front of the optical fiber output of the Fibox 4 to measure the emission spectrum, which is given Figure 4.7. It can be seen that the peak emission is confirmed to be centered at 505nm. Then, we performed an analysis of the output signal for the excitation LED of the PreSens Fibox 4, by using a photodiode connected to a transimpedance (TIA) amplifier and observing the voltage output with a Tektronix TDS 210 oscilloscope. It was observed that excitation signal is a sine wave at a frequency of 5 kHz, with a total of 125 periods for each data acquisition. This is the same frequency used by Aanderaa optodes (that uses Pst3 sensor spots as well), and similar to the 3.84 kHz frequency used in SeaBird optodes[123].

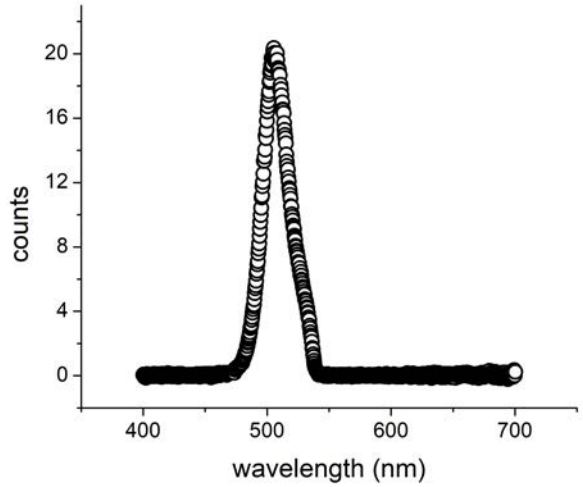

Figure 4.7. Measurement of the excitation light source spectra of the PreSens Fibox 4 using a spectrometer.

Once we had this information, the next step was the design of our first prototype, having in mind that we needed a sinusoidal signal as output for our LEDs (excitation and reference) at 5 kHz, a led driver, a photodiode with its TIA stage, and a phase detector in order to measure the phase shift. For the cyan excitation LED, we selected the OSRAM LV T64G that has its peak wavelength at 505 nm and a full width at half maximum (FWHM) of 26 nm[127]. For the red reference LED, we used the Luxeon LMX2 PH01 that has its peak wavelength at 615 nm and a FWHM of 20 nm[128]. For the filters, we used low-cost Roscolux filters, the #389 Chroma green, and the #26 Light Red. For the photodetectors, we used the BPW34 a PIN photodiode with high speed and high radiant sensitivity with a spectral sensitivity from 430 nm to 1100 nm[129]. Spectral information of the oxygen optode sensor are summarized Figure 4.8.

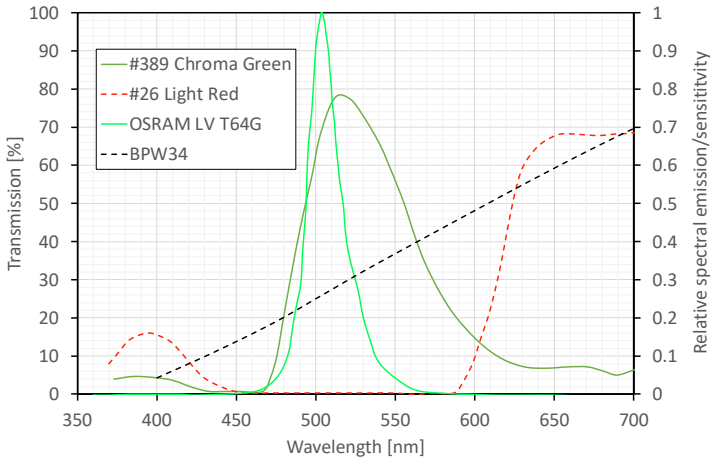

Figure 4.8 - Optical spectra of the optical components used for the oxygen optode sensor, with the cyan excitation light source (OSRAM LV T64G), the excitation filter #389 Chroma Green, the BPW34 silicon photodiode, and the emission filter #26 Light Red.

To generate a stable sine wave, we exploited the Direct Memory Access (DMA) functionality of the Adafruit Feather M0, in this way the central processing unit (CPU) is free from involvement with the data transfer, speeding up overall microcontroller operation. As the Adafruit Feather M0 has an internal 10-bits DAC (Digital-to-Analog Converter), we used this output for the sine wave generation to feed a LED driver connected to either the cyan excitation LED or the red reference LED, thanks to a MAX4528 analog switch [130]. The selection is done by connecting two of the digital outputs of the microcontroller to the A and B inputs of the MAX4528 switch. For the led driver, we use a Voltage Controlled Current Source (VCCS) circuit in the form of a Howland Current source, build around an Analog Devices LT1800 which has a low offset voltage, low input bias current, low quiescent current and low-power consumption [131]. For the TIA, we used the Texas instrument OPA380 which is a high-speed precision transimpedance amplifier for photodiode applications[132]. For phase shift measurement, we used the Analog Devices AD8302 Gain and Phase detector: this component has two inputs which are fed by the excitation and the emission signals, and outputs two analog voltages proportional to the phase shift (scaled to 10mV/degree) and gain or loss (scaled to 30mV/dB) difference between the two input signals [133]. The Figure 4.9 show a general block diagram of our sensor.

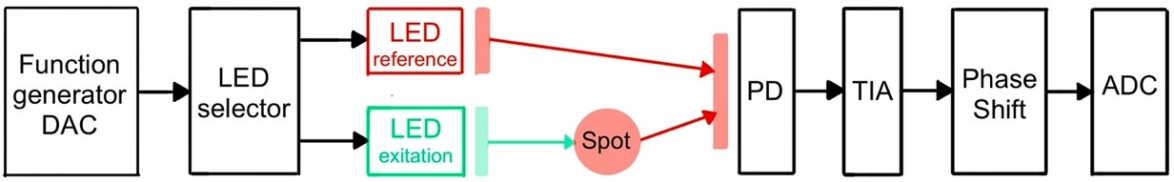

Figure 4.9. Block diagram of the OpenProbe Optode sensor.

In order to achieve the communication between the computer and the different components of the oxygen optode sensor, custom Arduino compatible code was developed.

4.3.2 Sensor Housing

In order to facilitate the testing of the optode electronic readout device, we separated the PreSens PSt3 spot from the optics and electronics, by using 3mm, sleeved PMMA optical fibers (Edmund Optics) to guide the light from the cyan LED to the sensing foil, and collect the emission light from the sensing foil to the photodetector. Figure 4.10 shows a schematic

view of the optode housing, as well as a picture of the complete assembly. The small cylinder and the optical fibers can be fully immersed in water, thus facilitating laboratory testing. Apart from the PMMA plastic fibers, all parts were printed with a Formlabs Form 3 SLA printer with Black V4 resin. We placed the optics inside the case which has two holes to connect the two optical fibers. Besides, we printed a second piece for the sensing foil which has two holes for the optical fibers, after development in isopropanol we did overnight cure at 60°C, this unusually long curing time is required for the polydimethylsiloxane (PDMS) polymerization [134], then this piece was filled with PDMS and degassed to suppress air bubbles. Finally, we glued the Spot SP-PSt3 after PDMS polymerization.

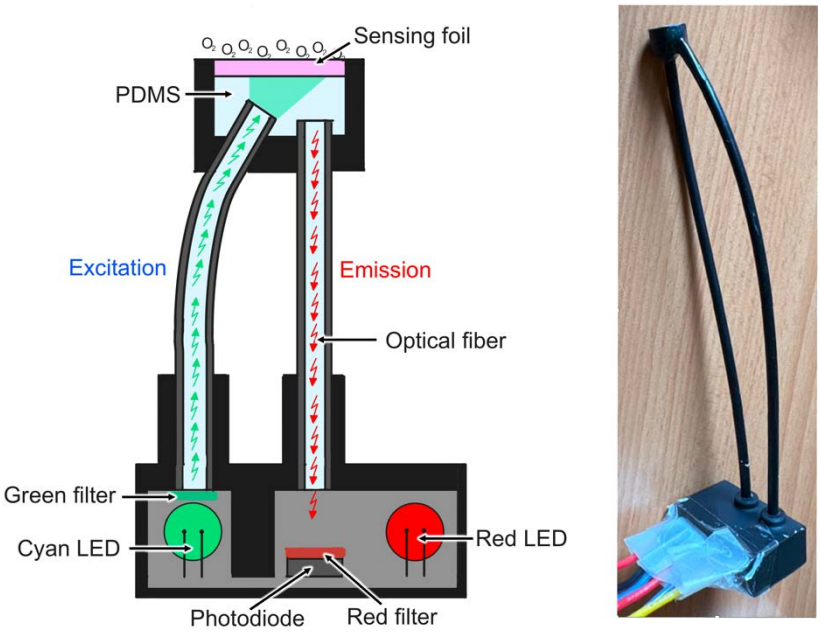

Figure 4.10. Optical hosing.

4.3.3 AD8302 phase shift measurement

The working principle of the AD8302 is to compare two input voltage signals (V_{IN_A} and V_{IN_B}) and generates two output voltage signals (V_{MAG} and V_{PHS}). Where the V_{MAG} is output voltage proportional to the decibel ratio between V_{IN_A} and V_{IN_B} and the V_{PHS} is output voltage proportional to the phase difference between V_{IN_A} and V_{IN_B}. The V_{PHS} output provides an accurate measurement of phase shift over a 0° to 180° range scaled to 10 mV/degree, with an output swing from 0 V to 1.8 V, giving a direct reading of the phase shift (i.e. 900 mV corresponds to +/-90°). The ideal transfer function for the gain and phase measurement mode is showed in Figure 4.11 [135]. Finally, V_{PHS} is sampled using the internal 12-bits ADC of the Adafruit Feather M0.

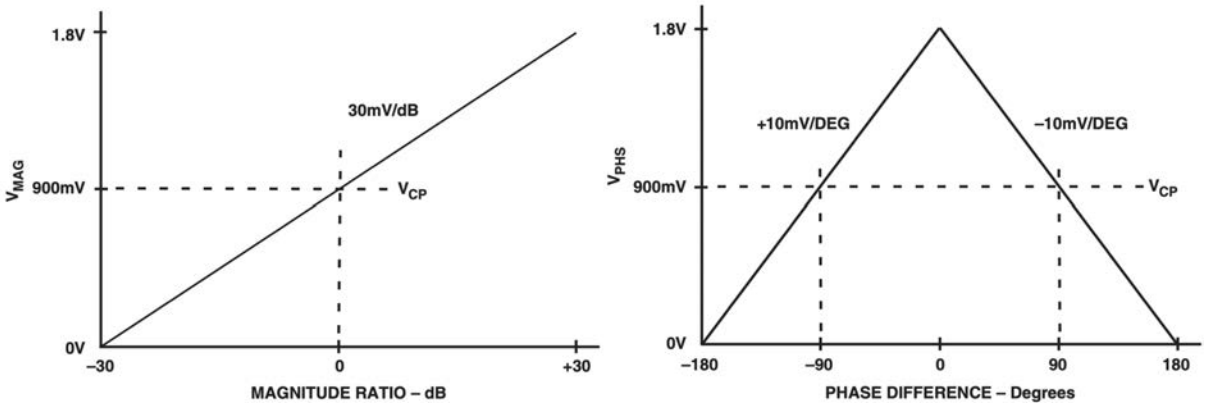

Figure 4.11. The ideal transfer for the gain and phase measurement mode[133]

As show in Figure 4.11 the equation for calculate V_{PHS} is:

$$V_{PHS} = \left(\frac{10mV}{degree}\right) * \left(\theta_{IN\_A} - \theta_{IN\_B}\right) \tag{10}$$

Where $\theta_{IN\_A} - \theta_{IN_B}$ is the phase shift between the two input signals, the phase shift degree can be written as:

$$\theta(degree) = \left(\theta_{IN\_A} - \theta_{IN\_B}\right) = \frac{1800mV - V_{PHS}}{10mV} \tag{11}$$

As we want to measure the phase shift between the reference LED (red LED) and emission LED (cyan LED) we read the data in two phases which are alternatively selected using the MAX4528 analog switch:

- During phase A, the red reference LED is ON (Figure 4.12): the photodetector collects this red-light reference signal, which is amplified by the TIA and fed to the first input of the AD8302 while the second input is connected to the DAC sine generator. The phase shift between these two signals is sampled by the ADC and stored as PhaseShiftA. We used equations (12) and (13) to get the values of PhaseShiftA in Volts and degrees:

$$PhaseShiftA(V) = \left(\frac{10mV}{degree}\right) * \left(\theta_{DAC} - \theta_{Reference}\right) \tag{12}$$

$$PhaseShiftA(°) = \left(\theta_{DAC} - \theta_{Reference}\right) = \frac{1800mV - V_{PHS}}{10mV} \tag{13}$$

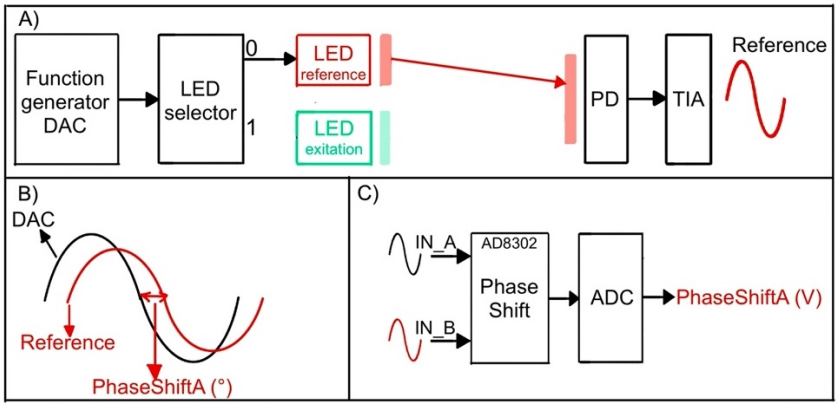

Figure 4.12. Phase A. A) Reference sine signal. B) Reference PhaseShiftA in degrees. C) Two inputs for the AD8302, IN_A for DAC and IN_B for Reference. PhaseShiftA output in Volts

- During phase B the cyan emission LED is switched ON (Figure 4.13): the photodetector now collects the fluorescence emission sine signal coming from the Pst3 spot. After amplification by the TIA this signal is fed to the AD8302, with the second input still connected to the DAC signal. The sampled output is noted PhaseShiftB. We used the equations (14) and (15) to get the values of PhaseShiftB in Volts and degrees:

$$PhaseShiftB(V) = \left(\frac{10mV}{degree}\right) * (\theta_{DAC} - \theta_{Emission}) \quad (14)$$

$$PhaseShiftB(°) = (\theta_{DAC} - \theta_{Emission}) = \frac{1800mV - V_{PHS}}{10mV} \quad (15)$$

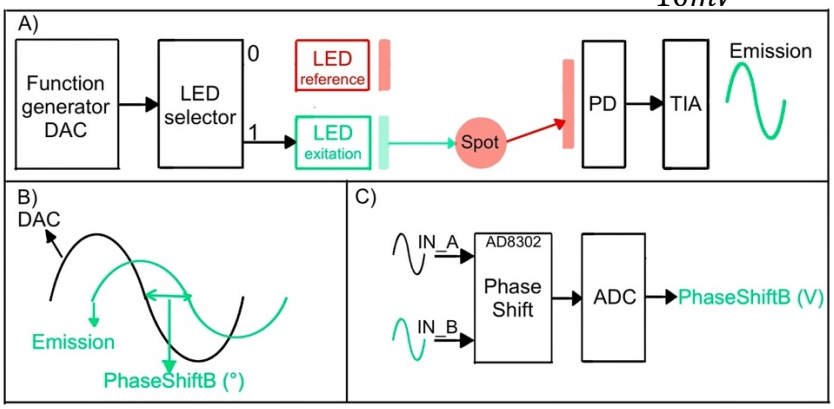

Figure 4.13. Phase B. A) Emission sine signal. B) Emission PhaseShiftB in degrees. C) Two inputs for the AD8302, IN_A for DAC and IN_B for Emission. PhaseShiftB output in Volts.

Phase shift between the reference signal (red LED) and the emission signal (spot fluorescence) is named PhaseShift and is simply the subtraction of phase A and B readings:

$$PhaseShift(°) = PhaseShiftB(°) - PhaseShiftA(°) \quad (16)$$

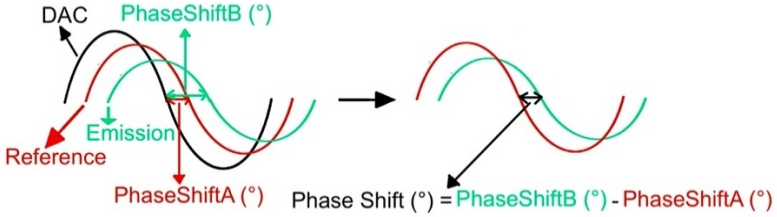

Figure 4.14. Phase shift between reference and emission signals.

4.4 Experimental results

Our first oxygen optode prototype was developed using a breadboard in order to validate the electronic architecture. Figure 4.15 shows the different elements of the prototype, with the Adafruit Feather M0 connected through jumper cables to the breadboard prototype optode circuit, and the optical components (red and cyan LED, photodiode) in the 3D-printed housing, with the sensor spots glued on top.

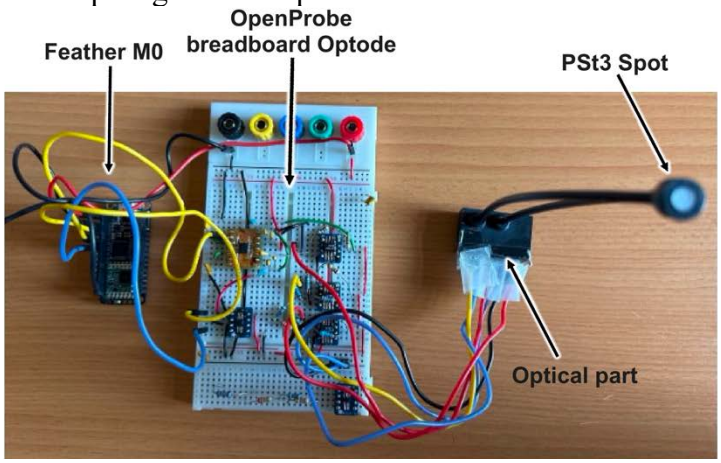

Figure 4.15 Rapid prototyping of the first prototype with a breadboard.

The next step was the validation of the signals obtained by the photodetector, that is, to obtain the two required sine signals with a phase shift between them, the first signal coming from the reference LED and the second signal coming from the emission of the PreSens PSt3 spot. As it can be used both in gases and liquids, it was decided to make the initial measurements in air. As we do not have the information about the intensity of the cyan LED required to excite the PSt3 spot, we conducted a first experiment at different intensities. With our code and using the DAC of the Feather M0 we have the possibility to generate a sinusoidal signal with different frequency, peak-to-peak voltage (V_{pp}) and offset (V_{offset}) settings. LED sources are typically driven in current due to their I-V characteristics. As we're using a VCCS Howland current source driven by the DAC, it was first required to study the characteristics of the selected LEDs to operate at appropriate voltages. These characteristics are presented in Figure 4.16.

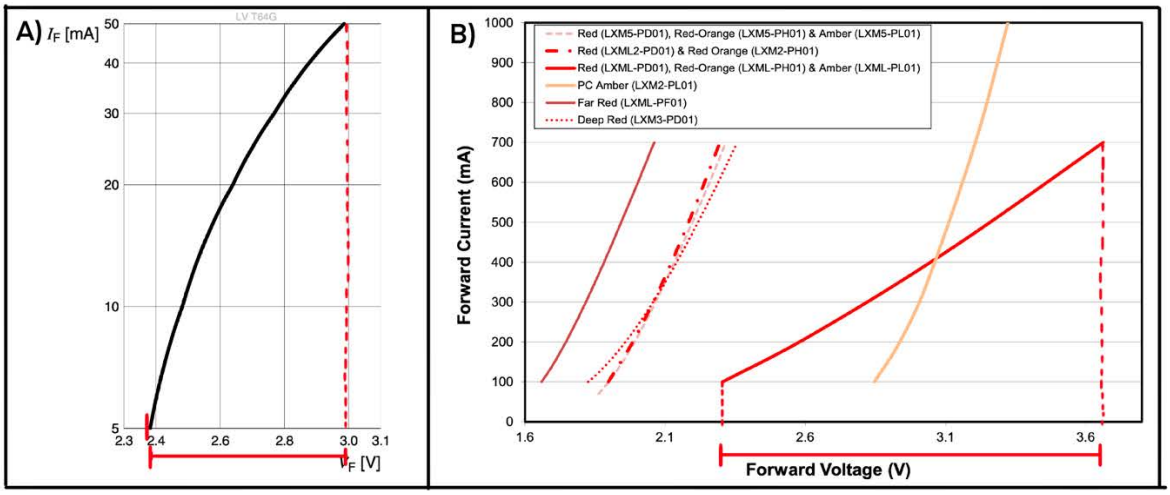

Figure 4.16. Operating voltage range of the LEDs. A) For the cyan LED (LV T64G). B) For the red LED (LMX2 PH01)

After looking at the operating range of each LED, we use an output signal that suits both LEDs. For the first configuration we use a Vpp of 418 mV and an Voffset of 2.6 V. We then checked with an oscilloscope the corresponding output signals collected by the photodiode after amplification which are plotted Figure 4.17. It can be observed that both signals are not saturated, and are low noise sinusoidal signals.

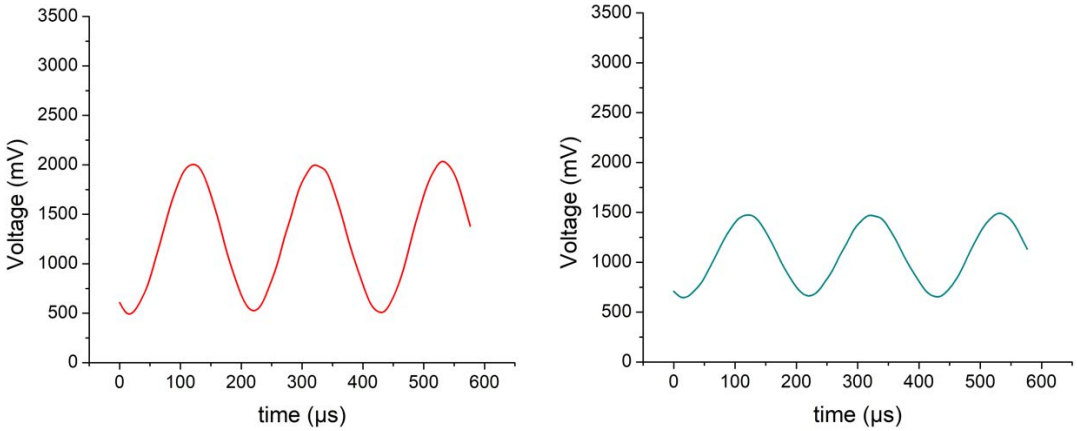

Figure 4.17. Left: Sine signal received for the PD coming from the reference LED. Right: Sine signal received for the PD coming from the emission of the Spot PSt3.

After the sine signals validation, the next step is to calibrate the sensor for which we use the oxygen saturation technique. We filled a container with a closed top ¾ full of deionized water, then we agitated the container vigorously for approximately 30 seconds to make the sample 100% oxygen-saturated water. We filled a 20 ml vial of 100% oxygen-saturated water, and we placed it inside a dark case, to ensure no ambient light perturbations. We then use a nitrogen flow bubbling into the sample in order to progressively replace the oxygen molecules. This flow was precisely regulated at 7mBar with Fluigent MFCS Pressure Controller equipment commonly used for microfluidics experiments. Dissolved oxygen was continuously monitored using a PreSens Fibox 4 PreSens and its Pst3 spot, simultaneously with the developed optode sensor with its Pst3 spot. Experiment setup is pictured in Figure 4.18.

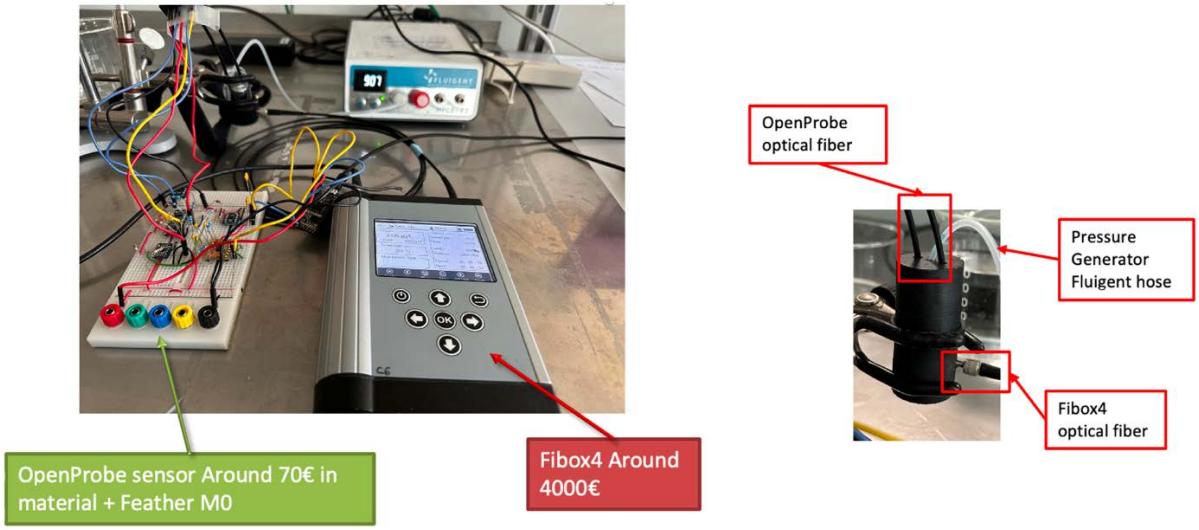

Figure 4.18. Testing apparatus used for the first optode sensor prototype, in intercomparison with the PreSens Fibox 4 system

Phase shift was recorded every 20 seconds with both sensors (the Fibox 4 and the OpenProbe Optode) during approximately 7 min, which is the time required for the oxygen concentration to vary from 8000 µg /L to 300 µg/L approximately.

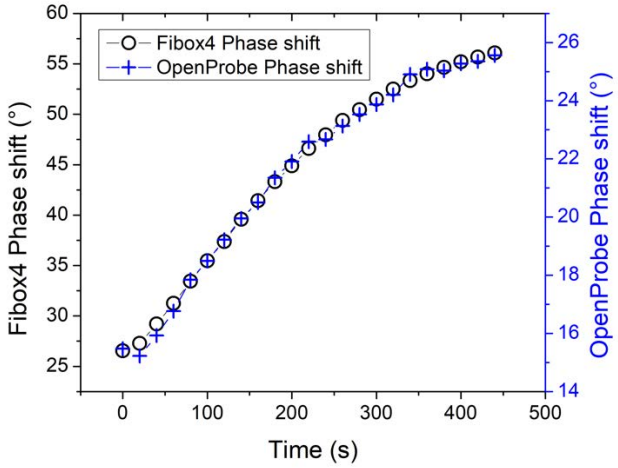

Figure 4.19. Plot of comparation in phase shift of both sensors, the Fibox 4 and breadboard OpenProbe Optode sensor prototype versus time

This result is presented Figure 4.19, where it can be seen that the trendline of both sensors are very similar; however, the total phase shift between the highest and the lowest signals is quite different with 29° for the Fibox 4 and 10° for our sensor. as the dissolved oxygen data was taken with the Fibox 4 and our sensor at the same time, and the Fibox 4 gives us the actual dissolved oxygen value, thus the actual dissolved oxygen value for both sensors was known, the results are shown in Figure 4.20.

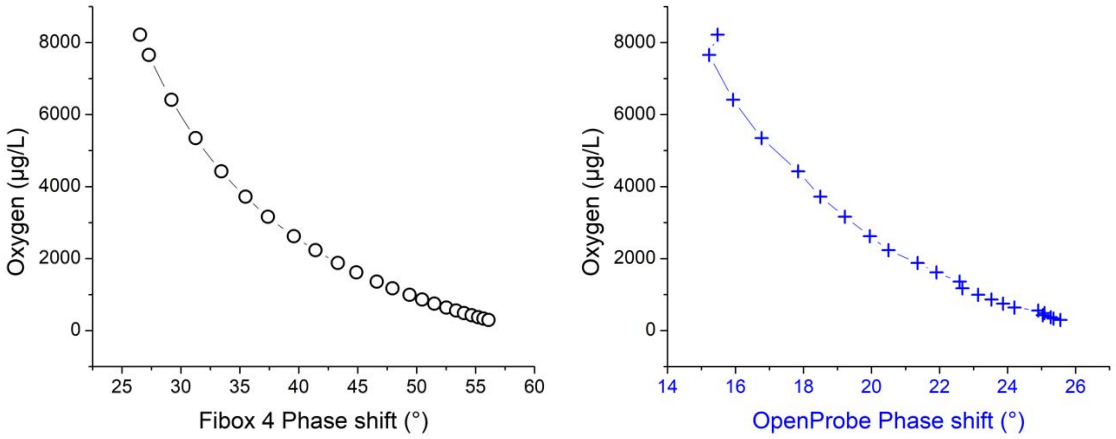

Figure 4.20. Phase shift vs oxygen concentration for both sensors. Left: Fibox 4 sensor. Right: Breadboard OpenProbe sensor prototype.

The large difference of total phase shift between the two systems was attributed to the fact that the optical part in our sensor was not correctly isolated from the ambient light. The next step was to improve the sensor enclosure to improve the optical part of the sensor and decrease the external noise, to achieve this we designed a PCB using Eagle CAD software, which was manufactured by Beta Layout Gmbh and assembled in-house. All components, including passive, active and opto-electronic components were integrated on a single PCB. The LED driver and the TIA stage were placed closed to the LEDs and the photodiode respectively, to limit noise and external signal. We placed the Roscolux #26 Light Red filter over the photodetector to limit contribution of unwanted wavelengths, and finally designed and printed

an updated housing. In order to facilitate the sensor testing and subsequent replication, we used a 6-pin Molex Picoblade connector to have the communication between the PCB and the Adafruit Feather M0. The updated prototype is shown in Figure 4.21.

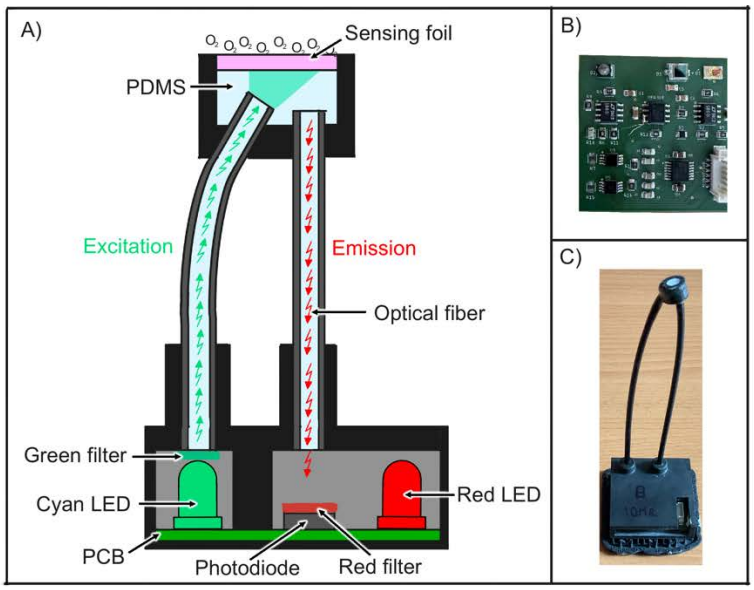

Figure 4.21. A) OpenProbe Optode sensor in breadboard. B) OpenProbe Optode sensor in PCB. C) First prototype, the OpenProbe Optode sensor inside the black case

The same testing protocol as for the breadboard prototype was conducted, with the setup presented in Figure 4.22.

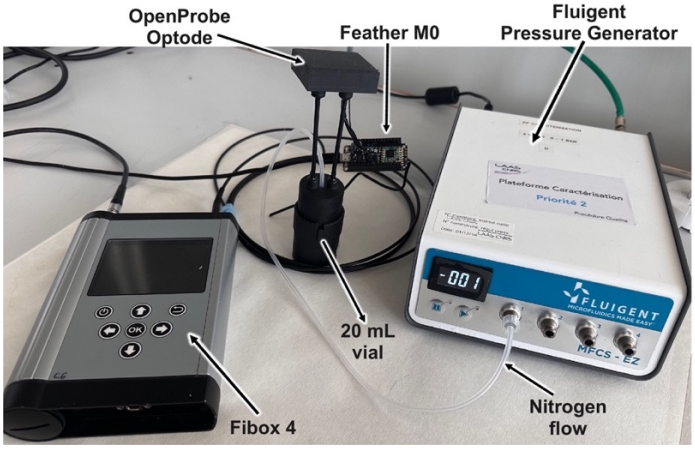

Figure 4.22. Fibox 4 vs the second prototype of OpenProbe Optode sensor.

Once configured, we did the second test, we started the nitrogen flow, and took the phase shift data every 20 seconds with both sensors for approximately 7 min. We observed the following result shown in Figure 4.23.

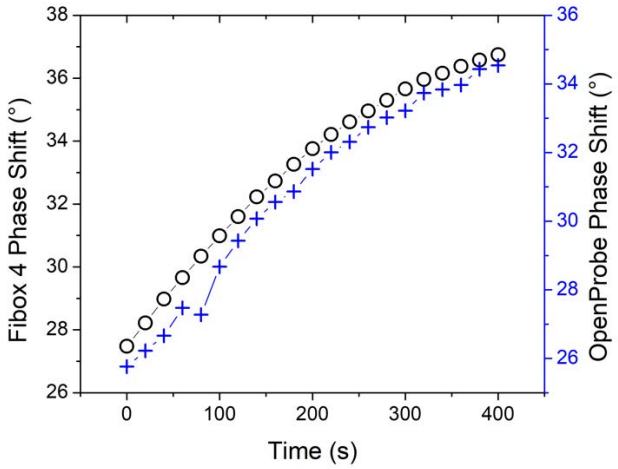

Figure 4.23. Intercomparison in phase shift against time for both sensors, the Fibox 4 and first PCB OpenProbe Optode prototype.

The trendline obtained with our second protype OpenProbe Optode sensor is similar to the commercial Fibox 4 sensor, but this time we observe also similar absolute phase values, indicating that the improvements made on the electronics and the enclosure have drastically improved the performance of our system. We then conducted a repeatability experiment with similar protocol 4 times during different days. Results of this experiments are reported Figure 4.24.

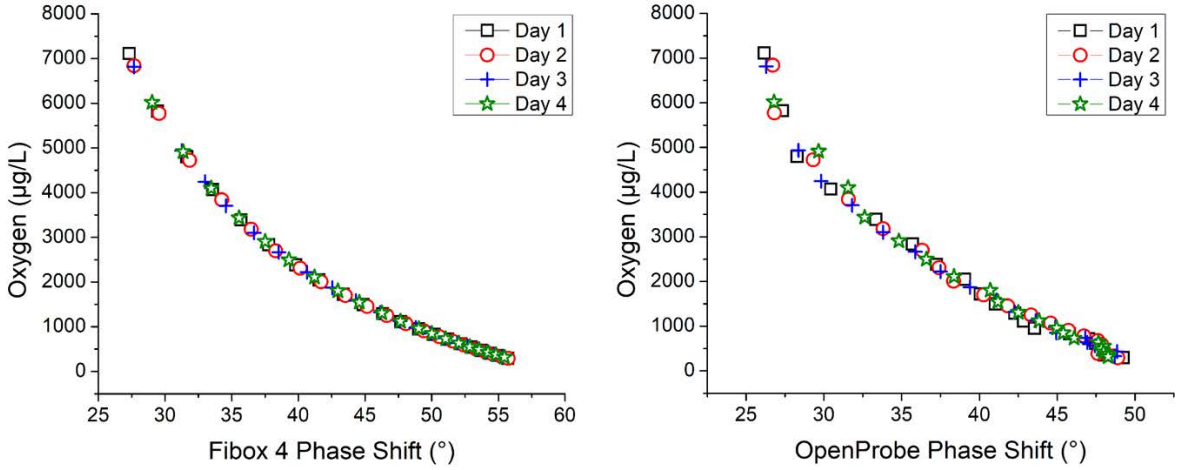

Figure 4.24. Phase shift vs oxygen concentration for both sensors. Left: Fibox 4 sensor. Right: first PCB OpenProbe sensor prototype.

It can be seen that our sensor, while slightly noisier than the PreSens Fibox 4 system, achieved reasonably good repeatability. As the relationship between the oxygen concentration and phase shift is not linear, we plot the oxygen concentration against phase shift of our second prototype OpenProbe Optode sensor data is showed in Figure 4.25.

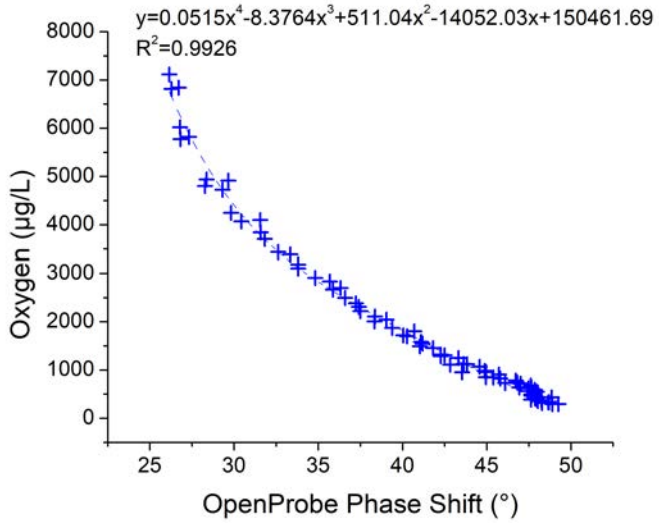

Figure 4.25. 4-degree polynomial calibration equation of the first PCB prototype OpenProbe Optode sensor.

We used a 4-degree polynomial equation as used in Aanderaa optodes [136], in order to fit this data and obtain a calibration equation:

$$y = 0.0515x^4 - 8.3764x^3 + 511.04x^2 - 14052.03x + 150461.69 \qquad (17)$$

Where y is the oxygen concentration and x is the phase shift. We wrote the calibration equation (17) in the code in order to have the actual oxygen values instead of phase shift. Finally, to test our sensor we took 20 different readings using both sensors, the Fibox 4 and the second prototype OpenProbe Optode, in similar conditions.

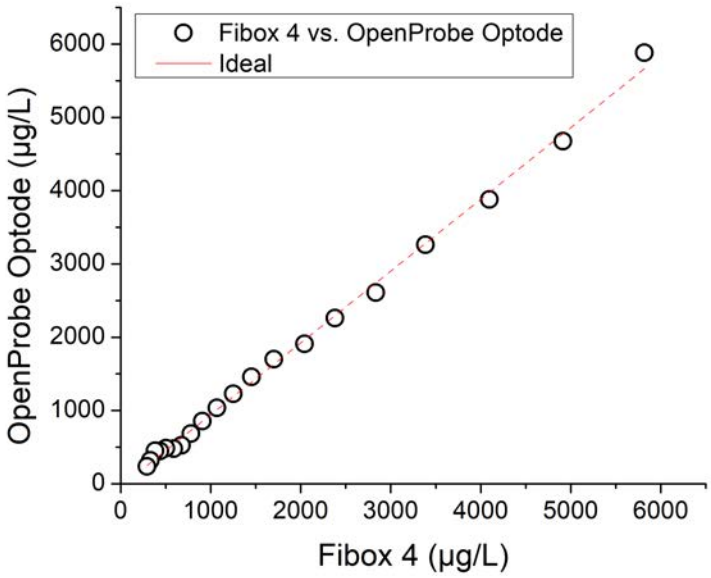

Figure 4.26. Comparation between Fibox 4 sensor and the first PCB OpenProbe Optode sensor prototype, 20 different samples

The results presented in Figure 4.26 shows that the data obtained is comparable between both systems. This is promising as this test was made with the same set up for the calibration step, under the same environmental conditions, and taking data from both sensor at the same time.

As this laboratory experiment was giving satisfying results, we decided to prepare an autonomous prototype for in-situ field testing, by adding an Adafruit Adalogger FeatherWing, which integrates a PCF8523 Real-Time Clock and a micro-SD memory card for datalogging. While this step was considered as trivial, we quickly discovered that adding the Adalogger FeatherWing was provoking malfunction of the system. Upon investigation, it was found that there is a conflict in the low-level Arduino Firmware causing DMA (used to generate the sinusoidal signal) to stop functioning when the SPI protocol is used. As the Adalogger FeatherWing needs the SPI bus to communicate with the SD card, this conflict was highly problematic. While there may have a software-based solution, we could not find an esay workaround to make the both the DMA sine generator and the SPI work, despite several exchanges with the Adafruit and the Arduino forum communities.

As using a SD card datalogger is mandatory for the complete multiparameter probe, we decided to find an alternative method to generate the sine wave excitation signal. We selected the Analog Devices AD9833 waveform generator that is able to generate square, triangle and sine waveforms up to 12MHz, with theoretically a more stable waveform than the one obtained from the Adafruit Feather M0 internal DAC.

In order to use it for our application, it was necessary to add a few external components to adjust its voltage amplitude and offset, to satisfy our needs of a sinusoidal excitation signal of 418 mV_{pp} and a V_{offset} of 2.288 V. This was achieved by the circuit presented Figure 4.27 where the potentiometer POT1 provides an adjustable offset voltage, while the potentiometer POT2 allows to change the gain of the amplifier U3 from 1 to 20 allowing the adjustment of V_{pp}.

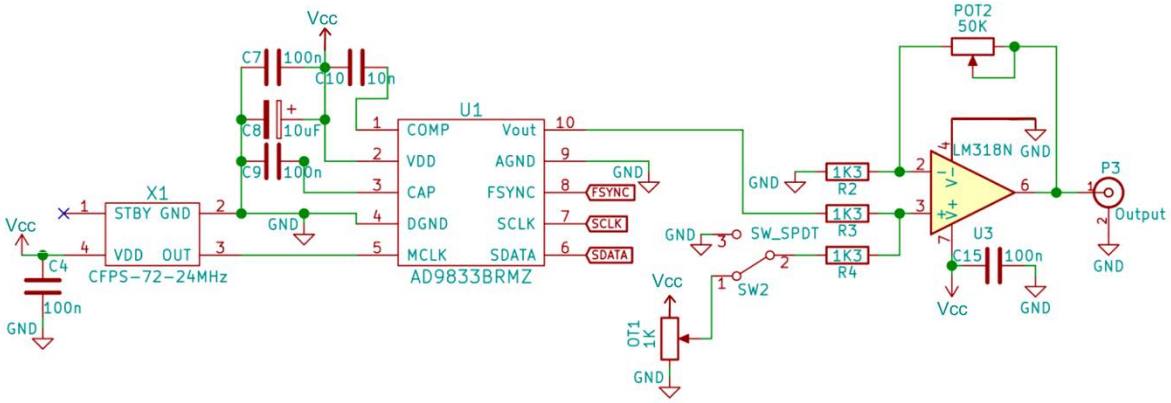

Figure 4.27. AD9833 waveform generator with its amplification stage for the Vpp and Voffset control.

Since our goal is to have the sensor take data in situ, which can imply strong sunlight radiations, we modified the version of the Pst3 spot to a version with a black coating that limits the ambient light, with the minor drawback of increasing slightly its response time. The updated block diagram of this updated prototype is presented Figure 4.28.

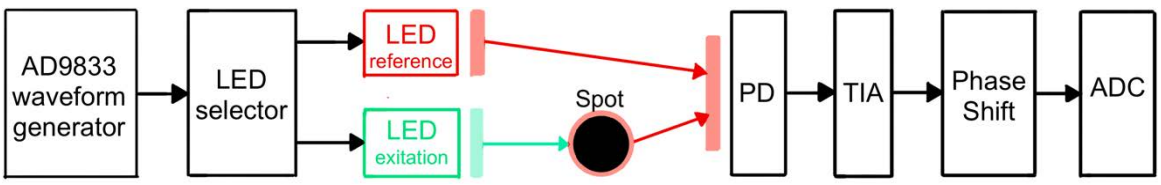

Figure 4.28. Block diagram of third prototype

Once we had the new prototype, we performed the same experiment as before with the same settings used, i.e. a sine excitation signal of 418 mV_{pp} and a V_{offset} of 2.288 V, but this time we used a larger volume, 500mL transparent beaker exposed to ambient light to see if our sensor was able to perform in a more realistic environment. The 500mL beaker was filled with 200 ml of 100% oxygen-saturated water, and a controlled nitrogen flow (20 mbar pressure using the Pressure Generator Fluigent equipment). With this setup the oxygen concentration varies from 7000 µg/L to 2000 µg/L in approximately 7 min. In order to validate the use of the AD9833 waveform generator to our existing prototype, we used a readily available prototyping board from Mikroe, the Waveform Click which contains the AD9833, and connected it to our PCB using jumper wires. While not ideal as it potentially add noise to the system, it allowed us to quickly evaluate the viability of this approach.

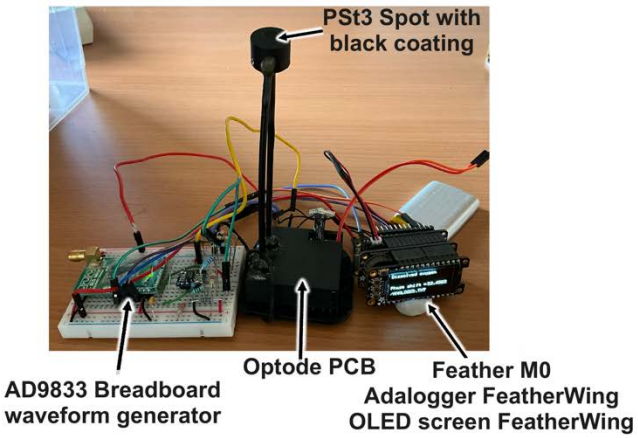

Figure 4.29. Third prototype OpenProbe Optode sensor, with the AD9833 waveform generator in breadboard, the PSt3 spot with black coating, the Adalogger and OLED screen FeatherWing

The nitrogen flow was started, and data was taken every 20 seconds, but it was quickly observed that with this new configuration and using a sinusoidal excitation signal of 418 mV_{pp} and a V_{offset} of 2.288 V, the results were not satisfying. Excitation LED settings were updated, with V_{pp} set at 1V and V_{offset} set at 2.40V, and the results were back to what was expected, as shown in Figure 4.30.

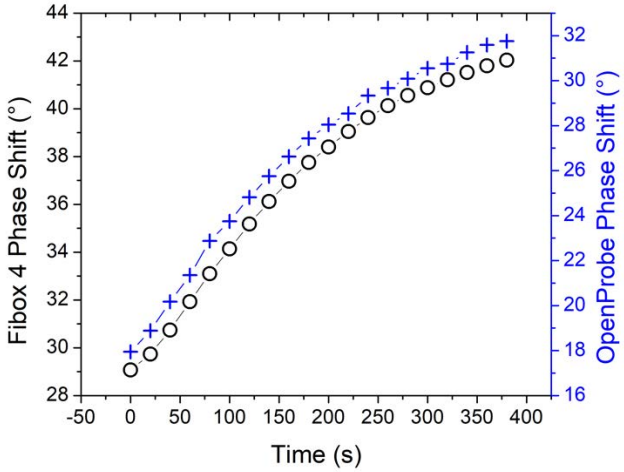

Figure 4.30 Intercomparison between the Fibox 4 and the third optode prototype using the external AD9833 waveform generator with updated settings

Both trendlines have almost the same behavior, it is also observed that by using the AD9833 waveform generator a cleaner trendline is obtained. While the absolute values of phase are different, the total difference between the lowest and the highest point are almost

identical, with 13° for the Fibox 4 and 14° for our sensor. The offset observed between both is probably due to a constant phase contribution of one of the added components for the excitation signal generation and does not impact the measurement.

The next step was to repeat this experiment but now measuring the phase shift with its current oxygen value, for this the same setup as before was performed and once the nitrogen flow into the water was started, the data was taken every 10 seconds during 7 min, in this period of time the oxygen concentration goes from 7000 µg/L to 2000 µg/L approximately, leading to the results is showed in Figure 4.31.

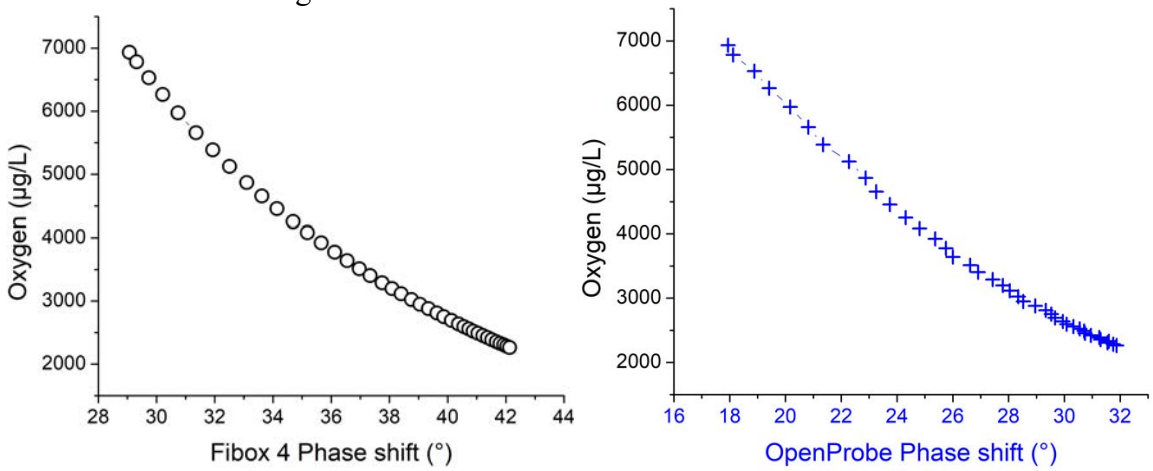

Figure 4.31. Phase shift vs oxygen concentration for both sensors. Left: Fibox 4 sensor, Right: Second PCB OpenProbe sensor prototype.

Then, as before, the 4-degree polynomial calibration equation of our third prototype OpenProbe Optode sensor was obtained, which is shown in the following graph.

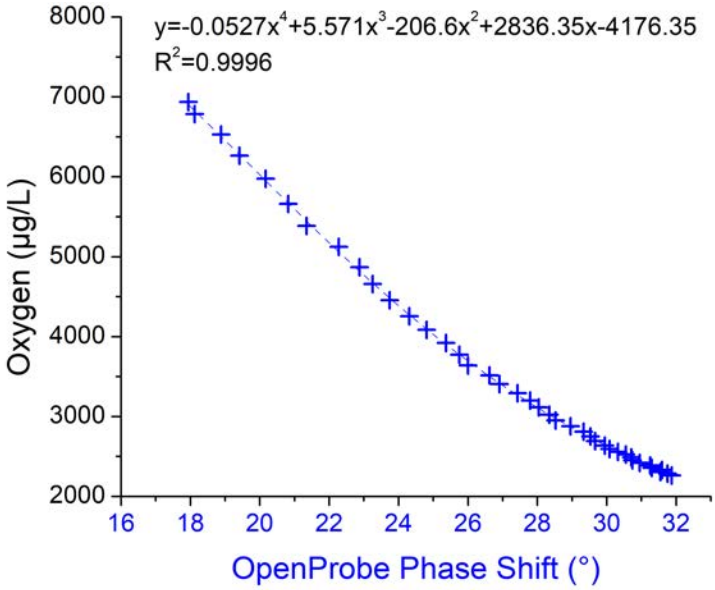

Figure 4.32. 4-degree polynomial calibration equation of the second PCB prototype OpenProbe Optode sensor.

The equation (18) shows the 4-degree polynomial calibration of our third prototype OpenProbe Opotde sensor.

$$y = -0.0527x^4 + 5.571x^3 - 206.6x^2 - 2836.35x + 4176.35 \quad (18)$$

Where *y* is the oxygen concentration and *x* is the phase shift. We wrote the calibration equation (16) in the code in order to have the actual oxygen values instead of phase shift. Finally, to test our sensor we took 20 different data using both sensors, the Fibox 4 and the third prototype OpenProbe Optode, the oxygen values obtained are show in the Figure 4.33.

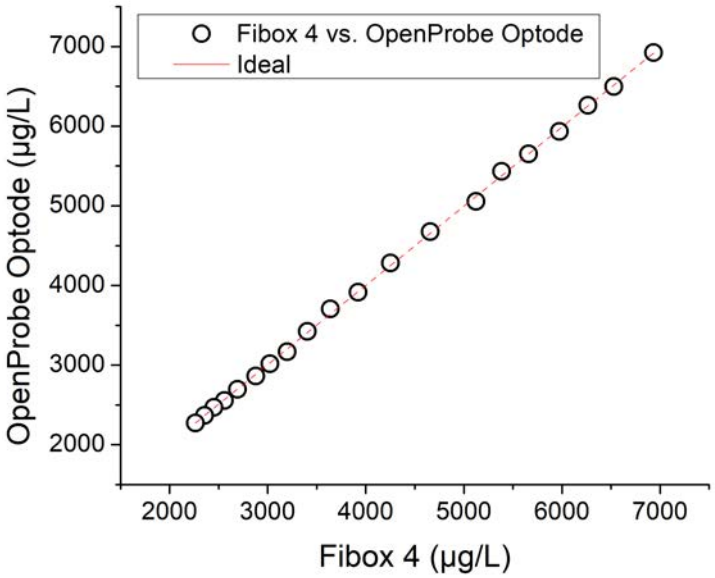

Figure 4.33. Intercomparison between Fibox 4 sensor and the second PCB OpenProbe Optode sensor prototype, 20 different samples

As can be seen in the figure, using the equation (18) the result obtained using our sensor is very similar to using the commercial sensor Fibox 4, it is worth mentioning that this result was obtained under laboratory circumstances, and also that the waveform generator AD9833 is connected externally.

4.5 Conclusion

Winkler's method is considered as one of the most accurate and precise method for DO measurements. However, it also has an error due to human manipulation and is currently cannot be performed continuously in-situ. In the research field, a low-cost DO meter with fast data acquisition is required, as well as sensors that can remain underwater over extended period of time while producing consistent data. In this project we developed a low-cost oxygen optode that works by measuring the luminescence lifetime rather than the luminescence intensity of the sensing material, as measuring the luminescence lifetime avoids much of the instability that can be experienced when measuring the luminescence intensity of the sensing material. We used commercially available PreSens Pst3 sensor spots which are routinely used in oceanography and have proved to be suitable for long-term, in-situ measurements. This method involves relatively complex electronics with two major sources of instability, which are the intensity of the light source and the efficiency of the photodetector as they can change unpredictably with time and temperature. However, by measuring the luminescence lifetime of the sensor material, these sources of instability can be limited. We used an integrated gain-phase detector which is typically used at RF frequencies in the GHz range, but proved to deliver high precision phase shift measurements even in the kHz range. The whole sensor can be built as a single prototype for around 80 € of material including the sensor spot, and could be useful in many use-cases requiring precise monitoring of dissolved oxygen.

Chapter 5 Photosynthetically Active Radiation

5.1 Introduction

Almost all energy on earth is derived directly or indirectly from solar radiation, which can be defined as the electromagnetic that provides light and heat to the Earth. Thanks to this energy, several processes occur that are necessary for the survival of our environment and its habitants[31]. Solar radiation covers a small part of the electromagnetic spectrum as illustrated Figure 5.1, mostly in the UV to IR, with approximately 8% of the radiation in the UV range (100 to 400nm), 42.3% in the visible range (400 to 700nm) and 49.4% in the IR range (above 700nm) [137]. Although the percentage of each range of solar radiation reaching the earth's surface is different, each of these has a different impact on the environment.

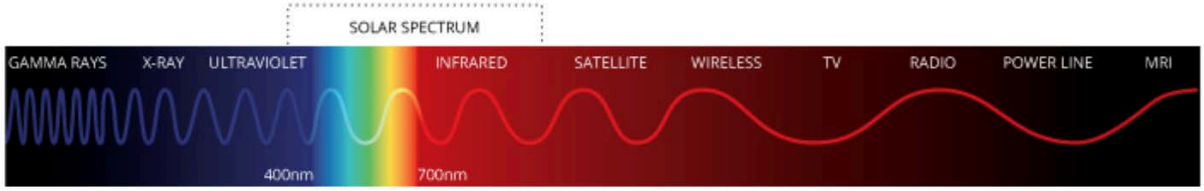

Figure 5.1. Electromagnetic spectrum, from 100 nm to 1 mm, which encompasses ultraviolet, visible, and infrared radiation.

Figure 5.2 shows the radiation of the entire electromagnetic spectrum found on earth, and also shows that at sea level there is less radiation than in the outside atmosphere which strongly attenuates UV light.

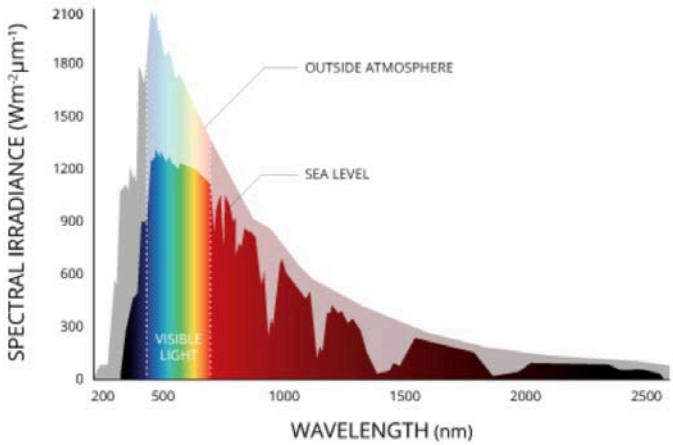

Figure 5.2. Spectral radiation, most of the solar radiation that reaches Earth comes from visible and infrared radiation, only small amount of ultraviolet radiation reaches the surface

5.1.1 Light in the water

Several parameters influence light behavior in water, including reflection, refraction, and absorption. The proportion of solar radiation reflected from the water surface varies with the angle of the sun and surface conditions [138]. Longer wavelengths are typically reflected more than shorter wavelengths[139]. In calm conditions, approximately 2% of surface light is reflected when the sun is directly overhead, with the relationship between reflection and solar elevation exhibiting exponential growth as solar elevation decreases. Refraction at the water surface alters light direction as it transitions from less dense air to denser water. The penetration depth of light in water correlates with water clarity; in turbid water bodies, light penetration is limited compared to clearer bodies of water [31].

Additionally, water absorbs light, particularly infrared light, within a certain distance below the surface. Around 90% of the infrared spectrum is absorbed within the first meter of the water's surface, with only 1% able to reach depths beyond two meters in pure water[138]. At greater depths, light predominantly consists of blue and green wavelengths, but there is rapid attenuation of blue light in the 400-500 nm waveband at shallower depths, particularly in coastal areas due to yellow substances (gilvin, gelbstoff) present in the water [140].

The ocean can be classified into three zones based on light penetration. The euphotic or sunlight zone, extending down to approximately 660 feet below the ocean surface, receives adequate sunlight for photosynthesis. Below this lies the disphotic (twilight) zone, where some light penetrates but is insufficient to support photosynthesis. The aphotic (midnight) zone begins around 1000 m beneath the ocean's surface, where sunlight cannot reach, and bioluminescent organisms provide the sole source of light[141]

Aquatic life relies on light for photosynthesis, with the sensitivity of photosynthetic apparatus varying across different wavelengths[142]. Despite this, organic particles primarily inhabit low and variable light environments. Light intensity is a crucial factor in phytoplankton growth, and light quality also plays a significant role[143]. Characterizing light in aquatic environments is desirable, often achieved through the ratio of integrated intensities of blue (400-500 nm), green (500-600 nm), and red (600-700 nm) wavelengths[138], [142], [144].

Photosynthetically Active Radiation (PAR), encompassing the visible radiation (400-700 nm) used for photosynthesis by Earth's plants, including marine species like phytoplankton, is a vital aspect studied in various applications [138]. PAR, measured as irradiance (radiant power flux density), is essential for understanding radiation climate, remote sensing of vegetation, and plant canopy radiation regimes [145]. It is also crucial in theoretical treatments of atmospheric radiative transfer, climate model validation, and determining Earth's surface radiation budget[146]. While the spectral quality of daylight PAR remains relatively constant, factors such as absorptance, reflectance, and transmittance induce spectral quality variations [142], [147]. Like PAR, the diffuse attenuation coefficient Kd is also one of the derived products of the Ocean Colour EOV [148].

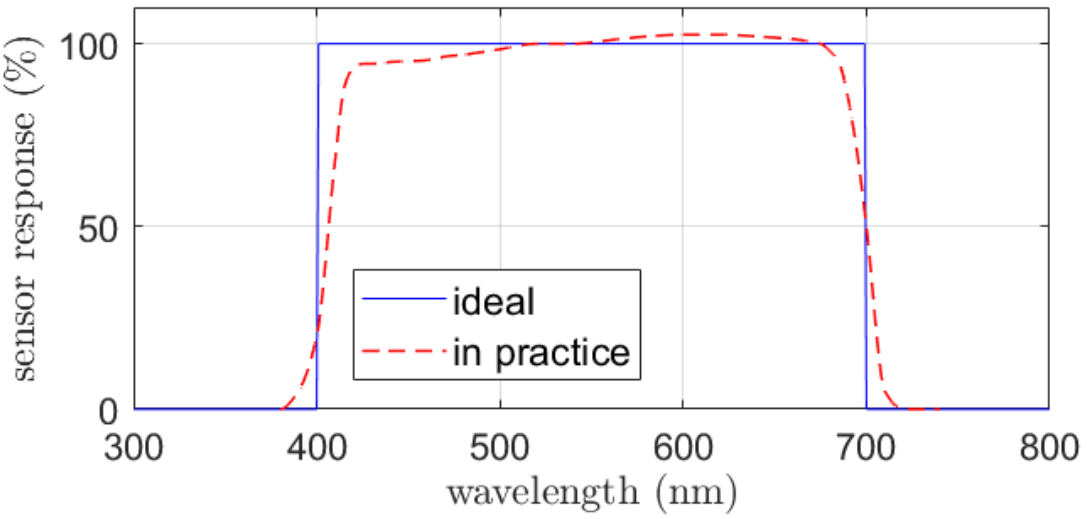

Figure 5.3 - Comparison between an ideal PAR sensor response (in blue) and a typical response of an actual sensor. Adapted from [149].

5.2 Measurement methods and state of the art

Compared to other parameters like turbidity, dissolved oxygen or chlorophyll a, where a variety of sensing principles can be observed, most of the measurement methods available to measure PAR shares a common architecture. Incoming light enters a PAR sensor through a diffuser, which ensures a cosine response[150], meaning the sensor possess a hemispheric field of view. The diffuser is spectrally non-selective, hence PAR sensors optical port look white. Almost all the actual commercial PAR sensors are based on a Silicon photodiode, hence with a typical spectral responsivity that differs from the ideal PAR sensor response showed in Figure 5.3. To approximate the ideal PAR response, an optical filter stack is placed in-front of the Si photodiode. In a good quality PAR sensor, this filter stack acts as a band-pass filter within 400 to 700nm, but also plays a role in "flattening" the typical Si photodiode responsivity in this band, by attenuating progressively wavelengths toward the red.

The photocurrent collected by the photodiode through the diffuser and the optical filter stack is then amplified by a Transimpedance Amplifier. The output of the TIA is then either directly measured (sensors with analog output), or fed through an Analog to Digital Converter (ADC) for digital sensors.

While the overall structure of a PAR sensor is simple, the price of a typical commercial sensor spans from 500 to 1500 € typically, without the logger system which is sold separately. A large portion of the cost PAR sensors is due to the optical filter stack. In their 2021 review[149], Regan et al. presented a table with the filters used in various PAR sensors. Common occurrences are Wratten 85C or 88A/B, Schott BG 38 or Newport 10SWF-750 filters, with a typical cost per filter of 40 to 150 € in the smallest size available (1" or ½"). Reference sensors like the LICOR LI-190SA uses a custom, purpose-built filter to obtain a responsivity close to an ideal PAR sensor.

In terms of academic work on the development of PAR sensors, almost all the articles are dedicated to terrestrial applications[143], [151], [152], [153]. While a handful of articles focused on the development of systems equipped with PAR sensors for ocean applications, they were either using commercial sensors[154], or simple light intensity sensors used as PAR sensors[75], hence providing large error on the generated output. Long et al. did an intercomparison between a reference LICOR LI-193SA PAR sensor (cost approx. 3000 €) and inexpensive HOBO Light sensors (cost approx. 150 €) [155], where they demonstrated that the HOBO light sensors could provide a good approximation of PAR, but only at the expense of individual calibration for each HOBO sensor and each measurement site, which is highly impractical and time consuming.

5.3 Development of a low-cost PAR sensor based on a multi-spectral sensor

As mentioned in the previous section, the structure of a PAR sensor is almost always based on the combination of the following elements: a diffuser, a filter-stack, a photodetector and conditioning electronics (transimpedance amplifier, ADC …), the most expensive part being the filter-stack to obtain the 400-700nm response.

Due to the constrained target budget within our project, we tried to look out for an alternative that would forego the expensive optical filter, while still providing a better solution

than the simple light sensors used in the literature[152] [155]. To fulfill these two conditions, we based our PAR sensor around the ams AS7341, a multi-spectral light sensor that is typically used for color detection, like the identification of paint color code or characterizing the color of objects by measuring reflectance. This component possesses 11 channels, with 8 of them in the visible range with peak wavelengths responsivity ranging from 415nm to 680nm, as illustrated in Figure 5.4.

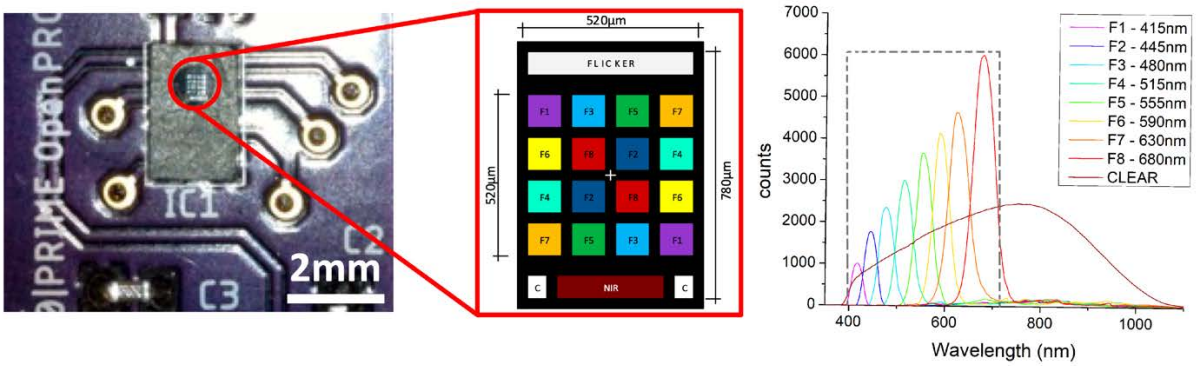

Figure 5.4 - Left: Picture of the ams AS7341 assembled on a custom PCB. Center: schematic of the photodiode matrix. Each number correspond to a different optical filter. Right: Transmission in counts vs. wavelength obtained for channels F1 to F8 at 512x gain. The clear photodiode (without filter) is also represented, with its typical Silicon photodiode spectral responsivity. Dotted line represents the ideal PAR transmission

To achieve these responsivities, each Silicon photodiode is actually covered by nano-optic interference filters that have been integrated into a standard CMOS process by the ams company. It can be observed from the spectrum of Figure 5.4 that each channels possess a different peak sensitivity, following the overall spectral responsivity of a conventional Silicon photodiode as visible on the CLEAR channel.

In order to use the AS7341 as a PAR sensor, several modifications were made. The first one consisted in adding a diffusion filter atop the optical opening, in order to obtain a cosine response. This is important to ensure proper behavior of the sensor: while the datasheet does not give any data on the sensitivity versus the light the Angle of Incidence (AOI), interference filters are by nature sensitive to this parameter. Increasing the AOI typically results in lowering the peak transmission wavelength and broadening the spectral response. To integrate a diffuser, 50µm thick double-sided adhesive (TESA 61532) and Roscolux #116 Tough White Diffusion filter were cut to the dimensions of the AS7341 package using xurography technique[156], with a Graphtec FC-8600-60 cutter plotter, and manually pressed as shown Figure 5.5.

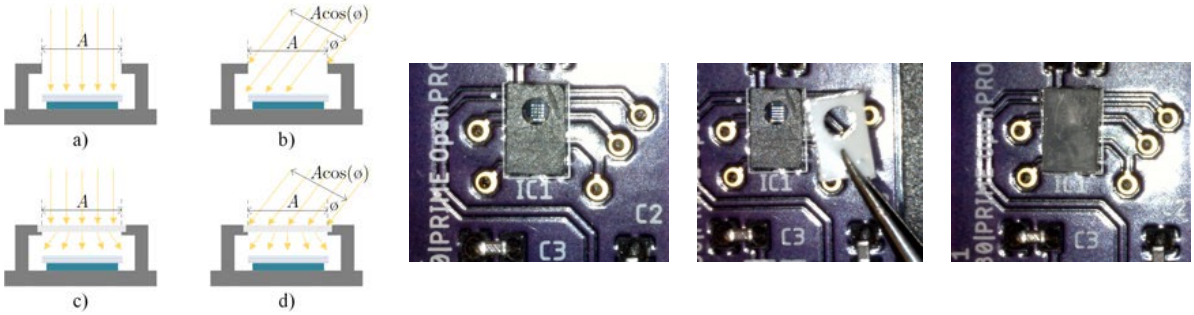

Figure 5.5 - Left: Comparison of a sensor without (a & b) and with (c & d) a diffuser, in the case of normal and oblique incidence. Adapted from[149]*. Right: integration of a light diffuser on the AS7341 using xurography. A double-sided adhesive is cut to dimensions with a hole for the optical opening, and a Roscolux #116 Tough White Diffusion filter is finally placed on top.*

The second modification consisted in the determination of corrections factors to normalize peaks from F1 to F8, with the sensor exposed to sunlight during a clear day, in order to approximate the ideal PAR responsivity which should be constant from 400 to 700nm. This was done after the addition of the diffuser in order to account for eventual unwanted absorption of the Roscolux #116 Tough White Diffusion filter. The result is presented in Figure 5.6, where channels from F1 to F7 are normalized according to the peak maximum of channel F8, with the corresponding calculated scaling factors.

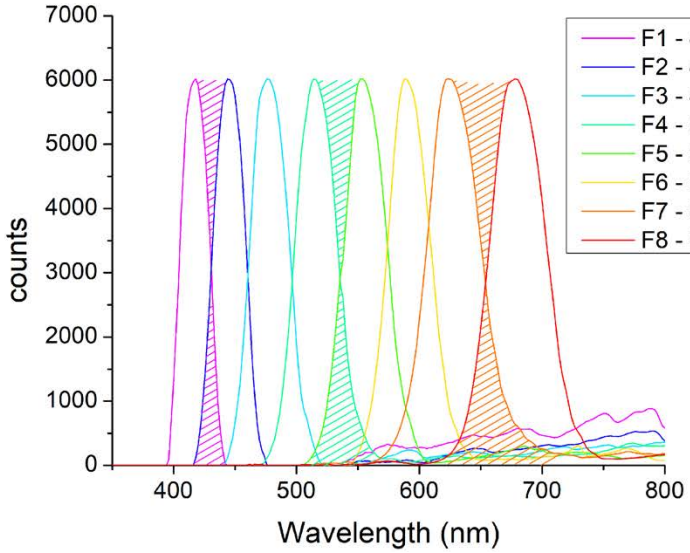

Channel	Scaling factor
F1 415nm	5.97
F2 445nm	3.40
F3 480nm	2.56
F4 515nm	2.00
F5 555nm	1.64
F6 630nm	1.45
F7 680nm	1.30

Figure 5.6 - Illustration of the normalization of channels F1 to F7 according to F8 with a correction factor obtained by exposure of the sensor equipped with its diffuser to sunlight on a clear day. Hatching at the bottom of the curves highlights the recovery between channels F1-F2, F4-F5, and F7-F8. While this recovery would be unwanted in a spectrometer, this is actually used as a feature in our PAR sensor, as this contribution (hatching in the upper part of the curves) corrects the lack of sensitivity observed between each channel peak. The table shows the calculated scaling factor applied to channels F1 to F7

Observing the spectrum response of the normalized channels, it can be seen that there is an overlap between each channel while this recovery is unwanted in a typical spectrometry experiment, this turns into a desirable feature for our PAR sensor. When adding the output of each channel, this overlap leads to an overestimation within the wavelength limits (for example 415 to 440nm for the overlap between F1 and F2); in our case, this overestimation ends up filling the gap which can be seen between each peak, thus improving the match between the sum of channels F1 to F8 compared to the ideal PAR spectrum.

The third modification is software based. The AS7341 is a digital sensor, which can be programmed and controlled using an I2C bus. Each channel possesses a dedicated 16 bit register from which data can be polled after an acquisition. Two parameters allow to adjust the sensor sensitivity, the gain setting (from 0.5x to 512x), and the integration time (from 2.78µs to 46.5s). In order to cover a large range of illuminating condition, we decided to implement a software-based automatic gain control, which increase the gain when data of clear channel is below 10% of the full scale and decrease the gain when it is above 90%, with a fixed integration time of 50 ms. The data available in each channel output register is expressed in counts, as they are obtained directly from the internal ADC. This data in counts is directly affected by the internal gain and integration time settings, hence for the same illumination conditions different data can be obtained, so the counts were converted to basic counts according to the following equation:

$$Basic_{counts} = \frac{Raw_{counts}}{(Gain \times Integration\ Time)} \quad (19)$$

This ensures that basic counts are not affected by the software-based automatic gain control, which is continuously adjusted to light conditions.

In order to evaluate the modified AS7341 sensor we performed an intercomparison experiment with an Apogee SQ-512-SS, which is a commercial PAR sensor as the reference. The Apogee sensor has an analog output that varies between 0 to 2.5V, with a sensitivity of 0.625mV per µmol.m^{-2}.s^{-1}. To synchronize the data acquisition, the Apogee output voltage was sampled with a Texas Instruments ADS1115 16 bits ADC connected to the same microcontroller as the AS7341, ensuring simultaneous measurements. Both sensors were mounted on a laser-cut PMMA plate on the same plane, and exposed to the sunlight during a clear day for several hours. Results are presented in Figure 5.7, where it can be observed that very good agreement is obtained as highlighted from the +/-5% confidence interval.

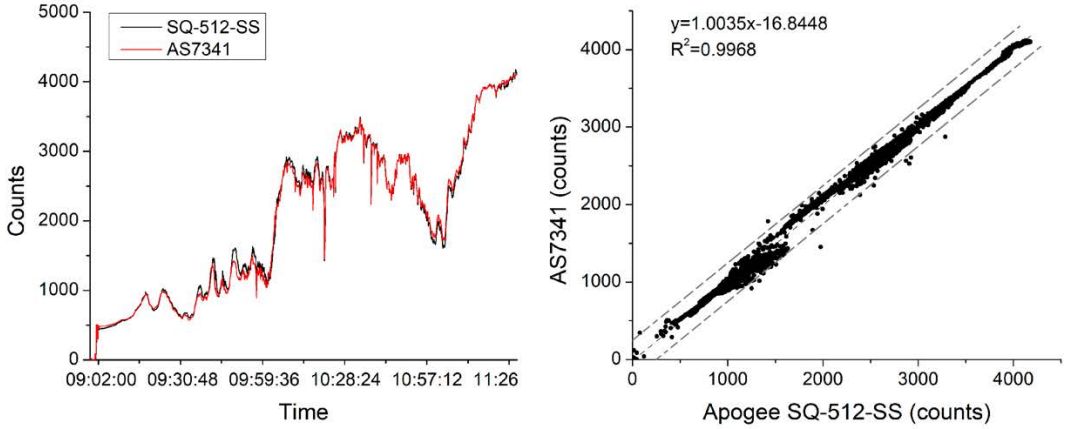

Figure 5.7 – Left: intercomparison between the Apogee SQ-512-SS reference sensor and the modified AS7341 sensor. Right: representation of the data with +/-5% confidence interval represented by dotted black lines.

Based on our literature review, it is commonly admitted that errors from a few percent are typically observed[157], even between two identical factory-calibrated PAR sensors[155], while manufactures like LICOR guaranteed their calibration within +/-5%. Based on these observations, we decided that our simple modifications were sufficient to obtain adequate performance for PAR measurements, however it should be noted that the results could be further improved by using machine learning-based techniques to calculate scaling factors instead of our basic arithmetic method as demonstrated by Zhang et al.[151].

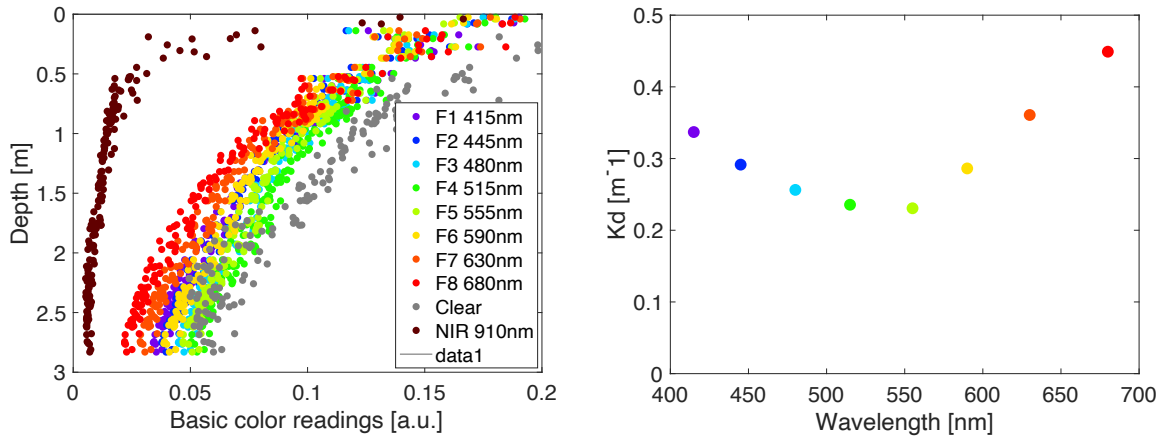

Figure 5.8 - Illustration of the capabilities of the modified AS7341 sensor to collect spectral data in the water column. Deployment was done in the port of Villefranche sur Mer on the 6th of October 2021 at 8H40 AM. Left: Basic color readings for each channel vs depth. Right: calculated diffuse attenuation parameter Kd vs wavelengths for channels 1 to 8.

Compared to a PAR sensor, our modified AS7341 is able to deliver the irradiance between 400 to 700nm, but also gives spectral data with 8 channels over this range. This is particularly interesting in oceanography, with potential for calibrating ocean color remote sensing data, or gathering information about plankton blooms or additional data for chlorophyll concentration. While we did not have enough time to evaluate the capabilities, we conducted a simple experiment where the sensor was immersed in the Mediterranean Sea, in the port of Villefranche sur Mer, from the surface to 2.80m depth. The result of this experiment is presented Figure 5.8, where data from channels F1 to F8 are presented in basic counts at each depth. The overall shape of the data follows the same trendline, with light absorption increasing with depth, with an exponential dependency. Absorption in the UV and in the red is known to be more pronounced than in the blue and green bands; while present in data of Figure 5.8 (left), these properties are not easy to visualize with that kind of representation. In order to demonstrate the capabilities of the modified AS7341 to generate ocean colour data, we calculated the diffuse attenuation coefficient Kd for each channel band, according to the following formula, presented here for channel F1 at 415nm[158]:

$$K_{d(415)} = \ln\left(\frac{I_{1(415)}}{I_{2(415)}}\right)/(Z_2 - Z_1) \qquad (20)$$

With $K_{d(415)}$ the diffuse attenuation coefficient calculated at 415nm, $I_{1(415)}$ and $I_{2(415)}$ the light intensities measured at 415nm at respective depths of Z_1 and Z_2. Figure 5.9 (right) shows the result of this calculation for channels 1 to 8, based on intensities measured are depth Z_1 = 1.05m and Z_2 = 2.83m. The calculated values of K_d for each wavelength are within the expected range for clear to ultra clear water [159], as it is the case in Villefranche sur Mer. Interestingly, the representation of K_d obtained also matches the typical pattern of light penetration in coastal waters which is illustrated Figure 5.9 (right), with attenuation more pronounced at both ends of the visible spectrum (violet and red), and less pronounced for the green (coastal area as with our experiment) or the blue (open ocean).

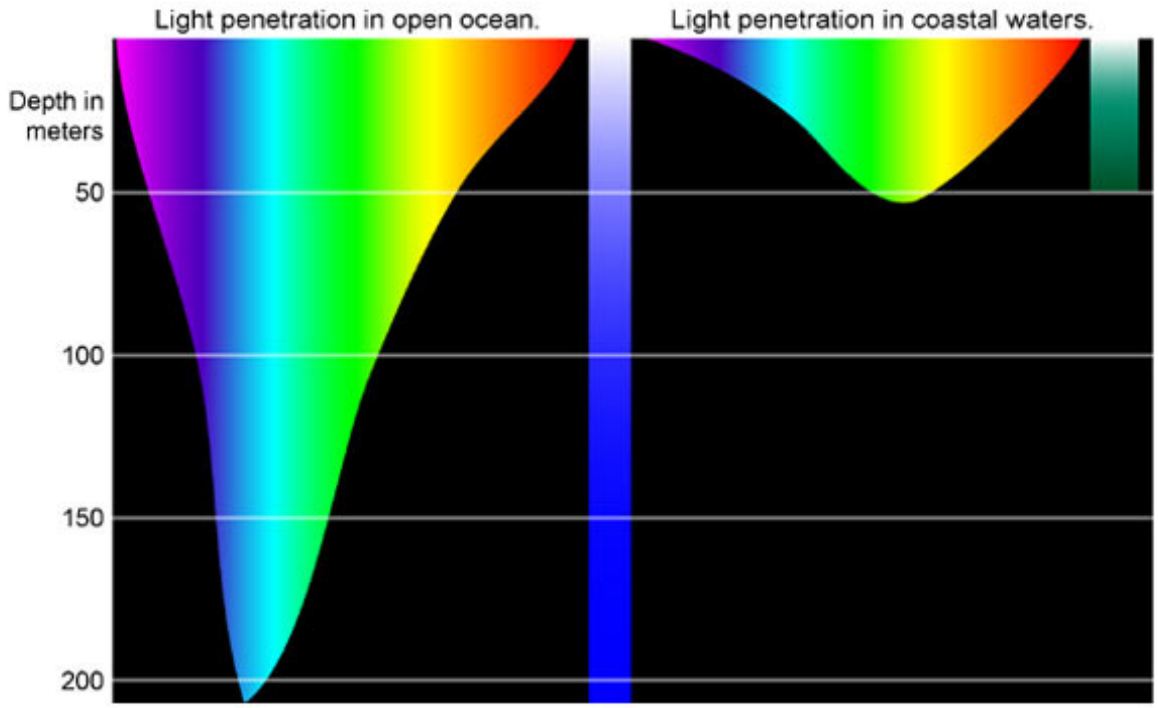

Figure 5.9 Illustration of light penetration versus depth in open ocean (left), and coastal areas (right), where it can be observed in both cases that UV and IR are rapidly attenuated. While the observation is the same for both ends of the spectrum, warm colors (orange, red and IR) are absorbed, while cooler colors are scattered. Image courtesy of Kyle Carothers, NOAA-OE.

While the testing conditions were far from ideal, with a bit of swell that was causing a lot of noise at very small depths, and a moderate deployment depth that limited the amount of absorption, this feature will be evaluated more thoroughly in future works, especially by applying aforementioned machine learning techniques[151] with ocean color datasets.

4.4 Conclusion

Compared to the other sensors developed within this project, the PAR sensor architecture was straightforward, as the ams AS7341 was already offering some desirable features. In particular, the integrated interference filters of this IC proved to be adequate to approximate the ideal PAR transmission after minor modifications, which included the addition of a light diffuser to obtain a cosine response, the calculation of scaling factors, and the implementation of an automatic gain control algorithm. While some improvements could still be made, the sensor in its current form is already achieving appropriate performance when intercompared with a reference sensor like the Apogee SQ-512-SS, with the additional benefit of being able to deliver additional spectral information, as well as classic light sensing (with the CLEAR channel) and NIR measurement. An experiment in Villefranche-sur-Mer demonstrated the additional capabilities of the modified AS7341 sensor for generating several derived products of the Ocean Color EOV, namely PAR and K_d at 8 wavelengths, and could potentially provide other information on chlorophyll content with appropriate data treatment [160].

Chapter 6 Chlorophyll-a

6. 1 Introduction

Chlorophyll is a color pigment present in plants, algae, and phytoplankton. Serving as a photoreceptor, this molecule plays a crucial role in photosynthesis[161]. Photoreceptors, including chlorophyll, absorb light energy from sunlight[162]. The green appearance of plants and algae is attributed to chlorophyll, as it reflects the green wavelengths present in sunlight while absorbing all other colors.

Contrary to common perception, chlorophyll is not a singular molecule; there are six distinct chlorophylls identified as A, B, C, D, E, and F, each variant reflects slightly different ranges of green wavelengths. Chlorophyll A holds the primary responsibility for photosynthesis, and it is universally present in all photosynthesizing organisms, spanning from terrestrial plants to algae and cyanobacteria[31], [163].

The additional chlorophyll forms function as accessory pigments, linked to specific plant and algae groups, contributing to taxonomic complexity. While these auxiliary chlorophylls absorb sunlight, they serve as support to photosynthesis by transferring absorbed energy to the primary chlorophyll A, rather than directly participating in the process[164]. Not all algae appear green: so-called accessory pigments are also found in phytoplankton, including carotenoids, phycoerythrin or phycocyanin. Due to their different absorption spectra, these pigments are responsible of the well-known blue-green cyanobacteria color caused by phycocyanin, while phycoerythrin is found in red algae, involved in "red tide" events caused by a bloom of these species. The absorption spectra of the major photopigments present in phytoplankton is shown

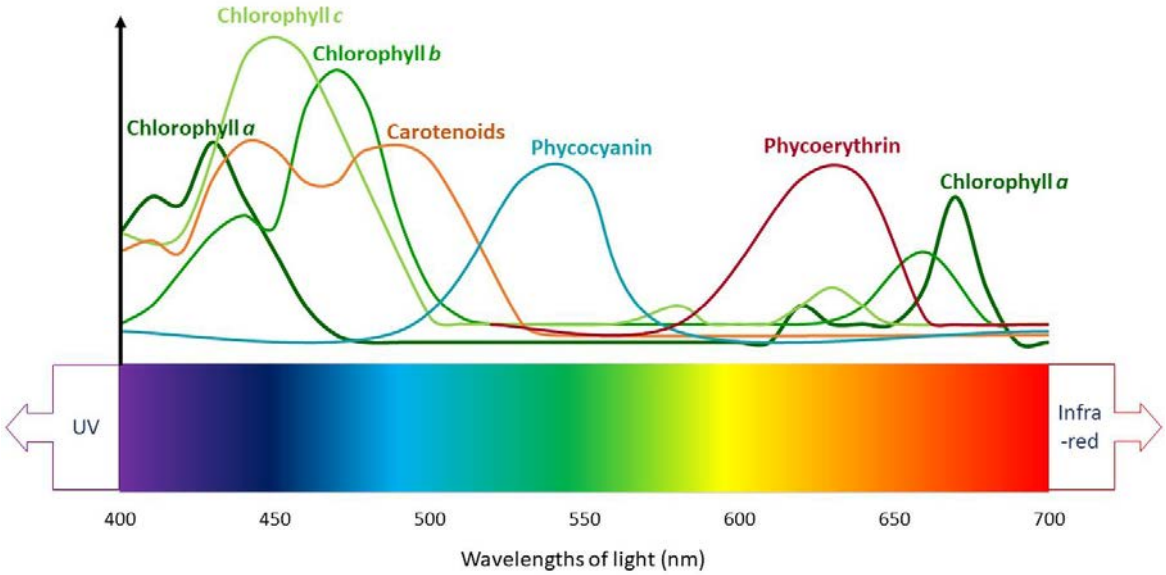

Figure 6.1 Absorption spectra of the major photopigments present in phytoplankton within the photosynthetic active radiation (PAR) range. Adapted from[165]

Due to its presence in all phytoplankton forms, chlorophyll a is considered as the best estimator for primary production in water bodies[166],and is part of the *phytoplankton biomass and diversity* Essential Ocean Variable. As phytoplankton is considered to account for roughly

half of Earth's primary production, produces 50% of Earth's oxygen, and contributes to 10% of anthropogenic CO_2 storage though the biologic carbon pump, it is pivotal to monitor it at the global scale. Relevant spatial resolution to collect phytoplankton data is within 1m to 10km (plankton blooms), while relevant temporal scale is considered to be within a couple of hours to a month, as illustrated in Figure 6.2 [167]

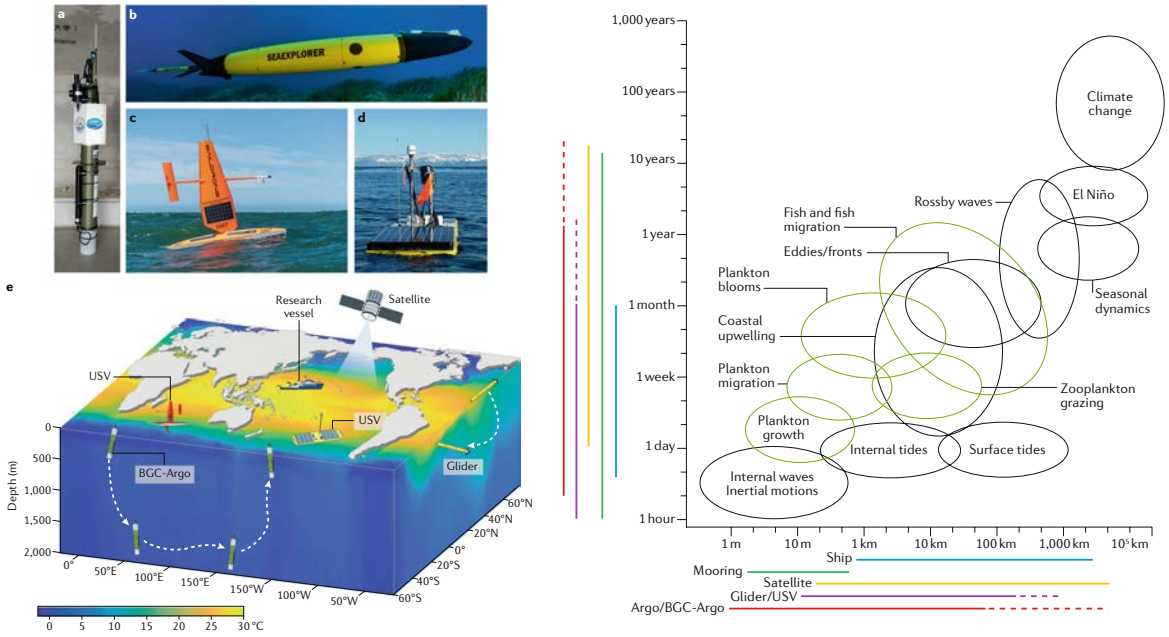

Figure 6.2 Left: illustration of various autonomous platforms used to collect biogeochemical data, including chlorophyll a levels. Right: Relevant spatial and temporal resolution needed per variables, and suitable autonomous platforms. Adapted from[167]

The aforementioned spatial distribution is on a horizontal scale, but phytoplankton is also distributed vertically in the water column, this distribution being influenced by parameters like currents, but also to nutrients or light penetration as recently demonstrated by Wirtz et al. as illustrated in Figure 6.3[168].

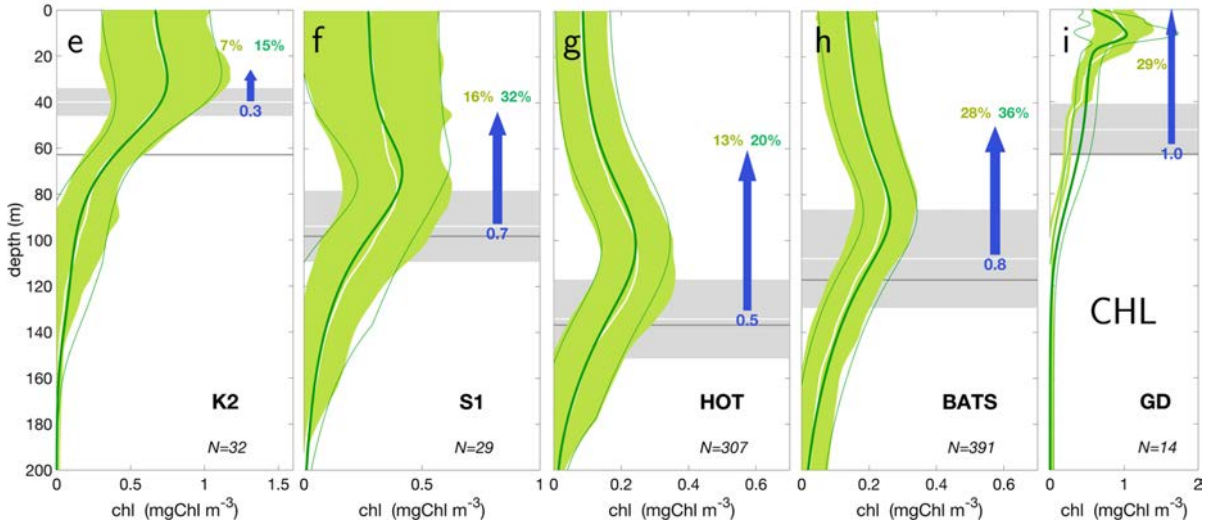

Figure 6.3 Distribution of chlorophyll a in the water column at various marine stations. Adapted from[168]

6.2 Measurement Methods and state of the art

Various techniques can be used to estimate chlorophyll a concentration in water, depending on the type of observation platform that is used to perform the measurements[167]

Remote sensing has become one of the main methods to obtain phytoplankton biomass data due to its ability to cover large spatial areas with an acceptable temporal resolution. In remote sensing, reflectance is exploited instead of fluorescence, as the latter cannot be currently measured due to its small intensity. A ratiometric calculation based on the reflectance at two wavelengths (typically green and blue, i.e. 443nm and 555nm) has been used extensively based on the previous optical sensors embedded in satellites (SeaWiFS, MODIS, MERIS, VIIRS …)[169] but the recent launch of PACE (Plankton, Aerosol, Cloud, ocean Ecosystem) in February 2024 will further improve the data collected thanks to the hyperspectral imaging system embedded.

While unbeatable in terms of surface coverage and temporal resolution, remote sensing suffers from several drawbacks; as it is based on reflectance, the collected data is integrated from the upper water column, with a depth depending on penetration depth of light. Another limitation is present in coastal areas, either due to the shallow waters or to absorbing species due to organic matter. As the light travels through the atmosphere, it is also highly impacted by its composition. Finally, remote sensing cannot retrieve information about the distribution of chlorophyll a in the water column, but only integrated data. In order to obtain robust chlorophyll a estimate from remote sensing, it is necessary to compensate for all of these limitations, hence the models used to estimate chlorophyll a from reflectance are complex and prone to errors.

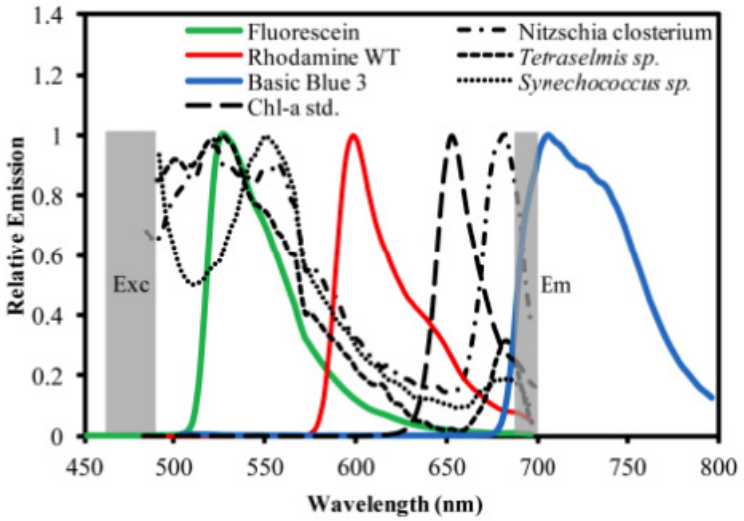

Figure 6.4 Fluorescence emission spectra of chl-a standard in acetone, reference dyes and three marine phytoplankton species in seawater. Adapted from[170]

Aside from remote sensing, several on-boat, or in-situ techniques are also routinely used to collect chlorophyll a measurement, that can also serve as reference calibration data for remote sensing complex algorithms. The reference method is High Performance Liquid Chromatography (HPLC), which is an analytical technique used to separate, identify, and quantify components in a mixture, HPLC is particularly useful because it can separate chlorophyll a from other pigments and derivatives, providing precise and accurate measurements. This method is widely used in

environmental monitoring, especially for assessing water quality and studying phytoplankton populations and is used to calibrate almost all other instruments. HPLC is typically used in laboratory settings due to its complexity and the need for precise control over conditions, using HPLC in the field for chlorophyll a measurements can still be challenging due to the need for sample preparation, solvent handling, and the sensitivity of the equipment to environmental conditions[171]. For field applications other techniques like spectrophotometry or flow cytometry can also be used on-boat. In-situ flow cytometers are also available, like the Imaging FlowCytoBot (ICFCB), but with a cost of about 220 k€ it is not a widespread instrument.

For cost-effective, in-situ measurements, absorption-based methods have been evaluated and even used in some commercial sensors from WET Labs (acquired by Seabird in 2010) [172], but this technique was not widely adopted by oceanographers who preferred fluorescence-based instruments, which is still considered nowadays as the method of choice for in-situ measurement of chlorophyll a. Figure 6.4 shows typical emission spectra of chlorophyll a standard in acetone, compared to well-known fluorescent dyes and actual in-vivo emission spectra from *Nitzchia closterium*, *Tetraselmis sp.* and *Synechococcus sp* in seawater. Corresponding excitation wavelength is done at 470nm. It can be observed that chlorophyll a in-vivo fluorescence peak is red shifted compared to the standard in acetone, a shift also observed on absorbance[170].

Instruments exploiting the fluorescence of chlorophyll are called fluorometers and are commercialized by several manufacturers like Seabird, BBE, Chelsea… Most of the commercially available fluorometers are described in the 2010 Deltares report[173], with a price ranging from 2.5 k€ to 75 k€. While being used in most cases, chlorophyll fluorometers are still considered as perfectible, as the fluorescence intensity is influenced by many factors, including species, photo-acclimation, nutrient limitation and acclimation, growth phase, or non-photochemical quenching (NPQ). Roesler et al. recommends applying a correction factor of 2 over the measurement made by a calibrated Wetlabs ECO fluorometer to match the actual concentration measured by HPLC, while the data obtained by different fluorometers on the same samples have shown some large variation of slope factors, ranging from 1.7 to 2.6 (calculated as chl.a from fluorometer vs chl.a from HPLC) [174]. While these discrepancies would appear as crippling, these fluorometers are still the most widely used instruments to measure chl. a levels in-vivo and in-situ due to the absence of cost-effective, viable alternatives.

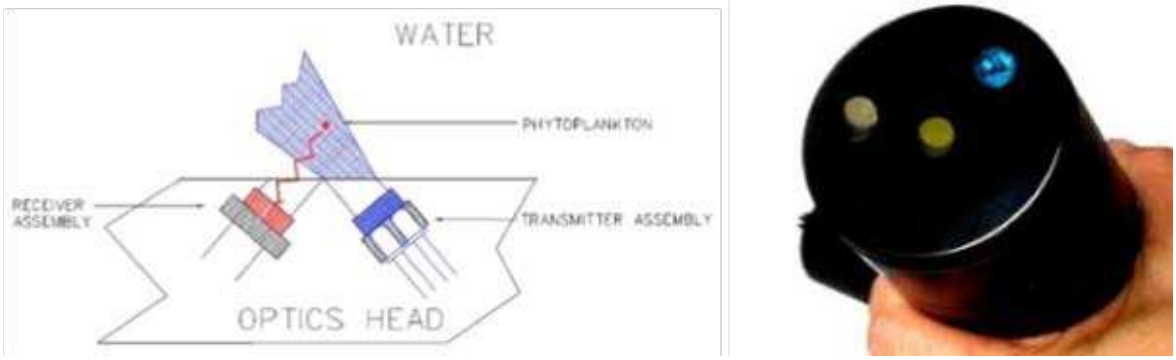

Figure 6.5 Side view of a WET Labs ECO-FL chlorophyl fluorometer. Blue LEDs emits the excitation light at 470nm with a shortpass filter, while a photodiode equipped with a longpass red filter collect the emitted fluorescence signal around 685nm. Optical components are protected from the water by an optical window, quartz typically. Adapted from Seabird Electronics

A review by Zeng and Li in 2015 listed a comprehensive list of both commercial and academic research chlorophyll fluorometers[175] which could be completed by a few more

recent works[176], [177], [178], [179]. Most of these systems are based on single wavelength excitation, ranging from 410 to 470 nm approximately, using LED, laser diode or Xenon flash lamp light sources, while detection is achieved by Photomultipliers (PMT), silicon photodiodes or CMOS sensors. Figure 6.5 show a schematic and an actual picture of a Seabird ECO fluorescence sensor, one of the most popular sensor for in-situ chlorophyll measurement, which is also typically used on BioGeochemical Argo profilers [180].

A few systems are using multiple wavelength excitation as it allows to discriminate between different pigments, and in some cases to differentiate between different taxonomic groups among the phytoplankton species[181]. One of the most remarkable works on this topic was achieved by Zieger et al. with the so-called ALPACA system, a multi-wavelength fluorometer that allows to discriminate between eight phyla of phytoplankton thanks to eight separate excitation wavelengths coupled with linear discriminant analysis [182], [183]. The system was intended to be commercialized by the Idronaut company, but to our knowledge have not yet been introduced to the market. While very promising, it is a flow-cell based system, which implies a pumping system and a filtering unit, which limits the overall sampling rate to 1.5mL/min, making it a low-cost alternative to flow cytometers rather than fluorometers.

6.3 Development of a low-cost chlorophyll fluorometer

As the scope of this thesis is to develop a complete low-cost multiparameter probe, the decision was made to use a conventional chlorophyll fluorometer setup, as developing an innovative configuration (using multi-wavelength excitation for example) that could solve some of the aforementioned issues of these instruments would mobilize at least one full-time complete PhD. In order to obtain a sensor which could be usable in coastal areas, the target was set to 0.1µg/L Limit Of Detection, 0 to 100µg/L operating range and built-in ambient light rejection.

6.3.1 First generation prototype

A typical chlorophyll fluorometer (like the WET Labs/Seabird ECO presented in the previous section) is based on a blue excitation light source with a shortpass filter (410 to 470nm) and a photodetector with a red longpass filter (> 600nm) to collect fluorescence signals around 685 to 695nm. As the fluorescence signal is in the visible range, excitation light is modulated in order to perform synchronous detection of the fluorescence and cancelling out ambient light contribution. A modulation frequency of a few hundred to a few kilo Hertz is sufficient to remove ambient light in most use cases. Both sine or square waveforms can be used for modulation.

While the operating principle is simple, it is actually challenging to obtain a working in-situ sensor that reach the required sensitivity, concentration range while being able to operate in daylight conditions, and maintaining good stability for long term deployment. This is tightly related to the poor fluorescence yield for in-vivo chlorophyll a in seawater, which spans from 1 to 5% typically[165], [184]. This small fluorescence yield implies that a very high sensitivity is required on the photodetector side. Photo-Multiplier Tubes (PMT) are used in some cases due to their high sensitivity, but these are not in-line with our objectives of cost and power-consumption, as such this option was ruled out.

Photodetector for fluorescence emission collection

The most common alternative, used in many commercial and academic sensors, is the use of a silicon photodiode coupled with a high-gain transimpedance amplifier (TIA). For the first prototype, we chose the TSL257 from TAOS (now ams-OSRAM) which is a light-to-voltage converter. It combines a Si photodiode, a TIA and associated feedback components on a single CMOS chip, managing to offer a transimpedance gain of 320 MΩ with good offset stability and low noise levels. The component directly outputs a voltage (rail-to-rail) proportional to light intensity: an Analog to Digital Converter is then used to sample this output voltage and turn it into a digital value. As designing a photodiode and TIA circuit with such a large gain is challenging, the TSL257 is used in several articles where a high sensitivity is required[177], [185], [186], [187], [188].

TSL257 is based around a silicon photodiode, but its spectral responsivity slightly differs from typical Si photodetectors toward the infrared as shown Figure 6.6. While no mention of an optical filter is made in the datasheet, it probably incorporates an infrared filter. For chlorophyll fluorescence peak measurement, located around 685nm to 695nm, the responsivity of the TSL257 is perfectly suited as its peak sensitivity is about the same.

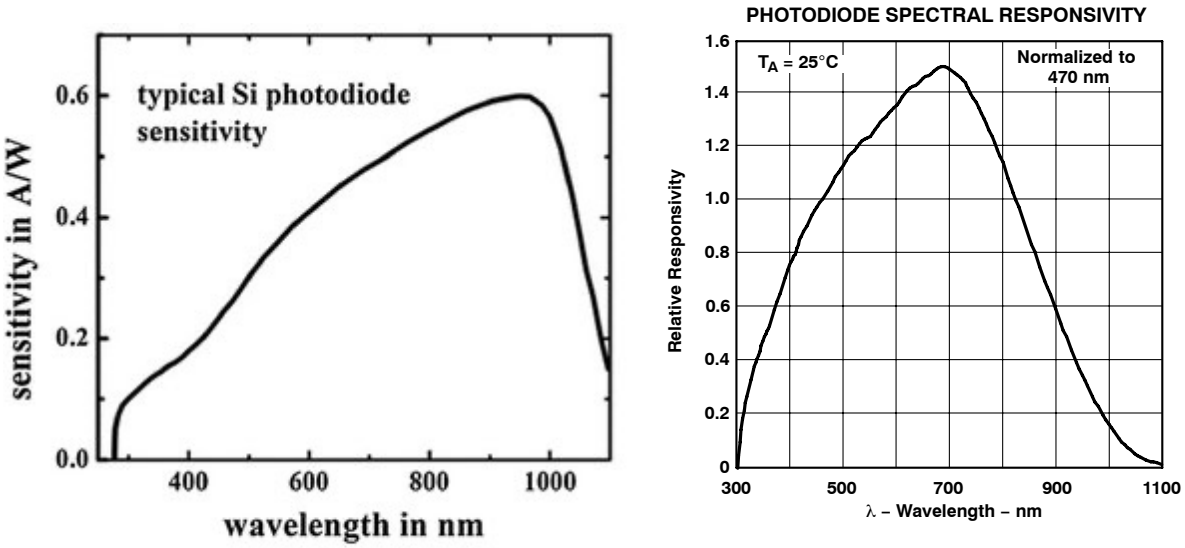

Figure 6.6 Left: typical silicon photodiode sensitivity (adapted from after Hamamatsu S 2386). Right: TSL257 spectral responsivity (ams OSRAM TSL257 datasheet)

Excitation light source

Fluorescence emission for chlorophyll a is maximized at an excitation wavelength between 410 to 470nm, which corresponds to violet to blue LEDs. While LEDs are considered ubiquitous, with a presence in almost all applications requiring the generation of light (cars, phones, lighting, microscope sources, UV sources in lithography equipment…), it should be emphasized that it is highly challenging to manufacture efficient blue and violet LEDs; in fact it took almost three decades after the advent of red and green LEDs to obtain efficient blue LEDs thanks to the work of Akasaki, Amano and Nakamura, who were awarded for the Nobel Prize in Physics in 2014 for their achievement on this topic [189]. Nowadays violet and blue LEDs can be sourced with ease, but some of the consumer electronics market have a relatively broad emission spectrum; even with a dominant wavelength peak at 430nm, some references still emit non-negligible light above 550nm. A few LEDs were characterized with a

spectrometer in order to ensure minimal overlap between blue excitation and red fluorescence emission.

Two of the selected LEDs measurements are presented Figure 6.7. The data is presented in counts vs wavelength. Due to the different efficiencies of the two LEDs, their operating current, generated by a source-meter, were set to obtain comparable counts output at their maximum peak intensity. Blue solid line data represent the direct LED output intensity vs wavelength, while red solid line data represent the LED output after passing through a longpass Roscolux #19 Fire optical filter (transmission represented in arbitrary units with a yellow solid line). It can be seen that for the CMD15 LED, some emission can still be seen after 550 nm, although the dominant wavelength of this LED is 430nm. The Full width at Half Maximum (FWHM) is about 70nm. With 5mA current, a maximum of 0.6 counts can be observed after the filter, which represents about 1.5% of the peak emission (45 counts @ 430nm). Considering the typical fluorescence yield of chlorophyll a is between 1 to 5%, this unwanted emission would be seen as a false fluorescence signal by the photodetector. While the addition of a blue excitation filter could mitigate the impact of this residual emission, the CMD15 is not an optimal choice for this application.

The LXML LED exhibits a sharper emission spectrum, with a FWHM of 15nm, no secondary peak, and less residual emission toward the red, although its dominant peak is at 450nm vs 430nm for the CMD15. When covered with the Roscolux #19 filter in the same conditions, the highest intensity collected is 0.011 counts, which correspond in that case to 0.017 % of the peak emission, i.e. two decades less than the CMD15.

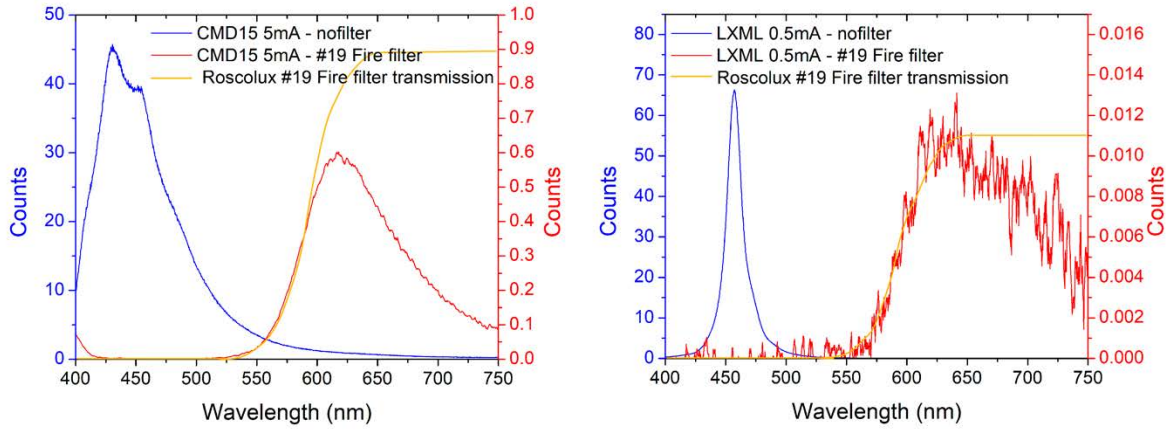

Figure 6.7 Comparison between two consumer electronics blue LEDs characterized with a spectrometer. Left: CMD15-21UBC has a 430nm dominant wavelength according to the manufacturer, but a secondary peak can be observed around 450nm, as well as residual emission in toward the red (blue solid line). When a Roscolux #19 Fire optical filter is placed in front (filter transmission curve in yellow solid line), LED emission is effectively rejected by the filter below 550nm, but the residual emission is visible and will be seen as fluorescence by the photodiode. Right: Lumileds Luxeon Rebel LXML-PR01-0500 Royal Blue has a 450nm dominant wavelength according to the manufacturer, which is confirmed by the spectrometer measurement. When couple to the same Roscolux #19 filter, only a negligible emission can be seen after the 550nm limit.

Based on this evaluation, we selected the Luxeon Rebel LXML-PR01-0500 Royal Blue as our emission source for the first-generation prototype.

Optical filtering

As already mentioned, in order to collect fluorescence emission, the excitation should not be collected by the photodetector, hence the need for appropriate filters. Most commercial fluorometers relies on high-end optical filters with longpass or even bandpass characteristics

to maximize collection of appropriate wavelengths and reject unwanted ones. While the performance of these filters is excellent, their cost is too high compared to the objectives of the project, with typical price around the 100 € mark for one filter.

The LED characterization experiment already presented the use of a cost-compatible alternative filter selected for the development of our fluorometer. The Roscolux filters are plastic based optical filters based on either co-extruded polycarbonate plastic of deep-dyed polyester, depending on the type of dye (color) used. These filters are mostly used in the theatre, film or photography industry in front of lighting equipment, and as such they are extremely resistant toward fading or discoloration caused by UV exposure. Some of these filters have been successfully used for chlorophyll fluorescence measurements[190], [191], hence they were selected for evaluation. Two references were chosen based on their transmission data: Roscolux #384 Midnight Blue for excitation and Roscolux #19 Fire for emission, both purchased from Edmund Optics. Roscolux filters are sold as sheets, so they were cut to the required dimensions either with scissors or using a Graphtec FC-8600 cutter plotter.

Another approach was also considered, with the use of commercial ink mixed into poly(dimethylsiloxane) (PDMS), as demonstrated in the paper from Llobera et al.[192]. The use of dyed PDMS can then serve a dual purpose: optical filtering and waterproofing of the optical components, thus replacing the need of a transparent window. Blue and red inks were obtained from Pelikan, while Sylgard 184 PDMS reference was used. Preparation was made according to Llobera et al., with different concentration depending on the desired thickness and/or absorption.

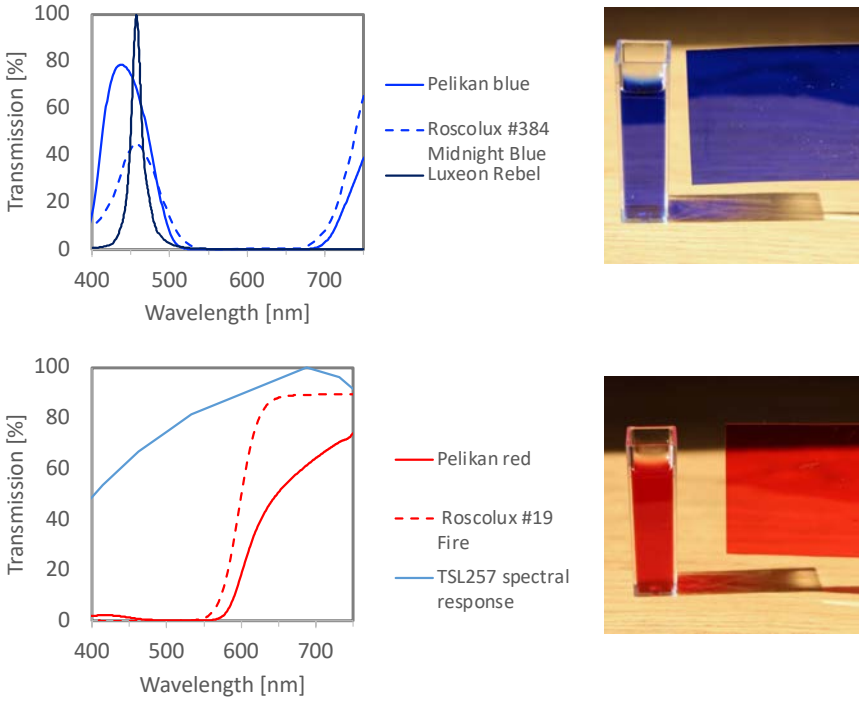

Figure 6.8 Optical filters characterization for the first-generation prototype. Top: transmission of the excitation filters, with the LXML Luxeon Rebel Royal Blue LED emission spectra superimposed. Picture shows the actual filters, Pelikan Blue ink dyed PDMS in a spectrometer cuvette on the left, Roscolux #384 Midnight Blue on the right. Bottom: transmission of the fluorescence emission filters, along with the spectral responsitivty of the TSL257 photodetector. Picture shows the Pelikan Red ink dyed PDMS in a cuvette, while Roscolux #19 Fire filter is on the right.

The two Roscolux and the two dyed PDMS filters were then characterized with a spectrometer to compare their transmission spectra and observe their adequacy with the TSL257 photodetector and the LXML blue LED. Dyed PDMS was poured in spectrometer cuvettes for polymerization, with a concentration adapted to obtain similar transmission characteristics as the Roscolux plastic filters. From the results observed Figure 6.8, it can be seen that both blue excitation filters give satisfactory results; the transmission maximum of the Pelikan blue is around 430nm, so slightly shifted compared to the LXML LED emission peak, while the Roscolux is perfectly centered. While the transmission values are higher for the blue dyed PMDS filter, it should be noted that this can be adjusted by the dye concentration.

For the red filters, differences in the transmission spectra are more visible, with the Roscolux #19 Fire offering ideal transmission curve with absorption in the blue wavelengths, and 90% transmission in the red wavelengths, from 650nm and above. The red Pelikan filter has several issues, with 1 to 2% transmission in the blue wavelengths, and only 60% transmission around 685nm, the chlorophyll a fluorescence emission peak.

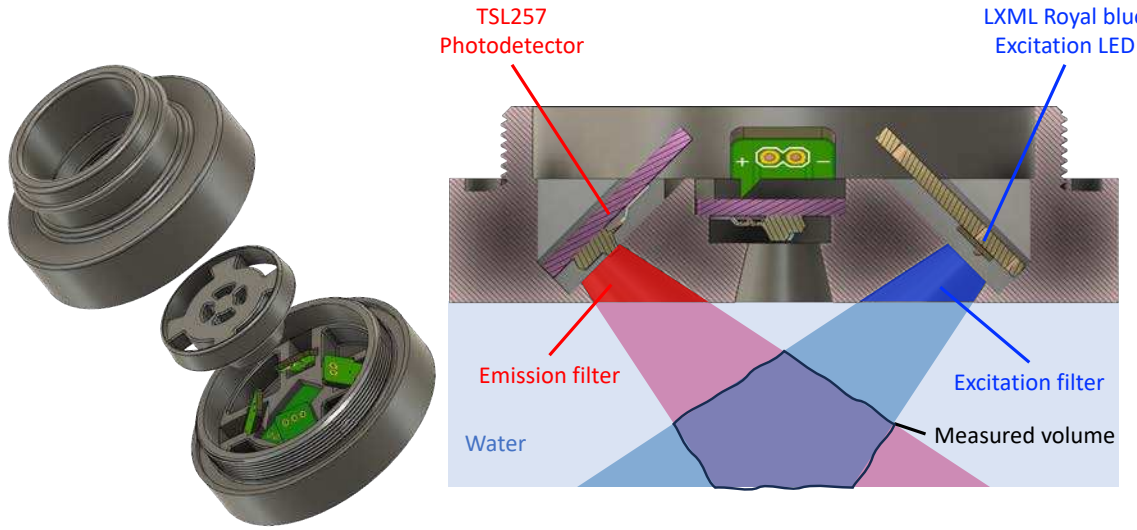

Figure 6.9 Integration of the blue excitation LXML Royal Blue LEDs, TSL257 photodetector, and optical filters. Both the LEDs and the TSL257 are mounted on custom PCB with similar dimensions. Excitation source and photodetector are positionned at an angle

6.3.2 Hardware and Electronics

Based on this choice of components, a prototype was assembled and evaluated, based on a former 3D design made by Chloé Paoletti, which allows the integration of several light sources and photodetectors with a similar form factor. The LXML Royal Blue LEDs are Surface Mounted Device (SMD) components, so a custom PCB was designed in EAGLE CAD software to integrate them in the 3D printed housing. Another PCB with similar form factor was designed for the TSL257. Both PCBs were fabricated by OSH Park company and soldered in the lab. The filters were integrated in two different ways: for the Roscolux filters, they were cut to dimensions and simply placed in front of the optoelectronics components, while a transparent PDMS window was made by pouring PDMS in the optical ports and polymerize it. For the Pelikan dyed PDMS filters, the protocol was similar to the transparent PDMS windows except that dyed PDMS was used.

An Adafruit Feather M0 microcontroller was in charge of controlling the LED excitation by generating a square signal, and the TSL257 analogue output was sampled by the

internal 12 bit Analog to Digital Converter. Arduino software was coded to control the system, and the ADC data was simply collected through the serial monitor as text values.

In order to evaluate the prototype, chlorophyll a stock solution was according to a protocol derived from Khalyfa et al.[193], 5g of spinach leaves which were finely cut and put in a mortar with 15mL of ethanol. The mixture was then crushed and grinded with a pestle in the mortar until the obtention of a green solution. The solution is finally passed through a paper filter. In order to obtain the concentration of the obtained stock solution, the spectrophotometric method from Jeffrey and Humphrey [194] is used: the solution is characterized in a spectrometer, and absorption at 664nm and 647nm are measured. Then the following equation can be applied to obtain the chlorophyll a:

$$C_{Chla} = 11{,}93\, E_{664} - 1{,}93\, EE_{647} \tag{21}$$

With E_{664} and E_{647} being the extinction coefficient measured at 664nm and 647nm respectively. While very simple, this protocol is actually fairly reproductible, as can be observed on the data presented Figure 6.10. It should be noted that the baseline obtained with pure ethanol is subtracted from the data, and the baseline is corrected at 750nm to correct for turbidity and contamination product [195], as the solution is only filtered and not treated with separation techniques. For the stock solution obtained in Figure 6.10, a concentration of 35.53 mg/L is obtained.

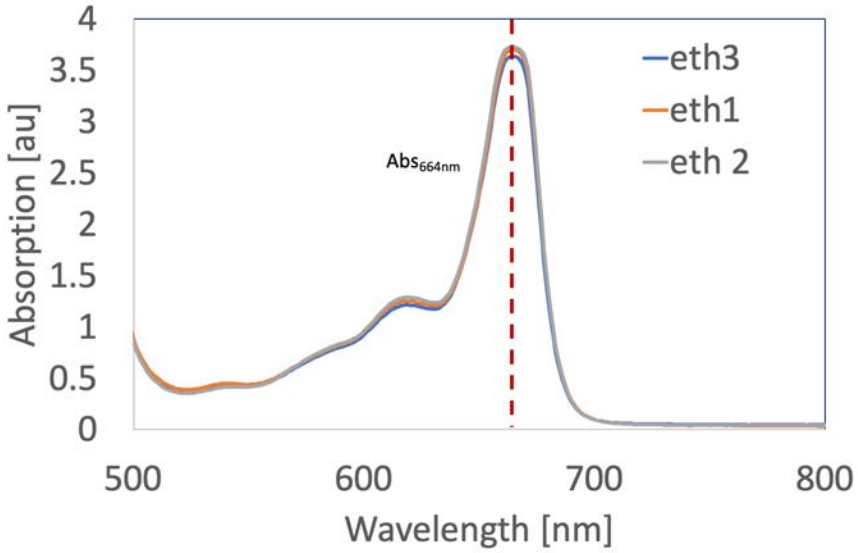

Figure 6.10 Absorption spectra measured of stock solution of chlorophyll a extracted from fresh spinach leaves in ethanol. The triplicate shows that the protocol is fairly reproducible.

This stock solution can then be diluted to calibrate our prototype and evaluate its performance. As ethanol is soluble in water, deionized water is used as the solvent for the dilution to limit the consumption of ethanol, as the size of the prototype requires around 500mL of solution to be immerged and tested.

Figure 6.11 shows the obtained fluorescence measurement at increasing chlorophyll a concentration and 4 excitation LED currents. Output from the TSL257 photodetector is sampled by the Adafruit Feather M0 internal 12 bits ADC. As the system is powered at 3.3V, the Least Significant Bit (LSB) is 806µV. Fluorescence intensity is correlated to the excitation light intensity, which is confirmed by the slope obtained which increase with the excitation

current. However, at high current it is observed that the values are less stable, especially at low concentration, i.e. below 50µg/L. This could be attributed to the modified beam of light obtained when increasing the current but further investigations would be required to validate this interpretation.

Sensitivity of the system varies from 0.32 to 1.81 counts per µg/L of chlorophyll a. With moderate averaging of 50 ADC samples per data point, counts are stable within +/-1 LSB, which would correspond to a 1 µg/L resolution at best, a decade worse than our objectives of 0.1 µg/L.

Considering the 320MΩ gain of the TSL257 transimpedance amplifier, an 806µV LSB corresponds to a photocurrent of 2.5 fA approximately, which highlights how challenging is to measure chlorophyll a fluorescence at concentrations naturally occurred in natural environments.

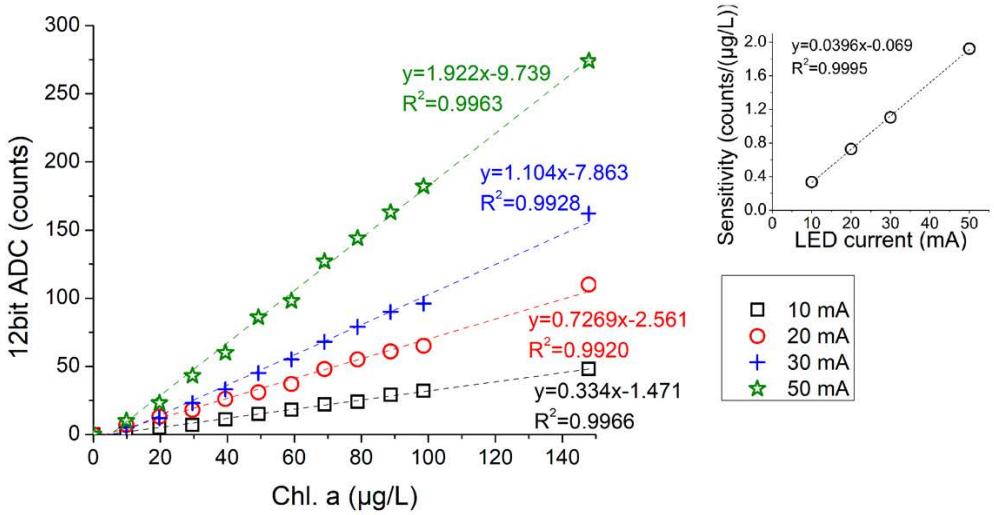

Figure 6.11 - First generation prototype characterization, presenting ADC counts vs. chlorophyll a concentration diluted in deionized water. Inset on the upper right shows the linear dependency of the sensitivity vs the excitation LED current.

6.3.3 Discussion

These experiments led to the following observations on this first-generation prototype:

- First observation is that the sensitivity with this prototype is not sufficient compared to our required specifications to work in coastal waters, where typical concentrations are in the 0 to tens of µg/L. However, the prototype could already be usable in productive areas, or waters affected by eutrophication where primary production is much higher, in the tens to hundreds of µg/L of chlorophyll a.

- Second observation concerns the optical filters: after several hours of continuous experiments using filter 2 optical port, which is indicated Figure 6.12, we observed that the optical properties of the filter were severely impacted. This is attributed to the photodegradation of the ink when exposed to blue light, similarly to the fade of ink on paper when exposed to sunlight. While stability of such filters was evaluated by Llobera et al.[192], it was evaluated against diffusion phenomenon that occurs with other dyes like Sudan II, and not against photobleaching under blue light exposure. This effect was not quantified and could

be mitigated by LED modulation and limiting the excitation intensity, as the final system is meant to be used in-situ, we choose to discard the dyed PDMS filters for the excitation light. Experiments with Roscolux filters shown no degradation in similar conditions, as their construction is more robust.

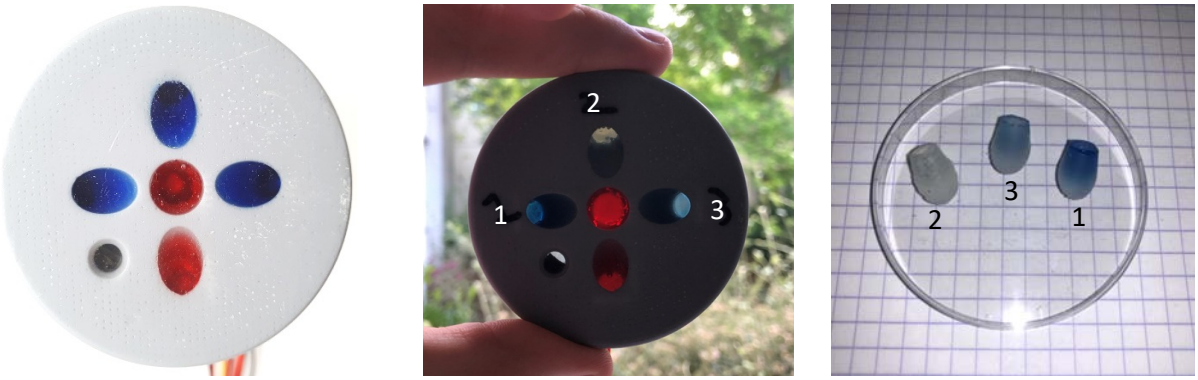

Figure 6.12 Left: Chlorophyll a fluorometer first generation prototype sensor head after fabrication, with PDMS dyed blue and red filters. Center and Right: illustration of the degradation of the Pelikan Blue dyed PDMS filters after prolonged exposition to blue LED excitation. The three filters were fabricated within the same batch, but have been exposed during different times to excitation light. Degradation of the filters is correlated with the exposure time, filter 1 being the less exposed and filter 2 the most exposed. Pelikan Red dyed PDMS filters do not exhibit visible degradation, as they are not directly exposed with high intensity blue light.

Atop of these experimental observations, ams company emitted and "End Of Life" notification for several optoelectronic components including the TSL257 in May 2021, announcing the last shipment of these components by the end of July 2022, with no replacement announced. While we could have improved the sensitivity by adding another amplification stage and a higher resolution ADC, we decided to develop a second-generation prototype based on up-to-date components in order to ensure that the developed sensor could be replicated and maintained for a long period of time, while improving the sensitivity as well.

6.3.2 Second-generation prototype

For the second-generation prototype, our objectives consisted mostly in improving the sensitivity of the sensor to reach our requirements of 0.1µg/L, (ii) update the component selection and avoid any obsolete components. Based on the issue with photodegradation of the PDMS dyed filters, Roscolux #19 Fire and#384 Midnight Blue filters were favored.

Experiments conducted with the first prototype showed that the photocurrent at typical chlorophyll a concentration was very low, in the fA range for µg/L levels. All silicon photodiode shows similar responsivity, approximately 0.4 A/W at 685nm, hence one way of increasing the photocurrent while keeping this sensor technology is to increase the surface of the photodiode. The TSL257 has a circular photodiode with a 0.75mm diameter, corresponding to a surface area of 1.76mm^2. A Thorlabs FDS100 photodiode was chosen as a replacement: with a 13mm^2 active area, it is more than seven times larger than the TSL257's detector, and was successfully used for chlorophyll fluorescence detection [190].

In order to implement ambient light rejection, we used a synchronous detection scheme similar to Orozco [196] which is presented Figure 6.13. The first stage is the transimpedance amplifier which converts the photocurrent generated by the photodiode (caused by fluorescence) to a voltage. The fluorescence as a similar waveform as the excitation signal, which is square wave at about 4kHz, generated by the Adafruit Feather M0 microcontroller with timer interrupts, referred as STROBE on the schematic. The photodiode is biased with a

1.6V voltage reference source, which corresponds to mid-rail voltage as the whole circuit is powered at 3.3V. The gain of the TIA is set the resistor R_f in the feedback loop, while a capacitor C_f stabilize the circuit. For the TIA amplifier, the MAX9636 was selected due to its high bandwidth and very low bias current of 0.1pA. This characteristic is important as every current coming from the photodiode that does not go into the feedback loop will result in a measurement error. After the first amplification stage, a square signal is obtained: the "low" state is when STROBE signal is off, i.e. when the excitation LED is off, so the output corresponds to the ambient light contribution only. The "high" state is when STROBE is on, i.e. when the excitation LED is ON, so the output is the sum of the fluorescence signal plus the ambient light. The ambient light can be seen as the DC (Direct Current) part of the signal, while the fluorescence is the AC (Alternative Current) part of the signal. The second stage works as an AC coupler. The high-pass filter formed by C2 and R1 as a 7.2Hz cut-off frequency, which removes any output offset voltage and attenuates low frequency light pollution. The filtered signal is biased at 1.6V by V_{ref}. The signal is then fed into the third stage, which is basically a programmable +1/-1 amplifier is driven by the STROBE signal. When the excitation LED is on (i.e. STROBE=ON), gain is +1, while when it's off (i.e. STROBE=OFF) gain is -1. This is achieved by combining ADG736 analog switches, with a INA152 difference amplifier. After this stage the signal is a DC voltage which value is the difference between fluorescence signal and ambient light. This DC voltage is finally low-pass filtered by R_6C_4 with a cut-off frequency of 16Hz. In the frequency domain, the action of stages 3 and 4 is similar to a bandpass filter around the STROBE frequency. For a 4kHz STROBE signal, it means detection is active for signal between 3.984kHz and 4.016kHz. The output V_{fluo} is finally sampled by a Ti ADS1115 16 bits ADC setup in differential mode with the V_{ref} voltage.

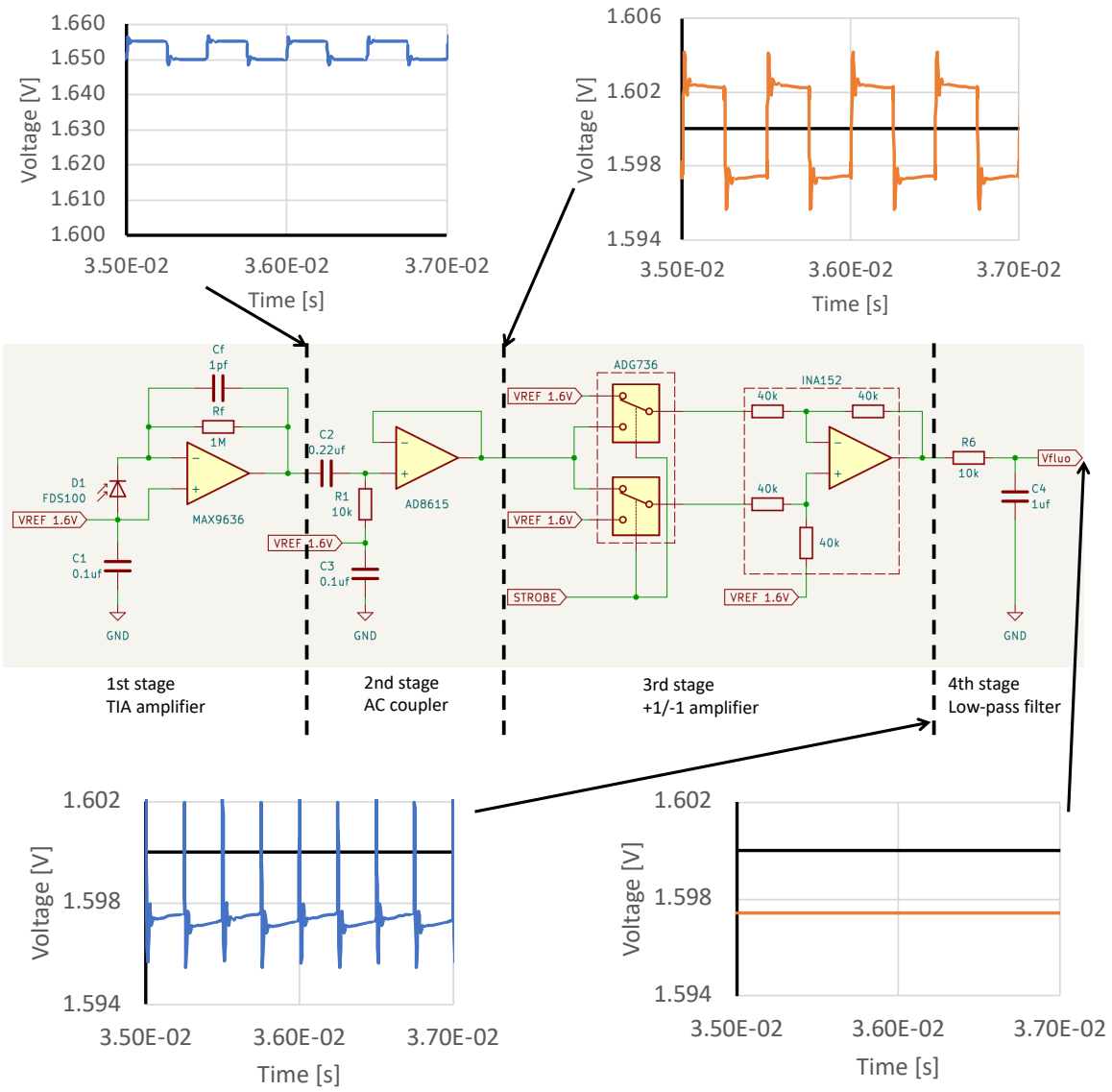

Figure 6.13 Synchronous detection circuit for ambient light rejection, based on the architecture proposed b Orozco [184]. Signals obtained by LTspice simulation at the output of each stage are presented to illustrate the behavior of each block. Black line on the x-axis represents the 1.6V voltage Vref.

LTspice simulations were performed with this architecture to verify the behavior of the circuit, verify the stability of the transimpedance amplifier, and the values for the RC filters. For the simulation, the photodiode was replaced with a current generator driven at the STROBE frequency, with a DC value of 50 nA (ambient light contribution), and an AC value of 5nA for the fluorescence signal.

For the excitation light, a Texas Instrument LM36011 LED driver was selected, coupled with a Thorlabs LED465E LED, in the standard 5mm through hole format. This LED was chosen in place of the LXML Royal Blue used in the first prototype in order to be able to use only one PCB: the first-generation system was using two distinct PCBs (one for the LED, one for the photodetector), which were then connected to an interface board and then to the Adafruit Feather M0 microcontroller. For the second-generation prototype, we choose to integrate everything on a single PCB, and use through hole LED and photodiode which can be easily bent to the 45° angle sensing position, in order to make the whole system easier to fabricate,

and limit the connector, cables and interfaces which are usually a weak point in low-cost systems.

The LM36011 LED driver is externally triggered by the STROBE signal issued from the Adafruit Feather M0 microcontroller, with an intensity which is digitally programmed using the I2C communication bus.

We then proceed to the design and fabrication of a PCB to build and evaluate the circuit. PCB design was done with Kicad 7.0, 2-layer PCBs were manufactured by AISLER Gmbh, and the final prototypes were assembled in-house with a reflow oven.

6.4 Fluorescein experiments

Calibration with chlorophyll a extracts from spinach leaves proved to be an accessible way of testing the first-generation prototype. However, as highlighted by Earp et al. [170], it is normally used on benchtop fluorometers where extraction methods in solvent are performed on the collected samples prior to analysis[197]. In the case of in situ fluorometers, alternatives are preferred as absorbance by in vivo chlorophyll a is shifted by 8 to 10nm toward the red compared to chlorophyll extracts. In their recommendations, Earp et al. compared several fluorescent dyes, and conclude that fluorescein was the most suitable liquid standard for chlorophyll a fluorometer calibration. For the calibration of the second-generation prototype, we moved on to this method. Fluorescein sodium salt (Sigma Aldrich) was purchased, as it is readily soluble in water. A stock solution at 16.6 mg/L was prepared in deionized water. The sensor was immersed in a large beaker containing 800mL of deionized water, and then small volumes of the Fluorescein stock solution were added sequentially using a micropipette. The solution was mixed after each addition of stock solution to ensure homogeneity of the sample, which was confirmed as well by the stability of the sensor output.

The sensor itself was immersed in the beaker, without protection from external light sources (fluorescent tubes and indirect sunlight) to validate the ambient light rejection feature. Each data point was averaged over 20 ADC acquisition. The ADS1115 16 bits ADC was set at a 128 sample per second rate, so acquisition time was 156ms per data point. The ADC possess an internal Programmable Gain Amplifier (PGA) which was set to gain four.

The LM36011 LED driver Flash Brightness Register was set to 0x01, corresponding to an excitation LED current of 22.7mA, and a higher value of current was also tested to ensure that increasing current was increasing the fluorescence output as expected.

Chlorophyll-a

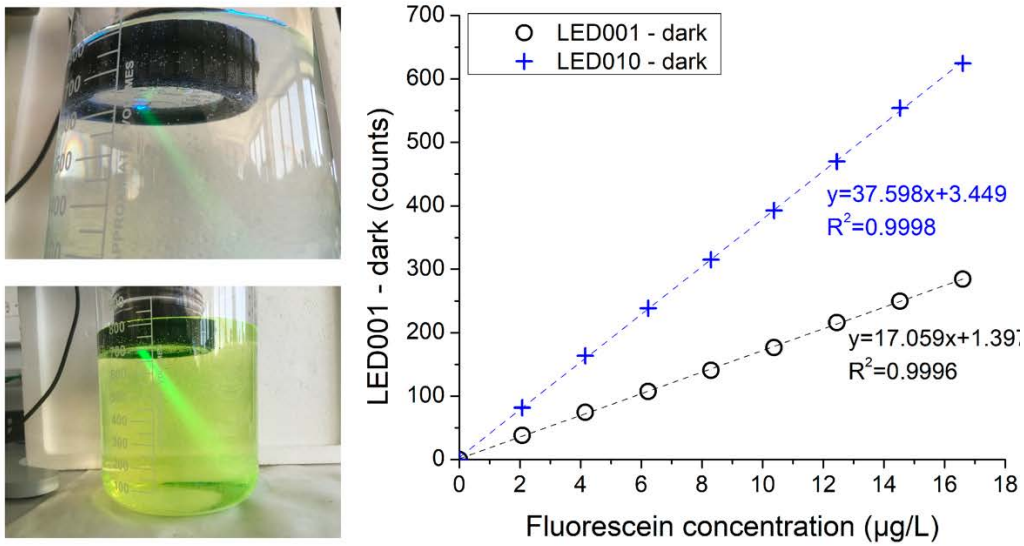

Figure 6.14 Left: photos of the second-generation prototype immersed in a beaker containing 800mL of deionized water. Upper left picture shows the fluorescence of the Fluorescein at a small concentration (2.075µg/L), while the lower left photo shows a highly concentrated solution (16.6 µg/L). Right: ADC counts for increasing Fluorescein concentration at two excitation currents. Each data point is obtained from the average of 20 ADC samples. Each dataset is dark corrected, meaning that the measured ADC output in absence of chlorophyll a in the solution is used as the reference level

Results are presented Figure 6.14. It can be observed that even at a low current (22.7mA, smallest setting available on the LM36011 LED driver), a sensitivity of 17 counts per µg/L of Fluorescein is obtained. This sensitivity increased to 37 counts per µg/L with a higher current. As the output of our system is a DC voltage, is can easily be averaged over a large number of measurements. In this test, averaging over 20 samples already allows to obtain a noise level of 1 LSB, which is very promising. These results were obtained with a PGA gain of the ADC set to 4. We performed additional experiments with the same protocol to ensure that increasing the PGA gain would linearly increase the sensitivity. The results are presented Figure 6.15, where once again each data point is obtained from the average of 20 consecutive ADC samples. The slope of the linear fit gives the sensitivity of the sensor in counts per µg/L for each PGA settings; it can be observed that doubling the gain doubles the sensitivity as expected.

Chlorophyll-a

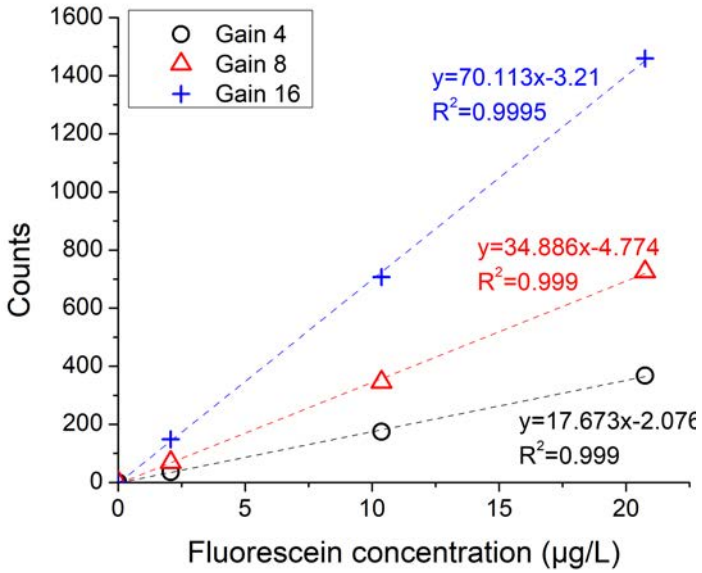

Figure 6.15 Averaged counts (over 20 ADC samples) obtained for 3 concentrations of Fluorescein with three ADC ADS1115 PGA gain of 4, 8 and 16. It can be observed from the slope that sensitivity increase is linear. All the settings were kept similar to the previous experiment, i.e. 22.7mA LED excitation.

Last experiment consisted in setting the PGA to 16 (maximum value), and increasing the LED excitation, however the results did not give the expected behavior, as the fluorescence intensity in counts was not increasing linearly with the excitation current as it should. The reason was a misunderstanding of the LM36011 datasheet: it is mention in its characteristics that is has a step-up DC-DC converter, so we initially thought that the driver was able to generate a voltage higher than its power supply to obtain the programmed current output. However, we found out that it was not the case, and that the maximum voltage applicable to the LED was in fact limited by V_{supply} (3.3V in our case). While not an issue for most of the red and green LEDs which possess a forward voltage of 2 to 3V, some blue LEDs do require a higher forward voltage to operate, especially at high current. This issue was not encountered in our previous experiments where the LM36011 driver was used with the LXML Royal blue LEDs, as these LEDs require a relatively low forward voltage for blue LEDs (between 2.5 to 3.1V). The LED465E forward voltage is typically 3.2V at 20mA, hence the headroom is very small with a 3.3V power supply. As we discovered this issue only toward the end of this study, we were not able to conduct additional experiments to study the LED current excitation limit on the sensitivity. While the Thorlabs LED465E maximum current is 50mA (probably in continuous excitation as it is not specified in the datasheet), the LXML Royal Blue used in the first prototype is able to handle up to 350mA, corresponding to a 500mW light output vs the 20mW light output of the LED465E.

It should however be noted that at the maximum current achievable by the LM36011 LED driver, a sensitivity of 150 counts per µg/L was obtained (PGA gain 16), with a noise level still within 1 LSB, in ambient light conditions. While no direct scaling factors exists to extrapolate the sensitivity of the sensor from Fluorescein to Chlorohyll a, as it depends on several parameters including the optical filters characteristics, WetLabs Eco FL fluorometers uses a scaling factor of 6 to convert from fluorescein to chlorophyll a concentrations (i.e. the sensitivity for chlorophyll a should be 6 times higher than for Fluorescein), which indicates that our prototype should perform adequately even in chl. a concentrations in the µg/L range.

6.5 Conclusion

The second-generation managed to solve the issues we initially encountered with the first prototype. The sensitivity was vastly improved, with up to 150 counts per µg/L of Fluorescein, with efficient ambient light rejection. This sensitivity could be further increased if needed, as all the results were obtained with a TIA gain of R_f = 1MΩ. LTspice simulations were performed and showed that this gain value could be increased up to 100MΩ, while paying attention to adjusting the C_f capacitor in the feedback loop to keep the circuit stable. This gain increase would however limit the ambient light levels that the system can withstand before saturation, hence a compromise shall be made between sensitivity and ambient light tolerance. Most of the commercial fluorometers uses a programmable gain amplifier, hence this could be an additional feature to further improve the current prototype. Some of them also uses an opaque sleeve around the sensor that limits direct sunlight, a solution that could be used in areas where productivity is low (low concentration levels of chlorophyll a), but ambient light levels are high.

Chapter 7 Complete integration: toward a low-cost multiparameter sonde

7.1 Introduction

During the previous chapters, we presented the development of each sensor of the multiparameter sonde as individual units. This approach was favored as it allowed to speed-up the prototyping phase, compared to the design and realization of a new complete system at each development phase. It was also easier for testing purposes, minimizing the volume of reactants and the overall sample volume. While some sensors where more challenging than others, initial objectives in terms of performance were met in laboratory conditions. As the main objective of the project was to demonstrate the feasibility to build a complete multiparameter probe for a fraction of the cost of commercial systems, while providing sufficient performance to generate scientific quality data, we tried during the last part of this PhD to combine all the developed sensors into a single system. While the complete system could not be fully tested due to a lack of time, it is based on the same architectures that were validated in the previous chapters, hence it should at least perform equally well, if not better as we took the opportunity to update a few components.

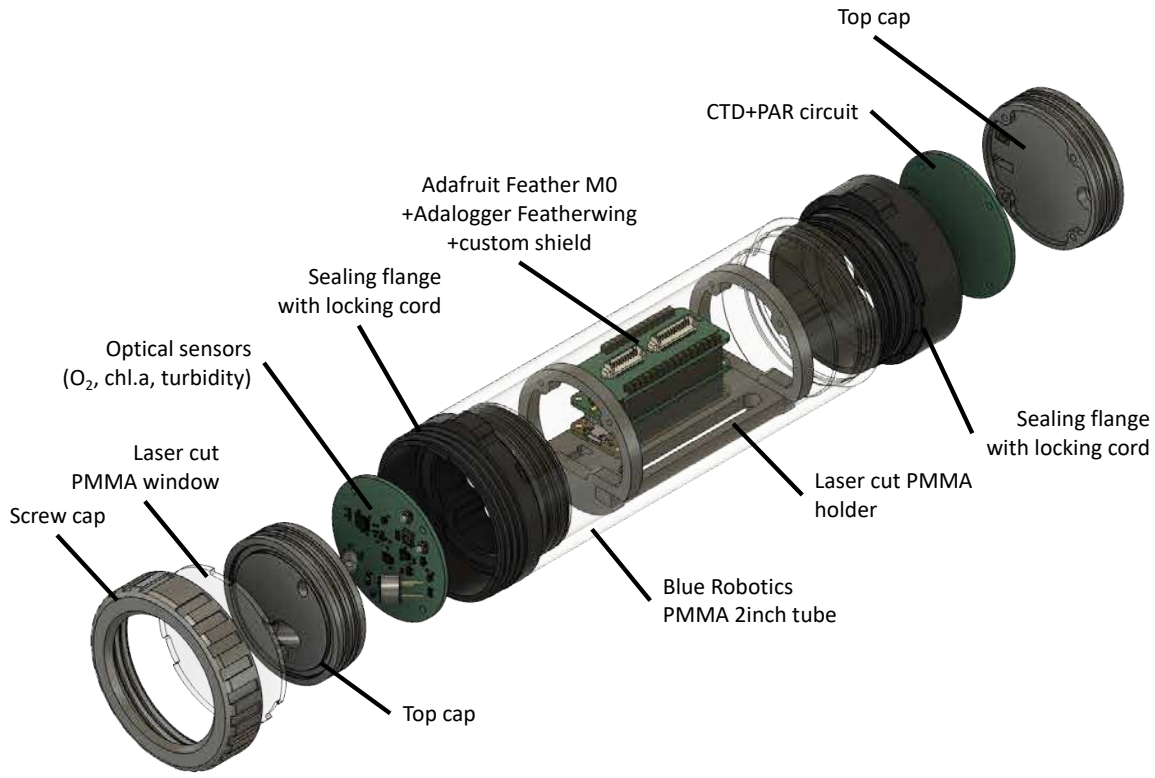

Figure 7.1 - Exploded view of the complete multiparameter probe based on the Blue Robotics 2inch enclosure standard

7.2 Description of the complete multiparameter probe

For the complete system, the design was made to be compatible around the Blue Robotics 2 inches watertight enclosure acrylic tubes, in their cylindrical locking series, as these tubes are easily sourced, relatively cheap (around 20 to 30 €), and able to withstand depths of up to 250m, which is well above the 100m depth target of the project. Cheaper alternatives do

exist, like the PVC fittings used in the OpenCTD project[198], their pressure resistance is lower, and their mechanical tolerances vary greatly from one manufacturer to the other, with sometimes cylindricity issues which cause leakage and damage to the electronics. The architecture is based on two main custom PCB boards: the one which is facing up contains the CTD (conductivity, temperature, depth/pressure) and the PAR sensor, while the second facing down contains the chlorophyll a, oxygen optode and turbidity sensor. As one of the objectives is to collect continuous in-situ data, all of the optical sensors of the final prototype have been integrated into a "flat-face" design, to make it compatible with the use of an external wiper that ensures that no biofouling will grow on the optical ports.

Figure 7.1 presents the CAD view of the complete system, which is going to be described in details within the next sections of this chapter.

7.3 Electronic integration

The aim of the OpenProbe project was to develop a low-cost multiparameter sonde with an open-source, open-hardware philosophy, in order to facilitate the replication of the sonde and its appropriation by the scientific community, but also through citizen science projects, as such we put emphasis on using off-the-shelf components or fabrication techniques whenever possible. This was notably the case for the choice of the microcontroller, where an Arduino compatible model was selected, as this greatly facilitates the software development process due to the numerous libraries available.

7.3.1 Controller and datalogger

At the heart of the system is a controller, which is in charge of driving all the sensors as well as the peripherals like the datalogger, the data transmission, while also controlling the energy. Many different references are able to handle these various tasks. Single-board-computers like the Raspberry Pi are commonly encountered in academic work[199], [200], however their power consumption is very high, and they are only suited to specific projects where computing power, or dealing with video or audio data is required. In our case microcontrollers are a better match. Since the advent of the Arduino UNO in 2010, a lot of user-friendly microcontrollers are now available, like STM32, ESP32, ESP8266. Due to its ubiquity on this market, we decided to use an Arduino compatible microcontroller: the Adafruit Feather M0, which is based on a low-power ATSAMD21G18 ARM cortex M0 processor clocked at 48 MHz and 3.3V logic, is compatible with any 3.7V Lithium polymer battery, offers SPI, I2C and UART communication, includes a 12-bits Analog to Digital Converter (ADC) and 10-bits Digital to Analog Converter (DAC). This microcontroller is available in different versions with wireless communication capabilities (BLE, LoRa, WiFi) with the same form-factor, which allows to select the most appropriate communication standard based on the user needs, and has already proved to be appropriate for environmental sensing platforms [198], [201]. Depending on the needs, we used either the RFM95 LoRa version, which allows long-range wireless transmission data, or the Bluefruit LE version (nRF51822 chipset for Bluetooth Low Energy communications) that allows easy short-distance communication with a smartphone or a laptop for example.

Functions can easily be added in the form of add-on boards, also referred as shields: for the data acquisition we use the Adafruit Adalogger FeatherWing which integrates a PCF8523 real time clock (RTC) and a microSD memory card socket to handle datalogging functions, i.e.

timestamping and data recording as text files, and as it is of low-power energy consumption it can last several days with continuous recording. Sampling rate is software defined and adapted to the use-case. For example, in a profiling application, a fast-sampling rate (1 Hz, i.e 1 complete acquisition per second) will be chosen, while for stationary observation the sampling rate will be slower (1 acquisition per hour or less typ.), as most parameters considered have rather slow dynamic temporal scales. A simple shield, stacked above the Adalogger FeatherWing, has been developed for the complete system, with the only function of proving appropriate connectors to connect the two sensor PCBs presented Figure 7.2.

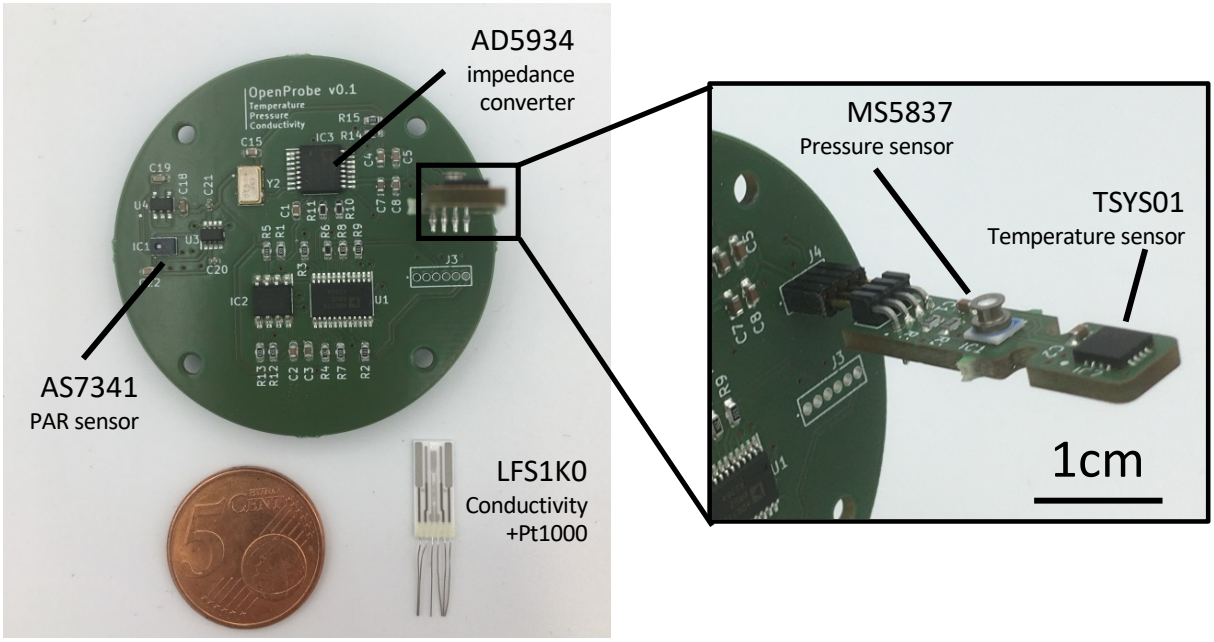

Figure 7.2 - CTD and PAR PCB. External diameter of the circuit is 50mm. Close-up view of the MS5837 pressure sensor and TSYS01 temperature sensor, prior to potting in thermally conductive epoxy. The connector interface between the LFS1K0 conductivity sensor and the J3 position on the main PCB is not present on the picture. At the back of the PCB is the connector to the microcontroller shield

7.3.2 CTD and PAR integrated circuit

The CTD and the PAR sensor are integrated at the top of the multiparameter probe. For the PAR sensor, this is directly due to its operating principle: as its role is to collect the downwelling irradiance, it has to face the sun to collect the radiation. For the CTD, the orientation is not critical, however as the bottom circuit of the multiparameter probe is densely populated by many components, it was decided to position it at the top, similarly to the Argo SOLO-II float for example. The electronic architecture is similar to the one presented in the CTD and PAR chapter. A picture of the PCB is presented Figure 7.2, where it can be observed that both the temperature-pressure sensor and the conductivity sensor are present as separate boards that connect vertically to the main PCB. This choice has been made over a complete planar integration for several reasons:

- The TSYS01 temperature sensor response time is directly related to the thermal inertia of its support. As almost all variables measured by the multiparameter probe requires temperature compensation, it is important to ensure that this response time is reasonably fast to guarantee proper compensation, especially during profiling. Integrating the temperature sensor on the main PCB would imply to do cut-outs to limit thermal diffusion and inertia, and would also require to completely cover the PCB with conductive epoxy, thus making any repair of the board almost impossible.

- The MS5837 pressure sensor is protected by a white silicone gel which makes it able to work underwater. While not described in scientific articles that uses this sensor, it has been observed than under certain conditions, this gel can be degraded by prolonged immersion in seawater (> 6 months) [202], hence it appeared to make sense mounting it on a removable PCB for better repairability
- The IST LFS1K0 conductivity sensor, while offering great performance, has doubled in price within a year (from 20 € to more than 40€), so it was decided to mount it as a replaceable component to allow for an evolution of the multiparameter probe. We did a few experiments on simple graphite electrodes (pencil rods) potted in epoxy with promising results, that could offer a cheaper alternative to the LFS1K0, however further investigation is required as this type of sensor is highly sensitive to temperature, as the difference in thermal expansion of the different materials directly affect the cell constant, hence the conductivity measurement

The marinization of the PCB and PAR sensor is achieved by a combination of 3D printing parts, O-rings, PDMS molding and thermally conductive, electrically insulating epoxy coating for the temperature and pressure sensors. As for all the mechanical designs of this manuscript, CAD was done with Autodesk Fusion360 software, and printed with standard Black Resin V4 with a stereolithography (SLA) Formlabs Form 3 3D printer, and the Preform software. For parts intended to be overmoulded with PDMS, a special thermal treatment was conducted following the recommendations of Venzac et al. to avoid the polymerization inhibition effect [203]. It is the case of the Top cap part of Figure 7.3, that presents the complete assembly.

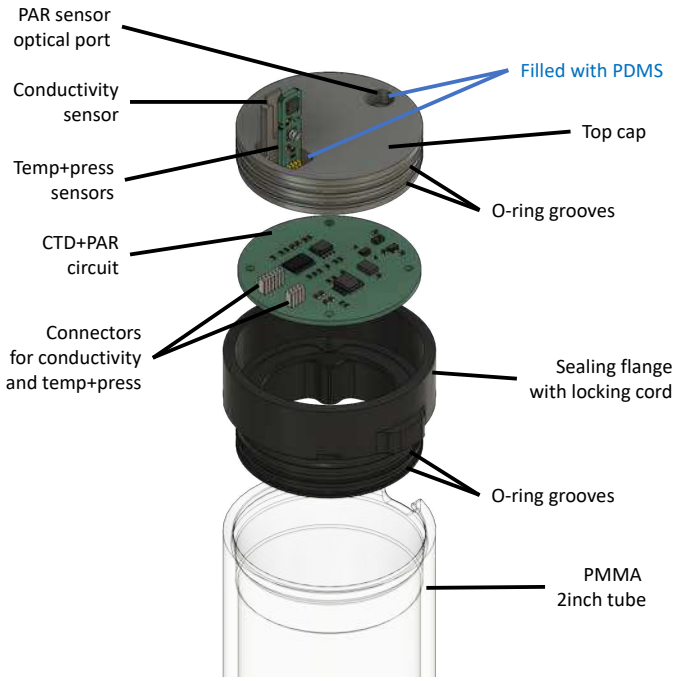

Figure 7.3 - Exploded view describing the assembly of the CTD+PAR sensor for marinization with a Blue Robotics compatible design.

As previously mentioned, this design is compatible with the Blue Robotics 2inch watertight enclosures. Watertightness of the assembly is achieved by the use of O-rings, two on the top cap, and two on the sealing flange. All the O-rings are identical (AS568-030, Buna-N material in 70A hardness), and are the same reference as the one used by Blue Robotics to facilitate maintenance.

7.3.3 Chlorophyll a, dissolved oxygen and turbidity integrated circuit

The chlorophyll a fluorometer, oxygen optode and turbidity sensors are located at the bottom of the multiparameter sonde, and integrated on a single PCB which shares the same dimensions as the CTD+PAR PCB, that is 50mm in diameter. The position of these optical sensor is important, especially the chlorophyll a fluorometer and the oxygen optode, as both are operating in the visible range to excite and collect the fluorescence signals, hence they are impacted by ambient light caused by the solar radiation. While they both include some ambient light rejection mechanisms, based on light modulation and synchronous detection, when the ambient light levels are too high, the photodetector (or more accurately the voltage output of the TIA which amplifies the photocurrent collected by the photodiode) can saturate. Positioning these sensors at the bottom of the probe efficiently limits the amount of sunlight reaching the photodetectors, especially in the red wavelengths as these are rapidly attenuated by absorption in the water as shown in the PAR chapter. In use-cases where the deployment is done in shallow, transparent water with high sunlight levels, a sleeve could be added around the sensor to further limit the amount of direct light reaching the sensors, a common practice for commercial multiparameter probes[204].

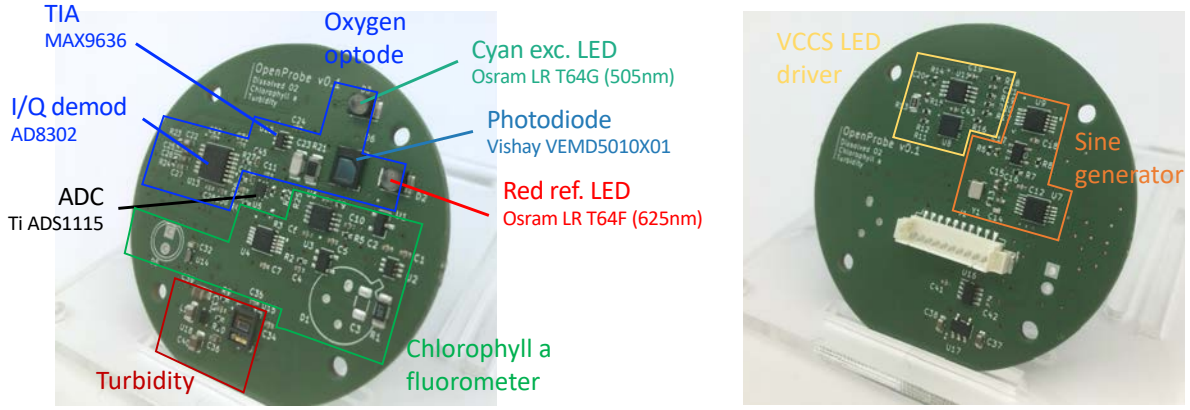

Figure 7.4 - Left: top copper of the optical sensors PCB, with the footprint of each sensor outlined in color. The excitation LED and the photodiode of the chlorophyll a fluorometer are not soldered on the picture (position D5 and D1) respectively. Right: bottom copper, showing the Voltage Controlled Current Source (VCCS) LED driver, which is based on a Howland source, and the sine generator used by the oxygen optode.

Figure 7.4 presents both sides of the PCB populated with all the components, minus the LED and photodiode of the chlorophyll a fluorometer which are the only through-hole components. This choice was made to facilitate the nephelometric configuration (i.e. 90° angle between light source and detector), which is the most common setup in fluorometers, as the pins of both components are simply bent to obtain the desired angle, while SMD components would require individual PCBs and thus additional connectors, a major source of failure in such systems. The precise positioning of these two components is guaranteed by the 3D printed enclosure shown Figure 7.5.

In terms of electronic design, the complete prototype is based on the same architecture as presented in the previous chapters, but some components were updated to more recent part numbers, or to match similar components on the board in order to limit the overall number of parts. For example, the TIA used in the oxygen optode chapter was replaced by a MAX9636, a reference which is also used as the TIA for the chlorophyll a fluorometer.

Each sensor componentry is outlined on Figure 7.4, giving an idea of the overall footprint required. The oxygen optode occupies the largest footprint, notably due to the AD9833 sine generator which is combined with a AD5243 dual digital potentiometer for offset and amplitude adjustment, and a Voltage Controlled Current Source (VCCS) LED driver in the form of a Howland source paired with a MAX4932 analog switch that select the LED output (excitation cyan LED or reference red LED). For the chlorophyll a fluorometer, the Thorlabs FDS100 (marked D1 on the PCB, not present on the picture) occupies a large footprint, but is required to ensure sufficient sensitivity as highlighted in the dedicated chapter.

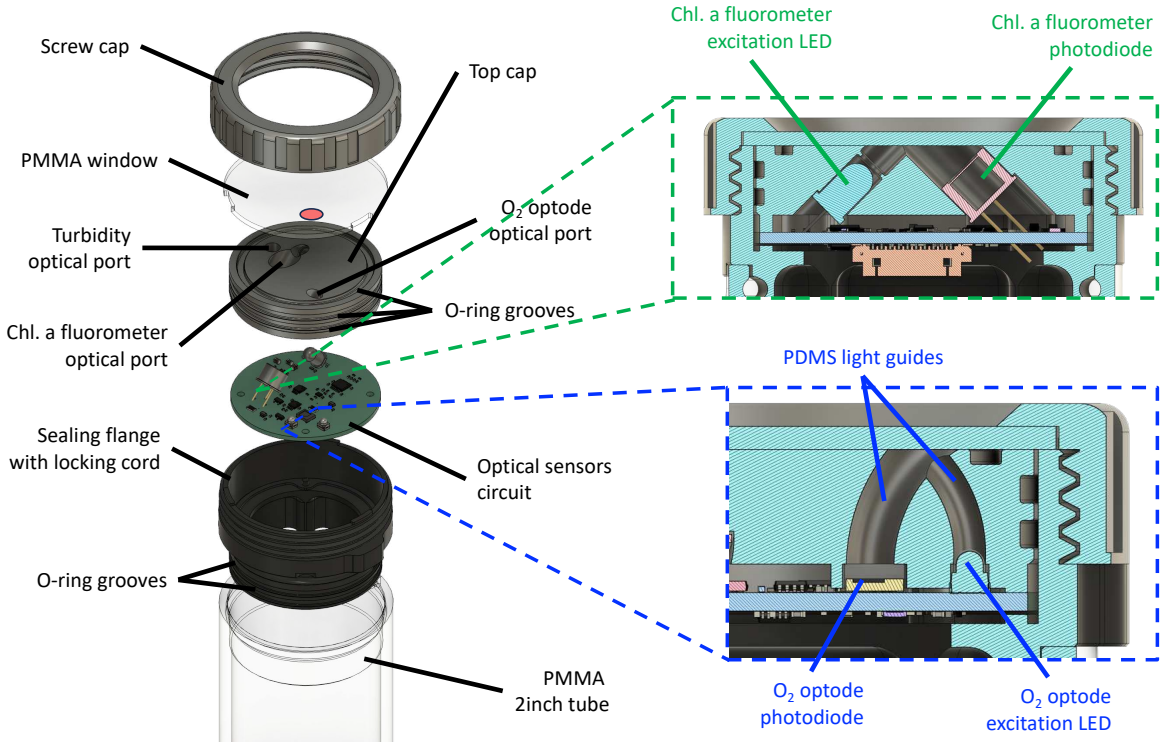

Figure 7.5 – Left: Exploded view describing the assembly of the chlorophyll a fluorometer, oxygen optode and turbidity sensors for marinization with a Blue Robotics compatible design. The oxygen optode Presens Pst3 sensor spot is simply glued on top of the PMMA window to be in contact with the water (materialized with a red circle on the picture), the alignment being done by laser engraving its position on the window. A screw cap presses the whole assembly, ensuring proper compression of the upper O-ring located between the top cap and the PMMA window. Upper right: cutout view of the chlorophyll a fluorometer, showing the 90° nephelometric arrangement between the excitation LED and the photodiode which is achieved by the 2D printed top cap. Lower right: cutout view of the O_2 optode, highlighting the PDMS light guides.

7.3.4 Cost breakdown

The initial objective of the OpenProbe project was to develop a complete multiparameter probe with a cost in materials of 100 €, in response to the very high cost of commercial probes which is greater than 15 k€ for the same parameters. While the comparison is not completely fair, as it compares a cost in material and a selling price, the main objective was to propose an alternative especially for the academics, and citizen science project, with a probe that could be replicated with simple equipments. It was observed that for citizen science projects, a cost in the range of 1000 € for an equipment is already high, and will limit the possibilities especially in developing countries. Our target cost objective of 100 € would drastically increase the diffusion of such a tool. Hereafter, we tried to provide an honest estimate by describing the cost breakdown for a single unit of the complete prototype.

Table 3 - Cost breakdown of the complete integrated prototype. Price is given excluding taxes, per unit.

Description	Price (per unit)	Manufacturer	Remarks
2-layer PCB	7.43 €	Aisler Gmbh	
Chl. a components	37.73 €	Mouser, Thorlabs	Most expensive component: Thorlabs photodiode FDS100 (7.21€)
O2 optode components	55.16 €	Mouser	Most expensive components: AD8302 (27.04€), AD9833 (9.66€)
Turbidity components	15.377 €	Mouser	
Passive components	5.82 €	Mouser	Including connectors
Sub-total	**111.81 €**		
2-layer PCB	7.43 €	Aisler Gmbh	
Conductivity components	73.45 €	Mouser	Most expensive components: IST LFS1K0 electrodes (38.50 €) and AD5934 impedance analyzer (22.17 €)
Temperature components	6.08 €	Mouser	
Pressure components	10.96 €	Mouser	
PAR components	8.52 €	Mouser	
Passive components	6.28 €	Mouser	Including connectors
Sub-total	**105.87**		
Adafruit Feather M0 BLE	27.85 €	Mouser	Bluetooth Low Energy version
Adafruit Adalogger Featherwing	13.32 €	Mouser	Including CR1220 battery and microSD card
LiPo battery RS PRO	22.33 €	RS	3.7V 2000mAh capacity
Sub-total	**63.5 €**		
Blue Robotics 2inch tube	19.80 €	Syera	
Formlabs Black V4 resin	15.55 €	Formlabs	Total volume required 120mL including supports (resin is 129.60 € per liter)
PMMA and Roscolux optical filters	5 €	RS, Edmund Optics	
Sub-total	**40.35 €**		
Total	**321.53 €**		

It should be noted that building in quantities would rapidly decrease the cost, especially for the electronic parts and PCBs, as ordering in 1000 quantities would decrease the total cost by 50% approximately, near the 100 € initial target. Savings could also be made individually on several expensive components, especially the IST LF1K0 conductivity electrodes which could be replaced by custom-made graphite electrodes potted in epoxy (more than 30 € saving), or replacing the AD8302 I/Q demodulator by a phase shift metering circuit (approx. 25 € savings). Developing a custom board with similar functions to the Adafruit Feather M0 BLE and Adafruit Adalogger Featherwing would also lead to important savings. Finally, a fully 3D printed housing would allow to remove the need for the Blue Robotics 2inch enclosure.

7.4 Conclusion and perspectives

In this thesis we presented the work for the development of a prototype of a portable probe capable of diving to a depth of 100 m at low cost, this probe will provide a quantitative description of the top of the coastal areas, which is essential for scientific research and decision making related to the environment, it is important to note that in this project our probe measures 7 different parameters, not only the most common for oceanographic study known as CTD, which are: conductivity, temperature and pressure, but also the biogeochemical parameters which are: chlorophyll a, turbidity, dissolved oxygen and photosynthetic active radiation. In addition, including the monitoring of biogeochemical parameters will help to understand the biological and chemical processes in the ocean. In short, it is necessary to know the temperature to understand thermal variations in the ocean and their influence on climate, salinity to evaluate ocean circulation and water mass formation, dissolved oxygen in the water which is crucial for marine life, the presence of chlorophyll a for photosynthetic activity, turbidity to measure the amount of suspended particles in the water. Knowing these data will provide a more complete understanding of the ocean and its impact on climate and biodiversity.

As a final prototype we were able to develop a low-cost probe at a final price of 321.53€ in raw material, which is equivalent to approximately 0.35% of the cost of the Argo program. Our probe consists of 3 different PCBs or modules, within these modules are separated the sensors needed for each parameter.

Within the first module are the sensors necessary for data collection of chlorophyll a, dissolved oxygen and turbidity, for chlorophyll a it was decided to use the fluorescence-based method, this method is based on the emission of fluorescent light by chlorophyll a when exposed to light, our device emits an excitation light that is directed towards the sample, chlorophyll a absorbs part of this light and emits fluorescence, the sensor or photodetector registers the intensity of the fluorescence, which is related to the efficiency of photosystem II (PSII) and the photochemical activity, for dissolved oxygen we decided to use the optical method which uses the dynamic luminescence quenching, it basically measures the intensity or time delay of the light emitted by the sensing material when it is excited, this intensity or time delay is proportional to the amount of oxygen in the sample, It was decided to use this method because compared to the Winkler method it can be used in-situ, and compared to the electrochemical method, it is relatively cheaper, finally for turbidity it was decided to use the backscattering method, this method measures the scattered light of the particles that are in the sample, this method is useful for high levels of turbidity, within this first prototype of our probe it was decided to use the backscattering method because of its easy integration, since trying to integrate the GLI-2 method which has a circular geometry where the LEDs and photodiodes are externally connected or trying to integrate the attenuation method where the LED and photodiode are externally connected would require an extra PCB for these methods, besides this PCB gets in the way of the sensors of the other methods.

The second module is the simplest, where only the temperature and pressure sensors are located, for temperature a digital temperature sensor based on a RTD was used and for pressure a piezo-resistive sensor was used, where the pressure cell is deformed when pressure is applied, modifying the resistance of the strain gauges in the cell.

In the third module are the remaining sensors for the data collection of conductivity and photosynthetic active radiation, for conductivity we used the two-electrode conductive method, which is normally used to measure a wide range of conductivity levels, this method excels at

low levels of conductivity, However, by varying some characteristics such as cell cost and frequency, it can be used for high levels of conductivity. It was also decided to use this method because of its easy integration, since the inductive method has a more complex design, is relatively more expensive and has electromagnetic interferences that would alter the other sensors, Finally, for photosynthetic active radiation we used a sensor that is typically used for color detection, this component possesses 11 channels, with 8 of them in the visible range with peak wavelengths responsivity ranging from 415nm to 680nm, which covers the visible range of the electromagnetic spectrum to be measured.

Thanks to the structure of our probe which is divided into several modules, if any type of sensor for a specific parameter is damaged, it can be easily replaced by a new one without the need to replace the entire electronic system, another advantage is that our prototype is open-source and it is not necessary to use expensive and difficult to access equipment for its reproduction and all codes, stl files, Gerber are available in GitLab.

In order to control and obtain the data from these sensors, codes were developed in C language, these codes are compatible with the Arduino IDE, another advantage that our probe has is that, having the sensors in different modules, the code can be easily modified to obtain the data of the 7 parameters, or only the data of the parameter that the user wants. As this code is compatible with the Arduino IDE, it is possible to use different microcontrollers.

Our sonde uses the Feather M0 because has a low-power ATSAMD21G18 ARM cortex M0 processor, clocked at 48 MHz and 3.3V logic, it can work with any 3.7V Lithium polymer batteries as power supply, it is compatible with SPI & I2C communication, includes a 12-bits Analogic-Digital Converter (ADC) and 10-bits Digital-Analogic Converter (DAC). This microcontroller is available in different versions with wireless communication capabilities (BLE, LoRa, WiFi) with the same form-factor, which allows to select the most appropriate communication standard based on the user needs. Depending on our needs, we used either the RFM95 LoRa version, which allows long-range wireless transmission data, or the Bluefruit LE version (nRF51822 chipset for Bluetooth Low Energy communications) that allows easy short-distance communication with a smartphone or a laptop for example. Functions can easily be added in the form of add-on board: for the data acquisition we use the Adafruit Adalogger FeatherWing which integrates a PCF8523 real time clock and a microSD memory card socket to handle datalogging functions, i.e. timestamping and data recording as text files, and as it is of low-power energy consumption it can last several days with continuous data taking. It has the possibility to configure the data taking of each parameter in different time, that is to say to take the data of a parameter every hour, or every 6 hours or every day, the time will depend on the parameter to take, since the time of data taking of each parameter is different.

Although our prototype works as desired and meets the objective of this thesis project, it is important to mention that it has some limitations compared to some commercial probes, for example the case that uses our prototype is designed for a depth of 300m, therefore our sensor cannot be submerged deeper than this depth, compared to the Argo program that can dive to 6000m, our prototype does not have an automatic system to control the up and down movement of the sensor in the water. In addition, our prototype cannot remain underwater for more than a week because biofouling can form on the surface of the sensors, which affects data acquisition.

For future work and although we managed to have the first prototype finished, we need to make the calibration of each sensor and the validation of these in open field, we also plan to

make the second version of this prototype with some improvements, thanks to its structure in modules it is easy to make changes in this prototype, for the second prototype we plan to change the method to measure turbidity from backscattering to nephelometric, In this way our second version would be useful to measure low levels of turbidity, we would add a humidity sensor inside the probe to disconcert and protect the electronic system when detecting water inside it, another addition which would make our probe a little robust, is to add an automatic cleaning system on top of the sensors to be able to combat biofouling.

References

[1] "The Global Ocean Observing System 2030 Strategy-2."

[2] B. M. Sloyan, M. Roughan, and K. Hill, "The Global Ocean Observing System," in *New Frontiers in Operational Oceanography*, GODAE OceanView, 2018. doi: 10.17125/gov2018.ch03.

[3] Global Climate Observing System, "The GCOS Essential Climate Variables (ECVs)".

[4] R. H. Stewart, "Introduction To Physical Oceanography," 1997.

[5] W. Munk, "The Evolution of Physical Oceanography in the Last Hundred Years," *Oceanography*, vol. 15, no. 1, pp. 135–141, 2002, doi: 10.5670/oceanog.2002.45.

[6] "Argo." Accessed: Jan. 17, 2024. [Online]. Available: https://argo.ucsd.edu/about/

[7] HELCOM, "Guidelines for sampling and determination of pH in seawater 1 Background." [Online]. Available: www.eptis.bam.de.

[8] W. Chou, G. Gong, C. Yang, and K. Chuang, "A comparison between field and laboratory pH measurements for seawater on the <scp>E</scp> ast <scp>C</scp> hina <scp>S</scp> ea shelf," *Limnol Oceanogr Methods*, vol. 14, no. 5, pp. 315–322, May 2016, doi: 10.1002/lom3.10091.

[9] J. F. Waters, K. W. Pratt, and R. A. Easley, "A Rigorous Metrological Basis for Seawater pH."

[10] Y. Wang, M. Yang, and C. Wu, "Design and Implementation of a pH Sensor for Micro Solution Based on Nanostructured Ion-Sensitive Field-Effect Transistor," *Sensors*, vol. 20, no. 23, p. 6921, Dec. 2020, doi: 10.3390/s20236921.

[11] A. Porwal, C. Sahu, and N. Shafi, "Proposal, Design, and Performance Investigation of ZnO-Based ISFET pH Sensor," 2024, pp. 441–452. doi: 10.1007/978-981-99-4495-8_34.

[12] T. L. Rosa, A. M. Piecho-Santos, R. Vettor, and C. Guedes Soares, "Review and Prospects for Autonomous Observing Systems in Vessels of Opportunity," *J Mar Sci Eng*, vol. 9, no. 4, p. 366, Mar. 2021, doi: 10.3390/jmse9040366.

[13] Ocean Exploration and Research, "Exploring the Deep Ocean with NOAA Professional Development for Educators of Grades 6-12 Introduction to Water Column Investigations," 2016.

[14] Sea-Bird Scientific, "Types of CTDs Profiling CTDs."

[15] G. C. Johnson, J. M. Toole, and N. G. Larson, "Sensor Corrections for Sea-Bird SBE-41CP and SBE-41 CTDs," *J Atmos Ocean Technol*, vol. 24, no. 6, pp. 1117–1130, Jun. 2007, doi: 10.1175/JTECH2016.1.

[16] S. Hosoda, M. Hirano, T. Hashimukai, S. Asai, and N. Kawakami, "New method of temperature and conductivity sensor calibration with improved efficiency for screening SBE41 CTD on Argo floats," *Prog Earth Planet Sci*, vol. 6, no. 1, Dec. 2019, doi: 10.1186/s40645-019-0310-1.

[17] M. Hirano *et al.*, "SBE41CTD sensor pre-deployment calibration in JAMSTEC."

[18] M. Halverson, E. Siegel, and G. Johnson, "Inductive-Conductivity Cell A Primer on High-Accuracy CTD Technology."

[19] M. Dever *et al.*, "Static and Dynamic Performance of the RBRargo3 CTD," *J Atmos Ocean Technol*, vol. 39, no. 10, pp. 1525–1539, Oct. 2022, doi: 10.1175/JTECH-D-21-0186.1.

[20] M. Halverson *et al.*, "Guidelines for processing RBR CTD profiles Canadian Technical Report of Hydrography and Ocean Sciences 314."

[21] T. S. Light, S. Licht, A. C. Bevilacqua, and K. R. Morash, "The Fundamental Conductivity and Resistivity of Water," *Electrochemical and Solid-State Letters*, vol. 8, no. 1, p. E16, 2005, doi: 10.1149/1.1836121.

[22] R. L. Miller, W. L. Bradford, and N. E. Peters, "Specific Conductance: Theoretical Considerations and Application to Analytical Quality Control."

[23] Richard J. Wagner, Robert W. Boulger, C. J. O. Jr., and Brett A. Smith, "Guidelines and Standard Procedures for Continuous Water-Quality Monitors: Station Operation, Record Computation, and Data Reporting."

[24] Unesco, ICES, SCOR, and IAPSO, "Tenth report of the Joint Panel on Oceanographic Tables and Standards," 1980.

References

[25] Y. Yara, M. Fujii, H. Yamano, and Y. Yamanaka, "Projected coral bleaching in response to future sea surface temperature rises and the uncertainties among climate models," *Hydrobiologia*, vol. 733, no. 1, pp. 19–29, 2014, doi: 10.1007/s10750-014-1838-0.

[26] K. Drushka, S. T. Gille, and J. Sprintall, "The diurnal salinity cycle in the tropics," *J Geophys Res Oceans*, vol. 119, no. 9, pp. 5874–5890, Sep. 2014, doi: 10.1002/2014JC009924.

[27] W. U. Sheng *et al.*, "Investigation of the Performance of an Inductive Seawater Conductivity Sensor," 2015.

[28] A. Paytan, "Lecture 4: Major Ions, Conservative Elements and Dissolved Gases in Seawater."

[29] "EPA. (2012). 5.9 Conductivity." Accessed: Jan. 03, 2024. [Online]. Available: https://archive.epa.gov/water/archive/web/html/vms59.html

[30] Franceska D. Wilde, "TEMPERATURE 6.1".

[31] ROBERT G. WETZEL, *Limnology*. Elsevier, 2001. doi: 10.1016/C2009-0-02112-6.

[32] V. Di Santo and W. A. Bennett, "Effect of rapid temperature change on resting routine metabolic rates of two benthic elasmobranchs," *Fish Physiol Biochem*, vol. 37, no. 4, pp. 929–934, Dec. 2011, doi: 10.1007/s10695-011-9490-3.

[33] J. P. Michaud, "A Citizens' Guide to Understanding and Monitoring Lakes and-Streams," 1991.

[34] W. A. Wurts, "Daily pH Cycle and Ammonia Toxicity."

[35] C. J. Nin and S. Rodgher, "Effect of a temperature rise on metal toxicity for the aquatic biota: a systematic review," *Revista Brasileira de Ciências Ambientais*, vol. 56, no. 4, pp. 710–720, Nov. 2021, doi: 10.5327/Z217694781010.

[36] P. Webb, "Introduction to Oceanography 1.3 Marine Provinces."

[37] B. Delorme and Y. Eddebbar, "Ocean Circulation and Climate: an Overview."

[38] P. Webb, "Introduction to Oceanography 6.2 Temperature."

[39] Heather Allison Broadbent, "Development of a CTD System for Environmental Measurements," 2005.

[40] R. Paradis and S. L. Wood, *Inexpensive Expendable Conductivity Temperature and Depth (CTD) Sensor*. IEEE, 2013.

[41] H. A. Broadbent, S. Z. Ivanov, and D. P. Fries, "A miniature, low cost CTD system for coastal salinity measurements," *Meas Sci Technol*, vol. 18, no. 11, pp. 3295–3302, Nov. 2007, doi: 10.1088/0957-0233/18/11/005.

[42] J. Auråen, "Low-cost CTD Instrument Arduino based CTD for autonomous measurement platform," 2019.

[43] A. Thaler, S. K. Sturdivant, R. Y. Neches, and J. J. Levenson, "A LOW-COST, OPEN-SOURCE CTD FOR COLLECTING BASELINE OCEANOGRAPHIC DATA IN COASTAL WATERS."

[44] L. A. Méndez-Barroso, J. A. Rivas-Márquez, I. Sosa-Tinoco, and A. Robles-Morúa, "Design and implementation of a low-cost multiparameter probe to evaluate the temporal variations of water quality conditions on an estuarine lagoon system," *Environ Monit Assess*, vol. 192, no. 11, p. 710, Nov. 2020, doi: 10.1007/s10661-020-08677-5.

[45] J. H. Lim *et al.*, "Importance of Hydroxide Ion Conductivity Measurement for Alkaline Water Electrolysis Membranes," *Membranes (Basel)*, vol. 12, no. 6, Jun. 2022, doi: 10.3390/membranes12060556.

[46] C. Thirstrup and L. Deleebeeck, "Review on Electrolytic Conductivity Sensors," *IEEE Trans Instrum Meas*, vol. 70, 2021, doi: 10.1109/TIM.2021.3083562.

[47] S. H. Lu, Y. Li, and X. Wang, "Soft, flexible conductivity sensors for ocean salinity monitoring," *J Mater Chem B*, vol. 11, no. 31, pp. 7334–7343, Jun. 2023, doi: 10.1039/d3tb01167d.

[48] H. Ma, Y. Su, and A. Nathan, "Cell constant studies of bipolar and tetrapolar electrode systems for impedance measurement," *Sens Actuators B Chem*, vol. 221, pp. 1264–1270, Dec. 2015, doi: 10.1016/j.snb.2015.07.089.

[49] H. Liquid Analysis, "Conductivity measurement in industrial processes."

[50] W. Olthuis, W. Streekstra, and P. Bergveld, "Theoretical and experimental determination of cell constants of planar-interdigitated electrolyte conductivity sensors."

[51] A. Kaidaorva *et al.*, "Flexible, four-electrode conductivity cell for biologging applications," *Results in Materials*, vol. 1, Aug. 2019, doi: 10.1016/j.rinma.2019.100009.

References

[52] X. Li and G. C. M. Meijer, "A low-cost and accurate interface for four-electrode conductivity sensors," *IEEE Trans Instrum Meas*, vol. 54, no. 6, pp. 2433–2437, Dec. 2005, doi: 10.1109/TIM.2005.858130.

[53] Z. Liao *et al.*, "A Direct-Reading MEMS Conductivity Sensor with a Parallel-Symmetric Four-Electrode Configuration," *Micromachines (Basel)*, vol. 13, no. 7, Jul. 2022, doi: 10.3390/mi13071153.

[54] Z. Moroń and T. Grysiński, "How to measure electrolytic conductivity succesfully," 2015.

[55] M. Le Menn and R. Naïr, "Review of acoustical and optical techniques to measure absolute salinity of seawater," Nov. 28, 2022, *Frontiers Media S.A.* doi: 10.3389/fmars.2022.1031824.

[56] J. Chen, W. Guo, M. Xia, W. Li, and K. Yang, "In situ measurement of seawater salinity with an optical refractometer based on total internal reflection method," *Opt Express*, vol. 26, no. 20, p. 25510, Oct. 2018, doi: 10.1364/oe.26.025510.

[57] L. Gu, X. He, M. Zhang, and H. Lu, "Advances in the Technologies for Marine Salinity Measurement," Dec. 01, 2022, *MDPI*. doi: 10.3390/jmse10122024.

[58] J. Harms and T. A. Kern, "Theory and Modeling of Eddy Current Type Inductive Conductivity Sensors †," *Engineering Proceedings*, vol. 6, no. 1, 2021, doi: 10.3390/I3S2021Dresden-10103.

[59] Endress+Hauser, "Conductivity sensors and transmitters." Accessed: Jan. 23, 2024. [Online]. Available: https://www.endress.com/en/field-instruments-overview/liquid-analysis-product-overview/conductivity-sensors-transmitters?filter.p=3&filter.fb=true&s.category=search-product

[60] R. S. Diarah, C. Osueke, A. Adekunle, S. Adebayo, A. Banji Aaron, and O. Olawale Joshua, "Types of Temperature Sensors," in *Wireless Sensor Networks - Design, Applications and Challenges*, IntechOpen, 2023. doi: 10.5772/intechopen.110648.

[61] J. Wu, "A Basic Guide to Thermocouple Measurements," 2023.

[62] J. Wu, "A Basic Guide to RTD Measurements," 2023.

[63] OMEGA, "Sensor Theory of Operation What Makes Transducers and Load Cells Work?," 2015.

[64] C. Li, F. Cordovilla, and J. L. Ocaña, "The design and analysis of a novel structural piezoresistive pressure sensor for low pressure measurement," *Microsystem Technologies*, vol. 23, no. 12, pp. 5677–5687, Dec. 2017, doi: 10.1007/s00542-017-3427-4.

[65] X. Hu *et al.*, "A Highly Sensitive Deep-Sea Hydrodynamic Pressure Sensor Inspired by Fish Lateral Line," *Biomimetics*, vol. 9, no. 3, p. 190, Mar. 2024, doi: 10.3390/biomimetics9030190.

[66] R. B. Mishra, N. El-Atab, A. M. Hussain, and M. M. Hussain, "Recent Progress on Flexible Capacitive Pressure Sensors: From Design and Materials to Applications," *Adv Mater Technol*, vol. 6, no. 4, Apr. 2021, doi: 10.1002/admt.202001023.

[67] C. Rada and C. Schoof, "Subglacial drainage characterization from eight years of continuous borehole data on a small glacier in the Yukon Territory, Canada", doi: 10.5194/tc-2017-270.

[68] J. W. Lauer, P. Klinger, S. O'Shea, and S. Y. Lee, "Development and validation of an open-source four-pole electrical conductivity, temperature, depth sensor for in situ water quality monitoring in an estuary," *Environ Monit Assess*, vol. 195, no. 1, Jan. 2023, doi: 10.1007/s10661-022-10493-y.

[69] E. Poulsen, M. Eggertsen, E. H. Jepsen, C. Melvad, and S. Rysgaard, "Lightweight drone-deployed autonomous ocean profiler for repeated measurements in hazardous areas-Example from glacier fronts in NE Greenland Specifications table," 2022, doi: 10.17632/zdvb5hzv2x.1.

[70] "MS5837-30BA Ultra-small, gel-filled pressure sensor with stainless steel cap."

[71] T. Matos, C. L. Faria, M. S. Martins, R. Henriques, P. A. Gomes, and L. M. Goncalves, "Development of a cost-effective optical sensor for continuous monitoring of turbidity and suspended particulate matter in marine environment," *Sensors (Switzerland)*, vol. 19, no. 20, Oct. 2019, doi: 10.3390/s19204439.

[72] T. P. Lambrou, C. G. Panayiotou, and C. C. Anastasiou, "A low-cost system for real time monitoring and assessment of potable water quality at consumer sites," in *Proceedings of IEEE Sensors*, 2012. doi: 10.1109/ICSENS.2012.6411190.

[73] J. Trevathan, W. Read, and A. Sattar, "Implementation and Calibration of an IoT Light Attenuation Turbidity Sensor _ Elsevier Enhanced Reader," *Internet Things*, vol. 19, Aug. 2022, doi: 10.1016/j.iot.2022.100576.

References

[74] J. Trevathan, W. Read, and S. Schmidtke, "Towards the development of an affordable and practical light attenuation turbidity sensor for remote near real-time aquatic monitoring," *Sensors (Switzerland)*, vol. 20, no. 7, Apr. 2020, doi: 10.3390/s20071993.

[75] J. Trevathan and R. Johnstone, "Smart Environmental Monitoring and Assessment Technologies (SEMAT)—A New Paradigm for Low-Cost, Remote Aquatic Environmental Monitoring," *Sensors*, vol. 18, no. 7, p. 2248, Jul. 2018, doi: 10.3390/s18072248.

[76] M. Sadar, "Turbidimeter Instrument Comparison: Low-level Sample Measurements Technical Information Series."

[77] "EPA Guidance Manual".

[78] B. Gareth and B. Kitchener, "Reinterpreting turbidity: new methodologies for suspended-sediment research," 2019.

[79] A. F. Bin Omar and M. Z. Bin MatJafri, "Turbidimeter design and analysis: A review on optical fiber sensors for the measurement of water turbidity," Oct. 2009. doi: 10.3390/s91008311.

[80] Fondriest Environmental Learning Center, "Measuring Turbidity, TSS, and Water Clarity." Accessed: Jan. 29, 2024. [Online]. Available: https://www.fondriest.com/environmental-measurements/measurements/measuring-water-quality/turbidity-sensors-meters-and-methods/

[81] M. Sadar, "Turbidity Measurement: A Simple, Effective Indicator of Water Quality Change."

[82] Usepa, "Method 180.1: Determination of Turbidity by Nephelometry," 1993.

[83] U. Epa, O. of Ground Water, and D. Water, "Guidance Manual for Compliance with the Surface Water Treatment Rules: Turbidity Provisions."

[84] "Water quality-Determination of turbidity-Part 1," 2016.

[85] B. G. B. Kitchener, J. Wainwright, and A. J. Parsons, "A review of the principles of turbidity measurement," *Prog Phys Geogr*, vol. 41, no. 5, pp. 620–642, Oct. 2017, doi: 10.1177/0309133317726540.

[86] A. Rymszewicz *et al.*, "Measurement differences between turbidity instruments, and their implications for suspended sediment concentration and load calculations: A sensor inter-comparison study," *J Environ Manage*, vol. 199, pp. 99–108, Sep. 2017, doi: 10.1016/j.jenvman.2017.05.017.

[87] USGS, "Chapter A6. Section 6.7. Turbidity," 2005. doi: 10.3133/twri09A6.7.

[88] F. GANTOIS (LNE), N. GUIGUES (LNE), S. RAVEAU (LNE), B. LEPOT (INERIS), and F. GAL (BRGM), "Panorama de l'existant sur les capteurs et analyseurs en ligne pour la mesure des paramètres physico-chimiques dans l'eau," 2017.

[89] C. D. Fay and A. Nattestad, "Advances in optical based turbidity sensing using led photometry (Pedd)," *Sensors*, vol. 22, no. 1, 2022, doi: 10.3390/s22010254.

[90] B. G. B. Kitchener *et al.*, "A low-cost bench-top research device for turbidity measurement by radially distributed illumination intensity sensing at multiple wavelengths," *HardwareX*, vol. 5, Apr. 2019, doi: 10.1016/j.ohx.2019.e00052.

[91] D. Gillett and A. Marchiori, "A low-cost continuous turbidity monitor," *Sensors (Switzerland)*, vol. 19, no. 14, Jul. 2019, doi: 10.3390/s19143039.

[92] J. Trevathan, W. Read, and S. Schmidtke, "Towards the development of an affordable and practical light attenuation turbidity sensor for remote near real-time aquatic monitoring," *Sensors (Switzerland)*, vol. 20, no. 7, 2020, doi: 10.3390/s20071993.

[93] Z. Zang *et al.*, "A novel low-cost turbidity sensor for in-situ extraction in TCM using spectral components of transmitted and scattered light," *Measurement (Lond)*, vol. 160, Aug. 2020, doi: 10.1016/j.measurement.2020.107838.

[94] T. Matos, C. L. Faria, M. S. Martins, R. Henriques, P. A. Gomes, and L. M. Goncalves, "Development of a cost-effective optical sensor for continuous monitoring of turbidity and suspended particulate matter in marine environment," *Sensors (Switzerland)*, vol. 19, no. 20, Oct. 2019, doi: 10.3390/s19204439.

[95] M. Metzger *et al.*, "Low-cost GRIN-Lens-based nephelometric turbidity sensing in the range of 0.1–1000 NTU," *Sensors (Switzerland)*, vol. 18, no. 4, Apr. 2018, doi: 10.3390/s18041115.

[96] L. Parra, J. Rocher, J. Escrivá, and J. Lloret, "Design and development of low cost smart turbidity sensor for water quality monitoring in fish farms," *Aquac Eng*, vol. 81, pp. 10–18, May 2018, doi: 10.1016/j.aquaeng.2018.01.004.

References

[97] C. D. Kelley *et al.*, "An affordable open-source turbidimeter," *Sensors (Switzerland)*, vol. 14, no. 4, pp. 7142–7155, Apr. 2014, doi: 10.3390/s140407142.

[98] E. W. Rice, "The preparation of formazin standards for nephelometry," *Anal Chim Acta*, vol. 87, no. 1, pp. 251–253, Nov. 1976, doi: 10.1016/S0003-2670(01)83146-9.

[99] R. Davies-Colley, A. O. Hughes, A. G. Vincent, and S. Heubeck, "Weak numerical comparability of <scp>ISO</scp> -7027-compliant nephelometers. Ramifications for turbidity measurement applications," *Hydrol Process*, vol. 35, no. 12, Dec. 2021, doi: 10.1002/hyp.14399.

[100] B. G. B. Kitchener *et al.*, "A low-cost bench-top research device for turbidity measurement by radially distributed illumination intensity sensing at multiple wavelengths," *HardwareX*, vol. 5, p. e00052, Apr. 2019, doi: 10.1016/j.ohx.2019.e00052.

[101] W. L. Hakim, L. Hasanah, B. Mulyanti, and A. Aminudin, "Characterization of turbidity water sensor SEN0189 on the changes of total suspended solids in the water," in *Journal of Physics: Conference Series*, Institute of Physics Publishing, Nov. 2019. doi: 10.1088/1742-6596/1280/2/022064.

[102] J. Droujko and P. Molnar, "Open-source, low-cost, in-situ turbidity sensor for river network monitoring," *Sci Rep*, vol. 12, no. 1, Dec. 2022, doi: 10.1038/s41598-022-14228-4.

[103] B. T. Phillips *et al.*, "DEEPi: A miniaturized, robust, and economical camera and computer system for deep-sea exploration: A miniaturized deep-sea camera system," *Deep Sea Res 1 Oceanogr Res Pap*, vol. 153, Nov. 2019, doi: 10.1016/j.dsr.2019.103136.

[104] B. G. B. Kitchener, J. Wainwright, and A. J. Parsons, "A review of the principles of turbidity measurement," *Prog Phys Geogr*, vol. 41, no. 5, pp. 620–642, Oct. 2017, doi: 10.1177/0309133317726540.

[105] A. Rymszewicz *et al.*, "Measurement differences between turbidity instruments, and their implications for suspended sediment concentration and load calculations: A sensor inter-comparison study," *J Environ Manage*, vol. 199, pp. 99–108, Sep. 2017, doi: 10.1016/j.jenvman.2017.05.017.

[106] B. Nguyen, B. Goto, J. S. Selker, and C. Udell, "Hypnos board: A low-cost all-in-one solution for environment sensor power management, data storage, and task scheduling," *HardwareX*, vol. 10, 2021, doi: 10.1016/j.ohx.2021.e00213.

[107] A. Thaler, K. Sturdivant, R. Neches, and I. Black, "OpenCTD Construction and Operation."

[108] A. M. Nightingale *et al.*, "A Droplet Microfluidic-Based Sensor for Simultaneous in Situ Monitoring of Nitrate and Nitrite in Natural Waters," *Environ Sci Technol*, vol. 53, no. 16, pp. 9677–9685, 2019, doi: 10.1021/acs.est.9b01032.

[109] Paulmier and Aurélien, "Oxygen and the ocean," 2017.

[110] X. D. Wang and O. S. Wolfbeis, "Optical methods for sensing and imaging oxygen: Materials, spectroscopies and applications," May 21, 2014, *Royal Society of Chemistry*. doi: 10.1039/c4cs00039k.

[111] Robert G. Wetz, "Limnology: Lake and River Ecosystems (3rd ed.)," San Diego, 2001.

[112] A. M. Mavropoulou, V. Vervatis, and S. Sofianos, "Dissolved oxygen variability in the Mediterranean Sea," *Journal of Marine Systems*, vol. 208, Aug. 2020, doi: 10.1016/j.jmarsys.2020.103348.

[113] R. J. Matear, A. C. Hirst, and B. I. McNeil, "Changes in dissolved oxygen in the Southern Ocean with climate change," *Geochemistry, Geophysics, Geosystems*, vol. 1, no. 11, Nov. 2000, doi: 10.1029/2000GC000086.

[114] K. P. Helm, N. L. Bindoff, and J. A. Church, "Observed decreases in oxygen content of the global ocean," *Geophys Res Lett*, vol. 38, no. 23, Dec. 2011, doi: 10.1029/2011GL049513.

[115] Manca B, Burca M, Giorgetti A, and et al, "Physical and biochemical averaged vertical profiles in the Mediterranean regions- an important tool to trace the climatology of water masses and to validate incoming data from operational oceanography," 2004, doi: 10.1016/j.jmarsys.2003.11.025.

[116] APHA, "Standard Methods for the Examination of Water and Wastewater," 1999.

[117] P. Webb, "Introduction to Oceanography 5.4 Dissolved Gases: Oxygen."

[118] U. Geological Survey, "Dissolved Oxygen Chapter 6.2 of Section A, National Field Manual for the Collection of Water-Quality Data Book 9, Handbooks for Water-Resources Investigations."

References

[119] "Volunteer Stream Monitoring: A Methods Manual," 1997.
[120] YSI, "The Dissolved Oxygen Handbook," 2009.
[121] O. S. Wolfbeis, "Luminescent sensing and imaging of oxygen: Fierce competition to the Clark electrode," *BioEssays*, vol. 37, no. 8, pp. 921–928, Aug. 2015, doi: 10.1002/bies.201500002.
[122] M. V. Miniaev, M. B. Belyakova, N. V. Kostiuk, D. V. Leshchenko, and T. A. Fedotova, "Non-obvious Problems in Clark Electrode Application at Elevated Temperature and Ways of Their Elimination," *J Anal Methods Chem*, vol. 2013, pp. 1–8, 2013, doi: 10.1155/2013/249752.
[123] H. C. Bittig *et al.*, "Oxygen Optode Sensors: Principle, Characterization, Calibration, and Application in the Ocean," *Front Mar Sci*, vol. 4, Jan. 2018, doi: 10.3389/fmars.2017.00429.
[124] M. A. Omary and H. H. Patterson, "Luminescence, theory," in *Encyclopedia of Spectroscopy and Spectrometry*, Elsevier, 2016, pp. 636–653. doi: 10.1016/B978-0-12-803224-4.00193-X.
[125] PreSens, "Instruction Manual Oxygen Sensor Spots PSt3 / PSt6 SENSOR PROBES," 2021.
[126] C. Mcdonagh *et al.*, "Phase ¯uorometric dissolved oxygen sensor."
[127] Osram, "LV T64G TOPLED ® Black."
[128] Limileds, "IllumInatIon DS68 LUXEON Rebel Color Line Product Datasheet."
[129] Vishay, "Silicon PIN Photodiode BPW34, BPW34S." [Online]. Available: www.vishay.com/doc?91000
[130] A. Devices, "Low-Voltage, Phase-Reversal Analog Switch MAX4528."
[131] L. Technology Corporation, "LT1800 - 80MHz, 25V/µs Low Power Rail-to-Rail Input and Output Precision Op Amp."
[132] Texas Instruments, "OPA380 - Precision, High-Speed Transimpedance Amplifier."
[133] A. Devices, "AD8302 LF-2.7 GHz RF/IF Gain and Phase Detector FUNCTIONAL BLOCK DIAGRAM."
[134] B. Venzac *et al.*, "PDMS Curing Inhibition on 3D-Printed Molds: Why? Also, How to Avoid It?," *Anal Chem*, vol. 93, no. 19, pp. 7180–7187, May 2021, doi: 10.1021/acs.analchem.0c04944.
[135] D. R. Santoso, B. Pitaloka, C. S. Widodo, and U. P. Juswono, "Low-cost, compact, and rapid bio-impedance spectrometer with real-time bode and nyquist plots," *Applied Sciences (Switzerland)*, vol. 10, no. 3, Feb. 2020, doi: 10.3390/app10030878.
[136] H. Uchida, G.C. Johnson, and K.E. McTaggart, "CTD Oxygen Sensor Calibration Procedures," 2010.
[137] Wei Gao, "The Solar Radiation Spectrum."
[138] T. J. B. Carruthers, B. J. Longstaff, W. C. Dennison, E. G. Abal, and K. Aioi, "Chapter t9 Measurement of light penetration in relation to seagrass Chapter Objective."
[139] J. J. Cole and M. L. Pace, "The Discipline of Limnology," in *Encyclopedia of Inland Waters*, Elsevier, 2022, pp. 11–18. doi: 10.1016/B978-0-12-819166-8.00006-2.
[140] J. T. 0 Kirk, "Spectral Distribution of Photosynthetically Active Radiation in some South-eastern Australian Waters," 1979.
[141] NOAA, "Learning Ocean Science through Ocean Exploration Section 5: Ocean Zones."
[142] K. J. Mccree, "2 Photosynthetically Active Radiation."
[143] E. Bäumker, D. Zimmermann, S. Schierle, and P. Woias, "A novel approach to obtain par with a multi-channel spectral microsensor, suitable for sensor node integration," *Sensors*, vol. 21, no. 10, May 2021, doi: 10.3390/s21103390.
[144] K. J. Mccree, "TEST OF CURRENT DEFINITIONS OF PHOTOSYNTHETICALLY ACTIVE RADIATION AGAINST LEAF PHOTOSYNTHESIS DATA."
[145] T. BAT-OYUN, M. SHINODA, and M. TSUBO, "Effects of cloud, atmospheric water vapor, and dust on photosynthetically active radiation and total solar ra-diation in a Mongolian grassland," *J Arid Land*, vol. 4, no. 4, pp. 349–356, Sep. 2012, doi: 10.3724/sp.j.1227.2012.00349.
[146] B. Hu, Y. Wang, and G. Liu, "Spatiotemporal characteristics of photosynthetically active radiation in China," *Journal of Geophysical Research Atmospheres*, vol. 112, no. 14, Jul. 2007, doi: 10.1029/2006JD007965.
[147] K. J. Mccree, "THE MEASUREMENT OF PHOTOSYNTHETICALLY ACTIVE RADIATION," Pergamon Press, 1973.

References

[148] A. Valente *et al.*, "A compilation of global bio-optical in situ data for ocean colour satellite applications – version three," *Earth Syst Sci Data*, vol. 14, no. 12, pp. 5737–5770, Dec. 2022, doi: 10.5194/essd-14-5737-2022.

[149] R. Jegan, W. D. Leon-Salas, M. A. Vizcardo, and M. Postigo-Malaga, "Photosynthetically Active Radiation (PAR): A Review of Sensing Solutions," 2023, *Tamkang University*. doi: 10.6180/jase.202303_26(3).0010.

[150] M. Mõttus, M. Sulev, F. Baret, R. Lopez-Lozano, and A. Reinart, "Photosynthetically Active Radiation: Measurement and Modeling," in *Encyclopedia of Sustainability Science and Technology*, New York, NY: Springer New York, 2012, pp. 7902–7932. doi: 10.1007/978-1-4419-0851-3_451.

[151] Y. Zhang, L. O. H. Wijeratne, S. Talebi, and D. J. Lary, "Machine Learning for Light Sensor Calibration," *Sensors*, vol. 21, no. 18, p. 6259, Sep. 2021, doi: 10.3390/s21186259.

[152] Y. Dong and H. Hansen, "Design of an Internet of Things (IoT)-Based Photosynthetically Active Radiation (PAR) Monitoring System," *AgriEngineering*, vol. 6, no. 1, pp. 773–785, Mar. 2024, doi: 10.3390/agriengineering6010044.

[153] J. Rajendran, W. D. Leon-Salas, X. Fan, Y. Zhang, M. A. Vizcardo, and M. Postigo, "On the Development of a Low-Cost Photosynthetically Active Radiation (PAR) Sensor," in *2020 IEEE International Symposium on Circuits and Systems (ISCAS)*, IEEE, Oct. 2020, pp. 1–5. doi: 10.1109/ISCAS45731.2020.9181220.

[154] D. Langis, P. J. Stabeno, C. Meinig, C. W. Mordy, S. W. Bell, and H. M. Tabisola, "Low-Cost Expendable Buoys for Under Ice Data Collection," in *OCEANS 2018 MTS/IEEE Charleston*, IEEE, Oct. 2018, pp. 1–9. doi: 10.1109/OCEANS.2018.8604752.

[155] M. H. Long, J. E. Rheuban, P. Berg, and J. C. Zieman, "A comparison and correction of light intensity loggers to photosynthetically active radiation sensors," *Limnol Oceanogr Methods*, vol. 10, no. 6, pp. 416–424, Jun. 2012, doi: 10.4319/lom.2012.10.416.

[156] D. A. Bartholomeusz, R. W. Boutte, and J. D. Andrade, "Xurography: rapid prototyping of microstructures using a cutting plotter," *Journal of Microelectromechanical Systems*, vol. 14, no. 6, pp. 1364–1374, Dec. 2005, doi: 10.1109/JMEMS.2005.859087.

[157] H. R. Barnard, M. C. Findley, and J. Csavina, "PARduino: a simple and inexpensive device for logging photosynthetically active radiation," *Tree Physiol*, vol. 34, no. 6, pp. 640–645, Jun. 2014, doi: 10.1093/treephys/tpu044.

[158] R. B. Domingues and A. B. Barbosa, "Evaluating Underwater Light Availability for Phytoplankton: Mean Light Intensity in the Mixed Layer versus Attenuation Coefficient," *Water (Basel)*, vol. 15, no. 16, p. 2966, Aug. 2023, doi: 10.3390/w15162966.

[159] C. Rodero, E. Olmedo, R. Bardaji, and J. Piera, "New Radiometric Approaches to Compute Underwater Irradiances: Potential Applications for High-Resolution and Citizen Science-Based Water Quality Monitoring Programs," *Sensors*, vol. 21, no. 16, p. 5537, Aug. 2021, doi: 10.3390/s21165537.

[160] R. Bardaji, A.-M. Sánchez, C. Simon, M. Wernand, and J. Piera, "Estimating the Underwater Diffuse Attenuation Coefficient with a Low-Cost Instrument: The KdUINO DIY Buoy," *Sensors*, vol. 16, no. 3, p. 373, Mar. 2016, doi: 10.3390/s16030373.

[161] P. May, J. Priestley, A. Lavoisier, and J. Ingenhousz, "Chlorophyll The green colour of plants."

[162] Muriel Gargaud, *Encyclopedia of Astrobiology*. Springer Berlin Heidelberg, 2011. doi: 10.1007/978-3-642-11274-4.

[163] University of Sydney, "Scientists discover first new chlorophyll in 60 years," 2010.

[164] J. Beskenis, R. W. Golledge, and G. Haas, "Appendix E CONNECTICUT RIVER WATERSHED 2003 Chlorophyll a and Periphyton Technical Memorandum Commonwealth of Massachusetts Executive Office of Environmental Affairs Division of Watershed Management," 2006.

[165] Roy, C. A. Llewellyn, E. S. Egeland, and G. Johnsen, "Phytoplankton pigments characterization, chemotaxonomy and applications in oceanography," 2011.

[166] Y. Huot, M. Babin, F. Bruyant, C. Grob, M. S. Twardowski, and H. Claustre, "Relationship between photosynthetic parameters and different proxies of phytoplankton biomass in the subtropical ocean," *Biogeosciences*, vol. 4, no. 5, pp. 853–868, Oct. 2007, doi: 10.5194/bg-4-853-2007.

References

[167] F. Chai *et al.*, "Monitoring ocean biogeochemistry with autonomous platforms," *Nat Rev Earth Environ*, vol. 1, no. 6, pp. 315–326, May 2020, doi: 10.1038/s43017-020-0053-y.

[168] K. Wirtz and S. L. Smith, "Vertical migration by bulk phytoplankton sustains biodiversity and nutrient input to the surface ocean," *Sci Rep*, vol. 10, no. 1, p. 1142, Jan. 2020, doi: 10.1038/s41598-020-57890-2.

[169] C. Hu *et al.*, "Improving Satellite Global Chlorophyll *a* Data Products Through Algorithm Refinement and Data Recovery," *J Geophys Res Oceans*, vol. 124, no. 3, pp. 1524–1543, Mar. 2019, doi: 10.1029/2019JC014941.

[170] A. Earp *et al.*, "Review of fluorescent standards for calibration of in situ fluorometers: Recommendations applied in coastal and ocean observing programs," Cambridge University Press, 2010.

[171] J. Salaün and M. Le Menn, "In Situ Calibration of Wetlabs Chlorophyll Sensors: A Methodology Adapted to Profile Measurements," *Sensors*, vol. 23, no. 5, p. 2825, Mar. 2023, doi: 10.3390/s23052825.

[172] C. S. Roesler and A. H. Barnard, "Optical proxy for phytoplankton biomass in the absence of photophysiology: Rethinking the absorption line height," *Methods in Oceanography*, vol. 7, pp. 79–94, 2013, doi: 10.1016/j.mio.2013.12.003.

[173] Miguel Dionisio Pires, "Evaluation of fluorometers for the in situ monitoring of chlorophyll and/or cyanobacteria," 2010.

[174] C. Roesler *et al.*, "Recommendations for obtaining unbiased chlorophyll estimates from in situ chlorophyll fluorometers: A global analysis of WET Labs ECO sensors," *Limnol Oceanogr Methods*, vol. 15, no. 6, pp. 572–585, Jun. 2017, doi: 10.1002/lom3.10185.

[175] L. Zeng and D. Li, "Development of In Situ Sensors for Chlorophyll Concentration Measurement," *J Sens*, vol. 2015, pp. 1–16, 2015, doi: 10.1155/2015/903509.

[176] Y. Pan and L. Qiu, "A Submersible in-Situ Highly Sensitive Chlorophyll Fluorescence Detection System," *IOP Conf Ser Mater Sci Eng*, vol. 677, no. 2, p. 022065, Dec. 2019, doi: 10.1088/1757-899X/677/2/022065.

[177] K. T. Park, J. J. Creelman, A. S. Chua, T. S. Chambers, A. M. MacNeill, and V. J. Sieben, "A Low-Cost Fluorometer Applied to the Gulf of Saint Lawrence Rhodamine Tracer Experiment," *IEEE Sens J*, vol. 23, no. 15, pp. 16772–16787, Aug. 2023, doi: 10.1109/JSEN.2023.3283977.

[178] J. J. Creelman, "Low-Cost Submersible Fluorometer for Fresh and Marine Water Environments," 2022.

[179] W. Kirkey and W. H. Coulter, "New Designs for Submersible Water Quality Instrumentation Which Achieve High In Situ Accuracy at Low Total Cost," 2019.

[180] C. Schmechtig, H. Claustre, A. Poteau, C. Schallenberg, T. W. Trull, and X. Xing, "Biogeochemical-Argo quality control manual for chlorophyll-a concentration and chl-fluorescence Version 3.0 September 30th 2023 Argo data management Biogeochemical-Argo quality control manual for chlorophyll-a concentration", doi: 10.13155/35385.

[181] M. Yoshida, T. Horiuchi, and Y. Nagasawa, "In situ multi-excitation chlorophyll fluorometer for phytoplankton measurements: Technologies and applications beyond conventional fluorometers," in *OCEANS'11 MTS/IEEE KONA*, IEEE, Sep. 2011, pp. 1–4. doi: 10.23919/OCEANS.2011.6107049.

[182] S. E. Zieger, S. Seoane, A. Laza-Martínez, A. Knaus, G. Mistlberger, and I. Klimant, "Spectral Characterization of Eight Marine Phytoplankton Phyla and Assessing a Pigment-Based Taxonomic Discriminant Analysis for the in Situ Classification of Phytoplankton Blooms," *Environ Sci Technol*, vol. 52, no. 24, pp. 14266–14274, Dec. 2018, doi: 10.1021/acs.est.8b04528.

[183] S. E. Zieger, G. Mistlberger, L. Troi, A. Lang, F. Confalonieri, and I. Klimant, "Compact and Low-Cost Fluorescence Based Flow-Through Analyzer for Early-Stage Classification of Potentially Toxic Algae and in Situ Semiquantification," *Environ Sci Technol*, vol. 52, no. 13, pp. 7399–7408, Jul. 2018, doi: 10.1021/acs.est.8b00578.

[184] J. R. Morrison, "In situ determination of the quantum yield of phytoplankton chlorophyll *a* fluorescence: A simple algorithm, observations, and a model," *Limnol Oceanogr*, vol. 48, no. 2, pp. 618–631, Mar. 2003, doi: 10.4319/lo.2003.48.2.0618.

References

[185] Hannes Truter, "Using Low Cost Components To Determine Chlorophyll Concentration By Measuring Fluorescence Intensity Hannes Truter," 2015.

[186] E. Luy, J. Smith, I. Grundke, C. Sonnichsen, A. Furlong, and V. Sieben, "Two chemistries on a single lab-on-chip: Nitrate and orthophosphate sensing underwater with inlaid microfluidics," *Frontiers in Sensors*, vol. 3, Dec. 2022, doi: 10.3389/fsens.2022.1080020.

[187] A. M. Nightingale, S. Hassan, K. Makris, W. T. Bhuiyan, T. J. Harvey, and X. Niu, "Easily fabricated monolithic fluoropolymer chips for sensitive long-term absorbance measurement in droplet microfluidics," *RSC Adv*, vol. 10, no. 51, pp. 30975–30981, 2020, doi: 10.1039/D0RA05330A.

[188] B. Yang, M. C. Patsavas, R. H. Byrne, and J. Ma, "Seawater pH measurements in the field: A DIY photometer with 0.01 unit pH accuracy," *Mar Chem*, vol. 160, pp. 75–81, Mar. 2014, doi: 10.1016/j.marchem.2014.01.005.

[189] J. Heber, "Nobel Prize 2014: Akasaki, Amano & Nakamura," *Nat Phys*, vol. 10, no. 11, pp. 791–791, Nov. 2014, doi: 10.1038/nphys3147.

[190] T. Leeuw, E. Boss, and D. Wright, "In situ Measurements of Phytoplankton Fluorescence Using Low Cost Electronics," *Sensors*, vol. 13, no. 6, pp. 7872–7883, Jun. 2013, doi: 10.3390/s130607872.

[191] F. Sekli Belaïdi *et al.*, "Towards integrated multi-sensor platform using dual electrochemical and optical detection for on-site pollutant detection in water," *Biosens Bioelectron*, vol. 132, pp. 90–96, May 2019, doi: 10.1016/j.bios.2019.01.065.

[192] A. Llobera, S. Demming, H. N. Joensson, J. Vila-Planas, H. Andersson-Svahn, and S. Büttgenbach, "Monolithic PDMS passband filters for fluorescence detection," *Lab Chip*, vol. 10, no. 15, p. 1987, 2010, doi: 10.1039/c003575k.

[193] Abdelnaby. Khalyfa, Selim. Kermasha, and Inteaz. Alli, "Extraction, purification, and characterization of chlorophylls from spinach leaves," *J Agric Food Chem*, vol. 40, no. 2, pp. 215–220, Feb. 1992, doi: 10.1021/jf00014a010.

[194] S. W. Jeffrey and G. F. Humphrey, "New spectrophotometric equations for determining chlorophylls a, b, c1 and c2 in higher plants, algae and natural phytoplankton," *Biochemie und Physiologie der Pflanzen*, vol. 167, no. 2, pp. 191–194, 1975, doi: 10.1016/S0015-3796(17)30778-3.

[195] R. J. Ritchie, "Consistent Sets of Spectrophotometric Chlorophyll Equations for Acetone, Methanol and Ethanol Solvents," *Photosynth Res*, vol. 89, no. 1, pp. 27–41, Jul. 2006, doi: 10.1007/s11120-006-9065-9.

[196] L. Orozco, "Optimizing Precision Photodiode Sensor Circuit Design."

[197] S.W. Jeffrey, R.F.C. Mantoura, and S.W. Wright, "Phytoplankton pigments in oceanography : guidelines to modern methods," 1997.

[198] A. Thaler, K. Sturdivant, R. Neches, and J. Levenson, "The OpenCTD: A Low-Cost, Open-Source CTD for Collecting Baseline Oceanographic Data in Coastal Waters," *Oceanography*, 2024, doi: 10.5670/oceanog.2024.602.

[199] K. Murphy *et al.*, "A low-cost autonomous optical sensor for water quality monitoring," *Talanta*, vol. 132, pp. 520–527, Jan. 2015, doi: 10.1016/j.talanta.2014.09.045.

[200] R. I. Chowdhury, K. A. Wahid, K. Nugent, and H. Baulch, "Design and Development of Low-Cost, Portable, and Smart Chlorophyll-A Sensor," *IEEE Sens J*, vol. 20, no. 13, pp. 7362–7371, Jul. 2020, doi: 10.1109/JSEN.2020.2978758.

[201] B. Nguyen, B. Goto, J. S. Selker, and C. Udell, "Hypnos board: A low-cost all-in-one solution for environment sensor power management, data storage, and task scheduling," *HardwareX*, vol. 10, p. e00213, Oct. 2021, doi: 10.1016/j.ohx.2021.e00213.

[202] "Tutorial: Using an MS5803 pressure sensor with Arduino." Accessed: Apr. 08, 2024. [Online]. Available: https://thecavepearlproject.org/2014/03/27/adding-a-ms5803-02-high-resolution-pressure-sensor/

[203] B. Venzac *et al.*, "PDMS Curing Inhibition on 3D-Printed Molds: Why? Also, How to Avoid It?," *Anal Chem*, vol. 93, no. 19, pp. 7180–7187, May 2021, doi: 10.1021/acs.analchem.0c04944.

[204] "EXO User Manual. Advanced water quality monitoring platform. ITEM# 603789REF REVISION K."

References

RÉPUBLIQUE FRANÇAISE
Liberté
Égalité
Fraternité

Université de Toulouse

Titre : Développement d'une sonde multiparamètres à bas coût pour les eaux marines et continentales

Mots clés : oxygène dissous, lumière photosynthétique active, turbidité, fluorescence

Résumé : L'observation de l'océan est essentielle pour mieux comprendre l'impact du changement climatique sur son métabolisme, l'absorption du carbone, la production primaire et de nombreux autres paramètres directement liés à la société humaine et à toutes les formes de vie. Si la télédétection fournit des données extrêmement précieuses, les capteurs in situ restent essentiels pour comprendre les processus physiques et biogéochimiques complexes. Il existe sur le marché différents capteurs capables d'effectuer les mesures requises, tels que les flotteurs Argo : ces flotteurs sont capables d'établir des profils verticaux dans la colonne d'eau tout en mesurant la conductivité, la température et la profondeur. Les flotteurs biogéochimiques-Argo (BGC) ont récemment ajouté des paramètres tels que l'oxygène, les nitrates, la chlorophylle et le pH à la liste des variables acquises par les flotteurs Argo standard. Malgré le succès de ce programme international, l'un des facteurs les plus limitants de ces flotteurs est directement lié à leur coût, qui se situe entre 10 000 et 15 000 euros par unité dans le cas d'Argo, et autour de 100 000 euros pour un BGC Argo. Étant donné qu'environ 40 % de la population mondiale vit à moins de 100 km des côtes, il est particulièrement important de renforcer notre capacité à collecter des données dans ces zones clés afin d'améliorer les mesures spatiales et temporelles. Les zones côtières ne peuvent pas être mesurées avec précision par télédétection et ne sont pas encore couvertes de manière routinière par le programme Argo ; ceci est réalisé par divers programmes et observatoires (comme COAST-HF).
Pour tous ces cas d'utilisation, les océanographes expriment le besoin d'avoir accès à des capteurs abordables, compacts, de faible puissance, robustes et capables de fonctionner in situ dans des endroits éloignés sans intervention humaine pendant de longues périodes. Le projet OpenProbe vise à fournir un dispositif à bas coût pour compléter ces systèmes d'observation in-situ existants en développant une sonde multi-paramétrique à bas coût qui peut être intégrée dans tous les types de vecteurs marins (drones, profileurs, bouées...). Les paramètres mesurés sont la conductivité, la température, la profondeur (CTD), l'oxygène dissous, la chlorophylle a, la turbidité et le rayonnement photosynthétiquement actif. L'objectif principal est de fournir une précision, une résolution et une gamme dynamique appropriées pour chaque paramètre afin de générer des données utiles, à une fraction du coût des solutions actuelles telles que les sondes multiparamètres. Pour ce faire, notre approche repose sur l'utilisation de composants commerciaux disponibles sur étagère (COTS) qui sont réaffectés de leur utilisation principale et transformés en capteurs environnementaux. L'intégration et la marinisation sont réalisées à l'aide de techniques de prototypage rapide telles que la stéréolithographie, la xurographie ou le surmoulage. Une stratégie modulaire, open-source/open-hardware garantit que le système peut être facilement reproduit ou modifié par des utilisateurs potentiels pour des cas d'utilisation spécifiques, et ouvre la voie à des projets de science citoyenne visant à accroître la couverture spatiale et temporelle des zones côtières.
En fin de compte, ce travail démontre la capacité de construire une sonde multiparamétrique fonctionnelle capable de mesurer sept paramètres pour un coût de fabrication inférieur à 300 € avec des performances adéquates pour générer des données scientifiquement significatives. Ces données pourraient, dans un avenir proche, contribuer à la surveillance des zones côtières, à la compréhension de la circulation océanique, des processus climatiques et des phénomènes liés au changement climatique.

Title: Development of a low-cost multi-parameter probe for marine and continental waters

Key words: dissolved oxygen, photosynthetically active radiation, turbidity, fluorescence

Abstract: Observing the ocean is crucial for enhancing our comprehension of the impact climate change has on its metabolism, carbon uptake, primary production, and many other parameters directly linked to human society and all forms of life. While remote sensing delivers extremely valuable data, in-situ sensors are still essential for understanding the complex physical and biogeochemical processes. Various sensors are available on the market that can perform the required measurements, such as Argo floats: these floats are capable of making vertical profiles in the water column while measuring Conductivity, Temperature, and Depth. Biogeochemical-Argo (BGC) floats have recently added parameters such as oxygen, nitrate, chlorophyll, and pH to the list of variables acquired by standard Argo floats. Despite the success of this international program, one of the most limiting factors of these floats is directly related to their cost, which is between 10,000 and 15,000 euros per unit in the case of Argo, and around 100,000 euros for a BGC Argo. With about 40% of the world's population living within 100 km of the coast, reinforcing our ability to collect data in these key areas is particularly important for improving spatial and temporal measurements. Coastal areas cannot be accurately measured by remote sensing, and are currently not yet routinely covered by the Argo program; this is achieved by various programs and observatories (like COAST-HF).
For all these use-cases, oceanographers express the need to have access to affordable, compact, low-power, robust sensors with the ability to operate in-situ in remote locations without human intervention for long periods of time. The OpenProbe project aims to provide a low-cost device to complement these existing in-situ observation systems by developing a low-cost multi-parametric probe that can be integrated into all types of marine vectors (drones, profilers, buoys...). The parameters measured include conductivity, temperature, depth (CTD), dissolved oxygen, chlorophyll a, turbidity, and photosynthetically active radiation. The main objective is to deliver relevant accuracy, resolution, and dynamic range for each parameter to generate useful data, at a fraction of the cost of current solutions like multiparameter sondes. To do so, our approach builds upon the use of Commercial Off-The-Shelf (COTS) components which are repurposed from their primary use and turned into environmental sensors. Integration and marinization are achieved using rapid prototyping techniques like stereolithography, xurography, or overmolding. A modular, open-source/open-hardware strategy ensures that the system can be easily replicated or modified by potential users for specific use-cases, and paves the way towards citizen science projects to increase spatial and temporal coverage of coastal areas.
Ultimately, this work demonstrates the capability of building a functional multiparameter probe capable of measuring seven parameters for a manufacturing cost of less than 300€ with adequate performance to generate scientifically meaningful data. This data could, in the near future, contribute to the monitoring of coastal areas, understanding ocean circulation, climate processes, and phenomena related to climate change.